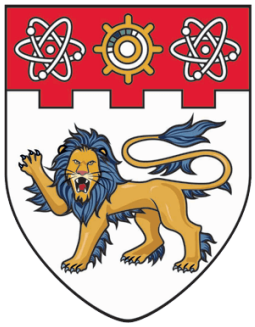

NANYANG TECHNOLOGICAL UNIVERSITY
SINGAPORE

RATIONAL CONSTRUCTION OF SELF-STANDING FIBER-SHAPED AQUEOUS RECHARGEABLE BATTERIES

YANG JIAO

SCHOOL OF ELECTRICAL & ELECTRONIC ENGINEERING

2020

Rational Construction of Self-Standing Fiber-Shaped Aqueous Rechargeable Batteries

Yang Jiao

School of Electrical & Electronic Engineering

A thesis submitted to the Nanyang Technological University in partial fulfillment of the requirement for the degree of Doctor of Philosophy

2020

Statement of Originality

I hereby certify that the work embodied in this thesis is the result of original research, is free of plagiarised materials, and has not been submitted for a higher degree to any other University or Institution.

22/07/2020

. . . . . .

Date

Yang Jiao

. . . . . .

Yang Jiao

Supervisor Declaration Statement

I have reviewed the content and presentation style of this thesis and declare it is free of plagiarism and of sufficient grammatical clarity to be examined. To the best of my knowledge, the research and writing are those of the candidate except as acknowledged in the Author Attribution Statement. I confirm that the investigations were conducted in accord with the ethics policies and integrity standards of Nanyang Technological University and that the research data are presented honestly and without prejudice.

22/07/2020

. . . . . .

Date

. . . . . .

Wei Lei

Authorship Attribution Statement

This thesis contains material from two papers published in the following peer-reviewed journals in which I am listed as an author.

Chapter 4 is published as J. Yang, Q. Zhang, Z. Wang, Z. Wang, L. Kang, M. Qi, M. Chen, W. Liu, W. Gong, W. Lu, P. Shum, and L. Wei, Rational construction of self-standing sulphur-doped Fe_2O_3 anodes with promoted energy storage capability for wearable aqueous rechargeable NiCo-Fe batteries, Advanced Energy Materials, (2020).

The contributions of the co-authors are as follows:

- Prof. Wei, Prof. Shum and Dr. Zhang provided the initial project direction and edited the manuscript drafts.
- I prepared the manuscript drafts. The manuscript was revised by Dr. Zhang.
- I conducted the hydrothermal process, measured the electrodes and battery electrochemical properties, analyzed data, assembled the NiCo-Fe battery, conducted XRD measurement.
- Dr. L. Kang assisted in the sulfur-doping process.
- Dr. W. Gong and Dr. W. Lu performed DFT simulation and analyzed the relevant data.
- Z. Wang conducted the SEM measurement.
- Z. Wang conducted the TEM measurement.
- M. Qi, M. Chen and W. Liu helped in the discussion of flow behavior.

Chapter 5 is published as J. Yang, Z. Wang, Z. Wang, J. Zhang, Q. Zhang, P. Shum, and L. Wei, All metal phosphide electrodes for high-performance quasi-solid-state fiber-

shaped aqueous rechargeable Ni-Fe batteries, ACS Applied Materials & Interfaces 12, 12801-12808 (2020).

The contributions of the co-authors are as follows:

- Prof. Wei, Prof. Shum and Dr. Zhang provided the initial project direction and edited the manuscript drafts.
- I prepared the manuscript drafts. The manuscript was revised by Dr. Q. Zhang.
- I conducted the hydrothermal process and in situ phosphide, measured the electrodes and battery electrochemical properties, analyzed data, assembled the Ni-Fe battery, and conducted the part of XRD measurement.
- Z. Wang conducted the SEM measurement.
- Z. Wang conducted the TEM measurement.
- J. Zhang assisted in XRD measurement.

22/07/2020 Yang Jiao

. . . . . .

Date

. . . . . .

Yang Jiao

Contents

Acknowledgements

I would like to express my sincere thanks to all professors, colleagues and relatives who have given me help and support in my study and life in the last four years. Thanks for your kindness and encouragement all the way.

First of all, I would like to give my great appreciation to my professors Prof. Shum Ping and Prof. Wei Lei. My Ph.D. study was completed under their kind care and guidance. I felt very grateful to my supervisors for their care, support and selfless help in my study and life. In the past four years, I have been deeply influenced by their modest personality, profound knowledge, rigorous attitude towards life and the academic style. They have led me to set up a correct attitude towards scientific research and provided me a comfortable scientific research environment, so that I can grow up quickly and healthy. Here, I would like to express my sincere thanks and high respect to them.

I would like to express my gratitude to Dr. Zhang Qichong for his guidance and advice on the research projects. I would like to thank Dr. Zhang Nan, Dr. Xu Zhilin, Dr. Wu Zhifang, and Dr. Jin Yunxia for their guidance and assistance in scientific research and life. Thanks to Wang Zhe and Wang Zhixun for their help and support in the characterization experiments. I would like to thank Dr. Zhang Mengying, Dr. Li Huizi, Dr. Cui Dongyao, Dr. Luo Yuemei, Dr. Hu Wenchao, Dr. Zhang Hailiang, Dr. Chen Mengxiao, Dr. Zhang Ting, Dr. Wu Tingting, Dr. Zhang Jing, Dr. Chen Ming, Dr. Ma Shaoyang, Zang Jichao, Zheng Yu, Qi Miao, Wang Chenlu, they also provide me a lot of help and give me much joys to fulfill my daily life.

Finally yet importantly, thank my parents for raising me. They always put my study in the first place. They give me the greatest support and the most selfless love. Thanks to my brother, your silent support has been my motivation. Wish my family healthy and happy!

Summary

With the large consumption of non-renewable resources and the increasingly serious global environmental problems, the development of clean, efficient and abundant new energy has attracted great attention from all over the world. Among many new energy storage devices, aqueous batteries take advantage of high safety, low cost, and excellent ion conductivity, showing promising prospects for application in wearable energy storage. In addition, with the ever-growing consumer usage of portable and wearable electronics, small, flexible and lightweight, fiber-shaped batteries are regarded as promising energy supply devices. Aqueous nickel-based rechargeable batteries with the abundant constituent elements, low cost, and ultra-flat discharge plateau have attracted widespread attention. However, the problem of low energy density and short cycle life requires more attempts to improve the performance of the electrodes. Therefore, this thesis designs and prepares the flexible self-supporting electrodes through direct hydrothermal growth, sulfur doping and gas-solid phosphating methods to increase the volume/area capacity of the electrodes and construct the high-performance wearable aqueous batteries. The main research content is divided into the following parts:

A facile and cost-effective method strategy is reported to fabricate three-dimensionally well-aligned zinc-nickel-cobalt oxide@$Ni(OH)_2$ nanowire arrays on the carbon nanotube fibers as a promising heterostructure anode for fiber-shaped Ni-Zn batteries. Taking advantage of the accessible surface area, rich reaction sites and short electron/ion diffusion path of zinc-nickel-cobalt oxide@$Ni(OH)_2$ nanowire arrays, a high capacity of 2.07 mAh/cm^2 (516.7 mAh/g) and an impressive energy density of 3.71 mWh/cm^2 (916.6 Wh/kg) were achieved for our as-assembled fiber-shaped Ni-Zn batteries, outperforming most previously reported aqueous Zn-based batteries.

Successfully fabricating the sulfur-doped Fe_2O_3 nanowire arrays grown on carbon nanotube fibers as an innovative anode material. The novel developed S-Fe_2O_3 electrode is further demonstrated to deliver very high capacity equal to 0.81 mAh/cm^2 at 4 mA/cm^2.

This value is almost 6 times higher than of the pristine Fe_2O_3-based electrode. When a cathode containing zinc-nickel-cobalt oxide@$Ni(OH)_2$ NWAs heterostructures as cathode material was used, 0.45 mAh/cm^2 capacity and 67.32 mWh/cm^3 energy density were obtained for the fiber-shaped NiCo-Fe batteries containing polyvinyl alcohol-potassium hydroxide gel electrolyte.

A novel flexible Ni-Fe battery using all metal phosphides as electrodes on highly conductive fibers is successfully designed and fabricated with improved electrochemical performance. Hierarchical NiCoP nanosheet arrays and FeP nanowire arrays were fabricated firstly using hydrothermal synthesis then pursuant gas phosphating process. With the assistance of PVA-KOH gel electrolyte, the fiber-shaped aqueous rechargeable battery presented negligible capacity loss after bending 3000 times. Meanwhile, the assembled battery had a significant capacity of 0.294 mAh/cm^2 under the current density of 2 mA/cm^2 and a high energy density of 235.6 μWh/cm^2.

List of Figures

List of Tables

Chapter 1 Introduction

1.1 Background and Motivation

With the rapid development of human civilization and the global economy, non-renewable resources such as fossil energy (oil, coal and natural gas) is consumed in large amounts, accounting for more than 85% of the total global energy consumption and the reserves of fossil energy on the earth are limited. The growth of energy demand and the uncontrolled exploitation of fossil energy will inevitably trigger an energy crisis and even lead to the depletion of fossil energy[1]. At the same time, environmental pollution, greenhouse effect and other environmental problems caused by their massive combustion become increasingly serious. Therefore, the search for new energy systems and the development of new ways of energy are significant issues to be resolved in the worldwide.

According to the 2019 BP Statistical Yearbook on World Energy in Figure 1-1, the global energy market is in a transition period 2. Primary energy consumption rose by 1.3% last year less than half its rate in 2018 (2.8%). Global coal consumption fell for the fourth time in six years (-0.9 EJ). Renewable energy, including biofuels, is once again the fastest-growing source of energy. Growth was driven by renewables (3.2 EJ) and natural gas (2.8 EJ), which together contributed three quarters of the increase. Although the share of renewables in primary energy is only 4%, their growth rate accounts for nearly 30% of the growth in primary energy.

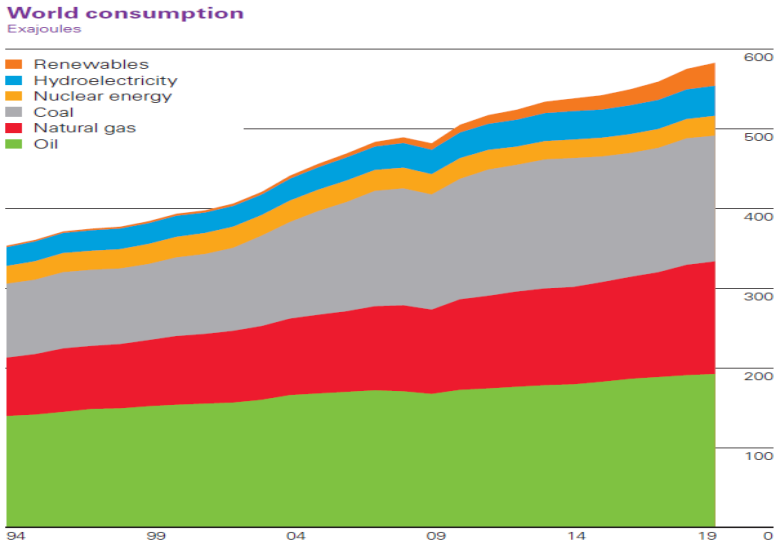

Figure 1-1 Diagram of global energy consumption between 1991 to 2019. [1]

New energy includes solar energy, biomass energy, nuclear energy, wind energy, geothermal energy, marine energy and other primary energy as well as hydrogen energy in secondary power sources. New energy materials are the core and fundamental materials used in the conversion and utilization of new energy and in the development of new energy technologies. In the process of new energy development, it is of great strategic significance to make full use of natural forces such as wind energy, tidal energy and solar energy to realize the sustainable development of human society[2-4]. However, due to the uneven distribution of renewable energy in space and time, it is highly vulnerable to natural factors. This results many technical problems in the efficient use of these energy sources. An important way to solve the above-mentioned problems is to convert renewable energy into electric energy, relying on the mature electric energy storage system to make it the main energy that can be utilized by human society[5]. Therefore, as shown in Figure 1-2, developing a cheap and efficient electric energy storage system is the main way to realize the efficient utilization of renewable energy. Energy storage could improve the performance of the power grid, facilitate wide spread use renewable energy on different scales, and enable transportation electrification and integration with the grid[6].

A power storage system is a process in which one kind of energy (mainly electricity) can be converted into another energy and converted back in different ways. As a result, stored energy can be converted into electricity to meet a variety of needs[7]. As shown in Figure 1-3, there are various types of power storage systems[8]. Electrochemical energy storage system has a series of excellent characteristics, such as pollution-free operation, high cycle efficiency, long cycle life, low maintenance cost and so on[9]. As an excellent energy storage technology, batteries can fully integrate renewable resources. Their compact size makes them well adapted to different needs. Electrochemical energy storage technology has a history of more than two hundred years and been widely used so far. It divided into three categories: supercapacitors, fluid flow batteries and rechargeable batteries [10-12].

As a charge storage device, a supercapacitor is similar to a battery in structure and design. The supercapacitor consists of two electrodes, an electrolyte and a diaphragm, of which the most important component is the electrode material. Normally, the electrodes of supercapacitors are made of nanomaterials with high specific surface area and high porosity [13]. According to the different storage mechanism, supercapacitors can be divided into two-layer capacitance mechanism and Faraday pseudocapacitance mechanism [14-16]. For double-layer capacitors, the capacitance mainly comes from the accumulation of charge at the electrode/electrolyte interface, so the capacitance of such capacitors is closely related to the specific surface area of the electrode material. For Faraday pseudocapacitance, the electroactive material generates capacitance through a fast, reversible Faraday process. Due to the different properties of different electrode materials, the two mechanisms can occur simultaneously on the same electrode[17-18]. Supercapacitors have been widely used in mobile devices and electric vehicles due to their advantages such as fast charging and discharging speed, long cycle life, quick response, strong power output capability and wide range of temperature. However, due to the low energy density caused by the working principle, the application of supercapacitors in large-scale energy storage systems is limited[19].

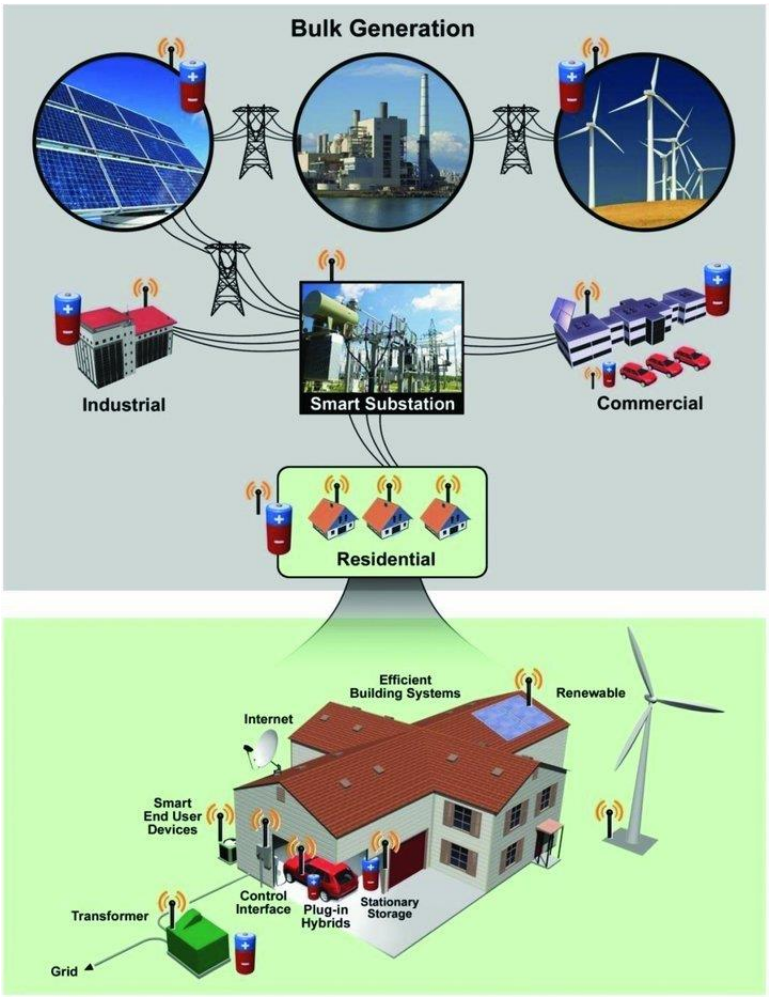

Figure 1-2 Future smart power grid.[7]

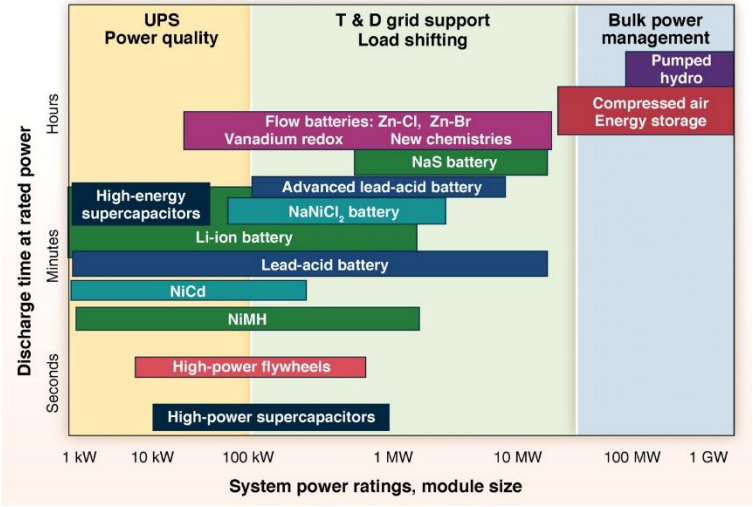

Figure 1-3 Comparison of discharge time and power rating for various energy storage system technologies.[8]

As early as the 1880s, researchers such as Maria Skyllas-Kazacos proposed operable liquid flow batteries [20]. As shown in Figure 1-4, the structure is composed of the electric reactor unit, electrolyte and electrolyte storage and supply unit, control and management unit, etc. The positive and negative electrodes are all redox pairs of electrolytes, which are stored in two storage tanks and circulated through the pump in the battery [21].

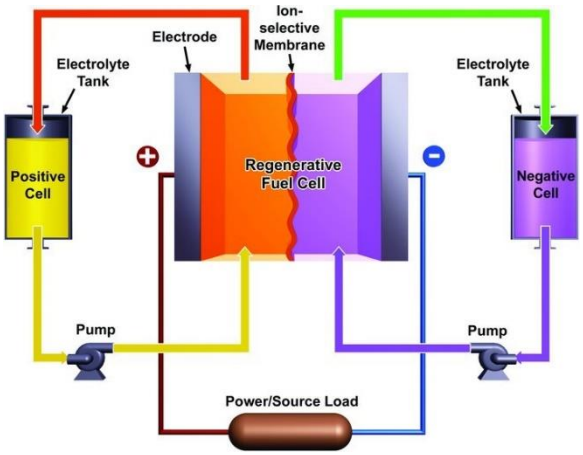

Figure 1-4 A schematic illustration of the structure of a redox flow battery.[21]

In a flow battery, the energy is controlled by the tank size, while the power is controlled by the battery area and the number of reactors[22]. The separation of power and energy allows fluid flow batteries to be designed to meet vastly different equipment requirements. At the same time, it is noted that in the liquid flow battery, the electrode only serves as the electrochemical active interface, where the redox reaction takes place. This mechanism prevents physical and chemical changes in the electrodes. In conventional batteries, however, the electrodes carry a variety of complex functions, such as phase transfer, crystal structure transformation, and morphological changes. In the flow battery, the electrode eliminates various physical and chemical processes so that the flow battery has a longer storage life. In addition, the liquid flow battery has the advantages of good safety and good thermal management ability[23-25]. However, the

low energy density and large volume of liquid, flow battery require complex auxiliary accessories, greatly reducing its reliability. At the same time, the high cost of materials such as electrodes and diaphragms and the poor selectivity of diaphragms reduce the energy efficiency and life of liquid flow batteries. Therefore, further exploration and research are needed to realize the wide application of liquid flow battery [26-29].

A rechargeable battery is a type of electrical battery that can be charged, discharged and recharged many times, as opposed to a disposable or primary battery, which is supplied fully charged and discarded after use. It is composed of one or more electrochemical cells. The redox reaction can be carried out in the rechargeable battery by using the electrode active material, and the conversion between chemical energy and electric energy can be realized. The rechargeable battery is generally a closed system and only energy exchange with the external environment. In general, the active substance is in non-separate conductive contact with the collector, and the positive and negative poles are separated by the diaphragm[30-31].

Meanwhile, with a growing demand for people who needs more portable, lighter and more economical products. Flexible electronics plays an important role in satisfying people's requirements, because they have the characteristics of low cost, small volume, portability, which have been widely used in these fields as shown in Figure 1-5. Therefore, the characteristics to achieve better wearability, energy storage devices must have the characteristics of high security, high flexibility and light quality to cope with different application environments. In many flexible energy storage devices, lithium ion batteries with high energy density and long cycle life has always been dominant[32-33]. However, the organic electrolytes used in conventional lithium-ion batteries are toxic and inflammability, which result in very big security risks, so it is not suitable for the power supply of wearable electronic devices[34-35].Aqueous batteries can effectively solve the problem, and has a high ionic conductivity and the characteristics of easy preparation. Therefore, aqueous rechargeable battery is considered as an ideal choice for energy supply of wearable devices [36-37]. Therefore, the development of high-performance flexible aqueous battery will contribute the great significance to the development of wearable electronic energy storage devices.

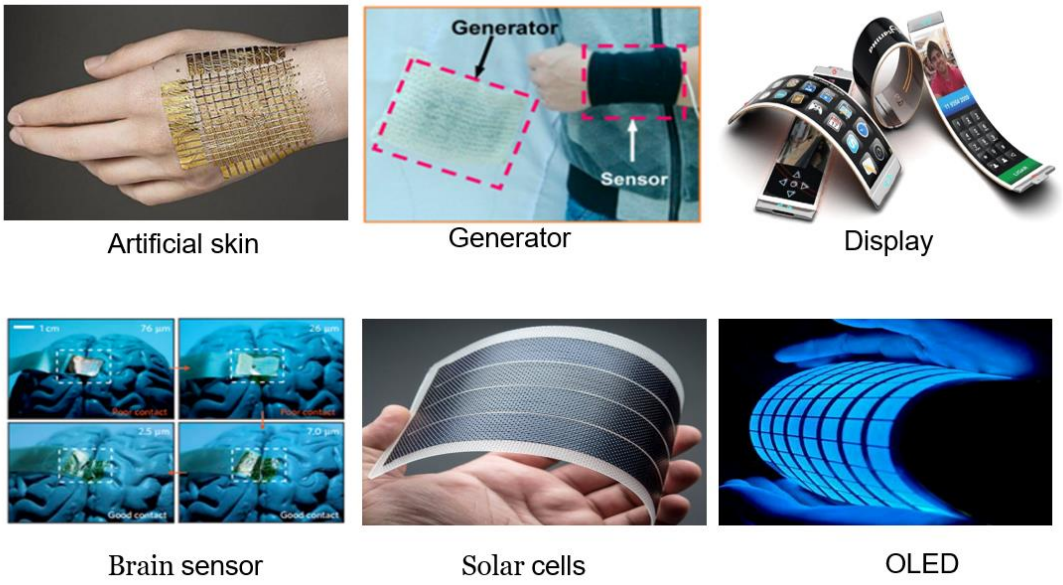

Figure 1-5 Different fields of applications of flexible electronics.

1.2 Objectives

In recent years, with the increasing consumption of fossil resources and the increasing environmental pollution, it becomes more and more important to achieve the clean and efficient storage of energy. Aqueous rechargeable batteries are characterized by high power density, fast charging and discharging speed and long service life. However, the low energy density of limits their further application in practice. Therefore, the development of high-energy batteries is an important issue that needs to be solved urgently. With the increasing developments towards miniaturization, portability, lightness and integration, the corresponding power supply devices also require wearable characteristics. In this thesis, we aim to design and prepare the flexible self-supporting electrodes through direct hydrothermal growth and subsequent gas-solid vapor deposition methods to increase the volume/area capacity of the electrodes and construct the high-performance wearable water-based battery. The main objectives of our works are:

1. To develop a facile and cost-effective method strategy to fabricate three-dimensionally well-aligned zinc-nickel-cobalt oxide@$Ni(OH)_2$ nanowire arrays (ZNCO@$Ni(OH)_2$ NWAs) on the carbon nanotube fiber (CNTF) using the simple hydrothermal method and subsequent the chemical solution deposition as a promising heterostructure cathode. The fabricated ZNCO@$Ni(OH)_2$ cathode matched with the high theoretical capacity of Zn anodes to construct the high-performance fiber-shaped Ni-Zn batteries.
2. To establish an effective strategy significantly improve the capacity, rate capability and cycling stability of Fe-based anode based on S-doped Fe_2O_3 NWAs due to their largely reduced band gap and the correspondingly enhanced electrical conductivity, making it an attractive anode for high-performance aqueous rechargeable NiCo-Fe batteries.
3. To demonstrate a new type of high-performance flexible Ni-Fe battery with binder-free electrodes on conductive carbon nanotube fibers. Hierarchical NiCoP nanosheet arrays (NSAs) and FeP NWAs grown directly on carbon nanotube fibers are fabricated firstly using hydrothermal synthesis then pursuant gas phosphating process. The adhesion of nanoscale materials to carbon nanotube not only reduces their own agglomeration but also prevents the accumulation of the carbon material, which increasing the specific surface area of the composite and improving the electrical conductivity.

1.3 Major Contribution

The novelty of the studies and my contributions to this thesis include:

1. Develop the flexible high-performance Ni-Zn batteries. A facile and cost-effective method strategy is reported to fabricate three-dimensionally well-aligned ZNCO@$Ni(OH)_2$ NWAs on a carbon nanotube fiber CNTF as a promising heterostructure cathode for fiber-shaped Ni-Zn batteries. Taking advantage of the accessible surface area, rich reaction sites and short electron/ion diffusion path of ZNCO@$Ni(OH)_2$ NWAs, a high capacity of 2.07 mAh/cm^2

(516.7 mAh/g) and an impressive energy density of 3.71 mWh/cm^2 (916.6 Wh/kg) are achieved for our as-assembled fiber-shaped Ni-Zn batteries, outperforming most previously reported aqueous Zn-based batteries.

2. Demonstrate the sulfur-doped Fe_2O_3 NWAs grown on carbon nanotube fibers as an innovative anode material. Through the first-principle calculations to calculate that S-doping in Fe_2O_3 can dramatically reduce the bandgap from 2.34 eV to 1.18 eV and thus enhance electronic conductivity. The novel developed S- Fe_2O_3 NWAs/CNTF electrode is further demonstrated to deliver very high capacity of 0.81 mAh/cm^2 at 4 mA/cm^2. This value is almost 6-fold higher than of the pristine Fe_2O_3 NWAs/CNTF electrode. When a cathode containing ZNCO@$Ni(OH)_2$ NWAs heterostructures is used, 0.46 mAh/cm^2 capacity and 67.32 mWh/cm^3 energy density are obtained for quasi-solid-state fiber-shaped NiCo-Fe batteries, which outperform most state-of-the-art fiber-shaped aqueous rechargeable batteries.
3. Construct a new type of high-performance flexible Ni-Fe battery with binder-free electrodes on conductive fiber substrates is successfully designed and fabricated. Hierarchical NiCoP NSAs and FeP NWAs grown directly on carbon nanotube fibers are fabricated firstly using hydrothermal synthesis then pursuant gas phosphating process. With the assistance of PVA-KOH gel electrolyte, the fiber-shaped aqueous rechargeable battery presents negligible capacity loss after bending 3000 times and shows excellent stability with the capacity retention rate of 89% after 4000 cycles. Meanwhile, the assembled rechargeable battery has a significant capacity of 0.294 mAh/cm^2 under 2 mA /cm^2 current density and a high volumetric energy density of 39.48 mWh/cm^3.

1.4 Organization

This thesis consists of six chapters:

Chapter 1 gives a brief introduction on the general background of the energy resources environment, the three different kinds of electrochemical energy storage and

demands of flexible batteries, as well as emphasizes on the objectives and scope of the research study. Meanwhile it states the motivations and the objectives of our works and outlines the thesis organization.

Chapter 2 reviews the literatures concerning the electrochemical mechanisms, structure and materials used in the aqueous rechargeable Ni-Zn and Ni-Fe batteries.

Chapter 3 demonstrates a facile and cost-effective method strategy to fabricate three-dimensionally well-aligned ZNCO@$Ni(OH)_2$ NWAs on the CNTF as a promising heterostructure cathode for fiber-shaped Ni-Zn batteries.

Chapter 4 describes an effective strategy significantly improve the capacity, rate capability and cycling stability of Fe-based anode based on S-doped Fe_2O_3 nanowire arrays due to their largely reduced band gap and the correspondingly enhanced electrical conductivity, making it an attractive anode for high-performance aqueous rechargeable NiCo-Fe batteries.

Chapter 5 demonstrate a new type of high-performance flexible Ni-Fe battery with binder-free electrodes on conductive carbon nanotube fibers. Hierarchical NiCoP NSAs and FeP NWAs grown directly on carbon nanotube fibers are fabricated firstly using hydrothermal synthesis then pursuant gas phosphating process.

Chapter 6 draws the conclusions and puts forward future research plans.

Chapter 2 Literature Review

Large-scale rechargeable batteries with high power and high energy while offering low cost, long lifetime, high safety and eco-friendliness are of great importance and highly demanded for applications in electrical vehicles and large portable devices. Lithium-ion and lead-acid batteries are currently mainly available in the market for the large-scale electric power sources but the former is not cost-effective and the later suffers greatly from environment and safety concerns[38-39]. The aqueous batteries are cost-effective and safe, and have attracted intensive research activity to develop high power and energy storage devices as alternatives for lithium-ion batteries. Different kinds of aqueous batteries have been reported, including MnO_2/Zn, $LiMn_2O_4$/VO2 , Ni/Zn, Ni/Fe and so on, which are comparable to lithium-ion batteries in specific energy [40-43].

2.1 Overview: Rechargeable batteries

2.1.1 Development of the rechargeable batteries

American scientist and inventor Franklin first proposed the term “battery” in 1749. He first introduced the concept of a battery when conducting electrical experiments with a series of capacitors. In 1800, the Italian physicist Volt laid a burlap sheet soaked in salt water between round copper and zinc sheets, and then stacked them together to prepare the world's first true battery[44]. In 1859, French engineer Plante placed two lead sheets in a sulfuric acid electrolyte separated by a separator to create a lead-acid battery that can be repeatedly charged and discharged. This is the oldest example of a rechargeable battery [45]. Nowadays, most start-up systems for internal combustion engines still use lead-acid batteries. In 1890, Edison of the United States successfully developed a Ni-Fe battery [46-47]. In 1899 Yanggen of Sweden developed a nickel-cadmium battery, and in the late 19th century, Drum of Russia developed a Ni-Zn battery [48]. The NiOOH electricity used for these batteries laid a foundation for the Ni-metal battery. In 1910, rechargeable Ni-Fe batteries were commercialized. In the 1960s, rechargeable nickel-

cadmium batteries were successfully developed. In 1990, the nickel metal hydride battery was successfully developed [49]. Large-scale production of secondary alkaline batteries began in 1992. Safety and environmental protection have become the theme of energy storage in the new era. At the same time, due to the power demand, a great number of large equipment and electric vehicles, battery systems with high energy density and high power density are attracting more and more attention of scientists from all over the world [50].

2.1.2 Structure and characteristics of rechargeable batteries

The industrial rechargeable battery is composed of a shell, a separator, a current collector, positive and negative electrodes, additives, and electrolyte. The requirements of rechargeable batteries for the shell are corrosion resistance, impact resistance, good thermal conductivity and adapting to harsh environments, which generally are made of iron or steel[51]. With the rapid development of battery research, more and more researchers began to use stainless steel as the shell, and plastic shells can be used in certain places. The diaphragm should be able to ensure the isolation and insulation between the anode and cathode to prevent short circuits due to poor contact between the anode and cathode and to ensure the normal migration of electrolyte ions between the electrodes. Common diaphragms include asbestos fibers, rubber diaphragms and polymer diaphragms. As for the current collector, which varied with different rechargeable batteries. At present, more and more researches use foamed nickel as a current collector for rechargeable batteries such as nickel-metal hydride and Ni-Zn batteries. This lightweight and high-porosity current collector increases the rate discharge of batteries and reduces their self-discharge. The electrolyte of the rechargeable batteries generally uses the KOH solution or a NaOH solution, and a small amount of LiOH is usually added to the electrolyte. Table 1.1 lists the main performances of rechargeable batteries commonly used in industry at this stage. It can be seen from the table that the Ni-based battery is a type of secondary alkaline battery with development prospects.

Cell chemistry	Electrode		Energy density		Specific power	Discharge efficiency	Self-discharge rate
	Anode	Cathode	by mass (Wh/kg)	by volume (Wh/L)			
Alkaline	Zinc	Manganese (IV) oxide	0.31–0.68	0.90–1.56	50	45–85	0.17
Lead-acid	Lead	Lead dioxide	0.11–0.14	0.22–0.27	180	50–92	3–20
Lithium-carbon monofluoride	Lithium	Carbon monofluoride	0.94–2.81	1.58–5.32			0.2–0.3
Lithium-iron disulfide	Lithium	Iron disulfide	1.07	2.1			
Nickel-metal hydride	Metal hydride	Nickel oxide hydroxide	0.34	1.27	250–1000		0.42
Mercury oxide-zinc	Zinc	Mercuric oxide	0.36–0.44	1.1–1.8			
Nickel-cadmium	Cadmium	Nickel oxide hydroxide	0.11	0.36	150-200		10
Nickel-hydrogen	Hydrogen	Nickel oxide hydroxide	0.16–0.23	0.22	150-2000		
Nickel-iron	Iron	Nickel oxide hydroxide	0.07–0.09	0.45	100		20–30
Nickel-metal hydride	Metal hydride	Nickel oxide hydroxide	0.36	1.44	250–1000		30
Ni-Zn	Zinc	Nickel oxide hydroxide			500		13
Rechargeable alkaline	Zinc	Manganese (IV) oxide					<1
Silver-oxide	Zinc	Silver oxide	0.47	1.8			
Zinc-air	Zinc	Oxygen	1.59	6.02	100	60–70	0.17
Zinc-carbon	Zinc	Manganese (IV) oxide	0.13	0.33	10–27	50–60	0.32

Table 2-1 Main performance comparison of rechargeable batteries [52]

2.2 Aqueous Ni-Zn batteries

2.2.1 Overview and structure of aqueous Ni-Zn batteries

Aqueous Ni-Zn batteries have the advantages of high safety, low cost and environmental friendliness. In addition, metallic zinc with high theoretical capacity (820 mAh /g) can be directly applied to the anode electrode of zinc-based batteries, which is beneficial to obtain high mass/volume energy density, making it one of the most ideal energy storage devices. In the early 19th century, Volta invented a galvanic cell, which provided electrical current through a chemical reaction. The voltaic battery stack is composed of a zinc plate anode and a silver plate or copper plate cathode. From then on, there has been a lot of research into this type of battery, and zinc has been considered an attractive negative material for a long time. In 1865, the Leclanche cell came out. Subsequently, the Le Kronche battery has been greatly improved, and eventually evolved into a "dry battery" which has been used to date [53-56]. All these primary batteries use metallic zinc as the electrode material. The most commonly used aqueous electrolytes in zinc-based batteries include potassium hydroxide (KOH), sodium hydroxide (NaOH), and lithium hydroxide (LiOH). Among these electrolyte cations, potassium ions have the highest ionic conductivity. Therefore, potassium hydroxide is widely used as an electrolyte in aqueous batteries. Under normal circumstances, the concentration range of potassium hydroxide solution in the battery is between 26% ~ 40%, which is 4.6 M ~ 7.0 M, corresponding to the highest at room temperature. Figure 2.1 also summarizes the changes in conductivity, ZnO solubility and solution concentration with the change of KOH concentration. When the KOH concentration increases, the electrode potential decreases and reacts Kinetics-related conductivity and exchange current are increased by approximately 30% [57].

Ni-Zn battery is composed of zinc electrode and nickel electrode. It has the characteristics of high capacity of zinc anode in zinc-silver battery and the superior performance of nickel cathode in nickel-cadmium battery. It is a new type of high-performance green power battery. The anode of the battery generally uses zinc, zinc oxides or zinc hydroxides in the discharged state. Compared with the anode material of

nickel battery and the current commercial positive electrode material of lithium ion battery, the price is significantly lower and has a rich storage capacity. The performance characteristics of Ni-Zn batteries are high operating voltage, high energy density, high power density, wide operating temperature, no pollution during production and usage, known as a true "green battery" and abundant zinc storage, relatively cheap price.

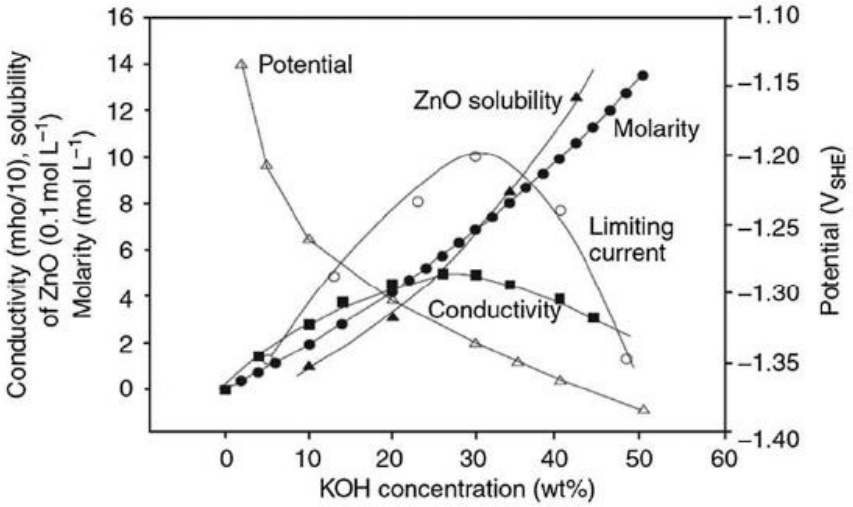

Figure 2-1 ZnO solubility and solution concentration with the change of KOH concentration.[57]

2.2.2 Anode materials of Ni-Zn batteries

Zinc electrodes have many advantages as anode for Ni-Zn batteries. The zinc element is located in the fourth period of the periodic table, the second group of the sub-group, the atomic number is 30, the atomic weight is 65.38 g/mol, the valence electron structure is $3d^{l0}4s^2$ and the zinc crystal is a close-packed hexagonal structure. With a resource of about 0.015% of the earth's crust and low in price and non-toxic, making it widely used as the anode material. The promotion and application of zinc-based batteries can not only fully and effectively use natural resources, but also avoid pollution to the environment. The reaction of the zinc anode is shown in Figure 2-2 [58].

$$Zn + 2OH^- \leftrightarrow ZnO + H_2O + 2e^-$$

The anode electrode of Zn in the alkaline electrolyte continues to suffer from serious irreversible problems caused by its low coulombic efficiency, dendrite growth during the

cycle, continuous water consumption and irreversible by-products such as zinc hydroxide or zincate as shown in Figure 2-3[59]. Although the zinc dendrite in neutral electrolyte can be minimized, its low coulombic efficiency is still a serious challenge. In previous reports, a large amount of zinc must be overused to compensate for the consumption of its side reactions, which leads to its specific theoretical capacity not being fully utilized and high charge/discharge rates must be used to reduce the effect of reversibility on cycle life. Therefore, the development of zinc anode still faces great challenges[60-61].

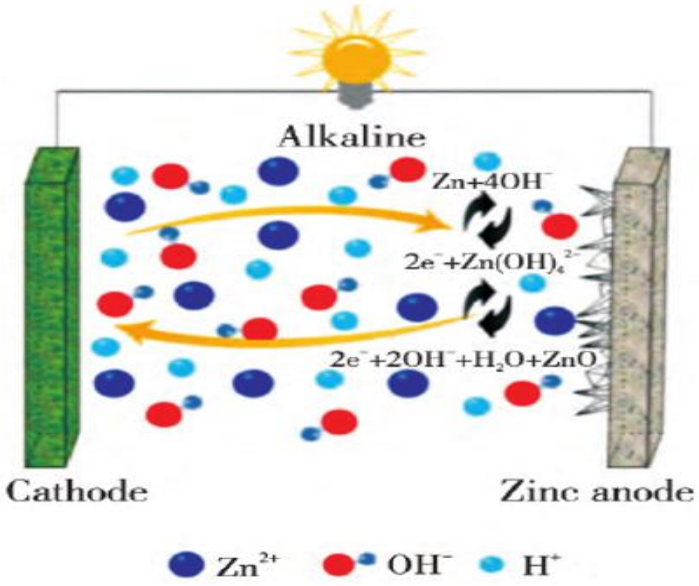

Figure 2-2 Schematic diagram of deposition/dissolution of Zn in alkaline electrolytes.[58]

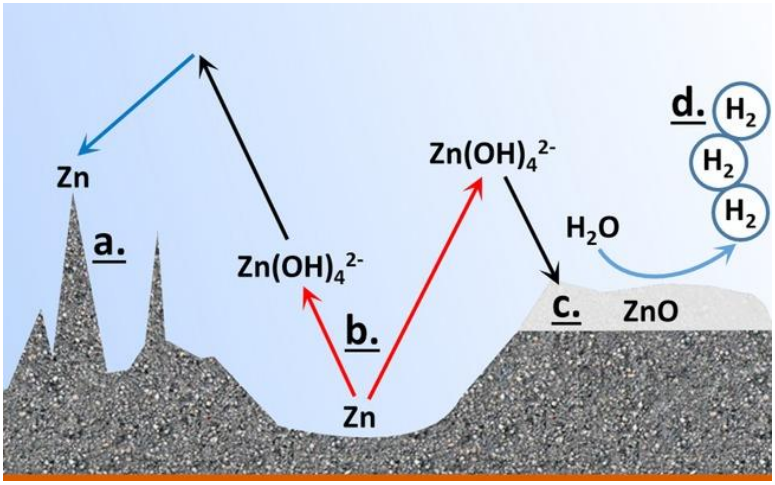

Figure 2-3 Schematic representation of performance-limiting phenomena that may occur on the zinc electrode: (a) dendrite growth (b) shape change (c)passivation and (d) hydrogen evolution.[59]

Optimization of electrode structure is a common method to improve the properties of zinc anode materials. The modified zinc anode usually has a large specific surface area, which increases the deposition site of zinc in the electrochemical reaction process, inhibits the growth of zinc dendrites and improves the reaction kinetics. Kang et al. put forward chemical etching and electrodeposition on porous copper frame as shown in Figure 2-4 prepared a new 3D zinc anode. The porous copper skeleton has excellent electrical conductivity and frame structure, which ensuring that zinc is deposited/dissolved uniformly during the battery cycle [62]. Rolison et al. shown in Figure 2-5 reported the high performance Ni-Zn battery with the zinc powder adding to a mixture of water and oil-like organic solvent to form a paste, which is poured into a specific mold, heated and dried overnight, and then solidified to form a uniform porous spongy zinc skeleton[63]. Using this material as the anode of the battery, the zinc metal can undergo more uniform oxidation during discharge without hot spots generating during the charging process of zinc oxide reduction to metallic zinc, which greatly avoids the formation of dendrites.

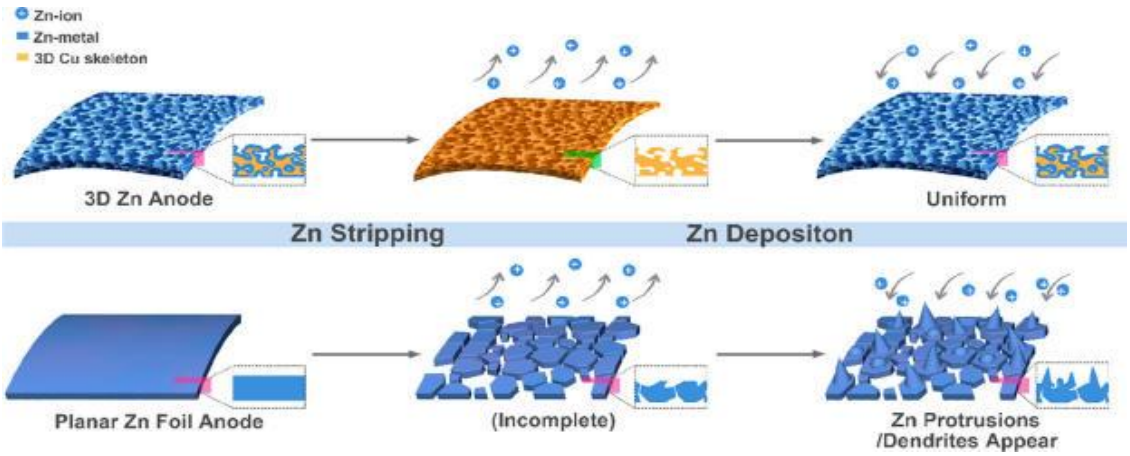

Figure 2-4 Schematic diagrams of Zn deposition/stripping processes on 3D Zn electrodes and planar Zn foil electrodes.[62]

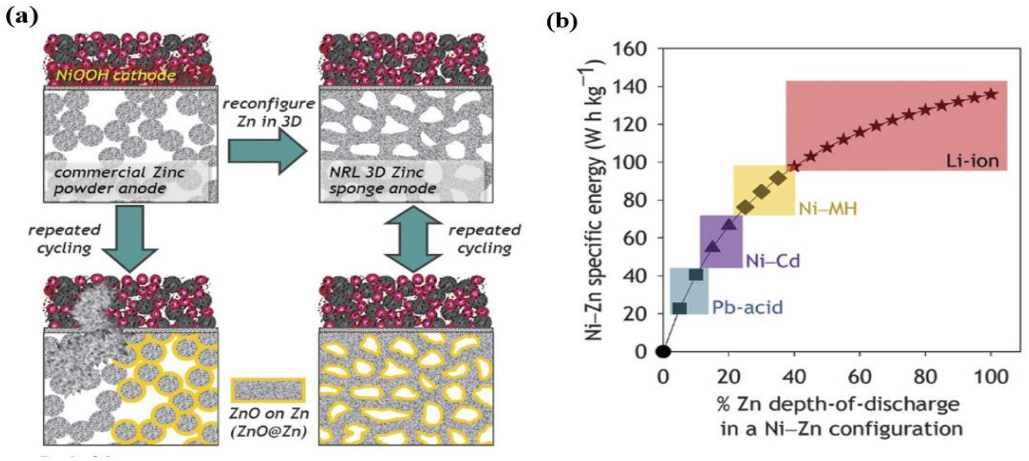

Figure 2-5 (a) Schematic of the effect of recharging Ni–Zn versus Ni–3D Zn in which the anode is redesigned as a monolithic aperiodic sponge ensuring persistent 3D wiring of the metallic Zn core. (b) The calculated specific energy of a fully packaged Ni–Zn battery as a function of increasing Zn depth of discharge versus a capacity-matched NiOOH electrode.[63]

In recent years, researchers have found that it is possible to introduce a functional protective layer on zinc surface to improve the properties of zinc anode. This method is usually to form protective coating on zinc sheet by electrodeposition or direct coating. On the one hand, the protective layer can effectively improve the deposition and kinetics,

leading the uniform deposition/dissolution of zinc and inhibiting the growth of zinc dendrites. On the other hand, the protective layer can also reduce the deformation of zinc anode and improve the utilization rate of metal zinc, to improve the circulation stability and coulomb efficiency. Kang et al. added polyvinylidene fluoride and nano-$CaCO_3$ (mass ratio of 1:9) to N-methyl pyrrolidone solvent and stirred them with magnetic force for 5 h. Then this paste was coated on zinc tablets to prepare Zn@nano-$CaCO_3$[64]. It can be seen from Figure 2-6 that coating the buffer layer on the surface of the zinc anode had the following advantages: (1) Nano-$CaCO_3$ has a high porosity and is easy to be permeated by electrolyte, which contributes to the formation of relatively uniform electrolyte flux and zinc deposition/dissolution on the whole Surface of zinc foil. (2) Nano-$CaCO_3$ coated nanopores prevent the growth of zinc anode by-products, which can significantly improve the polarization of the battery. (3) Nano-$CaCO_3$ is an insulator and zinc will not be deposited on its surface. This multi-guided uniform deposition/dissolution mechanism of zinc effectively avoid obvious polarization phenomenon and the growth of zinc dendrites. Zhao et al. deposited an amorphous TiO_2 protective layer on the surface of pure zinc sheet by atomic layer deposition technology to prepare a new type of Zn@TiO_2 electrode [65]. It can be seen from the diagram of zinc anode deposition/dissolution process (Figure 2-7) that TiO_2 coating can not only avoid direct contact between metal zinc and electrolyte, inhibitting zinc corrosion and hydrogen evolution reaction, but also improve the inset kinetics of zinc ions. Zhao et al (Figure 2-8) designed a polyamide/$Zn(TfO)_2$ layer coating layer, the possession of amide groups that can coordinate with Zn^{2+} and restrict the 2D diffusion for a flat deposition surface [66].

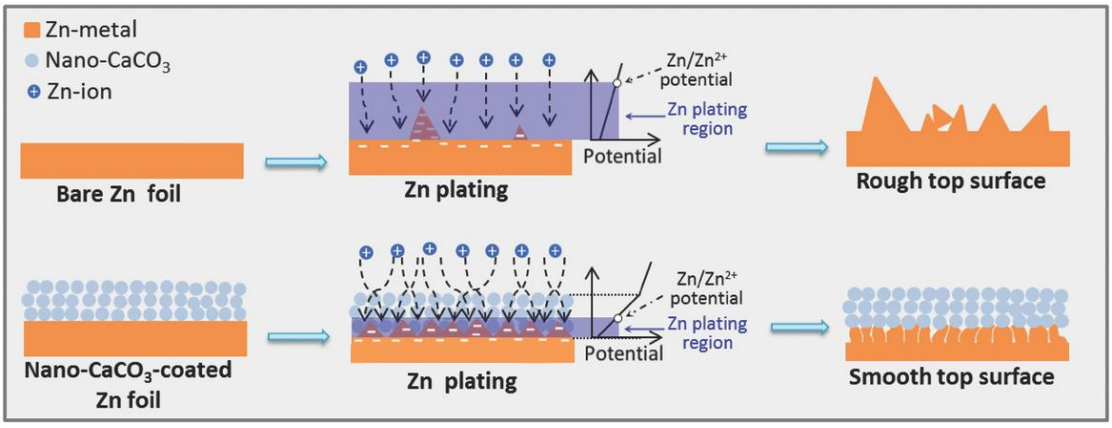

Figure 2-6 Schematic illustrations of morphology evolution for bare and nano-$CaCO_3$-coated Zn foils during Zn stripping/plating cycling.[64]

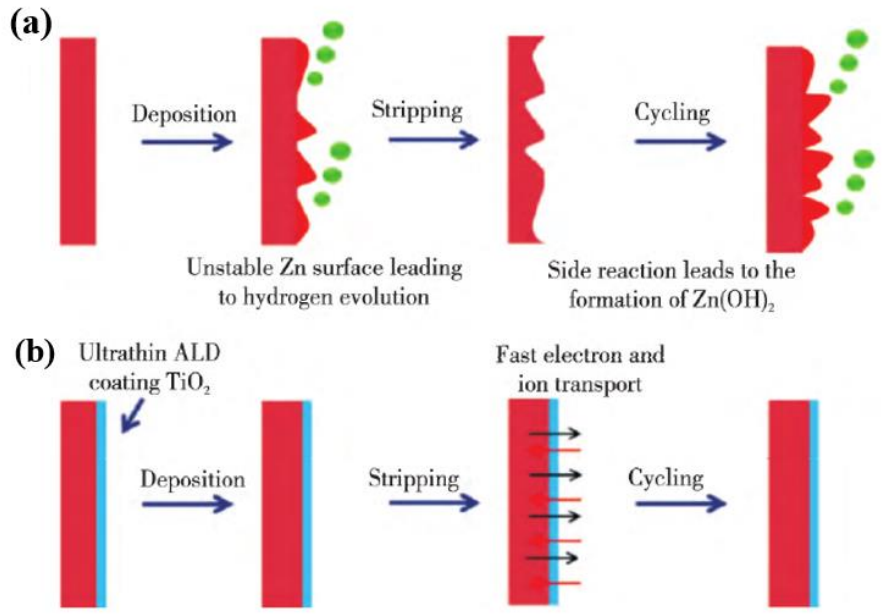

Figure 2-7 Schematic illustration of the stabilization of zinc anode with TiO_2 coating. [65]

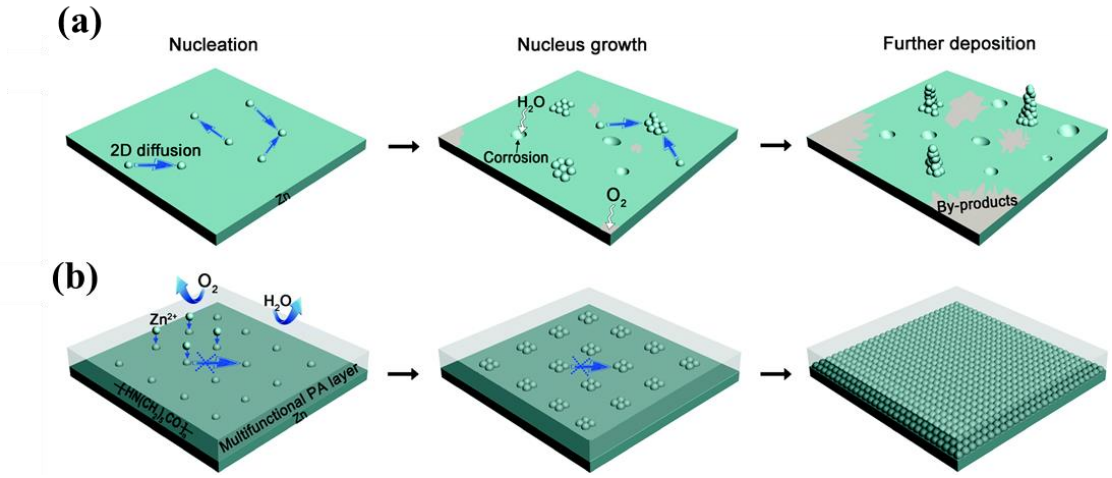

Figure 2-8 Schematic diagram of zinc deposition: (a) traditional zinc dendrite growth and accompanying side reactions. (b) uniform deposition of zinc metal under the protective film of PA.[66]

2.2.3 Cathode materials of Ni-Zn batteries

The nickel-based material can be used as the cathode not only in the Ni-Zn batteries, but also can be applied in the field of Ni-Cd, Ni-Fe, Ni-MH batteries with the alkaline electrolyte.

(1) Nickel Hydroxide. $Ni(OH)_2$ takes the dominant place as the cathode material in the nickel-based batteries, which has two crystal structures and the crystal pattern. β-$Ni(OH)_2$ takes place the dominant material with a theoretical specific capacity of 289 mAh/g. However, the actual specific capacity has approached the theoretical value, meanwhile the research value and development space are limited[67]. The reaction for the cathode in the nickel-based alkaline battery is shown in the following:

$$Ni(OH)_2 + OH^- \longleftrightarrow NiOOH+H_2O+e^-$$

α-$Ni(OH)_2$ has a special layered spiral structure, which is composed of homogeneous layered NiO_2. Each OH^- ion and some metal ions are inserted between the NiO_2 layer [68-69]. The average number of electrons transferred per nickel atom during charging and discharging of α-$Ni(OH)_2$ is 1.7 times that of the β-$Ni(OH)_2$ and the theoretical

specific capacity of α-$Ni(OH)_2$ is 482 mAh/g, with great development and research value. Once the electrochemical performance of nickel cathode is promoted, the capacity of alkaline batteries with $Ni(OH)_2$ as the cathode material will be improved, such as Ni/Cd, Ni/Fe, Ni/Zn, Ni/MH batteries. The improved alkaline batteries can replace the market mainstream with lead-acid battery as the power battery pack as shown in the following Table 2.2 with the $Ni(OH)_2$ as the cathode material. In the alkaline rechargeable battery system, $Ni(OH)_2$ and NiOOH exist respectively during the charging/discharging process. There are two crystal forms for $Ni(OH)_2$ and NiOOH, namely α-$Ni(OH)_2$ and β-$Ni(OH)_2$, β-NiOOH and γ-NiOOH, the cell parameter and density of active mass with different crystal shapes is summarized in Table 2-3. As shown in Figure 2-10, there is a certain conversion relationship between them: α-$Ni(OH)_2$ and γ-NiOOH, β-$Ni(OH)_2$ and β-NiOOH. It can be reversibly transformed during charging and discharging, and β-NiOOH can be transformed into γ-NiOOH during overcharging[70].

Table 2-2 The battery of the cathode active material with $Ni(OH)_2$

Type	Anode material	Operating Voltage (V)	Actual specific capacity (Wh/kg)	Theoretical specific capacity (Wh/kg)
Ni-Cd	Cd	1-1.25	35	85
Ni-MH	H2	1.15-1.3	64	275
Ni-Fe	Fe	1.05-1.25	30	267
Ni-Zn	Zn	1.4-1.7	50-80	334

Table 2-3 The cell parameter and density of active mass with different crystal shapes

Crystal structure	Cell parameter		Density (g/cm^3)
	a (nm)	c (nm)	
α-$Ni(OH)_2$	0.308	0.809	2.82
β-$Ni(OH)_2$	0.313	0.460	3.97
β-NiOOH	0.282	0.485	4.68
γ-NiOOH	0.282	2.065	3.79

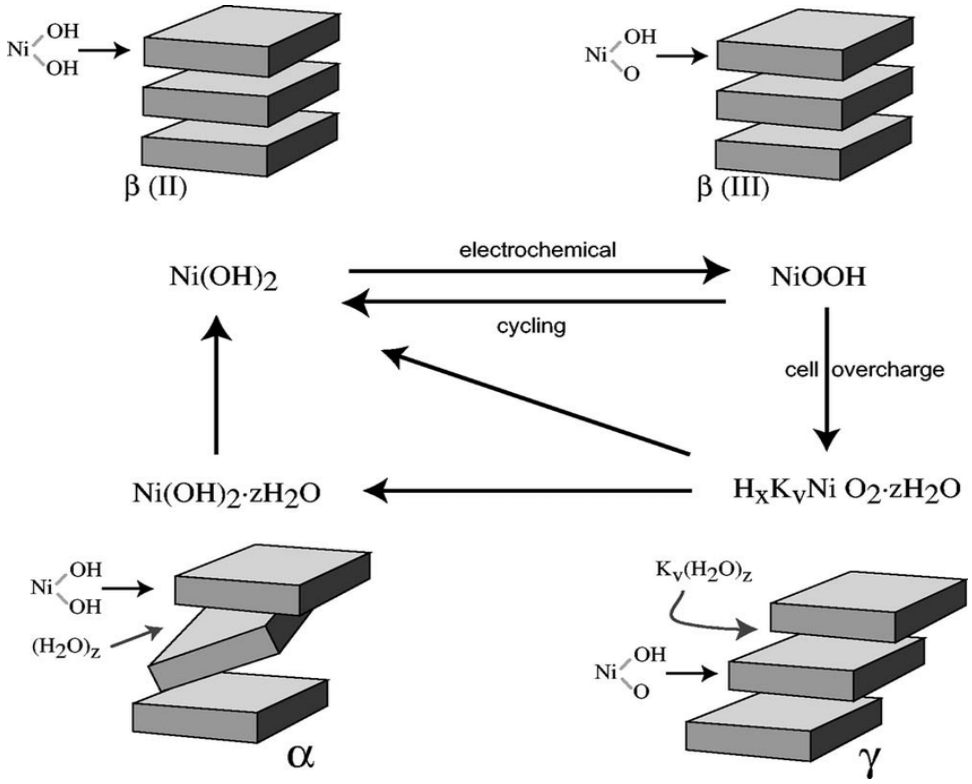

Figure 2-9 The Bode diagram illustrating the different variants of Ni hydroxide and the possible phase transformations between them.[70]

At present, the improvement of the properties of α-$Ni(OH)_2$ is mainly carried out by metal element phase doping [71-73]. Ni^{2+} was partially replaced by other metal ions such as bivalent Co^{2+}, Zn^{2+}, Cd^{2+}, Ba^{2+}, Be^{2+}, Mg^{2+}, trivalent Al^{3+}, Fe^{3+}, and $Cr3^{+}$ and so on to stabilize its structure. The stability of α-$Ni(OH)_2$ material in alkaline solution is improved from layered double hydroxides (LDHs), which is often attributed to the formation of more stable crystal structure from LDHs [74-76]. As a kind of anionic multifunctional nanomaterial similar to hydroxides, LDHs has many special and excellent properties. LDHs has a regular octahedral structure similar to $Mg(OH)_2$. Its crystal structure is shown in Figure 2-11, and its composition formula is $[M^{2+}_{1-x}M^{3+}_{x}(OH)_2](A^{m-})_{x/m}\cdot nH_2O$, where M^{n+} represents the metal cation located in the main layer plate and A is the interlamellar anion, and X is molar ration of M^{3+} / (M^{2+}+M^{3+}), n is the number of interlayer water molecules [77]. The unique structure not only makes LDHs have thermal stability, but also can be controlled in terms of the chemical

composition of the laminates, the type and number of anions between the laminates, grain size and distribution.

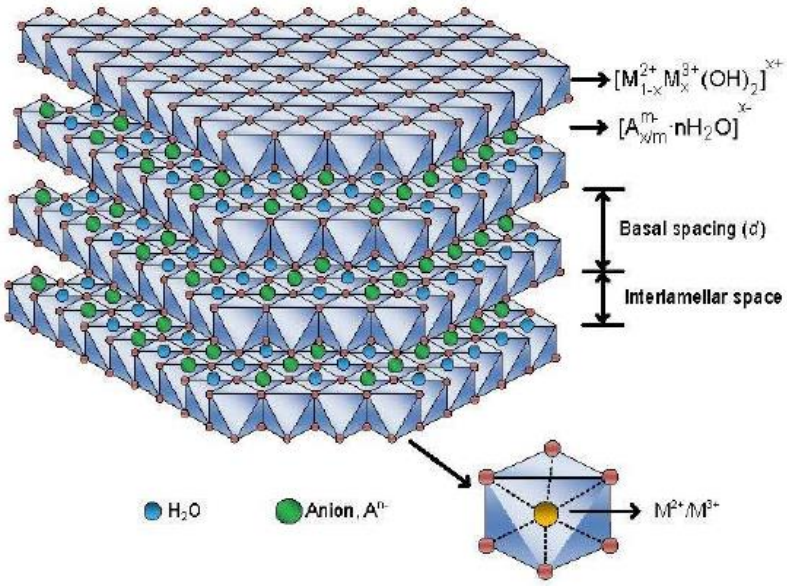

Figure 2-10 The crystal structure of Layered double hydroxides.[77]

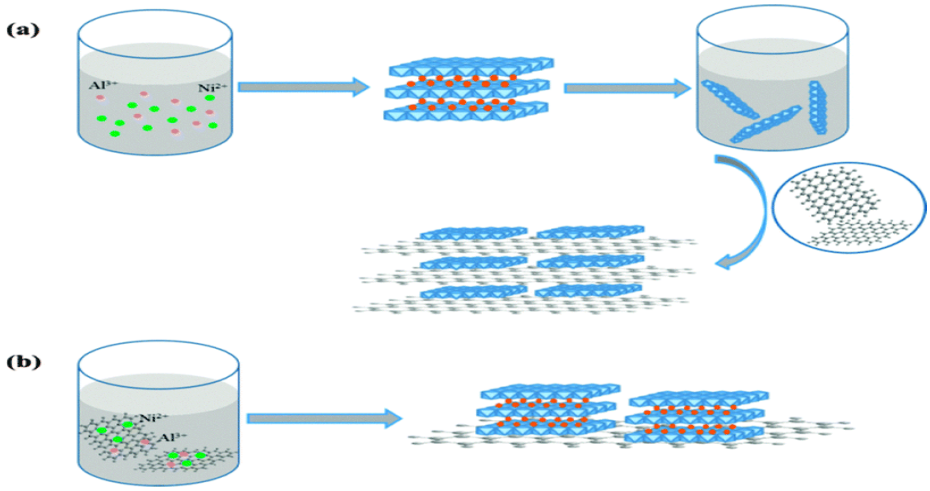

Figure 2-11 Schematic of the construction of the Ni–Al LDH–graphene composite. (a) Superlattice achieved via alternating assembly and (b) hybrid by deposition growth.[78]

The graphene Ni-Al double hydroxide prepared by Hu et al. [78] not only increases the discharge capacity, but also releases 2.4 times more energy than the original Ni-Al LDH when charging and discharging at a large current (5000 mA/g) as shown in Figure

2-12. Zhao et al. [79] described a single layer thick NiTi-LDH nanosheet prepared by reverse micro emulsion method. Ultrafine and ultra-thin NiO nanosheets stabilized by TiO_2 (size ~ 4nm, thickness ~ 1nm) were successfully prepared by calcination as shown in Figure 2-14. The porous Fe doped $Ni(OH)_2$ nanosheets were synthesized by cation exchange reaction as shown in Figure 2-15. Fe^{3+} ions were adsorbed on the $Ni(OH)_2$ nanometer surface and they tend to accumulate at edge and defect sites. At this point, Fe^{3+} and Ni^{2+} participate in the cation exchange process, that is some lattice points of Ni^{2+} were replaced by Fe^{3+}. It is well known that Ni^{2+} in the $Ni(OH)_2$ lattice can be replaced by Fe^{3+} to form a stable LDH structure[80].

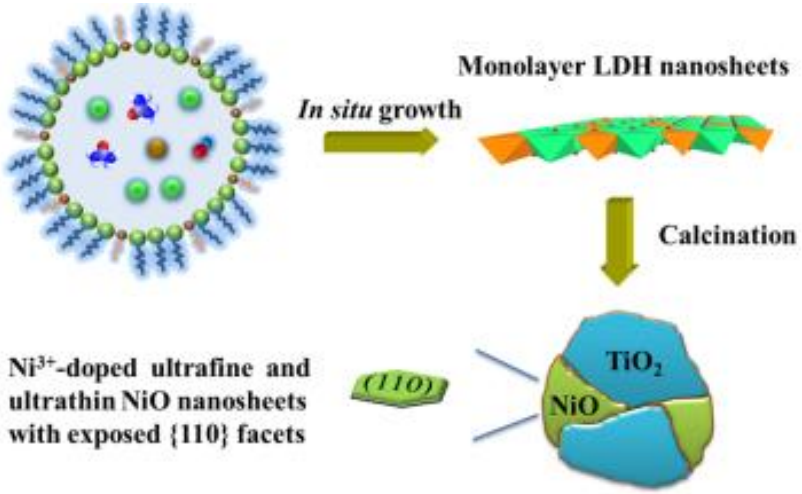

Figure 2-12 Schematic illustration of the synthesis of ultrafine and ultrathin NiO nanosheets stabilized by TiO_2 from monolayer NiTi-LDH nanosheet precursors.[79]

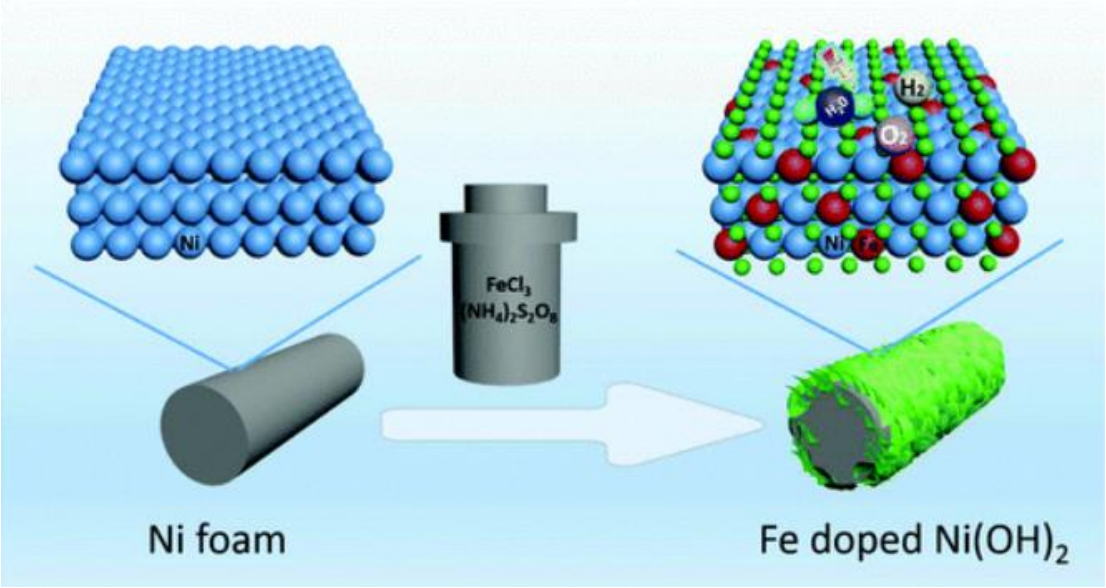

Figure 2-13 Schematic illustration of preparation of Fe-doped Ni $(OH)_2$ nanosheets.[80]

(2) Nickel-based Oxide. Nickel-based oxide is the main redox system for the cathode of alkaline rechargeable batteries[81]. When the simple nanostructured nickel oxide is used as the cathode material, the cycle performance and the specific capacity is not satisfied. The main reason is that the nanostructured nickel oxide has large energy band and low surface binding energy, which easily leads to electrode material reunion. Facing to the problem of the low voltage platform and small amount of stored charge, doping is the way to shorten the energy band thus enhancing the capacity. Jin et al.[82] took advantage of doping method to fabricate the Mn-NiO and Mn-Fe_2O_3 nanostructures modified on copper fiber electrodes. The introduction of Mn on the metal oxide surface brings nano-level defect rich characteristics, effectively optimizes the energy band and electronic structure of these less conductive NiO and Fe_2O_3, thus significantly improving the capacity, rate discharge performance and cyclic stability compared with the undoped samples (Figure 2-23). Qiu et al.[83] demonstrated a novel phosphating surface-modulated $NiCo_2O_4$ nanowire arrays as the cathode, matching with the α-Fe_2O_3 as the

anode directly grown on the carbon cloth respectively. The specific capacity of the prepared battery reach 134.5 mAh /g, maintains more than 82.7% capacity after 2600 cycles (Figure 2-24).

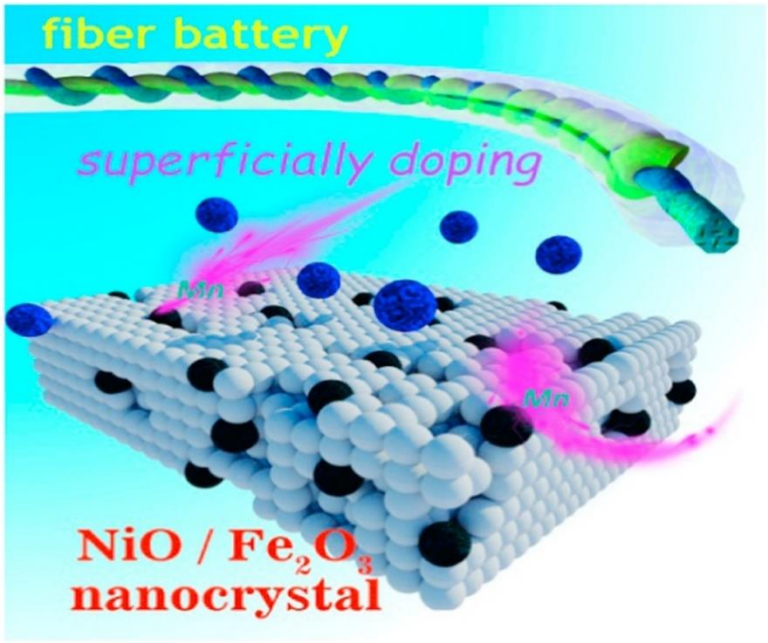

Figure 2-14 Schematics of the flexible Mn doping Ni/Fe cells.[82]

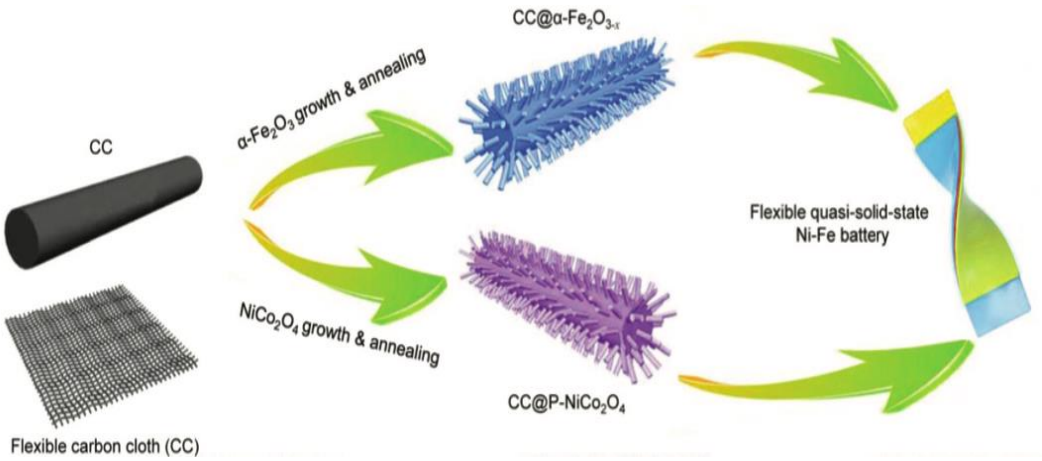

Figure 2-15 Schematic illustration of the preparation strategy for the flexible quasi-solid-state Ni–Fe battery.[83]

Figure 2-16 Schematic illustration on how to form $NiCo_2S_4$ hollow spheres and 3D porous rGO/ Fe_2O_3 hybrid structures as well as the device fabrication.[84]

(3) Nickel-based sulfide. Since sulfur is less electronegative than oxygen, sulfur and nickel atoms can form the nickel-based compounds with different stoichiometric ratios, such as α-NiS, β-NiS, NiS_2, Ni_3S_2, Ni_3S_4 and so on. Wang et al.[84] proposed the simple hydrothermal and subsequent etching method to fabricate the $NiCo_2S_4$ taking the advantage of the synergetic effects from both Ni and Co species for fast Faradaic reactions as the cathode, the as-prepared electrode delivered a high operating voltage range from 0 to 1.75V with the maximum energy density of 61.7 Wh/kg. Moreover, the device exhibits a high power density of 22 kW/kg and a long cycle life with 90% retention after 1000 cycles at the current density of 1 A/g. Li et al.[85] prepared a vertically grown Ni_3S_2 nanotube by simply heating on the nickel substrate and the process was shown in Figure 2-17. The self-supporting Ni_3S_2 electrode still has the 95.3% capacity after 100 cycles at the current density of 170 mA/g.

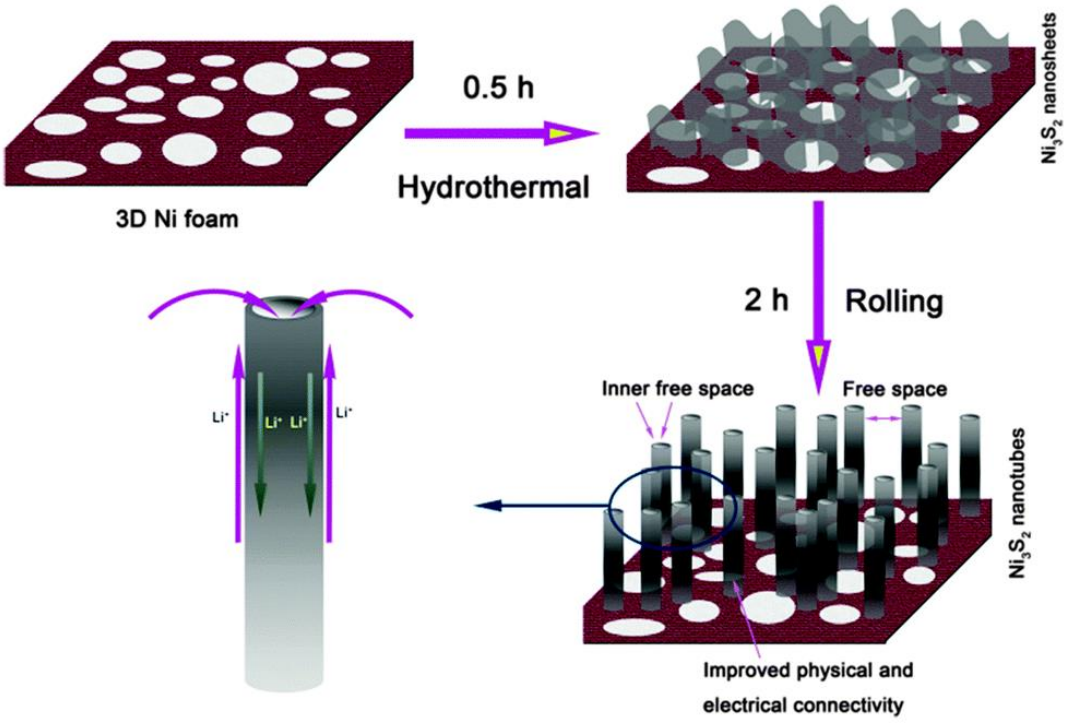

Figure 2-17 Schematic illustration showing the synthesis of the Ni_3S_2 nanotube array on Ni foam and a diagram.[85]

(4) Nickel-based phosphorus. Nickel phosphide is very suitable as the cathode material due to its low cost, high capacity. Nickel phosphide mainly includes the following phases: Ni_3P, Ni_2P, $Ni_{12}P_5$, Ni_5P_4, NiP_2, and NiP_3. Researchers have made many efforts to improve the cycle performance of nickel phosphide and reduce the irreversible capacity loss. Miao et al.[86] constructed 3D Ni_2P@C nanoparticles the through a solvothermal reaction and in situ phosphorization process, which can retain a specific capacity of 124.5 mA h/g at a current density of 1 A/g over 2000 cycles. Yan et al. fabricated the Ni_2P/rGO with an ultra-small particle size (average about 2.6 nm), which ensures a large active surface area and perfect dispersion of active sites. In addition, due to the specific interface between metal of framework and graphene oxide, the carbon/graphene surface tends to form homogeneous carbon during phosphating and calcination, which can be connected to the carbon network and used as an electron

channel to obtain satisfactory electrons Conductivity and enhance charge transfer efficiency[87].

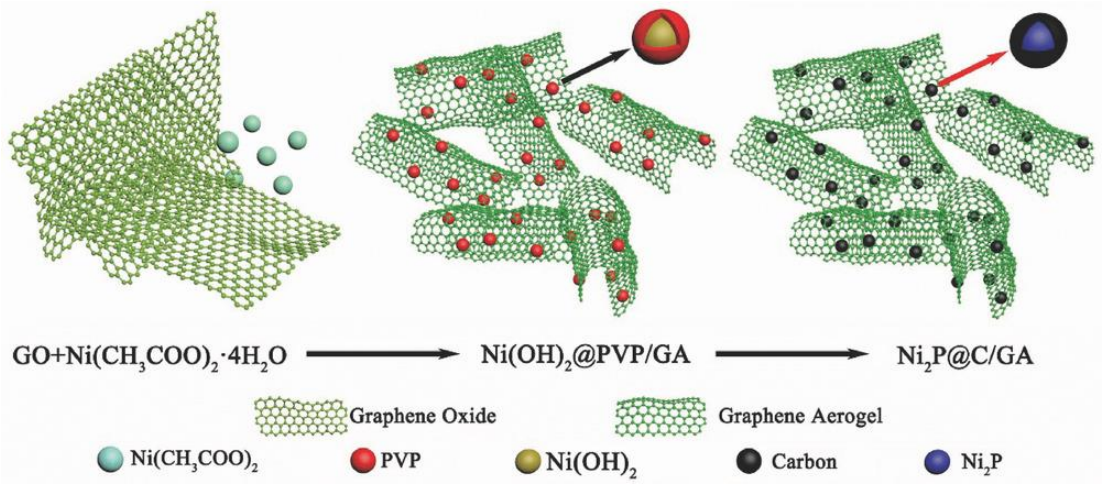

Figure 2-18 Schematic illustration of the synthesis process of Ni_2P@C/GA hybrid.[86]

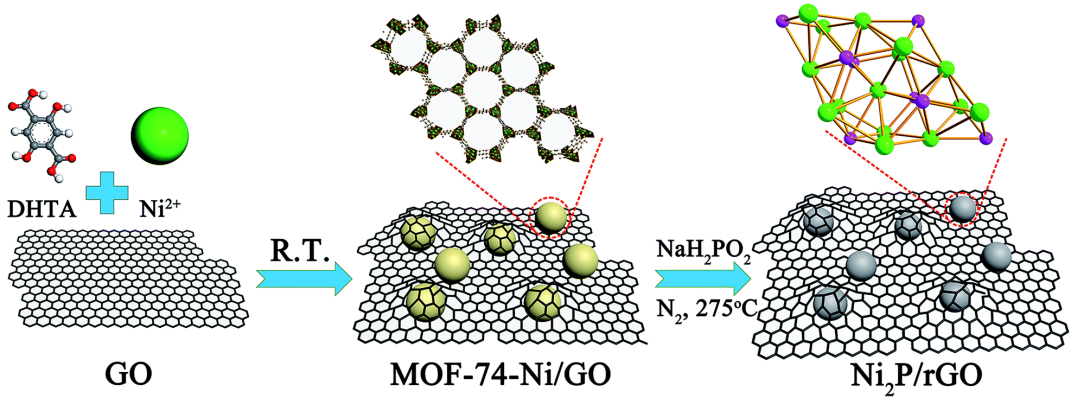

Figure 2-19 Illustration of the synthesis procedure for the Ni_2P/rGO.[87]

2.3 Aqueous Ni-Fe battery

2.3.1 Overview and structure of Ni-Fe battery

Swedish scientist Jungner and American scientist Edison jointly invented the alkaline rechargeable Ni-Fe battery, commonly known as the Edison battery, in the late 19th century. These batteries are based on the iron –based anode and nickel-oxide cathode, which are typically pocket-shaped and the electrolyte is a concentrated solution of KOH, so they are also called basic Ni-Fe batteries. Ni-Fe battery is a kind of typical alkaline battery that can be charged and discharged under long and medium current. It has the characteristics of safety, reliability, low cost, long service life and simple maintenance [88-89], whose voltage is usually 1.2V and the theoretical power is 267 Wh/kg [90]. Ni-Fe batteries have the specific energy 1.5 to 2 times higher than lead-acid batteries and perform fairly well in high-rate discharges [91]. They are also known for their durability and long cycle life (retaining 80% capacity after 2000 deep discharges), which can last a long time in the case of overcharge and discharge, short circuit and overheating. Therefore, the development of high performance Ni-Fe battery has a wide range of application prospects as shown in Figure 2-20 [92].

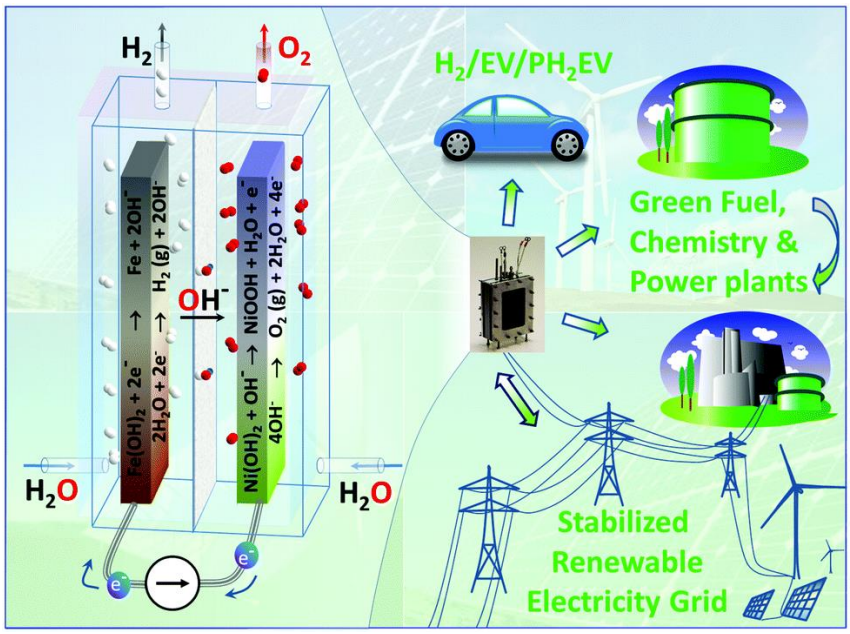

Figure 2-20 Battolyser functionality and application areas.[92]

Ni-Fe batteries use iron or iron oxide or its mixture as the anode material, such as Fe_3O_4, $Fe(OH)_2$, $Fe(OH)_3$, Fe_2O_3, iron powder and carbonyl iron powder [93]. In addition, the main active material of the cathode of Ni-Fe battery is nickel hydroxide, and the electrolyte is generally the alkaline mixed solution of sodium hydroxide or potassium hydroxide and a small amount of lithium hydroxide. In addition, compared to the other battery types, Ni-Fe batteries takes advantage of cost-effective, as shown in Table 2-4.

Table 2-4 Price for different types of batteries.

Battery Type	Zn-Mn	Li-Ion	Lead-acid	Ni-Fe
Price ($/kWh)	<$10	$135	$100	<$1

2.3.2 Anode materials of Ni-Fe batteries

Studies have carried out X-ray diffraction analysis on the iron negative electrode after deep discharge (up to 0.8v) and found the presence of FeOOH phase in the discharge products, confirming that FeOOH is indeed an intermediate product in the discharge process of iron negative electrode [47]. In addition, the reaction of the anode process in mainly in the following:

$$Fe + 2OH^- \longleftrightarrow Fe(OH)_2 + 2e^-$$

$$Fe(OH)_2 + OH^- \longleftrightarrow FeOOH + H_2O + e^-$$

One of the important reasons for the low capacity of the reactive material in the cathode of Ni-Fe battery is the low utilization rate due to the low reactivity of the reactive material. It is known that nanoparticles with high specific surface area have high chemical reactivity. Therefore, the preparation of nano-iron negative electrode materials will greatly increase the utilization rate of materials to improve the specific capacity of materials. Meanwhile fabricating composite material can meet the requirements of high performance electrode materials for excellent conductivity, high specific surface area and suitable pore size, so it can not only shorten the ion diffusion path but also improve the active surface area of ion insertion. At present, the iron anode materials of most Ni-Fe electrodes are composed of iron nanoparticles and carbon materials.

(1) Iron oxide and graphene composites. Wei et al.[94] proposed a novel graphene-based iron oxide nanocomposite was synthesized by high temperature solid-state reaction as shows in Figure 2-21. The results showed that the iron oxide particles were composed of Fe_3O_4 and Fe_2O_3, with a diameter of about 100 nanometers. The electrode provides a specific capacity of up to 552.1 mAh/g (at a current density of 200 mA/g) and retains 91% of its original capacity after 100 charge and discharge cycles. Due to the electrochemical activity and mechanical properties resulting from the binding between iron oxide nanoparticles and graphene layers, iron oxide/graphene compliant materials have shown enhanced discharge rate performance and cyclic stability. Lin et al. [95]demonstrated high specific capacity and good cycling stability when using graphene nanoribbon/iron oxide nanoparticle composites as the anode material (Figure 2-22). At a current density of 100 mA/g, the composite exhibits a high specific capacity of 910 mAh/g after 134 cycles, exceeding 90% of the storage capacity of iron oxide theoretical lithium ions. As a conductive platform for iron oxide nanoparticles, graphene nanoribbons combine the advantages of long carbon nanotubes and graphene surfaces. The high specific capacity and long cycle life are derived from the lead grid of graphene ribbons and the high lithium ion storage capacity of iron oxide nanoparticles. Quan et al.[96]proposed a novel way to fabricate the α-Fe_2O_3/rGO nanocomposites with the specific capacitances 903 F/g at the

current density of 1 A/g, which is superior to that of bare α-Fe_2O_3 nanoplates (Figure 2-23). Aadil et al. [97]used simple hydrothermal and ultrasonic treatment methods to wrap α-Fe_2O_3 in graphene oxide sheets to be used as electrode materials. The results show that graphene nanosheets enhance the electrical conductivity and electrochemical activity of α-Fe_2O_3. At a scanning speed of 5 mV/s, the α-Fe_2O_3/RGO nanocomposite exhibits a specific capacitance of 238 F/g, which is higher than that of pure α-Fe_2O_3 nanoparticles (153 F/g). In addition, many literatures have reported iron oxide/graphene composites with different morphologies, such as hexagonal Fe_2O_3 nanometer sheet/graphene composites [98], Fe_3O_4/threaded graphene complex [99], Fe_3O_4 nanoparticle/graphene complex [100] and nitrogen-doped graphene/Fe_2O_3 complex [101]. In situ synthesis, ferric oxide nanoparticles grow directly on the graphene surface, and the synthesis and modification process occur simultaneously. These iron Oxide/graphene composites not only utilize the porous framework of graphene but also optimize the electrochemical performance of iron oxide nanoparticles.

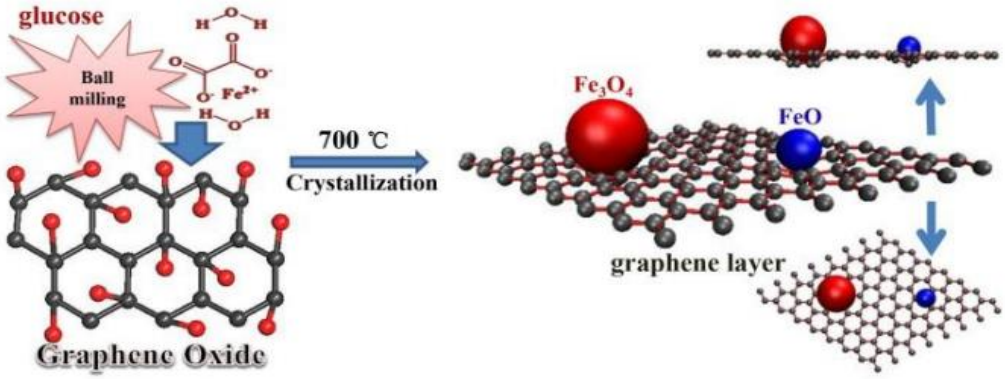

Figure 2-21 Schematic illustration of preparation iron oxide/graphene electrode.[94]

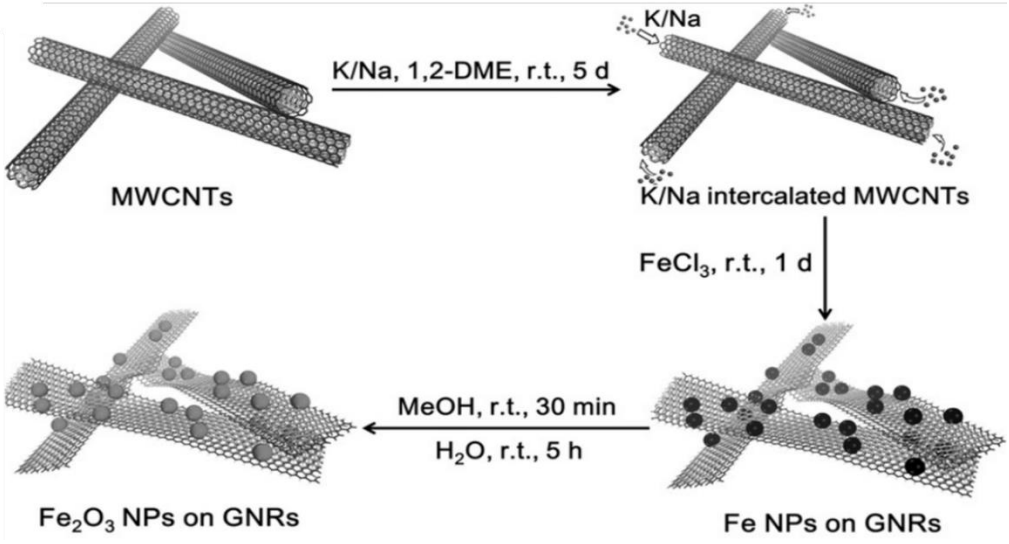

Figure 2-22 Graphene nanoribbon/iron oxide nanoparticle composites.[95]

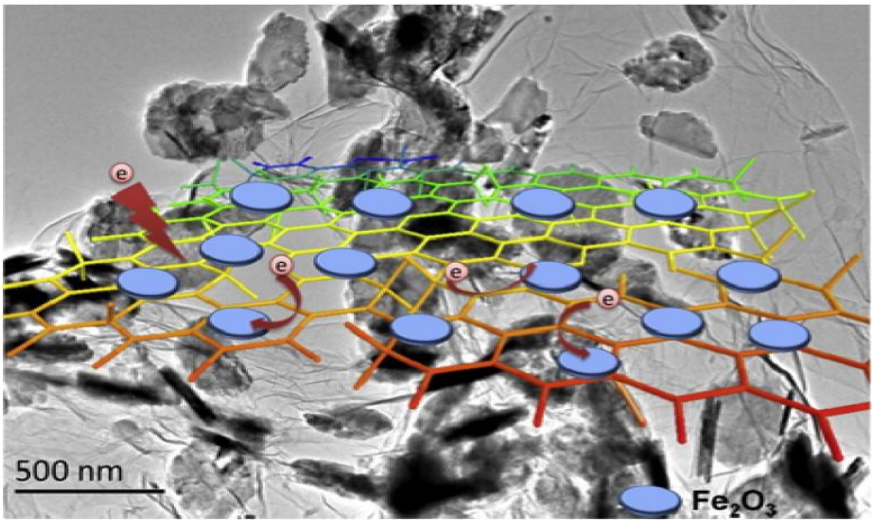

Figure 2-23 α-Fe_2O_3 nanoplates-reduced graphene oxide composites.[96]

(2) Iron and metal composite materials. High-purity carbonyl iron modified by in-situ bismuth electrodeposition has substantial kinetic inhibition effect on hydrogen evolution reaction[102]. Such rechargeable iron electrode can reduce hydrogen evolution rate by 10 times, achieve charging efficiency up to 96%, specific capacity up to 300 mAh/g, and improve discharge rate performance by 20 times (Figure 2-24). In addition, the new electrode can not only charge and discharge rapidly and satisfy large-scale

energy storage, but also overcome the short plate of poor stability of iron electrode, thus making Ni-Fe battery technology efficient, cheap and large-scale application. An iron/copper composite particle synthesized by chemical reduction has shown good performance as the anode for alkaline batteries. Copper is used to improve electron transfer between particles. Nanosized iron/copper composite not only has a high specific capacity of 800 mAh/g (current density is 3200 mA/g), but also has good multiplier performance. Compared with iron nanoparticles without copper composites, this compatible material maintains a smaller particle diameter during the electrochemical cycle, thus enhancing the stability of the iron electrode (Figure 2-25)[103].

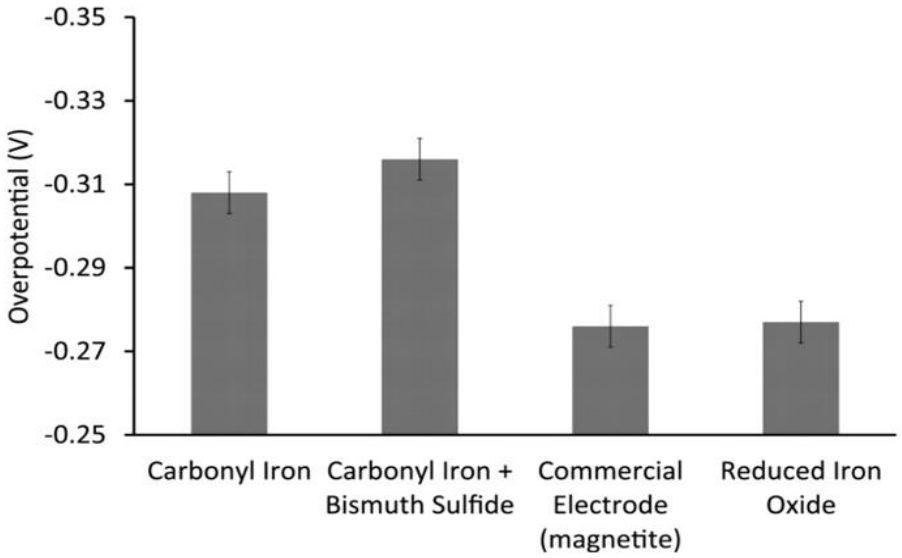

Figure 2-24 Hydrogen overpotential of various iron electrode materials during charging at C*/10 rate, where C* is the theoretical capacity based on the mass of the electrode material. [102]

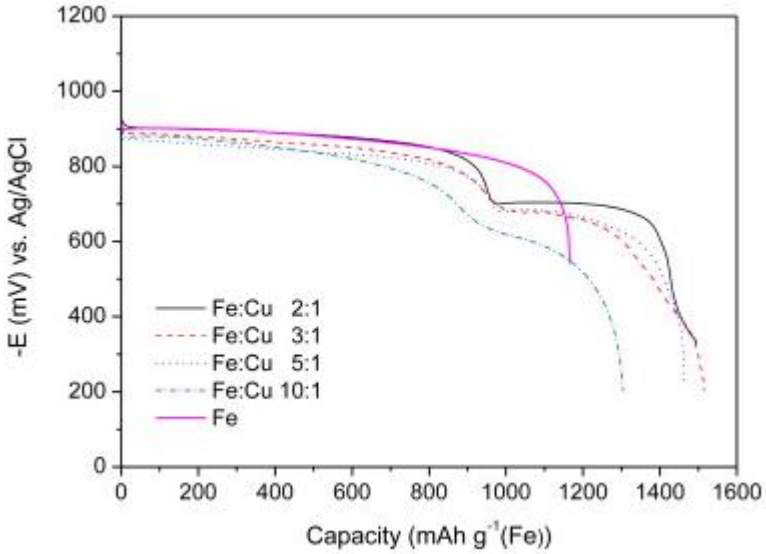

Figure 2-25 Discharge curves of pure iron and various iron/copper composites. A constant current of 200 mA/g was applied at 25 °C.[103]

(3) Iron oxide and carbon nanotube composite. More recently, Liu et al.[43] developed a porous hybrid film of ferric oxide nanorods growing on light graphene foam/carbon nanotubes, characterized by light-weight, ultra-thin, high conductivity and large-area to volume ratio. Nanoscale active materials can be deposited on this material for use as the negative electrode of high-performance electrochemical energy storage devices without the need for conductive agents and adhesives (Figure 2-26). Li et al.[104] wrapped iron tetroxide in a carbon shell to form an array of nanorods and used as a cathode material for the battery, thus increasing the cycle life of the iron electrode from hundreds of cycles to more than 5000 cycles. In addition, its specific capacity in alkaline solution reached 247.5 mAh/g, accounting for 71.4% of the theoretical capacity (Figure 2-27).

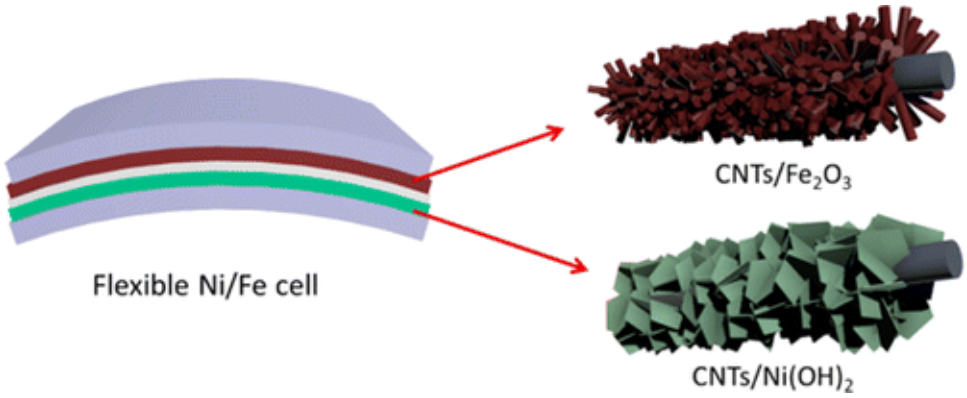

Figure 2-26 Schematics of the flexible Ni/Fe (f-Ni/Fe) cells.[43]

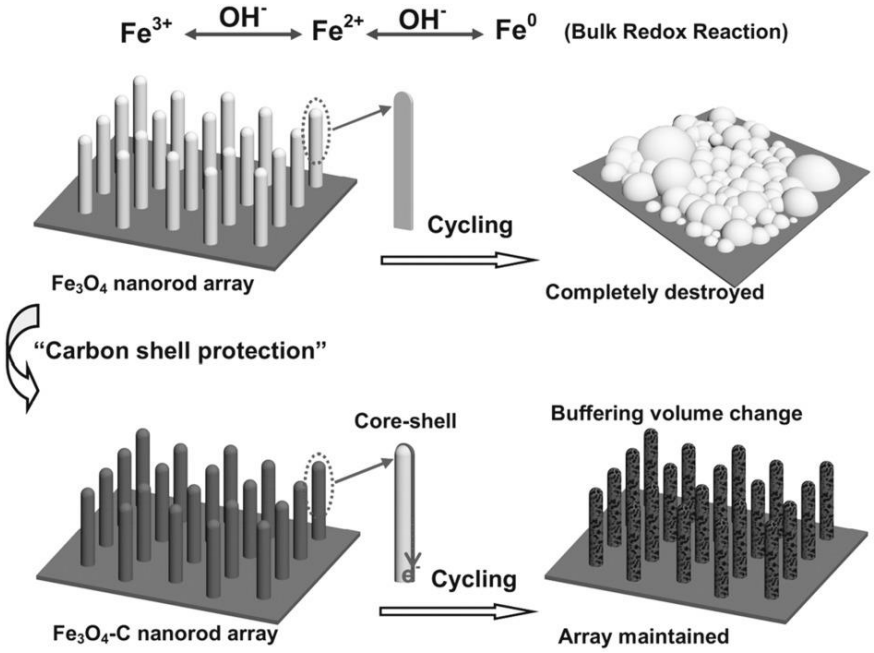

Figure 2-27 Schematic illustration of the functions of carbon shell on the stability improvement of Fe_3O_4 nanorod array during cycling.[104]

Chapter 3 Hierarchical Zinc-Nickel-Cobalt Oxide@$Ni(OH)_2$ Core-Shell Nanowire Arrays for Ultrahigh-Performance Fiber-Shaped Aqueous Rechargeable Ni-Zn Batteries

Aqueous rechargeable Ni-Zn batteries featured with high output voltage, low cost, and outstanding safety characteristics show great potential for application in large-scale energy storage. The boom in portable and wearable electronics have stimulated scientific researchers to develop prototype fiber-shaped Ni-Zn batteries. However, the lack of high-capacity fibrous Ni-based cathode is a major bottleneck to construct high-performance Ni-Zn batteries. Here, a facile and cost-effective method strategy is reported to fabricate three-dimensionally well-aligned ZNCO@$Ni(OH)_2$ NWAs on a CNTF as a promising heterostructure anode for fiber-shaped Ni-Zn batteries. Taking advantage of the accessible surface area, rich reaction sites and short electron/ion diffusion path of ZNCO@$Ni(OH)_2$ NWAs, a high capacity of 2.07 mAh/cm^2 (516.7 mAh/g) and an impressive energy density of 3.71 mWh/cm^2 (916.6 Wh/kg) were achieved for our as-assembled fiber-shaped Ni-Zn batteries, outperforming most previously reported aqueous Zn-based batteries. In addition, our device exhibits superior mechanical stability that its capacity has negligible decay at different bending angles. Finally, it is demonstrated that two series-connected newly developed fiber-shaped Ni-Zn batteries could drive water-splitting device for 3600 s. This work presents a new route to design high-performance Ni-based cathodes for next-generation wearable Ni-Zn batteries.

3.1 Introduction

Increased efforts have recently been made to develop high-performance aqueous rechargeable batteries as the frontrunner to replace dominant lithium-ion batteries for large-scale energy storage due to constrained lithium resources and toxic organic electrolyte [105-110]. Among various aqueous rechargeable batteries (ARBs), aqueous rechargeable Ni-Zn batteries with the abundant constituent elements and high operating voltage of 1.75 V have attracted widespread attention [111-115]. Unfortunately,

compared with the high theoretical capacity of Zn anodes (820 mAh/g), the lack of high-capacity cathode materials remains an obstacle to further improving the energy density of Ni-Zn batteries. With the ever-growing pursuit of portable and wearable electronics, fiber-shaped Ni-Zn batteries with tiny volume, lightweight, remarkable flexibility and wearability are regarded as promising energy supply device [116-120]. Thus, it is highly desirable to synthesize high-capacity fibrous Ni-based cathodes for use in high-energy-density wearable Ni-Zn battery.

In the past few years, considerable attempts have been devoted to fabricating various morphology and composition Ni-based cathodes for Ni-Zn batteries, such as NiAlCo-layered double hydroxide attached to few-walled carbon nanotube[121-123], nickel cobalt hydroxide nanosheets[124], NiO nanosheets[113], $NiCo_2O_4$ nanosheets[125], ultrathin $NiCo_2O_4$ nanosheets with oxygen-vacancy and surface phosphate ions and [126-128]. Despite significant achievements have been achieved, further improving the capacity of single Ni-based compound remains a major challenge. Together with rich reaction sites, convenient ion diffusion path and fast charge transport, core-shell heterostructures has been demonstrated to be promising design to address this issue [129-135]. Although 3D conductive skeletons enable to improve the mass loading and conductivity of the Ni-based compound, the specific capacity of as-assembled Ni-Zn batteries is far from satisfactory. Therefore, it is urgently desirable to develop remarkable synergistic Ni-based core-shell cathodes for use in high-performance aqueous rechargeable Ni-Zn battery. It is revealed that ZNCO NWAs possess superior electronic conductivity and electrochemical performance than the corresponding mono-metal and binary-metal oxide, rendering them as an attractive secondary nanostructured substrate for the growth of other materials. Herein, in this chapter the core-shell nanoarchitecture is constructed by anchoring ultrathin $Ni(OH)_2$ nanosheets on well-aligned ZNCO NWAs. Encouragingly, carbon nanotube fibers (CNTFs) exhibit lightweight, excellent mechanical flexibility and exceptional conductivity that can be widely used as fibrous electrodes of wearable energy storage devices. Contributed by the, accessible surface area, abundant reaction sites and short ion diffusion paths in the core-

shell heterostructures, the well-designed ZNCO@$Ni(OH)_2$/CNTF achieves significantly higher capacity than previously reported Ni-based cathodes.

3.2 Experimental

3.2.1 Materials Preparation of CNTF, ZNCO@$Ni(OH)_2$ NWAs/CNTF and Ni-Zn battery

***Preparation of CNTF*:** The CNTFs were fabricated by two processes including of floating catalyst chemical vapor deposition (FCCVD) method and twisting method. The pristine CNT strip used for fabrication of CNTFs was synthesized at 1300 °C using ethanol and ferrocene as carbon source and catalyst via FCCVD process. The typical thickness, mechanical strength, and electrical conductivity of the pristine CNT strip are around 10 μm, 30-50 MPa, and 105 S/m, respectively. The CNTFs were fabricated by twisting a CNT strip via a fast and scale process and were used for current collector.

***Preparation of ZNCO@$Ni(OH)_2$ NWAs/CNTF*:** The ZNCO NWAs on the CNTF were first synthesized fabricated via a facile hydrothermal method and high-temperature calcination. Prior to synthesis, the CNTFs were treated with O_2 plasma for 5 min at 150 W. 6 mmol $Co(NO_3)_2 \cdot 6H_2O$, 3 mmol $Ni(NO_3)_2 \cdot 6H_2O$, 3 mmol $Zn(NO_3)_2 \cdot 6H_2O$, 12 mmol $CO(NH_2)_2$ and 4 mmol NH_4F were dissolved in 40 mL distilled water with vigorous stirring to form homogeneous pink solution. The as-obtained solution was then transferred into a 50 mL Teflon-lined stainless steel autoclave and CNT fibers were immersed in the mixed solution. After a hydrothermal reaction for 130 °C for 5 h, the resulting CNTFs were washed repeatedly with distilled water and dried at 60 °C overnight, followed by annealed into ZNCO NWAs/CNTF at 350 °C in air for 4 h. The as-prepared ZNCO NWAs/CNTF attached on a polyethylene terephthalate trestle was then suspended into a stirring solution containing 10 g $NiSO_4 \cdot 6H_2O$, 2 g of $K_2S_2O_8$, 5 ml aqueous ammonia (28%) and 100 ml distilled water for 30 min. Finally, the resulting fiber was washed with deionized water for several times and dried at 60 °C in a vacuum overnight.

Assembling the fiber-shaped Ni-Zn battery: The ZNCO@$Ni(OH)_2$ NWAs/CNTF and a Zn wire were inserted into a heat-shrinkable tube in a parallel format. After injecting the ZnO-saturated 3 M KOH aqueous electrolyte into the heat-shrinkable tube, the tube was encapsulated via tight tube shrinkage through heating with a heat gun at 120 °C for about 1 min.

3.2.2 Materials Characterization

Morphology information of the synthesized materials was characterized by scanning electron microscopy (SEM, Hitachi S-4800, 5 kV) and the microstructure was observed on a Tecnai G2 F20 S-Twin transmission electron microscopy (TEM) equipped with energy dispersive X-ray spectrometry (EDX). High-resolution TEM images were recorded on a FEI Tecnai G2 20 high-resolution transmission electron microscope at an acceleration voltage of 200 kV. The crystal structure of the samples was identified utilizing a D8 Advance Bruker AXS X-ray diffractometer (XRD) with Cu Kα radiation (λ=0.15418 nm). An ESCALAB MKII X-ray photoelectron spectrometer (XPS) with non-monochromatized Al Kα X-rays as the excitation source was used to detect the chemical composition and oxidation states on the surface of the sample.

3.2.3 Equations

The area (A) and volume (V) of the anode and cathode are calculated by the equations as follows:

$$Ac = \pi DcLc \quad (1)$$

$$Aa = \pi DaLa \quad (2)$$

$$Vc = \pi Dc^2 Lc/4 \quad (3)$$

$$Va = \pi Da^2 La/4 \quad (4)$$

where *D*c (cm) is the diameter of cathode with active material and *L*c (cm) is the length of the cathode, *D*a (cm) is the diameter of anode with active material and *L*a (cm) is the length of the anode. Furthermore, the total volume of the twisted fiber-shaped NiCo-Fe battery is the sum of the volume of anode and cathode and active material. Therefore, the area (A_D) and volume (V_D) of the devices are calculated by the equations as follows:

$$A_D = Ac + Aa \quad (5)$$

$$V_D = Vc + Va \quad (6)$$

The areal specific capacity (C_A), volume specific capacity (C_V), energy density (E), and power density (P) are calculated according to the following equations:

$$C_A = I\Delta t / A_D \quad (7)$$

$$C_V = I\Delta t / V_D \quad (8)$$

$$E = C\Delta V \quad (9)$$

$$P = E/\Delta t \quad (10)$$

Where I is the charge/discharge current (mA), Δt is the discharge time (h), and ΔV is voltage platform, respectively.

3.3 Properties of ZNCO@$Ni(OH)_2$ cathode and Ni-Zn battery

The scanning electron microscopy (SEM) image in Figure 3-1a depicts the smooth surface of CNTF, it is notable the smooth surface of CNTF. The magnified SEM in Figure 3-1b shows the networking of CNTF, implying the large surface area, which can be ideal for the basement material. The SEM image in Figure 3-2a shows that the clean surface of the CNTF is evenly coated with the ZNCO NWAs after hydrothermal synthesis and subsequent calcination treatment. With the increased magnification (Figure 3-2b), it is noticeable that the ZNCO NWAs with smooth surfaces are vertically distributed in the hybrid fiber. The SEM image displayed in Figure 3-3a shows the homogeneous layer of $Ni(OH)_2$ nanosheets that are vertically grown over the entire CNTF surface. The magnified SEM image in Figure 3-3b clearly shows that the $Ni(OH)_2$ nanosheets were densely packed and highly ordered on the fiber surface.

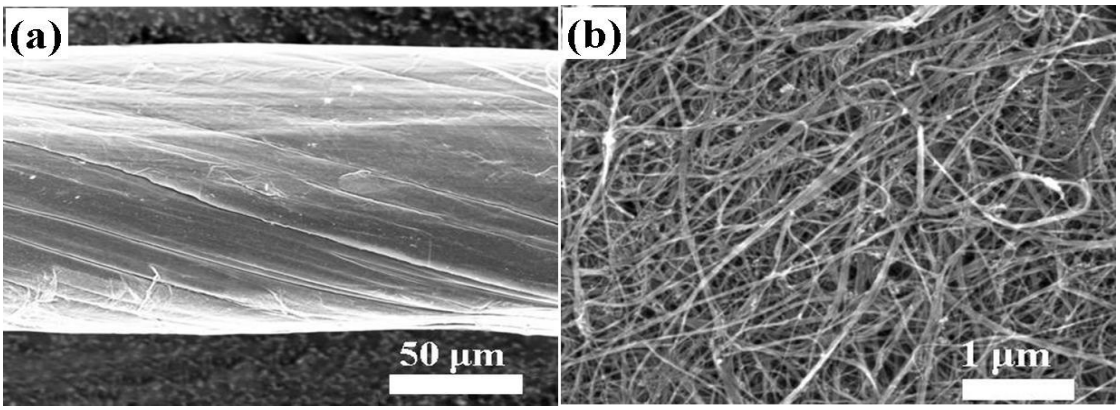

Figure 3-1 (a) Low magnification SEM of pristine CNTF. (b) High magnification SEM of pristine CNTF.

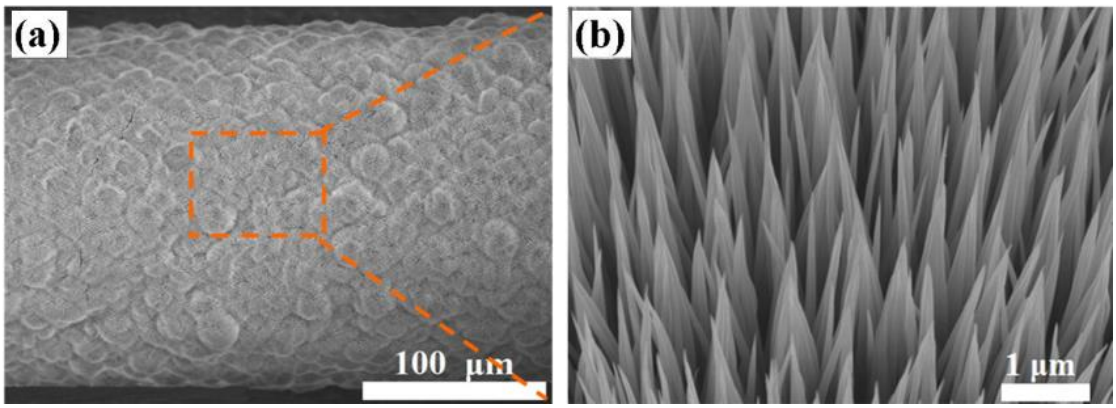

Figure 3-2 Low magnification SEM image of ZNCO/CNTF. (b) High magnification SEM image of ZNCO/CNTF.

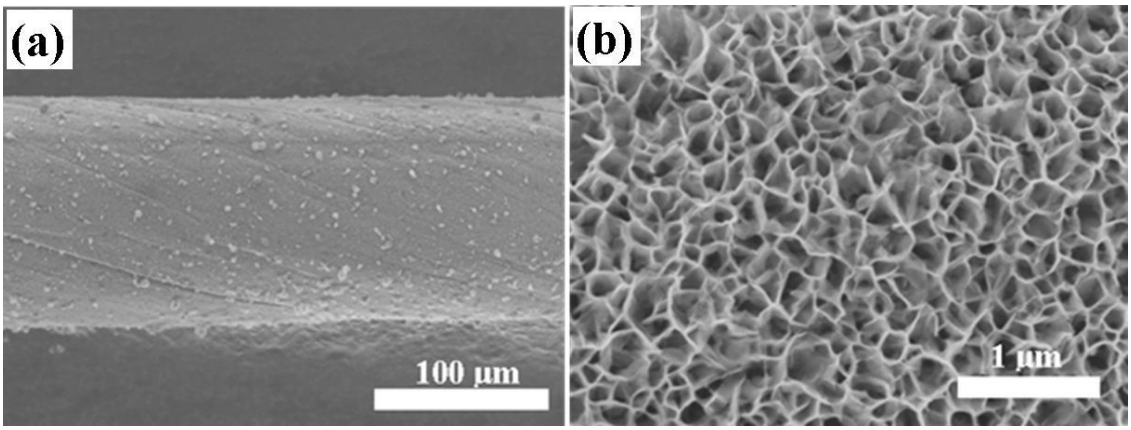

Figure 3-3 (a) Low magnification SEM image of $Ni(OH)_2$/CNTF. (b) High magnification SEM image of $Ni(OH)_2$/CNTF.

The transmission electron microscopy (TEM) image shown in Figure 3-4a reveals the nanowire morphology of ZNCO. The energy dispersive X-ray spectrometry (EDS) mappings in Figure 3-4b represents that existence of Zn, Ni, Co and O atoms of ZNCO nanowire, implying successful synthesis of the Zn/Ni co-doped Co_3O_4. After the chemical bath deposition for 40 mins at room temperature, the skeletons of ZNCO NWAs are homogeneously decorated with $Ni(OH)_2$ nanoflakes (Figure 3-5a), thus forming an interesting nanoflake@nanowires core-shell heterostructures (HSs). EDS mapping results given in Figure 3-5b further present the typical core-shell nanostructure constructed by the complete coverage of ultrathin $Ni(OH)_2$ nanosheets on the entire ZNCO NW skeleton.

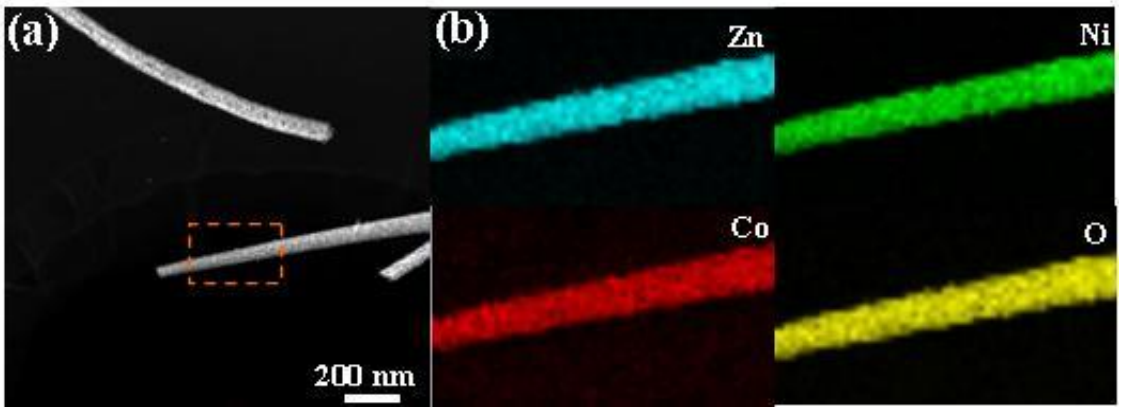

Figure 3-4 (a) Low-magnification TEM image of single ZNCO nanowire. (b) EDS element mappings of single ZNCO nanowire.

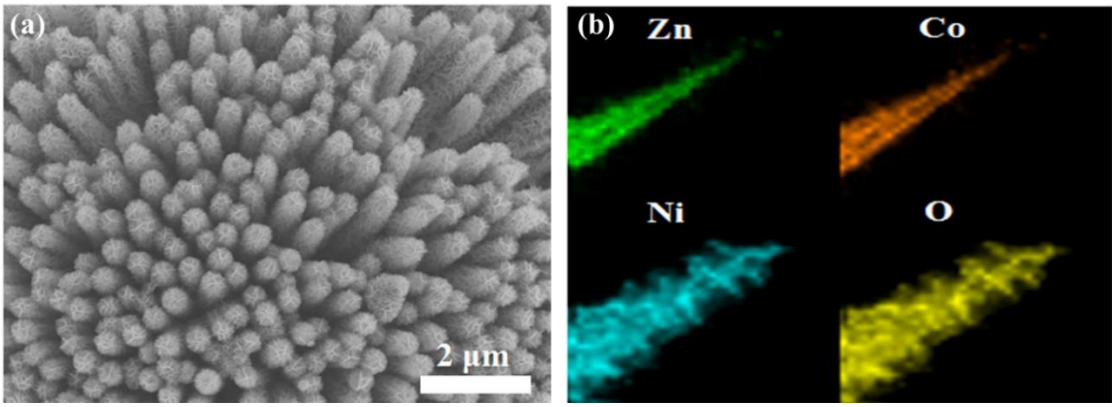

Figure 3-5 (a) High-magnification SEM image of ZNCO@$Ni(OH)_2$ NWAs. (b) EDS element mapping images of Zn, Co, Ni and O in single ZNCO@$Ni(OH)_2$ NWs.

The TEM images of ZNCO@$Ni(OH)_2$ NWA in Figure 3-6a further present the typical core-shell nanostructure constructed by the complete coverage of ultrathin $Ni(OH)_2$ nanosheets on the entire ZNCO NW skeleton. As is observed in Figure 3-6b, the EDS spectrum of ZNCO NWAs, Zn and Ni atoms partially replaced Co atoms, implying successful synthesis of the Zn/Ni co-doped Co_3O_3. Figure 3-7 shows the corresponding X-ray diffraction (XRD) patterns of the ZNCO, $Ni(OH)_2$ and ZNCO@$Ni(OH)_2$. It is noticeable that all major diffraction peaks of ZNCO@$Ni(OH)_2$ perfectly match with the overlay pattern of ZNCO and $Ni(OH)_2$ and no extra peak is detected, indicating that the fabricated hybrid is solely composed of ZNCO and Ni(OH). These results confirm the successful fabrication of ZNCO@$Ni(OH)_2$/CNTFs, which are

subsequently investigated as promising Ni-based anode materials for high-performance Ni-Zn batteries.

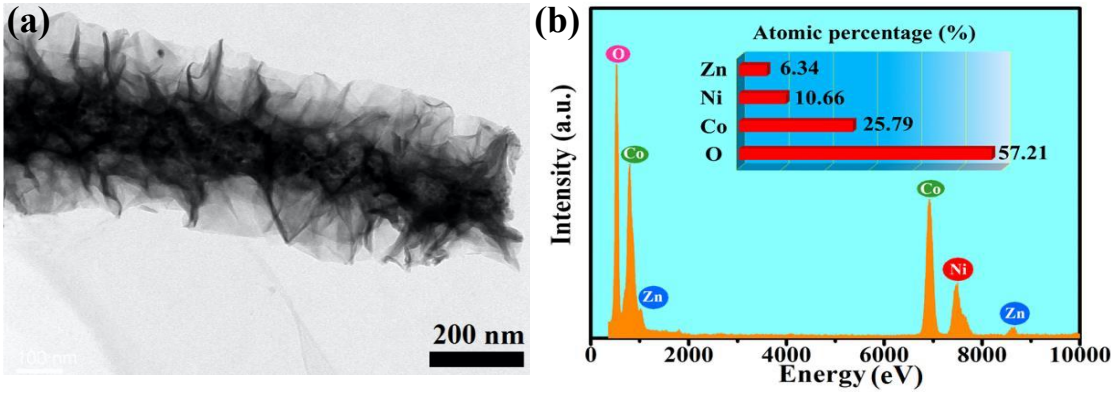

Figure 3-6 (a) Low-magnification TEM of single ZNCO@$Ni(OH)_2$ NW. (b) EDS spectrum of the ZNCO NWA.

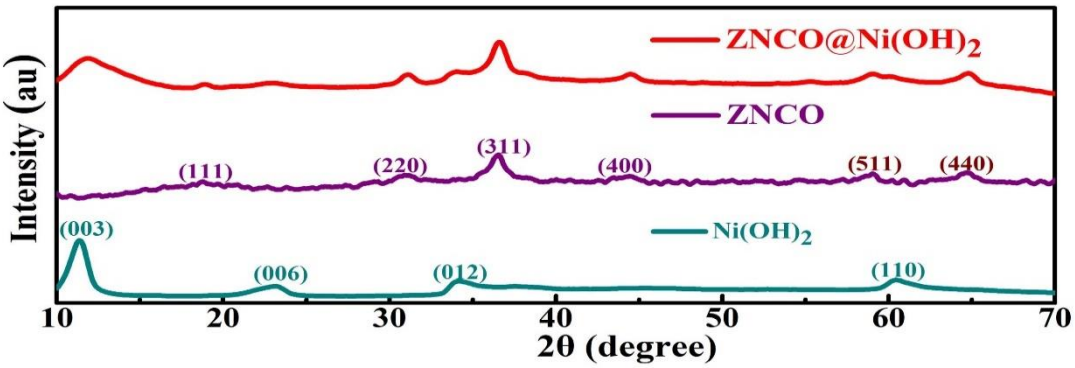

Figure 3-7 XRD patterns of $Ni(OH)_2$, ZNCO and ZNCO@$Ni(OH)_2$ samples.

The elemental compositions and valence states of the as-fabricated ZCNO@$Ni(OH)_2$ NWAs are determined by X-ray photoelectron spectroscopy (XPS). In Zn 2p XPS spectrum of ZCNO@$Ni(OH)_2$ NWAs (Figure 3-8a), two strong Zn 2p peaks are located at 1022.7 and 1045.8 eV, corresponding to Zn 2p3/2 and Zn 2p1/2, respectively. As shown in Figure 3-8b, the XPS spectrum of Ni 2p, two peaks at 873.3 and 855.6 eV can be assigned to the Ni 2p1/2 and Ni 2p3/2 spin-orbit peaks, respectively. Figure 3-8c shows that Co 2p can be divided into two peaks at 796.6 and 780.8 eV, which corresponds to binding energies for Co 2p1/2 and Co 2p3/2, respectively. The O1s signal peak at 529.8 eV presented in Figure 3-8d is divided into two peaks centered at 529.4 and 530.9 eV.

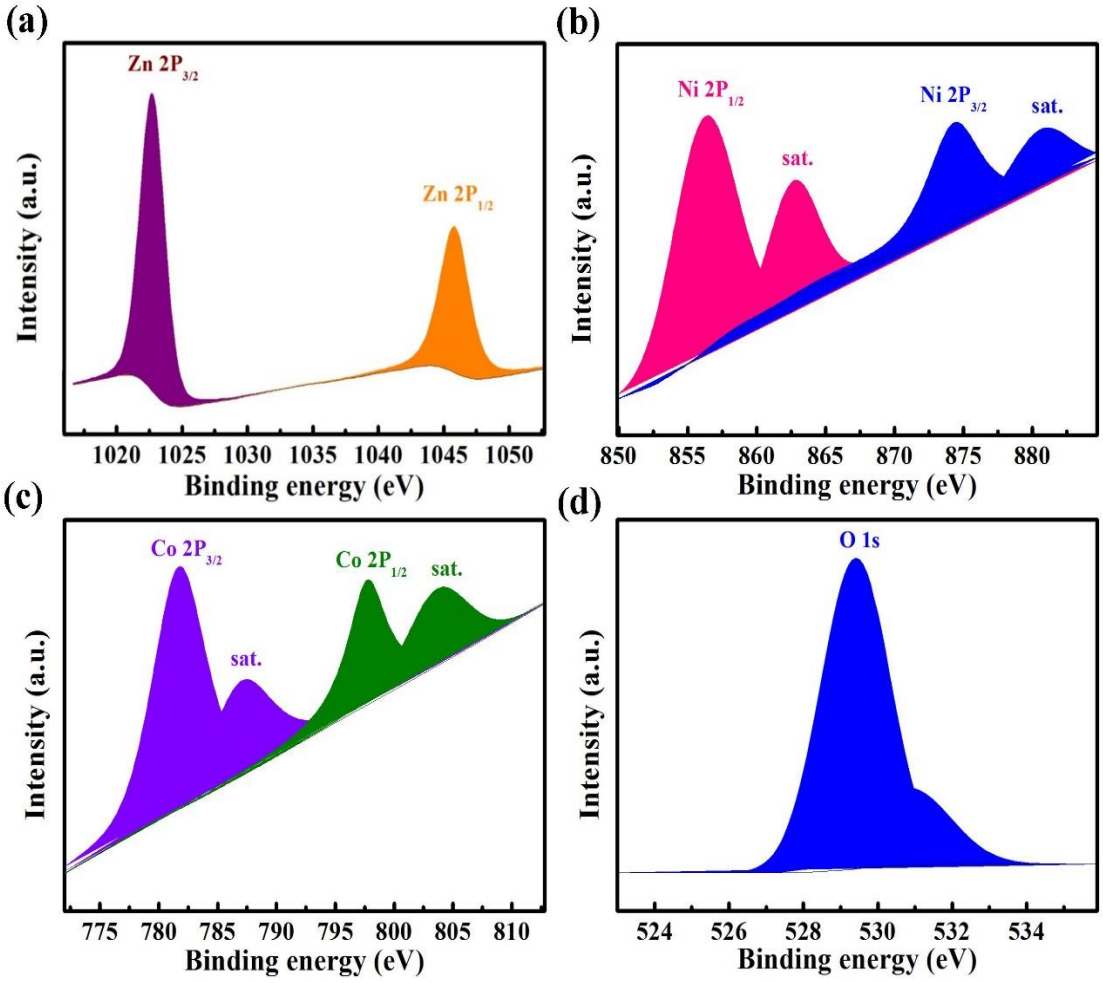

Figure 3-8 XPS spectra of (a) Zn 2p, (b) Ni 2p, (c) Co 2p and (d) O1s for the ZCNO@$Ni(OH)_2$ NWAs core-shell heterostructures.

The comparative cyclic voltammogram (CV) curves in Figure 3-9a shows the square area of CNTF, indicating CNTF have the capacitive behavior and contribute negligibly to the ZNCO@$Ni(OH)_2$ NWAs/CNTF electrode. The galvanostatic charge-discharge (GCD) in Figure 3-9b curve further prove this point of the small discharge time of CNTF. It is noted that a pair of redox peaks in the CV curve of ZNCO NWAs/CNTF, suggesting the ideal battery candidate (Figure 3-10). In addition, the electrode can achieve the maximum of 0.3 mAh/cm^2 at the current density of 1 mA/cm^2. The CV curves of the $Ni(OH)_2$ NWAs/CNTF electrode collected at various scan rates display a couple of prominent and well-defined redox peaks (Figure 3-11a), suggesting the ideal battery behavior and high electrochemical reaction reversibility. The discharge

curves of the $Ni(OH)_2$ NWAs/CNTF electrode in Figure 3-11b clearly demonstrate the distinct discharge voltage plateaus. The electrode can obtain a high capacity of 0.39 mAh/cm^2 at the current density of 1 mA/cm^2.

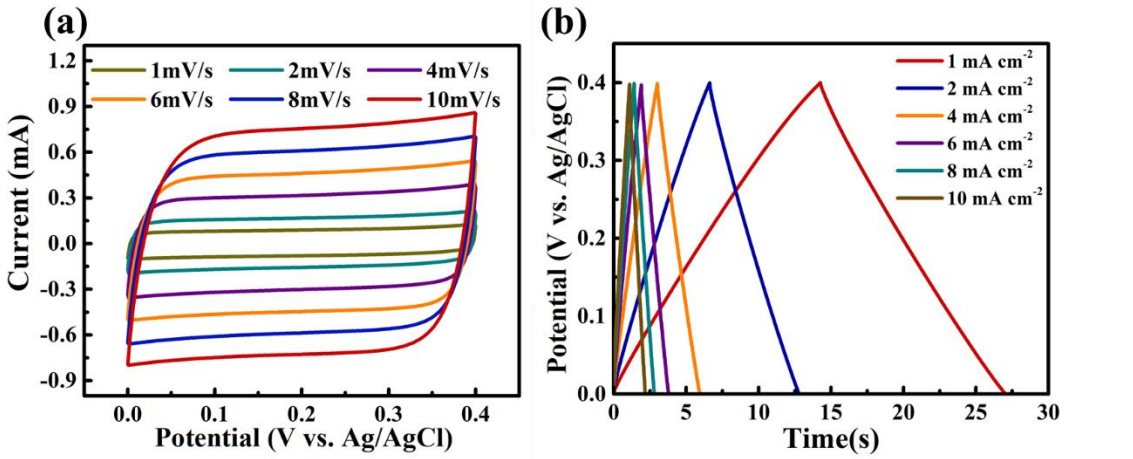

Figure 3-9 (a) CV curves and (b) GCD profiles of bare CNTF cathode.

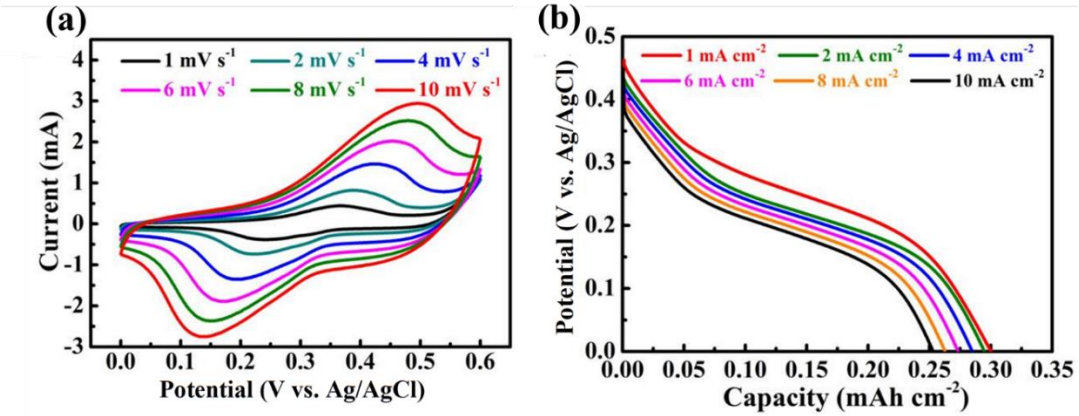

Figure 3-10 (a) CV and (b) GCD curves of ZNCO NWAs/CNTF electrode.

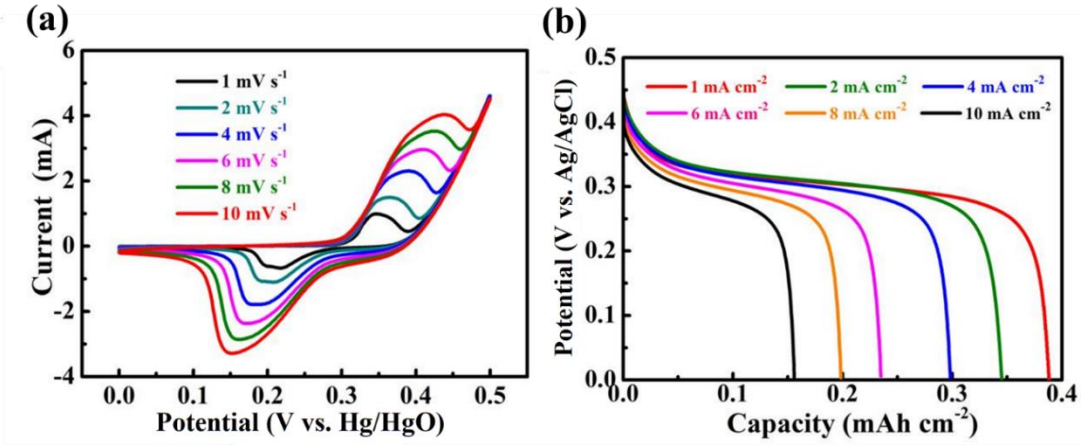

Figure 3-11 (a) CV and (b) GCD curves of $Ni(OH)_2$/CNTF electrode.

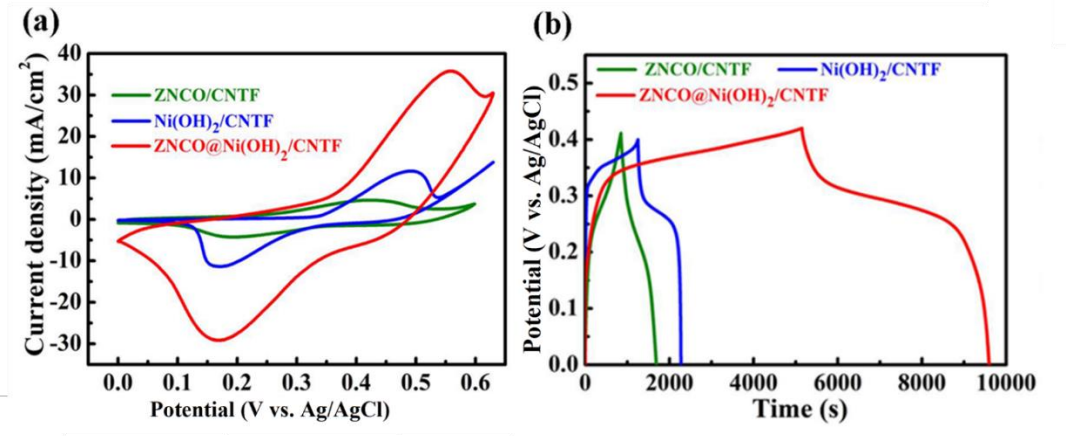

Figure 3-12 Comparison of the (a) CV and (b) GCD curves of ZNCO@$Ni(OH)_2$/CNTF//Zn, ZNCO/CNTF//Zn and $Ni(OH)_2$/CNTF//Zn batteries $Ni(OH)_2$/CNTF electrode.

Figure 3-12a shows the CV curves of ZNCO@Ni(OH)2 NWAs/CNTF, ZNCO NWAs/CNTF and Ni(OH)2/CNTF samples at a scan rate of 2 mV/s. Obviously, the ZNCO@$Ni(OH)_2$ NWAs/CNTF electrode exhibits a larger CV curve area and redox peak intensity than those with single component ZNCO NWAs/CNTF and $Ni(OH)_2$/CNTF, implying that the specific capacity and redox reaction kinetics of core-shell heterostructures electrode are significantly improved. Figure 3-12b further compares the galvanostatic charge/discharge curves of ZNCO@$Ni(OH)_2$ NWAs/CNTF,

ZNCO NWAs/CNTF and $Ni(OH)_2$/CNTF samples at a current density of 1 mA/cm^2. As observed, the discharge time of the fabricated ZNCO@$Ni(OH)_2$ NWAs/CNTF electrode is much longer than that for the ZNCO NWAs/CNTF and $Ni(OH)_2$/CNTF electrodes. The enhancement can be attributed to the increased electrical conductivity of the core electrode and synergistic effects of the well-aligned ZNCO NWAs and ultrathin $Ni(OH)_2$ nanosheets. The comparison of the GCD curves for ZNCO@$Ni(OH)_2$/CNTF//Zn, ZNCO/CNTF//Zn and $Ni(OH)_2$/CNTF//Zn batteries at a high current density of 2 mA/cm^2 is illustrated in Figure 3-13a. Significantly, the ZNCO@$Ni(OH)_2$/CNTF//Zn battery exhibits much longer discharge plateaus than that of the ZNCO/CNTF//Zn and $Ni(OH)_2$/CNTF//Zn batteries, revealing its enhanced capacity. The specific capacities of the ZNCO@$Ni(OH)_2$ NWAs/CNTF, ZNCO NWAs/CNTF and $Ni(OH)_2$/CNTF calculated from the corresponding discharge curves are compared in Figure 3-13b. It is obvious that the discharge areal capacity of ZNCO@$Ni(OH)_2$ NWAs/CNTF electrode is 1.49 mAh/cm^2 (volumetric capacity is 480.4 mAh/cm^3) under 4 mA/cm^2 and this is nearly five times higher than that of the ZNCO NWAs/CNTF electrode (0.30 mAh/cm^2 and 125.8 mAh/cm^3) and over four times higher than that of $Ni(OH)_2$/CNTF electrode (0.39 mAh/cm^2 and 97.5 mAh/cm^3). The CV curves of the ZNCO@$Ni(OH)_2$ NWAs/CNTF electrode collected at various scan rates display a couple of prominent and well-defined redox peaks (Figure 3-14a), suggesting the ideal battery behavior and high electrochemical reaction reversibility. The discharge curves of the ZNCO@$Ni(OH)_2$ NWAs/CNTF electrode in Figure 3-14b clearly demonstrate the distinct discharge voltage plateaus, suggesting the ideal battery behavior and high electrochemical reaction reversibility. To reveal the electrochemical kinetic mechanism of the ZNCO@$Ni(OH)_2$ electrodes, the redox peak currents plotted against the square root of the scan rate are shown in Figure 3-15. The corresponding slopes for the cathodic and anodic relationship were equal to 0.612 and 0.795. When the slope is ~0.5, the electrochemical processes are assumed dependent on the ion diffusion, while slope value equal to 1 implies capacitive-dependence. The calculated results illustrate that the charge storage reaction of ZNCO@$Ni(OH)_2$ NWAs/CNTF is a diffusion-controlled process. According to the Charge-discharge curves in Figure 3-16a and rate capability in Figure 3-16b of the

ZNCO@$Ni(OH)_2$ NWAs at different current densities, a high capacity of 418.12 mAh/g was achieved at 1.1 A/g, and the value was maintained at 362.37 mAh/g when the current density increased to 11 A/g.

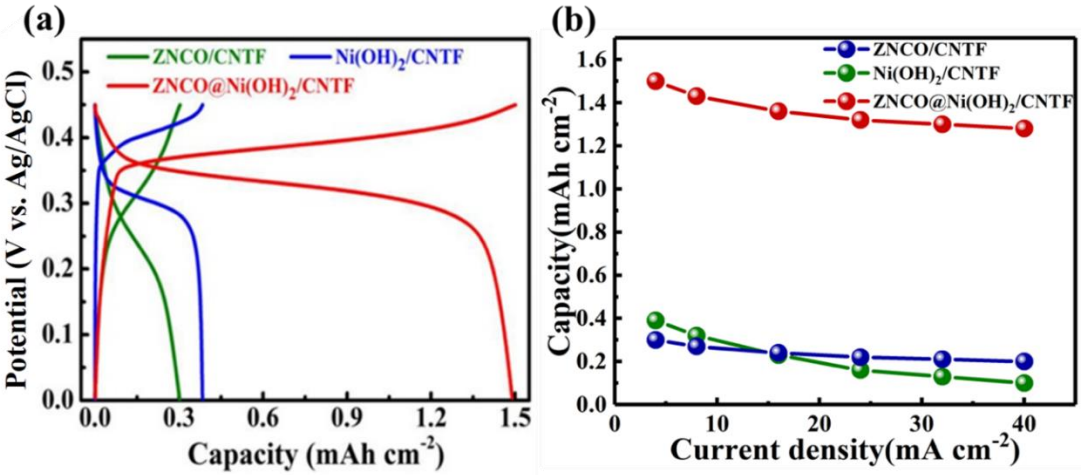

Figure 3-13 (a) Comparative GCD curves of $Ni(OH)_2$, ZNCO, and ZNCO@$Ni(OH)_2$ electrodes at 4 mA/cm^2 (b) The plots of capacities versus current densities for ZNCO@$Ni(OH)_2$/CNTF, ZNCO/CNTF and $Ni(OH)_2$/CNTF electrodes.

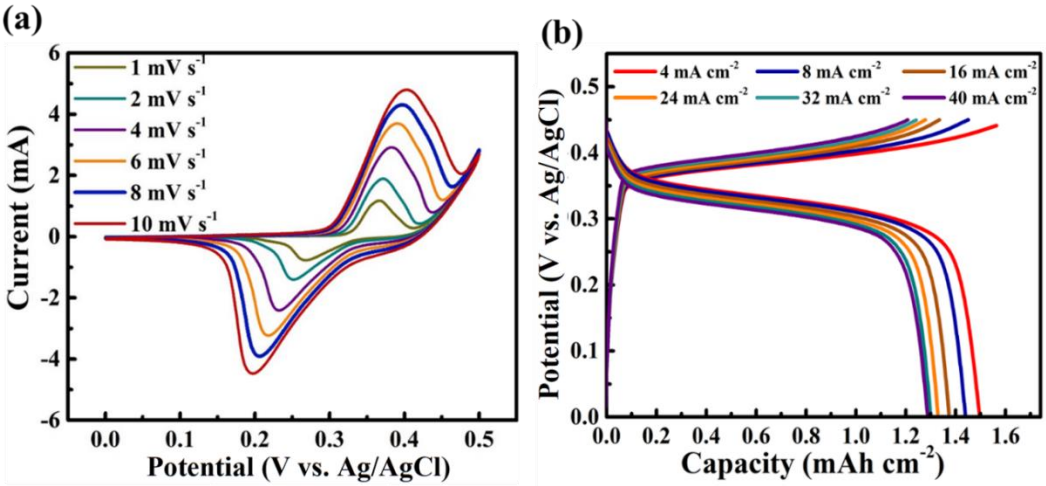

Figure 3-14 (a) CV curves for the $Ni(OH)_2$, ZNCO and ZNCO@$Ni(OH)_2$ electrodes at various scan rates. (b) GCD curves of the ZNCO@$Ni(OH)_2$ electrode at various current densities.

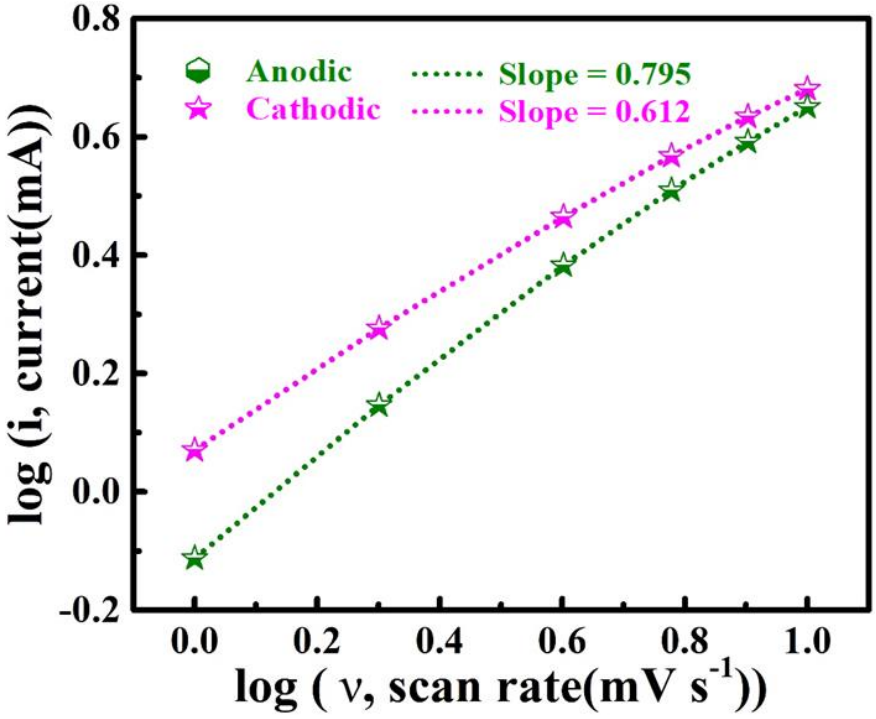

Figure 3-15 Linear fitting of the peak current versus scan rate for the cathodic and anodic peaks of the CV curves for the ZNCO@$Ni(OH)_2$ NWAs/CNTF electrode.

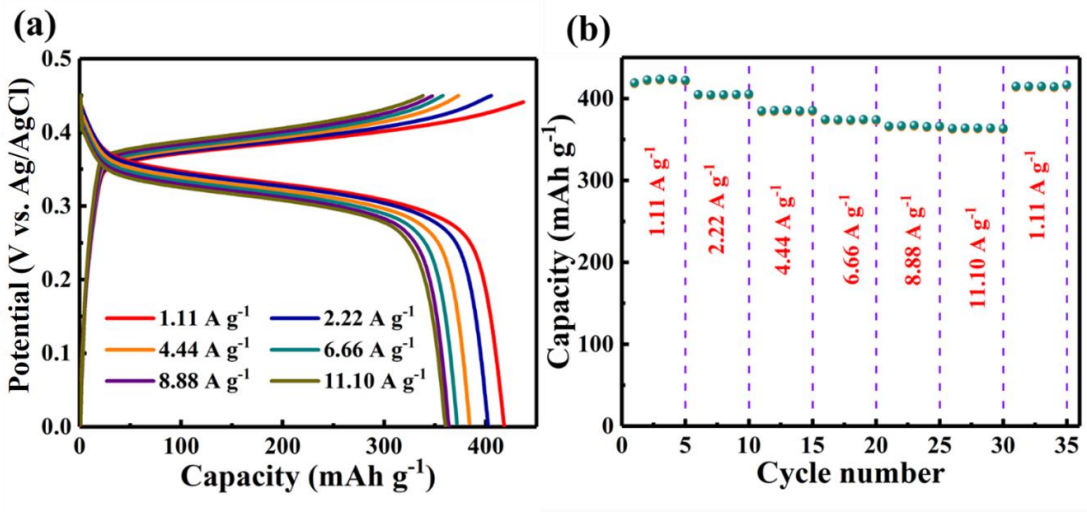

Figure 3-16 Charge-discharge curves (a) and rate capability (b) of the ZNCO@$Ni(OH)_2$ NWAs at different current densities.

As schematically illustrated in Figure 3-17, the fiber-shaped Ni-Zn battery is encapsulated into the heat-shrinkable tube by adopting ZNCO@$Ni(OH)_2$ NWAs/CNTF as the cathode, ZnO-saturated 3 M KOH aqueous solution as the electrolyte and the Zn wire as the anode. A pair of apparent well-defined redox peaks are observed in the CV curves of the as-assembled fiber-shaped Ni-Zn battery (Figure 3-18a), which can be well assigned to the following reactions:

Cathode reaction: $ZNCO + OH^- + H_2O \leftrightarrow ZNCOOH + e^-$ (1)

$Ni(OH)_2 + OH^- \leftrightarrow NiOOH + H_2O + e^-$ (2)

Anode reaction: $Zn(OH)_2 + 2e^- \leftrightarrow Zn + 2OH^-$ (3)

The GCD curves of our fiber-shaped Ni-Zn battery in Figure 3-18b show distinct discharge voltage plateau of 1.75 V and good symmetry, reflecting its desirable battery characteristic and excellent electrochemical reversibility.

Figure 3-17 Schematic illustration of the fiber-shaped Ni-Zn battery.

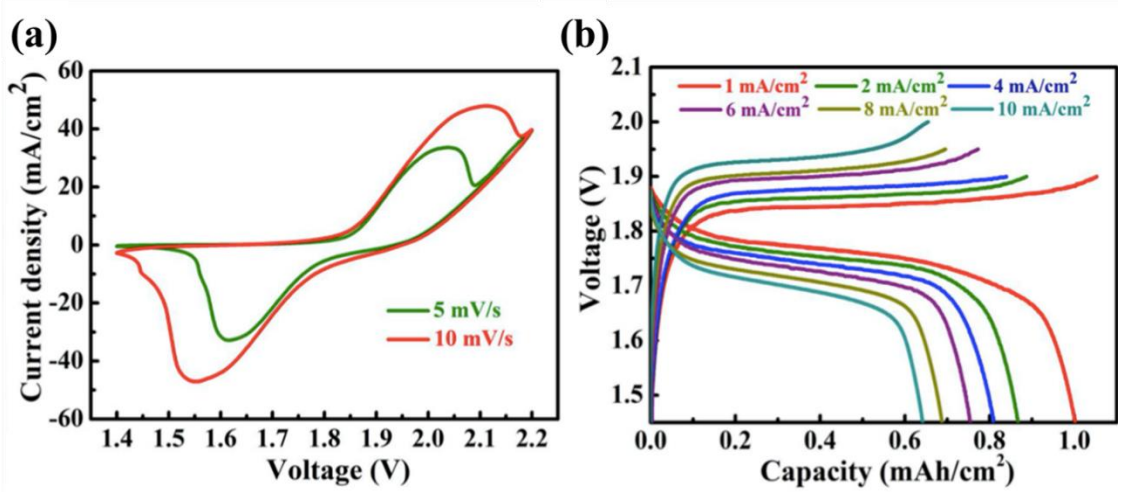

Figure 3-18 (a) CV curves of the as-assembled fiber-shaped Ni-Zn battery measured at different scan rates. (b) Charge-discharge curves collected at different current densities.

As illustrated in Figure 3-19a the as-assembled fiber-shaped Ni-Zn battery displays a high areal capacity of 1.01 mAh/cm^2 at the current density of 1 mA/cm^2 and it still retains 0.64 mAh/cm^2 at a high current density of 10 mA/cm^2, demonstrating superior rate capability. The areal energy and power densities of our fiber-shaped Ni-Zn battery in comparison with those state-of-the-art devices is depicted in Figure 3-19b. More importantly, a maximum energy density of 3.72 mWh/cm^2 and a maximum high power density of 17.13 mW/cm^2 are achieved for our device, which are considerably higher than those values of previously reported batteries such as. Additionally, our CFARSIB displays long-term cycling stability with a high capacity retention of 91.3% after 3000 cycles and high coulumbic efficiency of 99.2% (Figure 3-20).

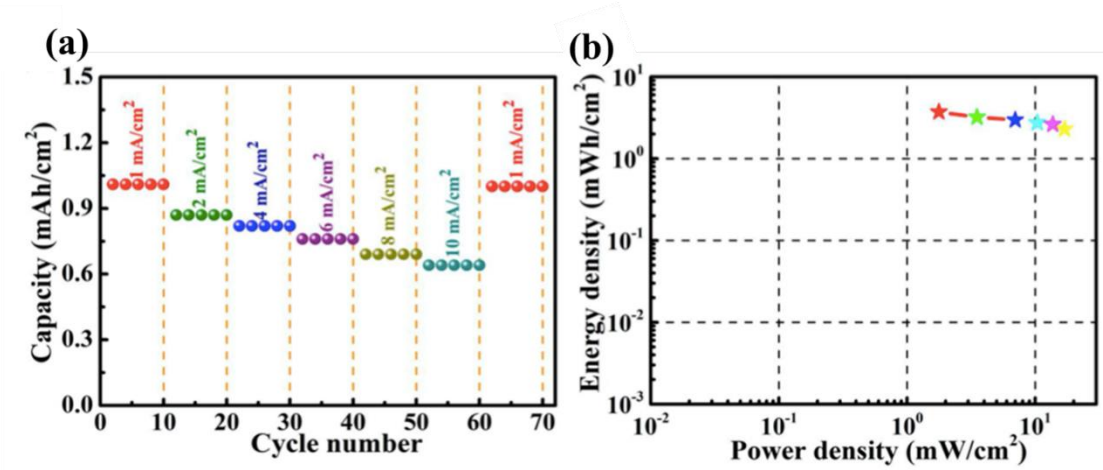

Figure 3-19 (a) Rate capability of our fiber-shaped Ni-Zn battery at varied current densities. (b) Comparison of volumetric energy and power densities of our fiber-shaped Ni-Zn battery with previously reported fiber-shaped aqueous rechargeable batteries.

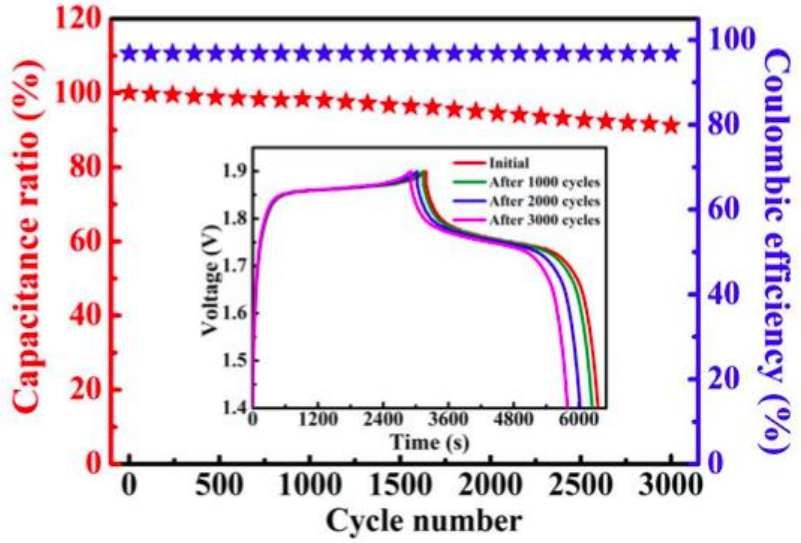

Figure 3-20 Long-term cycling stability and the corresponding Coulombic efficiency of our fiber-shaped Ni-Zn battery device. (Inset: charge-discharge curves at different cycles.)

To evaluate the practical application of the fiber-shaped Ni-Zn battery in portable and wearable energy-storage devices, a series of flexibility tests were performed on the device. Notably, the discharge curves were well maintained under increasing bending angles (Figure 3-21a), indicating its exceptional flexibility. It is encouraging that the

assembled device can be stably operated even under a dynamic bending and releasing process at a speed of 10 degrees per second (Figure 3-21b).

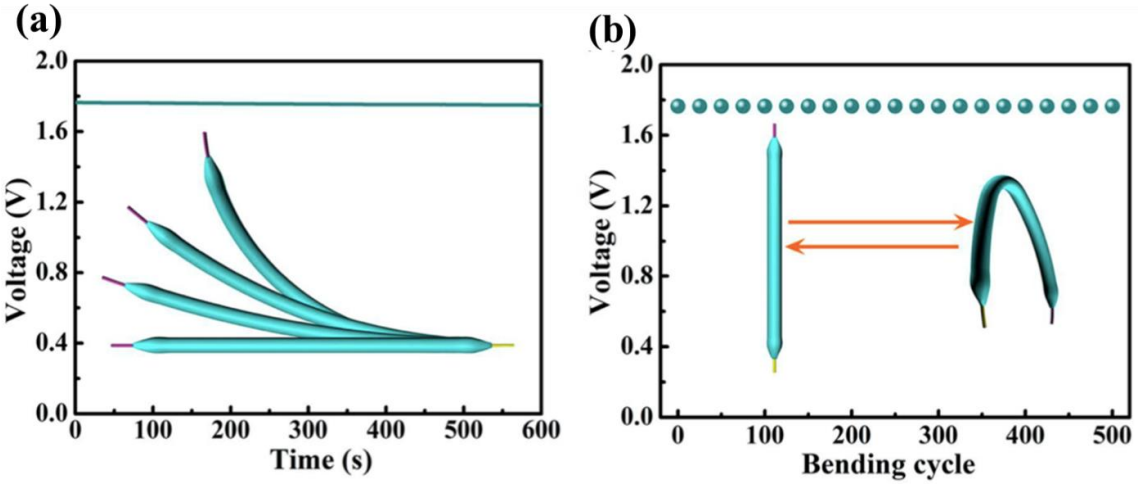

Figure 3-21 (a) Discharge curve of our fiber-shaped Ni-Zn battery under a dynamic bending and releasing process at a speed of 10 degree per second. (b) Normalized capacities of the as-assembled fiber-shaped Ni-Zn battery bent at 90° for 500 cycles.

It is well known that series connection of device is a simple and effective strategy to enlarge operating voltage. As illustrated in Figure 3-22a, two devices were connected in series can achieve a high operating voltage of 3.5 V with a similar charge-discharge time compared to a single device. More importantly, a long device is woven into a flexible textile via conventional weaving technology as a wearable power source to illuminate ten red light-emitting diodes (Figure 3-22b), manifesting the favorable weavability of our device. To further demonstrate promising application of our device, we used two fully charged series-connected fiber-shaped Ni-Zn batteries to drive an overall water-splitting device based on zinc-nicke-cobalt phosphide (ZNCP) bifunctional electrocatalyst. It can be observed from the SEM images in the inset of Figure 3-23a, the morphology of the ZNCP NWAs were well preserved after one-step phosphidation treatment. The overall water splitting electrocatalytic performance is measured in two-electrode system using ZNCP NWAs/CNTF as both anode and cathode, respectively. The steady-state polarization curve for overall water splitting of ZNCP NWAs/CNTF presents a cell voltage of 1.768 V to afford 20 mA/cm^2, implying its impressive overall

water-splitting characteristic. As shown in Figure 3-23b two series-connected fiber-shaped Ni-Zn batteries can offer steady output voltage for overall water splitting for 3600 s.

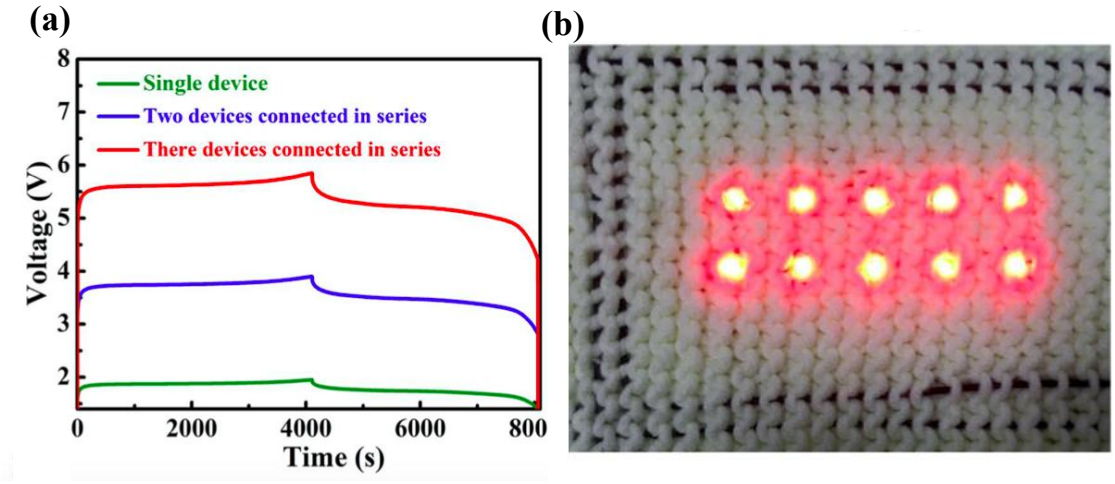

Figure 3-22 (a) Charge-discharge curves of three fiber-shaped Ni-Zn batteries connected in series. (b) Photograph of ten red LEDs illuminated by the charged power textile consisting of our fiber-shaped Ni-Zn batteries.

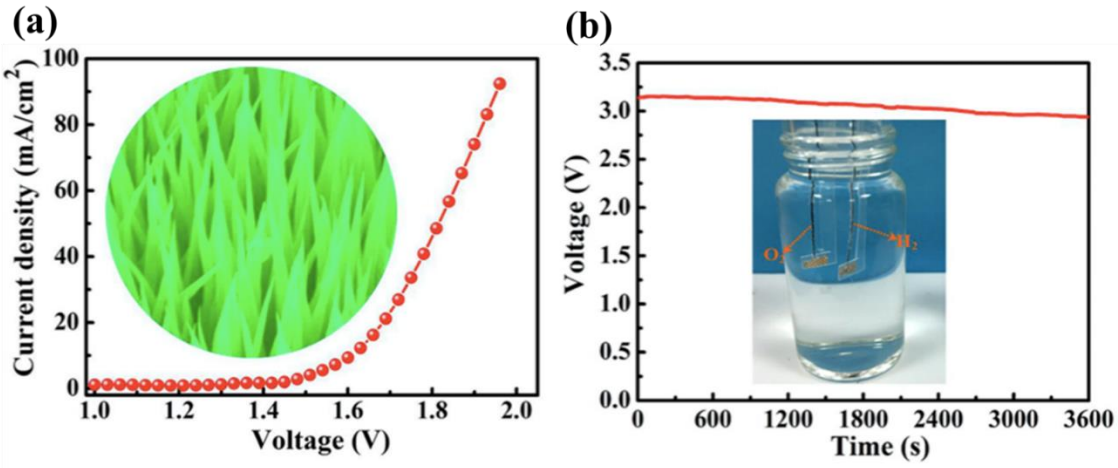

Figure 3-23 (a) Polarization curves of ZCNP/CNTF for overall water splitting in 1 M KOH solution at a scan rate of 5 mV/s (Inset: High-magnification SEM image of ZNCP NWAs). (b)Voltage-time curve of self-driven overall water splitting powered by two

series-connected fiber-shaped Ni-Zn batteries (Inset: Photograph of the overall water splitting device).

3.4 Conclusion

The novel ZNCO@$Ni(OH)_2$ NWAs core-shell heterostructures have been fabricated on a flexible and high conductivity CNTF via a facile and cost-effective synthesis approach. The well-designed ZNCO@$Ni(OH)_2$ NWAs electrode provides efficient electron transfer channels, short ion diffusion and abundant exposed active sites, leading to a significant improvement in electrochemical properties. By matching with Zn/CNTF hybrid fiber as cathode, a high-performance aqueous rechargeable fiber-shaped Ni-Zn battery with a stable operating voltage of 1.75 V is constructed. Electrochemical test results shows that our as-assembled devices deliver a high capacity of 2.07 mAh/cm^2 and an impressive energy density of 3.71 mWh/cm^2, outperforming most previously reported aqueous Zn-based batteries. To further demonstrate their practical applications, fiber-shaped Ni-Zn batteries were woven into the flexible power textile and two series-connected Ni-Zn batteries can drive overall water electrocatalysis splitting for 3600 s. This work may shed new light on rational design of novel Ni-based core-shell heterostructure cathodes for next-generation wearable Ni-Zn batteries

Chapter 4 Rational Construction of Self-Standing Sulphur-Doped Fe_2O_3 Anodes with Promoted Energy Storage Capability for Wearable Aqueous Rechargeable NiCo-Fe Batteries

Aqueous rechargeable Ni-Fe batteries featured with ultra-flat discharge plateau, low cost, and outstanding safety characteristics show promising prospects for application in wearable energy storage. In particular, fiber-shaped Ni-Fe batteries will enable the textile-based energy supply for wearable electronics. However, the development of fiber-shaped Ni-Fe batteries is currently challenged by the performance of fibrous Fe-based anode materials. Thus, this paper describes fabrication of sulfur-doped Fe_2O_3 nanowire arrays (S-Fe_2O_3 NWAs) grown on CNTF as an innovative anode material (S-Fe_2O_3 NWAs/CNTF). Encouragingly, first-principle calculations reveal that S-doping in Fe_2O_3 can dramatically reduce the bandgap from 2.34 eV to 1.18 eV and thus enhance electronic conductivity. The novel developed S-Fe_2O_3 NWAs/CNTF electrode is further demonstrated to deliver very high capacity of 0.81 mAh/cm^2 at 4 mA cm^2. This value is almost 6-fold higher than of the pristine Fe_2O_3 NWAs/CNTF electrode. When a cathode containing ZNCO@$Ni(OH)_2$ NWAs heterostructures was used, 0.46 mAh/cm^2 capacity and 67.32 mWh cm^3 energy density were obtained for quasi-solid-state fiber-shaped NiCo-Fe batteries. which outperform most state-of-the-art fiber-shaped aqueous rechargeable batteries. These findings offer an innovative and feasible route to design high-performance Fe-based anode and may inspire new development for the next-generation wearable Ni-Fe batteries.

4.1 Introduction

Increasing efforts are undertaken continuously to develop high-performance aqueous rechargeable batteries[136-147]. Among various aqueous rechargeable batteries, aqueous secondary Ni-Fe batteries with the abundant constituent elements, low cost, and ultra-flat discharge plateau have attracted widespread attention [148-154]. Although the

significant progress achieved for Ni-based cathode materials, the lack of high-capacity Fe-based anode materials remains a stumbling block preventing further improvements of the energy density of aqueous rechargeable Ni-Fe batteries. Moreover, with the ever-growing consumer usage of portable and wearable electronics, small, flexible and lightweight fiber-shaped Ni-Fe batteries are regarded as promising energy supply devices [155-159]. Therefore, the exploration of high-performance fibrous Fe-based anodes is still highly valuable and significant for the use in high-energy-density wearable Ni-Fe batteries.

In the past few years, Fe-based oxides were considered as a promising active anode material for aqueous rechargeable Ni-Fe batteries due to their high theoretical capacities [160-162]. However, the low capacity and poor rates capability of such electrodes fundamentally limit the development of Fe-based oxide anodes. Early studies have revealed that anion doping in transition-metal oxides is a straightforward and cost-effective strategy to tune the bandgap and electronic conductivity of active materials to enhance the electrochemical performance[163-165].Yang et al. designed nitrogen-doped Co_3O_4 nanowires on carbon cloth with significantly improved oxygen reduction reaction catalytic activity as an additive-free air-cathode for flexible solid-state Zn-air batteries[166]. Lu et at. reported phosphorus-doped ultrathin $NiCo_2O_4$ nanosheets with an ultrahigh capacity of 198.0 mAh g^{-1} at 60.4 A g^{-1}, nearly 15 times higher than that of unmodified $NiCo_2O_4$ electrode[167]. Qiao et al. successfully fabricated sulfur-doped $NiFe_2O_4$ nanosheets on nickel foam that could achieve enhanced catalytic properties for both the H_2 and O_2 evolution reactions[127]. Thanks to the rich reaction sites, convenient ion diffusion path, and fast charge transport, self-standing nanostructured Fe-based oxide electrodes have been demonstrated to be a promising design[168-169]. Encouragingly, CNTF exhibits lightweight, outstanding flexibility and excellent conductivity that can be widely used as fibrous electrodes of wearable energy-storage devices[170-172].Thus, it is urgently desirable to develop self-standing anion doped Fe-based oxide on CNTF as fibrous anodes to achieve high-performance Ni-Fe batteries.

In this chapter, the as-prepared ZNCO@$Ni(OH)_2$ NWAs in last chapter with superior high capacity with 1.49 mAh/cm^2 at 4 mA/cm^2, which is significantly higher

than other reported fibrous electrode materials. In order to assemble the battery to gain the high performance, the relationship of the charges between the two electrodes is Q+ = Q- and Q = C × A × V, where C is the specific capacity, V is the potential range, and A is the area of the electrode. Therefore, we aim to fabricate the anode with high capacity using the anion doping method.

4.2 Experimental

4.2.1 Materials Preparation of S-Fe_2O_3 NWAs/CNTF and NiCo-Fe battery

Fabrication of S-Fe_2O_3 NWAs/CNTF: S-Fe_2O_3 NWAs/CNTF was prepared by a two-step synthesis consisting of a hydrothermal step followed by the sulfuration process. Typically, 0.321 g of Na_2SO_4 and 0.3267 g of $FeCl_3$ were dissolved in 45 ml of deionized (DI) water under constant stirring for 30 min. The resulting clear orange solution was placed into a 50 ml Teflon-lined stainless steel autoclave, after which CNTFs taped onto the Teflon were placed inside the container. The autoclave was kept at 160 °C for 6 h, after which it was allowed to cool down naturally. The resulting Fe-O precursor/CNTF was rinsed several times distilled water, after which it was dried overnight at 60 °C. 0.4 g of S powder was positioned in the furnace center while Fe-O/CNTF precursor was placed at the bottom. To obtain S-Fe_2O_3 NWAs/CNTF, the as-fabricated Fe-O precursor/CNTF was heated at 200 °C for 4 h under 200 sccm Ar flow. The precursors were annealed under N_2 at 350 °C for 4 h to acquire Fe_2O_3/CNTF.

Assembly of NiCo-Fe battery: The gel electrode was obtained using 10 g of PVA and 11.2 g of KOH dissolved in 100 ml of DI water under vigorous stirring at 95 °C for 2 h until a clear solution was obtained. To assemble the NiCo-Fe battery, S-Fe_2O_3 NWAs/CNTF-based anode and ZNCO@$Ni(OH)_2$ NWAs/CNTF-based cathode were twisted together (both electrodes were percolated with PVA-KOH gel electrolyte.) and soaking it overnight until the electrolyte solidified.

4.2.2 Description of first-principle calculations

Spin-polarized density functional theory (DFT) simulations were performed by the Vienna ab initio simulation (VASP) package using the projector augmented wave (PAW) potentials with a plane wave cutoff at 500 eV. The generalized gradient approximation (GGA) of Perdew-Burke-Ernzerhof (PBE) functional was employed in our simulations.

Description of first-principle calculations for Fe_2O_3 and S-Fe_2O_3 NWAs: NWAs The pristine Fe_2O_3 was model by a 1×1×1 hexagonal cell, consisting of 12 iron and 18 oxygen atoms, with the lattice parameters of 5.03 Å, 5.03 Å and 13.55 Å. The S-doped Fe_2O_3 model was built by replacing two oxygen atoms with sulfur atoms in a hexagonal Fe_2O_3 cell to simulate the 6% S-doping based on the experimental observations. The *k*-point meshes of both pristine and S-doped Fe_2O_3 were 6×6×2 for the geometry optimizations, and 18×18×6 for the DOS calculations. The energy and force convergence criteria were set at 10^{-5} eV and 0.02 eV $Å^{-1}$, respectively.

Description of first-principle calculations for ZNCO@$Ni(OH)_2$ heterostructure: The interface model of cathode material was built as a single $Ni(OH)_2$ layer placed on the (111) surface of cubic Co_3O_4 cell (5.61 Å, 5.61 Å and 30 Å), which was doped with Ni and Zn atoms. The (111) surface was chosen in this study since it is one of the most stable surfaces of Co_3O_4, and its hexagonal pattern is the same with the Ni-LDH. The Ni-Zn-doped Co_3O_4 model consists of 11 Co atoms, 3 Zn atoms and 4 Ni atoms, which is very close to the experimental concentration. The *k*-point meshes were 5×5×1 for the geometry optimizations and 10×10×2 for the DOS calculations. The force and energy convergence criterions were set to be 0.02 eV $Å^{-1}$ and 10^{-5} eV, respectively. The antiferromagnetic states were set as the initial spin states of Co_3O_4 in all the calculations.

4.3 Properties of S-Fe_2O_3 anode and NiCo-Fe battery

The preparation schematics of S-Fe_2O_3 NWAs/CNTF anode consisting of simple hydrothermal synthesis and in-situ sulfuration is shown in Figure 4-1. The Fe-O

precursor directly grew on the surface of the original CNTF through hydrothermal, then the in-suit sulfuration in argon to successfully doping the sulfur element to the precursor. In addition, the SEM image displayed in Figure 4-2 presents that the Fe_2O_3 NWAs are well-distributed on the skeleton of the CNTF.

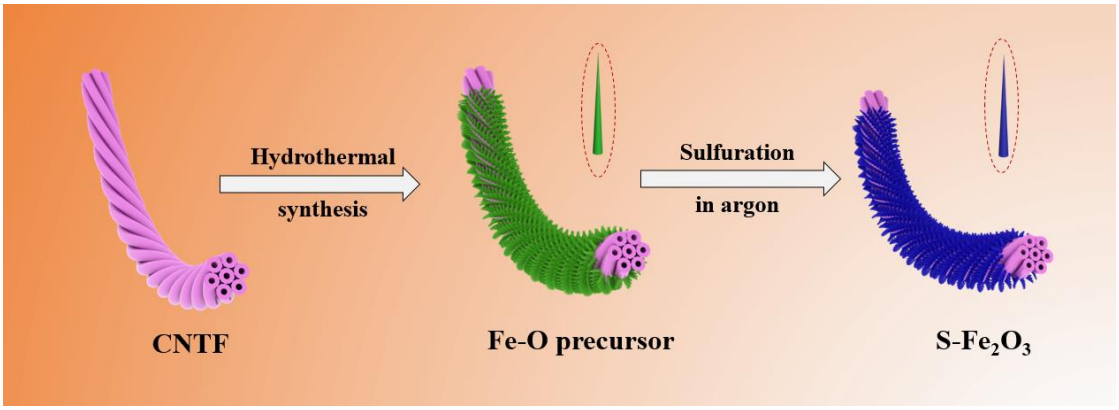

Figure 4-1 Preparation procedure of S-Fe_2O_3 NWAs/CNTF anode.

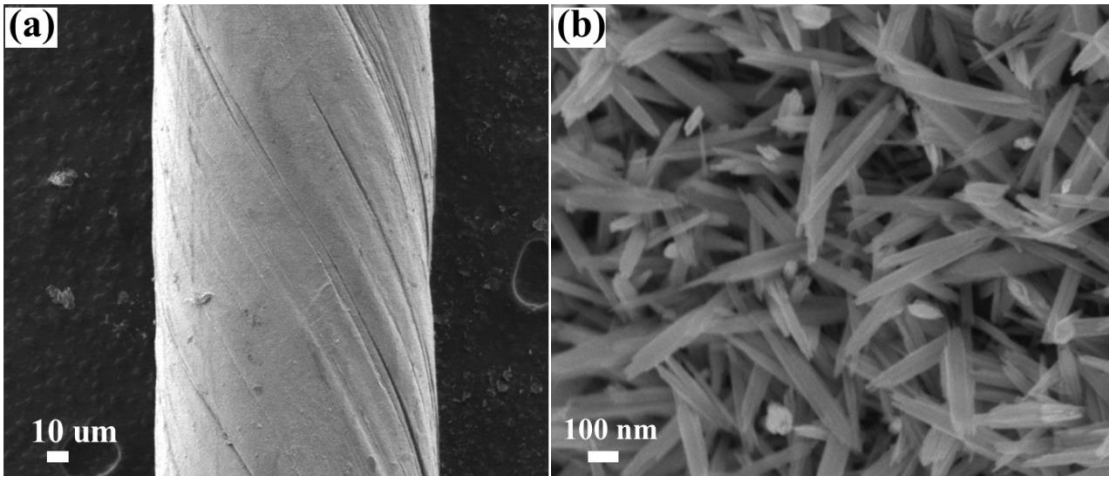

Figure 4-2 (a) Low magnification SEM image of Fe_2O_3 NWAs/CNTF. (b) High magnification SEM image of Fe_2O_3 NWAs/CNTF.

The SEM image in Figure 4-3 reveals that the entire surface of CNTF is uniformly and densely covered with S-Fe_2O_3 NWAs. The comparison between un-doped and S-doped samples clearly demonstrates that the structures of Fe_2O_3 NWAs are well preserved after thermal treating under S vapor. The EDS results shown in Figure 4-4a demonstrate the atom ratio of Fe: O: S is 2:2.43:0.29, implying that O atoms are partially

replaced by S atoms. The S-Fe_2O_3 NWs were crystalline nature judging by a series of diffraction signals from the selected area electron diffraction (SAED) pattern. It is easily found the diffraction rings can be readily indexed to (204) (006) (110) (102) in the SAED from the Figure 4-4b.

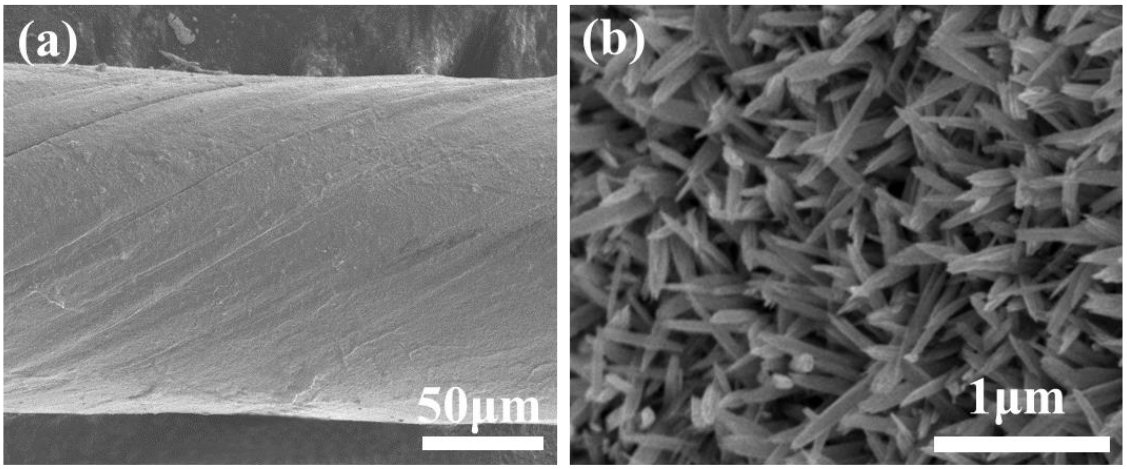

Figure 4-3 (a-b) SEM images with different magnifications of S-Fe_2O_3 NWAs/CNTF.

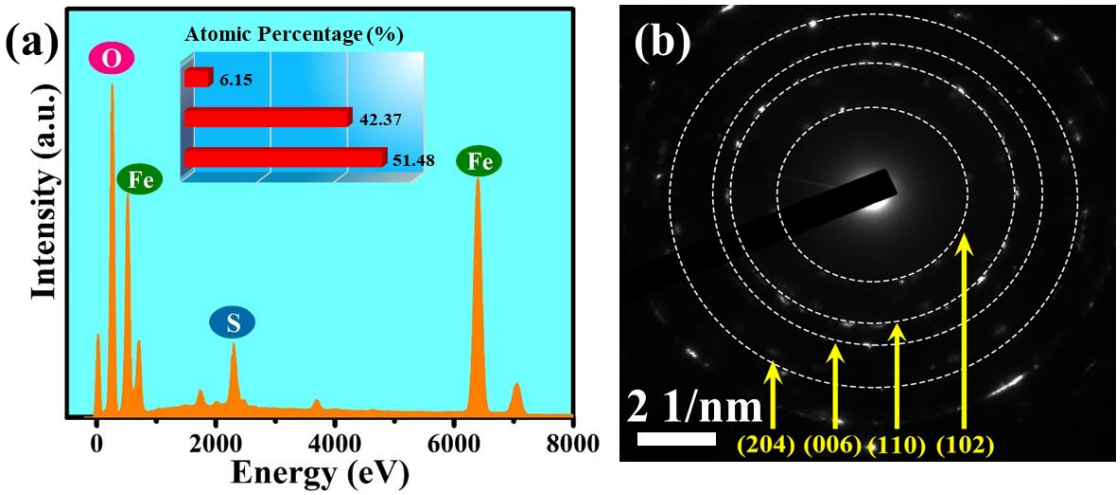

Figure 4-4 (a) EDS spectrum and (b) SAED pattern for S-Fe_2O_3 NWs.

The EDS demonstrated the homogeneous Fe, O, and S distribution throughout the NWs (Figure 4-5). However, EDS did not reveal the presence of S in Fe_2O_3 NWs (Figure 4-6). It just shows the homogenous distribution of Fe and O elements of the Fe_2O_3 nanowires. SAED pattern shown in Figure 4-7a implies the polycrystalline nature of S-Fe_2O_3 NW and the diffraction rings can be readily indexed to (116), (006), (104) and

(102) planes of hexagonal phase Fe_2O_3. High-resolution transmission electron microscopy (HRTEM) image in Figure 4-7b shows interplanar spacing of 0.369 nm, which is consistent with the (102) plane of Fe_2O_3. HRTEM image showed well-resolved lattice fringes 0.269 nm apart correspond to (104) planes of Fe_2O_3 (Figure 4-8).

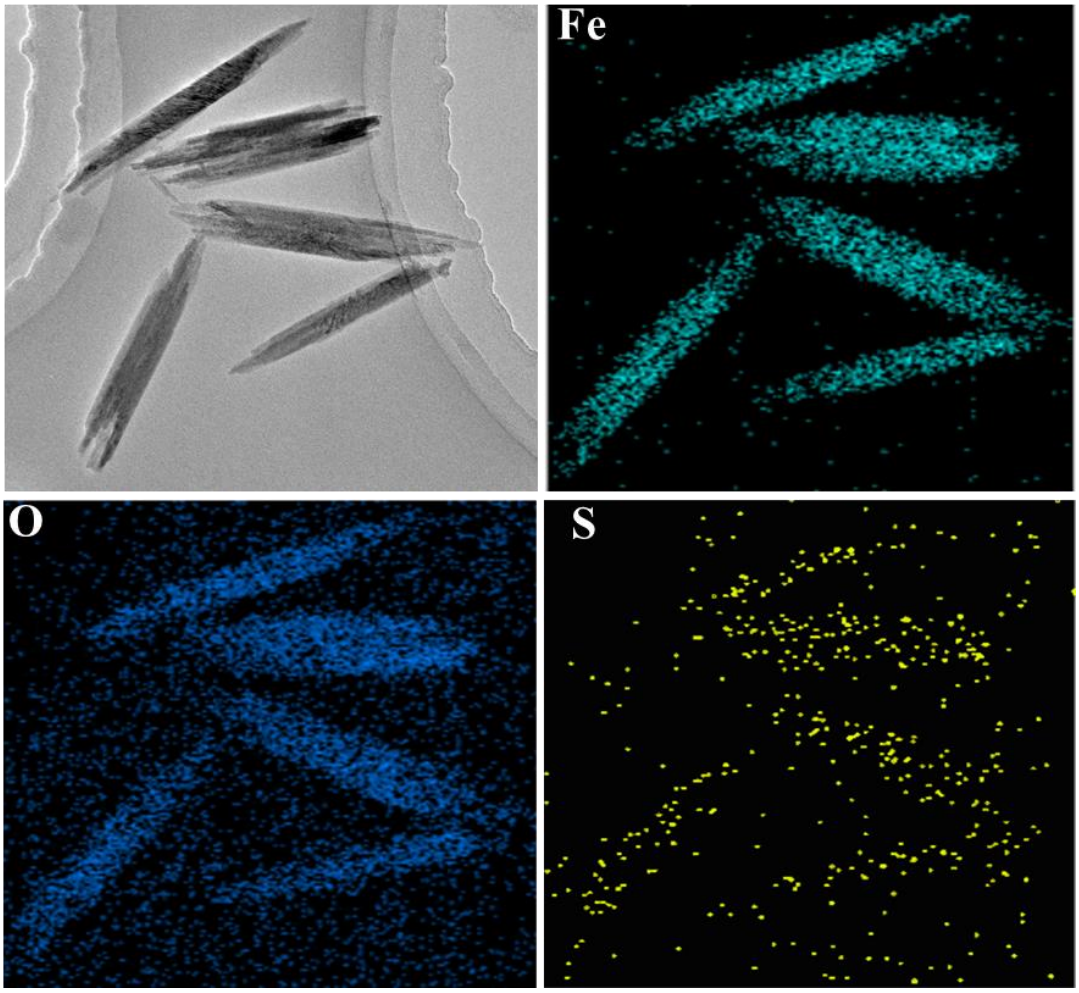

Figure 4-5 TEM image of S- Fe_2O_3 NWs and the corresponding EDS elemental mapping.

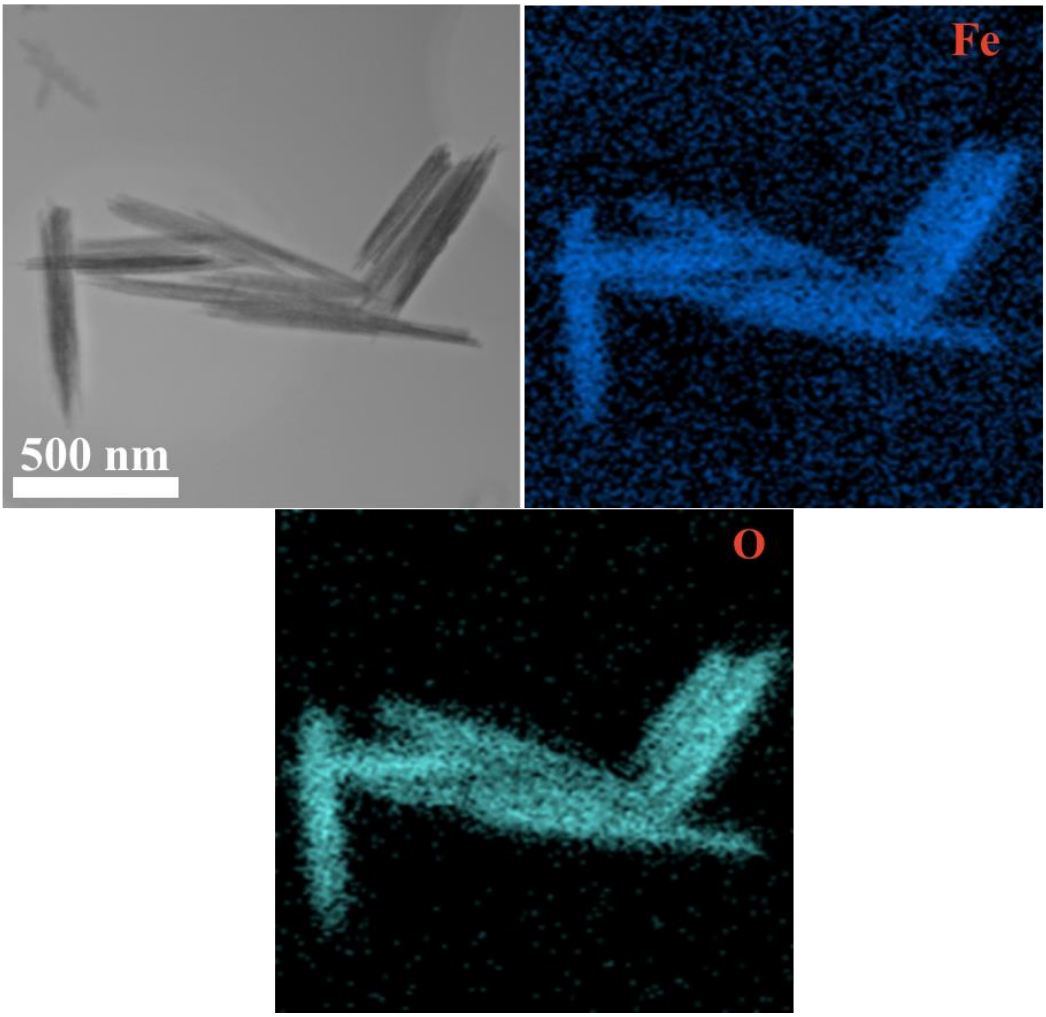

Figure 4-6 EDS elemental mappings of Fe and O of Fe_2O_3 nanowires.

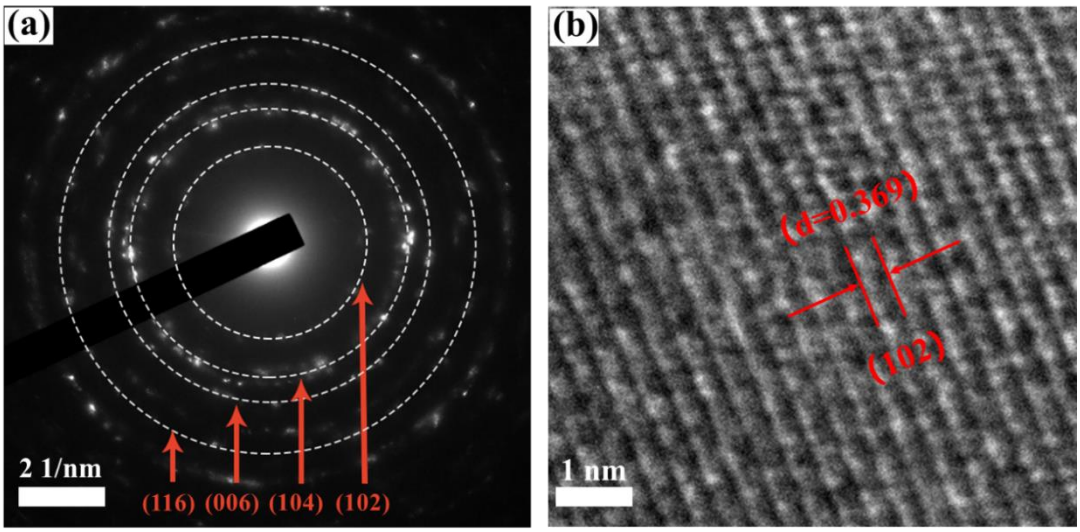

Figure 4-7 (a) SAED of Fe_2O_3 NWAs. (b) HRTEM of Fe_2O_3 NW.

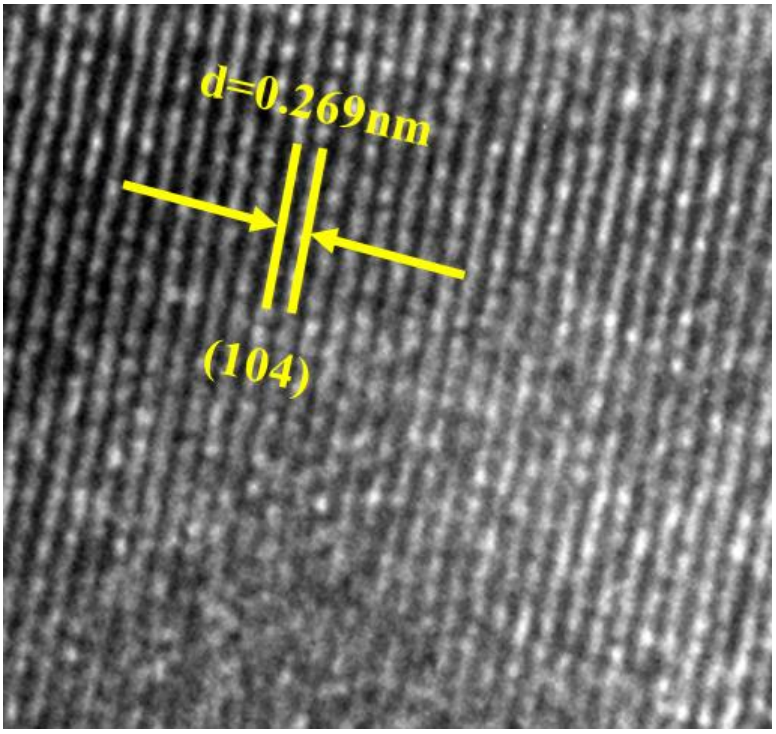

Figure 4-8 HRTEM image of S- Fe_2O_3 NW.

The crystal structure of the synthesized S-Fe_2O_3 NWAs and Fe_2O_3 NWAs were characterized by X-ray diffraction (Figure 4-9a). It should be noted that that the XRD patterns of the synthesized S-Fe_2O_3 NWAs and Fe_2O_3 NWAs are exactly corresponding to the standard Fe_2O_3 card (JCPDS No. 33-6640), indicating that the synthesized materials have high crystallinity and the S atoms partially replace the O atoms through low-temperature sulfuration. The elemental analysis of the surfaces of the as-prepared S-Fe_2O_3 NWAs/CNTF and Fe_2O_3 NWAs/CNTF samples was performed using X-ray photoelectron spectroscopy. Fe, O, S, and C elements were detected in the S-Fe_2O_3 NWAs/CNTF (Figure 4-9b). The chemical state of C atom corresponds to the one of initial CNTF. The chemical compositions and valence states of the Fe_2O_3 are investigated with XPS and the corresponding results is shown in Figure 4-10. The O 1s XPS spectrum (Figure 4-10a) shows two prominent peaks at 527.8 eV and 531.2 eV correspond to Fe–O and C–O, respectively. In the Fe 2p XPS shown in Figure 4-10b, two distinct peaks at 708.6 eV and 724.3 eV, corresponding to the Fe 2p3/2 and Fe 2p1/2 spin-orbit peaks,

respectively. Meanwhile, two sat peaks also be observed. Fe_2O_3 NWAs/CNTF is composed of Fe, O, and C elements, indicating that the S element comes from the sulfuration process. XPS spectrum of Fe 2p of S-Fe_2O_3 NWAs/CNTF is illustrated in Figure 4-11a and it is found that Fe 2p has two main different valence states. The peaks with bond energies equal to 708.8 and 726.3 eV belonged to the Fe $2p_{3/2}$ and Fe $2p_{1/2}$ states. Two satellites at 714.8 eV and 730.4 eV also appear in Fe 2p spectra. A distinct peak at 283.2 eV was found in the C 1s XPS spectrum of CNTF substrate (Figure 4-11b). S 2p spectrum showed two typical peaks at 161.9 and 166.4 eV (Figure 4-11c), which were ascribed to the S $2p_{3/2}$ and S $2p_{1/2}$ spin-orbit peaks, respectively. Furthermore, the peak at 530.1 eV was observed in the O 1s XPS spectrum (Figure 4-11d).

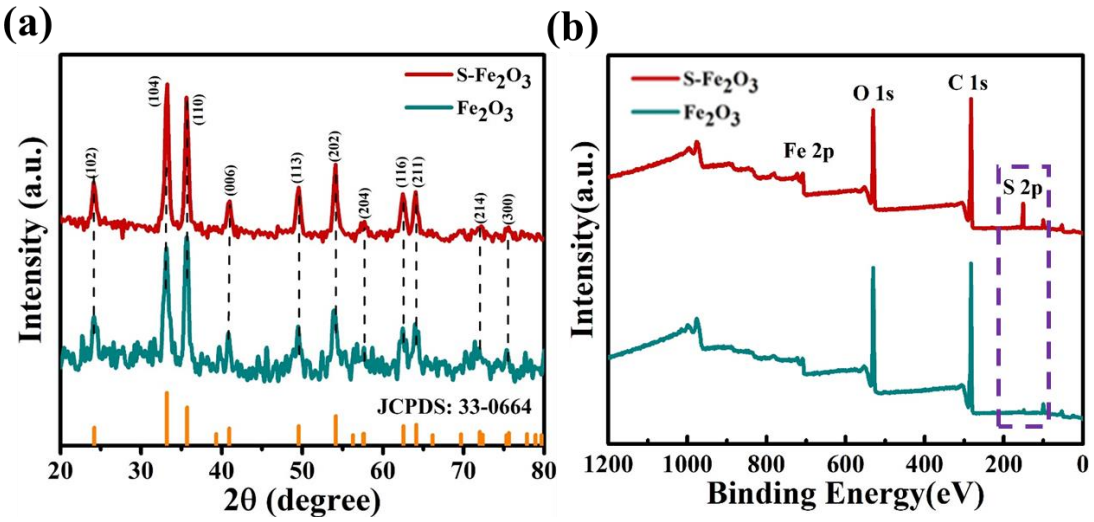

Figure 4-9 (a) XRD spectra for Fe_2O_3 and S- Fe_2O_3 NWAs. (b) Full XPS spectra comparison of Fe_2O_3 NWAs/CNTFs and S- Fe_2O_3 NWAs/CNTFs.

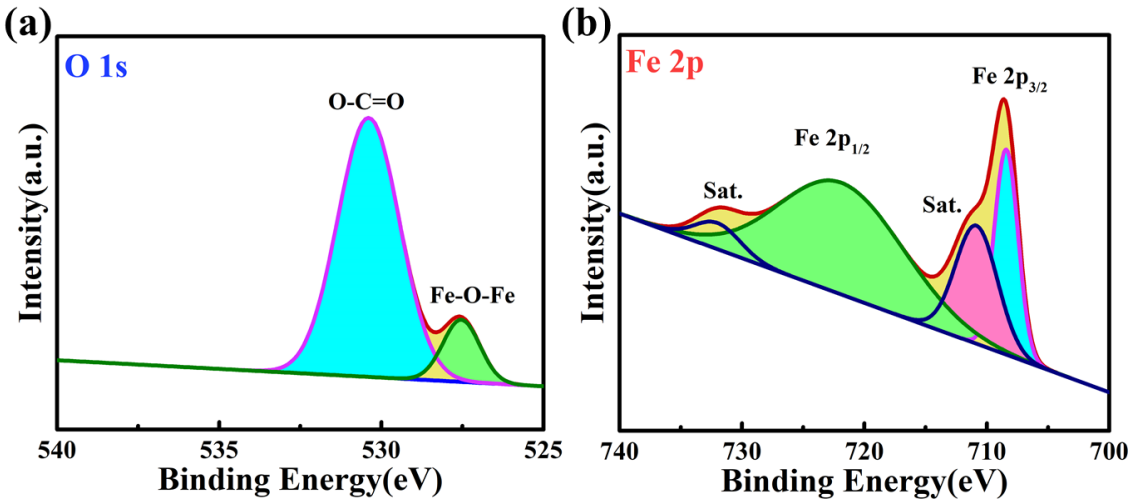

Figure 4-10 XPS spectrum of (a) O 1s and (b) Fe 2p for the Fe_2O_3 NWAs/CNTF.

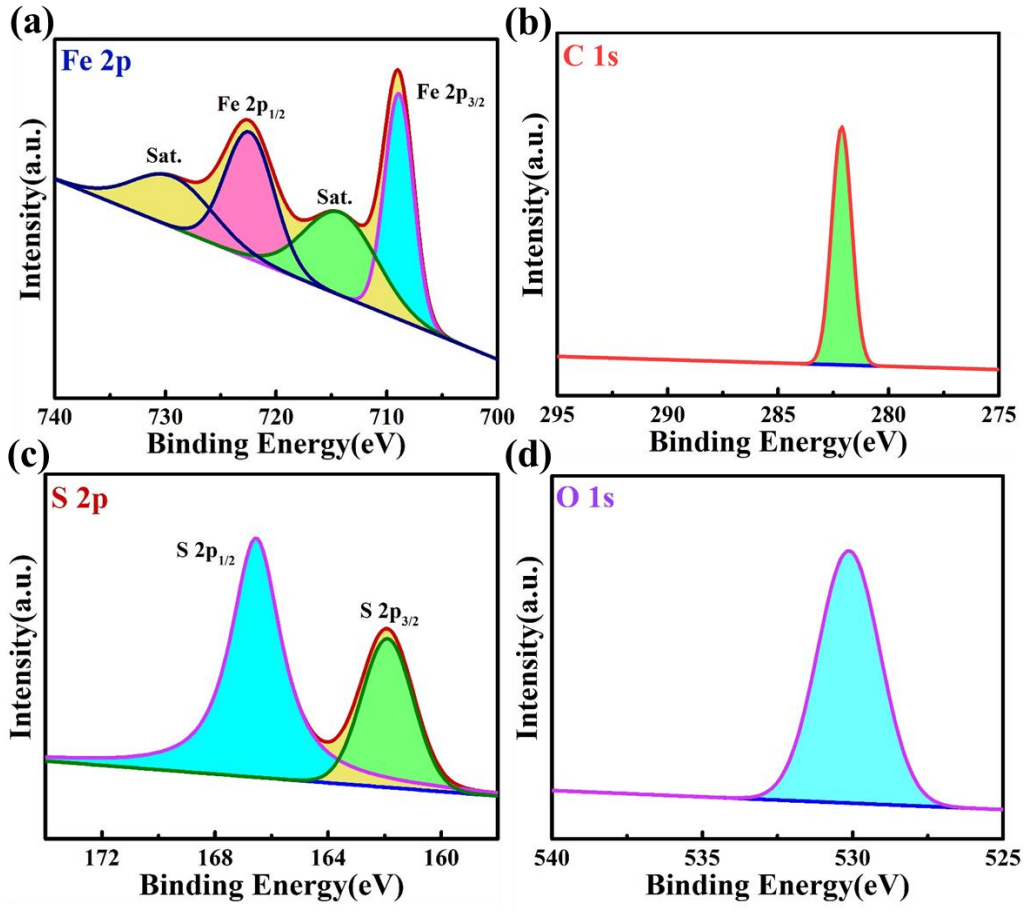

Figure 4-11 High resolution (a) Fe 2p, (b) C 1s, (c) S 2p and (d) O 1s XPS spectra of S-Fe_2O_3 NWAs/CNTF.

To understand the role of S in doping Fe_2O_3, first-principle calculations were conducted to investigate the electronic structures of both pristine Fe_2O_3 and S-Fe_2O_3.The atomic structure of Fe_2O_3 is displayed in Figure 4-12a. The S-Fe_2O_3 model is built by replacing two O atoms with S atoms in a hexagonal Fe_2O_3 cell to simulate the 6% S-doping based on the experimental observations. It should be noted that the S atoms prefer to locate in the same layer, as depicted in Figure 4-12b. Through the comparation, it is notably that the sulfur atoms partially replace the place of oxygen atoms. As the calculated density of states (DOS) shown in Figure 4-13, the pristine Fe_2O_3 is a semiconductor with a bandgap of 2.34 eV, while the bandgap dramatically reduces to 1.18 eV after S doping. This phenomenon is further supported by the band structures of pristine Fe_2O_3 (Figure 4-14a) and S-Fe_2O_3 (Figure 4-14b). Thus, the narrowed band gap of S-Fe_2O_3 demonstrates an enhancement of electrical conductivity, revealing that it is a promising active material for Fe-based anodes for advanced Ni-Fe batteries.

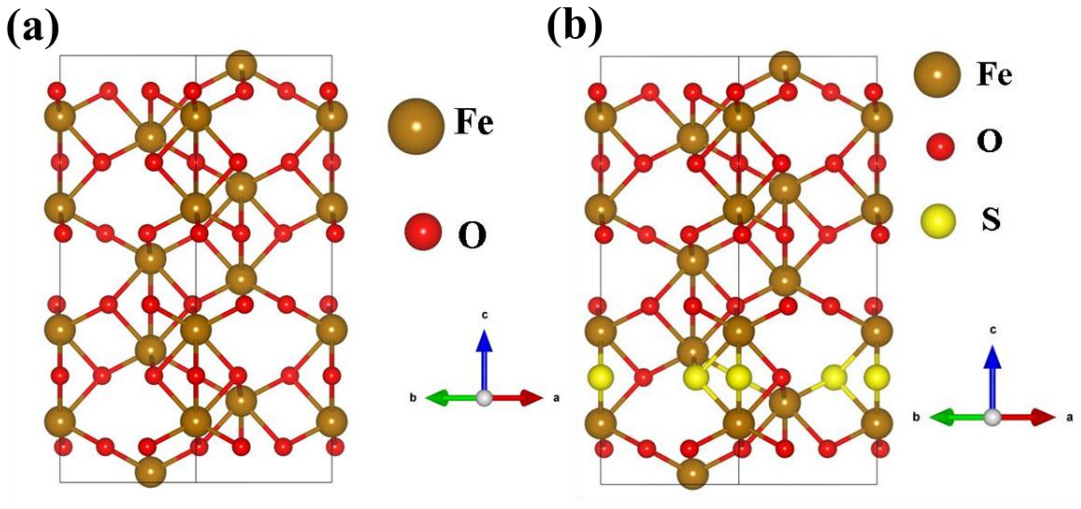

Figure 4-12 (a) Atomic structure of Fe_2O_3. (b) Energetical favorable atomic structure of 6% S-Fe_2O_3

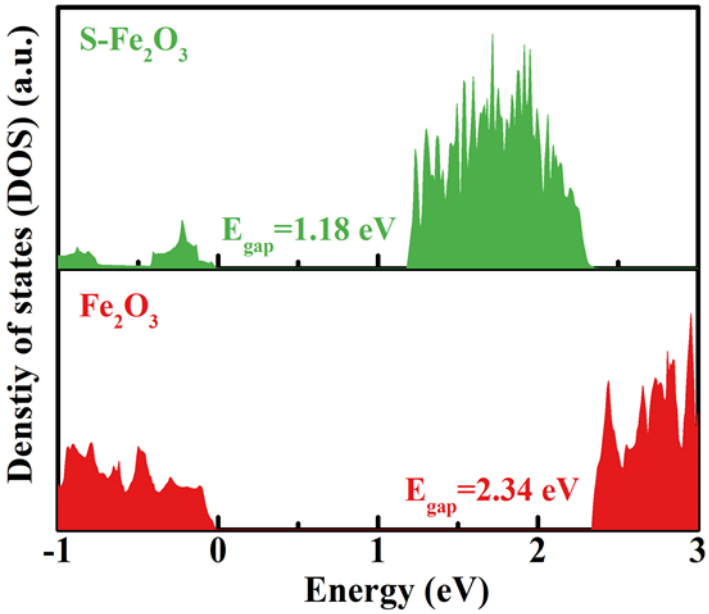

Figure 4-13 The calculated density of states of both pristine Fe_2O_3 and S- Fe_2O_3.

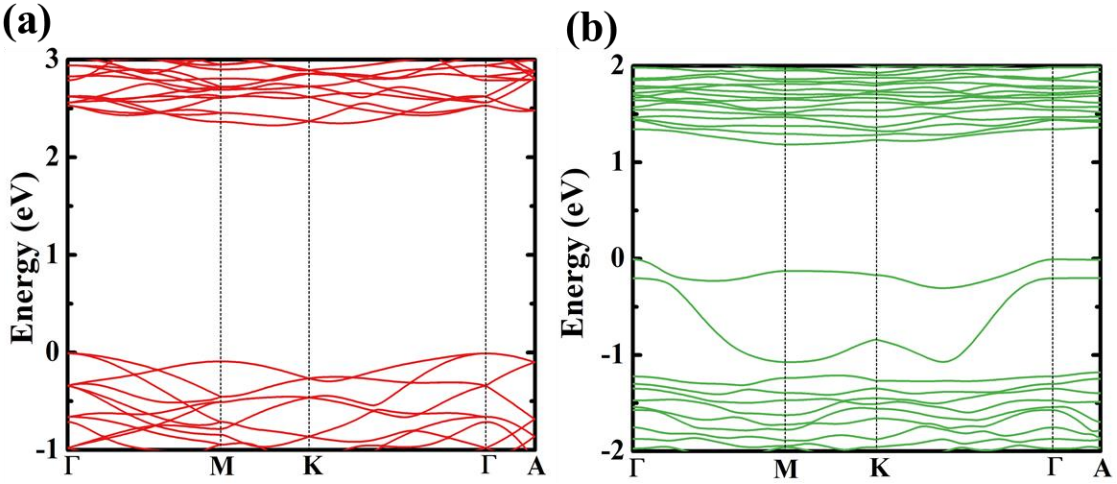

Figure 4-14 Band structures of (a) pristine Fe_2O_3 and (b) S-Fe_2O_3.

The CV curves in Figure 4-15a shows no redox peaks of CNTF as the anode, indicating CNTF have the capacitive behavior so it contributes negligibly for the S-Fe_2O_3 NWAs/CNTF electrode. The GCD curve in Figure4-15b further prove the small discharging time. A pair of distinct redox peaks is observed for every single curve shown in Figure 4-16a, indicating the battery-like behavior of Fe_2O_3 NWAs/CNTF. It obtains the areal capacity of 0.12 mAh/cm^2 under the scan rate of 2 mA/cm^2 (Figure 4-16b).

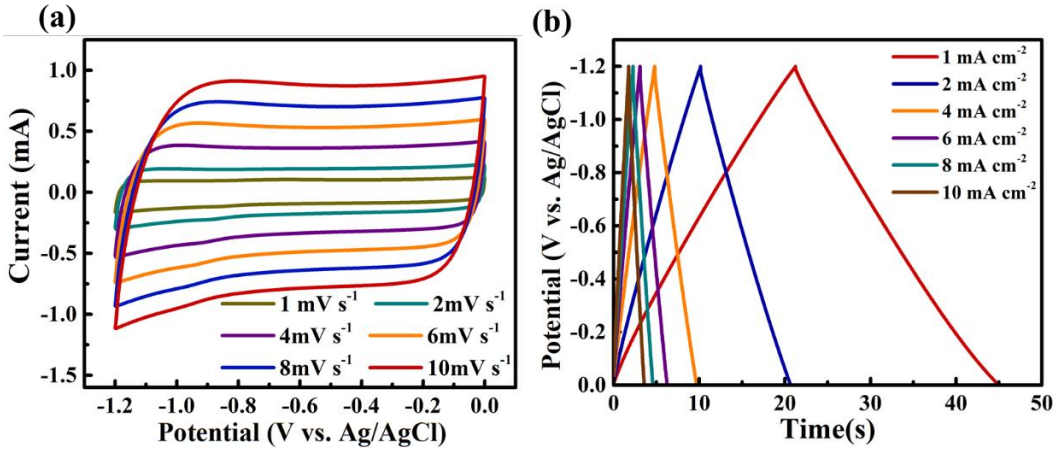

Figure 4-15 (a) CV curves and (b) GCD profiles of initial CNTF electrode anode.

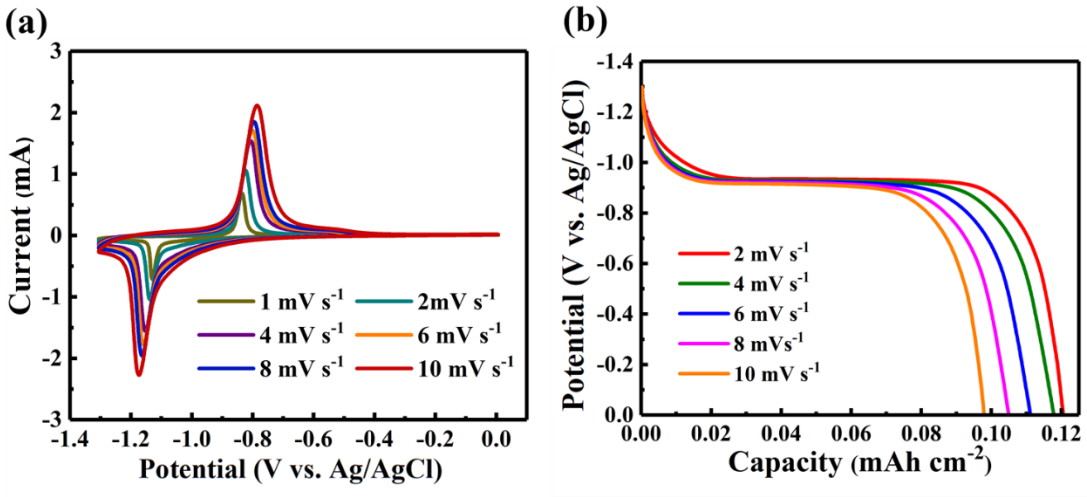

Figure 4-16 (a) CV and (b) GCD curves of Fe_2O_3 NWAs/CNTF electrode.

The electrochemical performance of Fe_2O_3 NWAs/CNTF and S-Fe_2O_3 NWAs/CNTF are used to prove these theoretically calculated results. As presented in Figure 4-17a, the charge transfer resistance value of S-Fe_2O_3 NWAs/CNTF electrode (5.83 Ω) is 1.52 times lower transfer resistance of Fe_2O_3 NWAs/CNTF electrode (which was equal to 14.71 Ω), demonstrating that the electronic/ionic transfer kinetics of Fe_2O_3 NWAs was significantly enhanced via the S doping. Figure 4-17b compares CV of electrodes containing Fe_2O_3 NWAs/CNTF and S-Fe_2O_3 NWAs/CNTFs as active materials at 10 mV s^{-1} within the voltage range of 0 to -1.4 V. Obviously, S-Fe_2O_3 NWAs/CNTF-based electrode showed a more substantial area under the CV curve and more significant redox peak intensity than unmodified CNTFs and Fe_2O_3 NWAs/CNTFs. Thus, the capacity contribution of the CNTF substrate could be neglected. At the same time, the capacity and redox reaction kinetics of fiber-containing electrodes were significantly improved after S doping. CV spectra of the electrodes containing S-Fe_2O_3 NWAs /CNTF as active materials at different scan rates displayed several prominent faradaic redox peaks (Figure 4-18a), indicating that the as-fabricated electrode has an ideal battery behavior, which is ascribed to the conversion between Fe^{3+} and Fe^{2+} by following the reaction:

$$S\text{-}Fe_2O_3 + 2e^- + 3H_2O \longleftrightarrow 2S\text{-}Fe(OH)_2 + 2OH^-$$

Meanwhile, it is noted that cathodic and anodic peaks move to both ends, respectively, with the increasing scan rate, which results from the continuous rising of the potential difference between the redox peak pairs. This polarization phenomenon is due to the fact that the ion migration rate in the electrolyte is less than the electron rate generated by the redox reaction. To reveal the electrochemical kinetics of the S-Fe_2O_3 NWAs/CNTF electrode, the linear relationship between the square root of the scan rate and the cathodic peak current densities at scan rates is presented in revised Figure 4-18b, implying a diffusion-controlled process during the electrode material redox reaction.

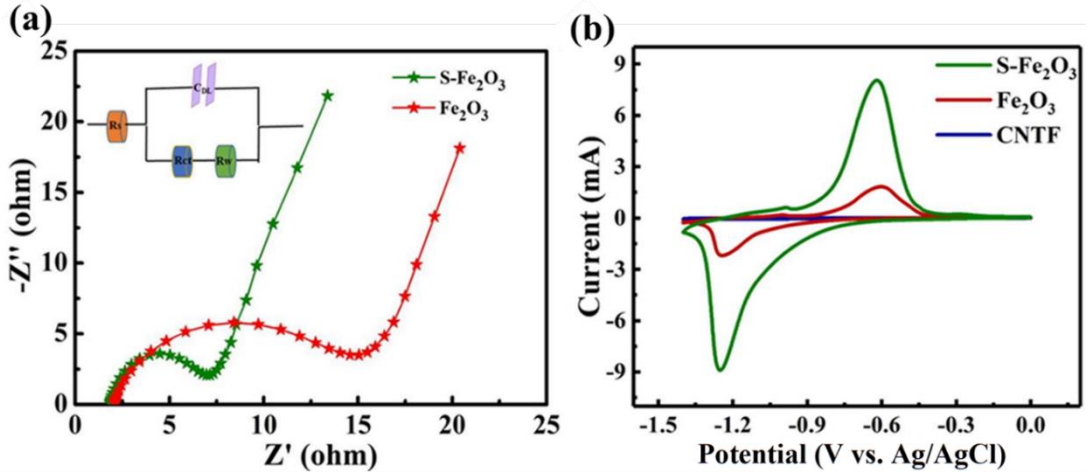

Figure 4-17 (a) Nyquist plots and fitted an equivalent circuit for the S-Fe_2O_3 and Fe_2O_3. (b) CV data for the electrodes containing S-Fe_2O_3, Fe_2O_3, and initial CNTF at 10 mV/s scan rate.

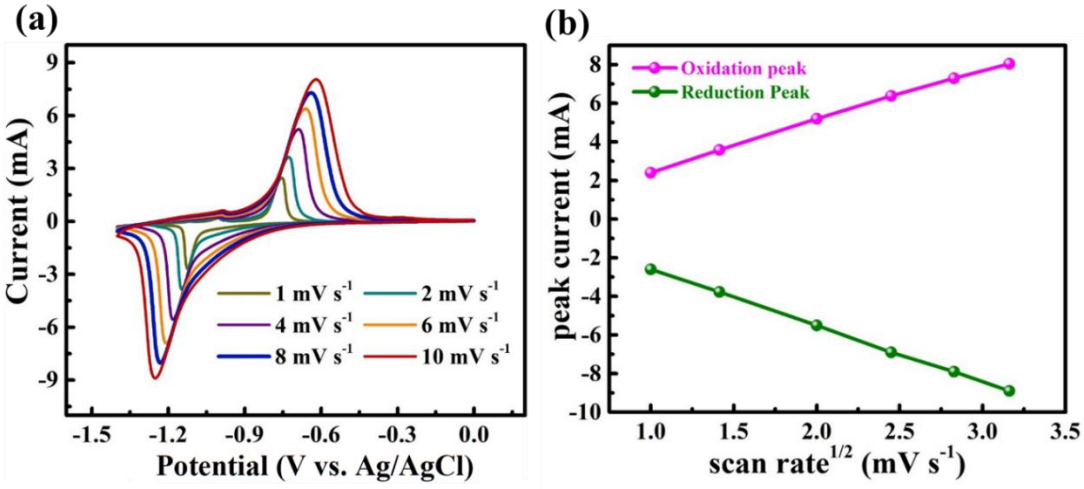

Figure 4-18 (a)CV curves for the S- Fe_2O_3 /CNTF electrodes at various scan rates. (b) The plots of redox peak currents with respect to square root of scan rates for the S-Fe_2O_3 NWAs/CNTF electrode.

Figure 4-19 demonstrates the relationships between log (peak current) and log (scan rate) from 1 to 10 mV/s for both the cathodic and anodic peaks. When the slope is ≈0.5, the electrochemical processes are assumed to be dependent on the ion diffusion, while slope value equal to 1 implies capacitive dependence. These slopes of the lines in Figure 4-19a are calculated to be ≈0.523 (cathodic) and ≈0.577 (anodic), further illustrating that the charge storage reaction of S-Fe_2O_3 NWAs/CNTF is a diffusion-controlled process. Similarly, the kinetic mechanism of Fe_2O_3 NWAs/CNTF electrode is controlled by ion-diffusion (Figure 4-19b).

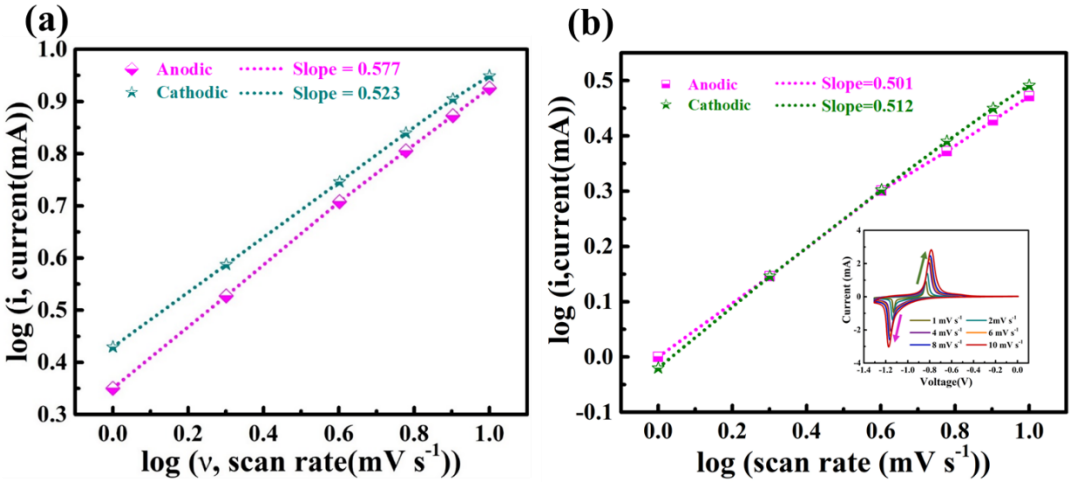

Figure 4-19 (a) Redox peak currents for the S-Fe_2O_3/CNTF electrode as function of the scan rates. (b) Linear fitting of the peak current versus scan rate for the cathodic and anodic peaks of the CV curves for the Fe_2O_3 NWAs/CNTF electrode.(Inset is the CV profile of the Fe_2O_3 NWAs/CNTF electrode)

The GCD data for the S-Fe_2O_3 NWAs/CNTF electrodes (Figure 4-20a) clearly exhibit the distinct charge-discharge voltage plateaus and high columbic efficiency. The areal discharge capacity of the S-Fe_2O_3 NWAs/CNTF-based electrode was 0.81 mAh/cm^2 (volumetric capacity is 259.2 mA/cm^3) at 4 mA/cm^2 (Figure 4-20b), which is 6 times higher than that of the Fe_2O_3 NWAs/CNTF electrode (0.12 mAh/cm^2). This value (0.81 mAh/cm^2) also surpasses other reported Fe-based electrodes summarized in Table

4-1. As presented in Figure 4-21, a high capacity of 308.57 mAh/g was achieved at 1.6 A/g, and the value was maintained at 255.24 mAh/g when the current density increased to 16 A/g.

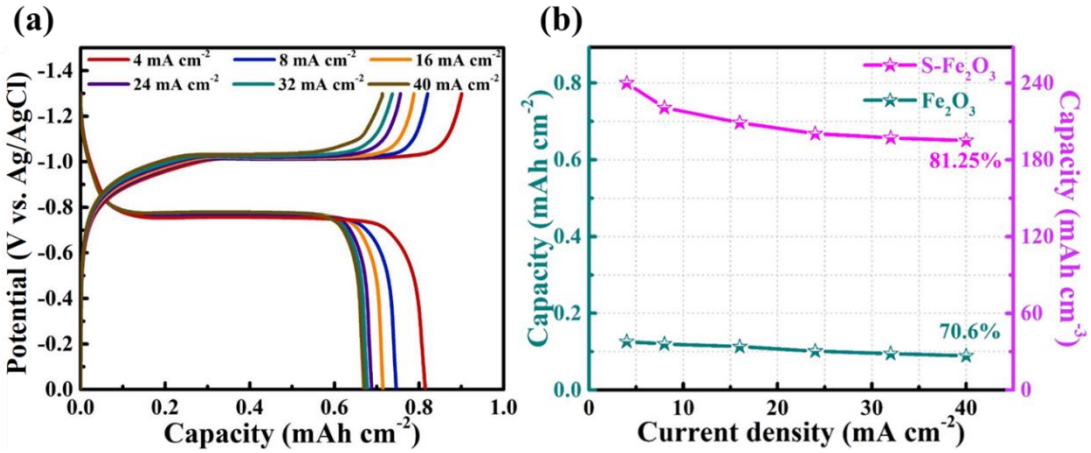

Figure 4-20 (a) GCD curves for the S-Fe_2O_3/CNTF electrodes. (b) Capacities plotted for S- Fe_2O_3/CNTF and Fe_2O_3/CNTF electrodes from 4 to 40 mA/cm^2 current densities.

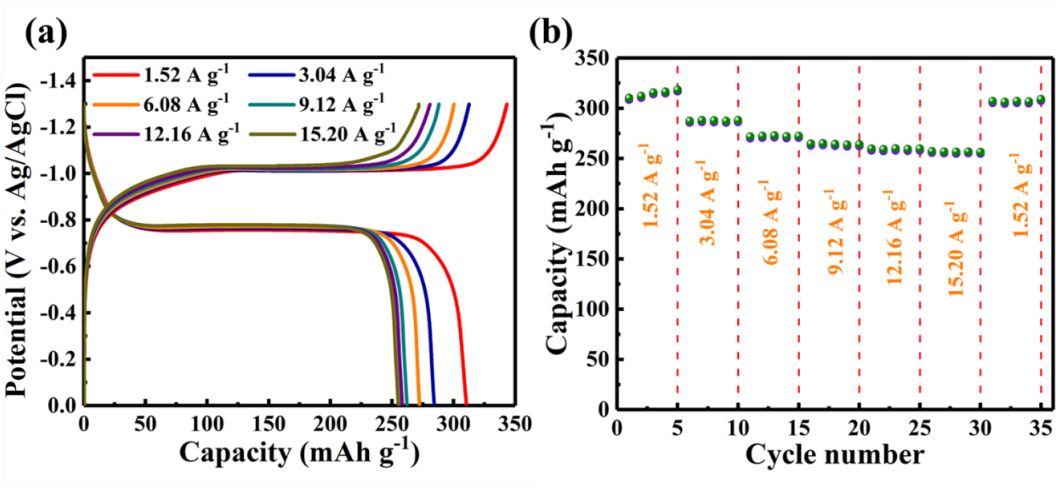

Figure 4-21 Charge-discharge curves (a) and rate capability (b) of the S-Fe_2O_3 NWAs under different current densities.

In addition, S-Fe_2O_3 NWAs/CNTF electrode can maintain 81.25% of the initial capacity at 40 mA/cm^2 current density, which demonstrates better rate performance than Fe_2O_3 NWAs/CNTF electrode (which was equal to 70.6% capacity retention). The long-term stability of S-Fe_2O_3 NWAs/CNTF electrode is given in Figure 4-22a, while the

corresponding SEM image is given in Figure 4-22b. The capacity retention was 92.4% after 5000 cycles at a current density of 40 mA/cm^2, which indicates excellent cycle stability of the as-fabricated S-Fe_2O_3 NWAs/CNTF electrodes.

Table 4-1 Comparison of the electrochemical performances of the as-fabricated S-Fe_2O_3 NWAs with previously reported Fe-based electrode in alkaline.

Number	Material	Capacity (mAh/cm^2)	Rate performance	Reference
1	Fe_2O_3/RGO/Fe_3O_4	0.075 (20 mA/cm^2)	0.025 (50 mA/cm^2)	[173]
2	Fe_2O_3	0.159 (1 mA/cm^2)	0.087 (20 mA/cm^2)	[174]
3	Porous Fe_2O_3	0.390 (10 mA/cm^2)	0.165 (50 mA/cm^2)	[175]
4	FeO-OH	0.475 (1.6 mA/cm^2)	0.354 (48 m/cm^2)	[176]
5	S-α-Fe_2O_3	0.210 (1 mA/cm^2)	0.130 (10 mA/cm^2)	[120]
6	FeP	0.634 (2 mA/cm^2)	0.540 (10 mA/cm^2)	[177]
7	S-α-Fe_2O_3	0.474 (2 mA/cm^2)	0.335 (20 mA/cm^2)	[148]
8	S-Fe_2O_3	0.810 (4 mA/cm^2)	0.650 (40 mA/cm^2)	This work

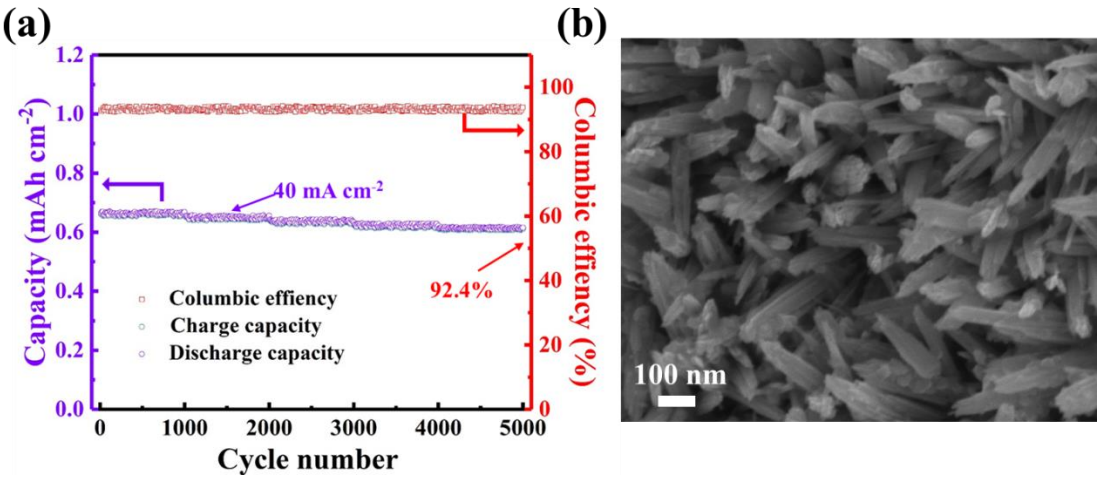

Figure 4-22 (a) Cycling stability of the S-Fe_2O_3/CNTF. (b)High-magnification SEM image S-Fe_2O_3 NWAs/CNTF electrode after 5000 GCD cycles under the scan rate of 10 mV/s.

In order to match the high capacity of the anode material, we take use of the ZNCO@$Ni(OH)_2$/CNTF as the cathode prepared in last chapter with superior the specific capacity. The unique core-shell structure of ZNCO@$Ni(OH)_2$ NWAs can provide a fast ion diffusion path and provide more active sites, which in turn promoting efficient, fast and reversible electrode reactions. ZNCO NWAs have higher electrical conductivity and electrochemical performance than corresponding single metal oxides and bimetal oxides. These superior properties make ZNCO NWAs widely accepted as secondary substrates for the growth of other active materials. Among them, the oriented ZNCO NWAs are the core part, and the ultra-thin Ni $(OH)_2$ is the shell layer. Based on this unique structural design, the capacity of as-prepared ZNCO@$Ni(OH)_2$-based electrode is 1.49 mAh/cm^2 at 4 mA/cm^2, which is significantly higher than other reported fibrous electrode materials. Obviously, the areal capacity of the ZNCO@$Ni(OH)_2$/CNTF electrodes was higher than that of recently reported Ni-based cathode materials (Table 4-2). Some electrochemical performance and material characterization have been demonstrated in the previous chapter. Moreover, we have added more theoretical density of states calculation using the DFT simulation. Here it is found that the heavy doping of Zn and Ni in Co_3O_4 even result in a transition from semiconductor to metal, which could clearly be seen from the ZNCO spin-up state in Figure 4-23. Meanwhile, the $Ni(OH)_2$ on ZNCO shows a

characteristic of hole doping, since the Fermi level shifts towards the deeper energy level. As a result, it is expected that the ZNCO@$Ni(OH)_2$ interface possesses a good conductivity, which is beneficial the battery-type performance

Table 4-2 Comparison of the electrochemical performances of the as-fabricated ZNCO@$Ni(OH)_2$/CNTF with previously reported Ni-based electrode in alkaline.

Number	Material	Capacity (mAh/cm^2)	Rate performance	Reference
1	$NiCo_2O_4$	0.35 (1.11 mA/cm^2)	0.09 (11.12 mA/cm^2)	[178]
2	$NiCo_2O_4$	0.44 (1.8 mA/cm^2)	0.26 (19.8 mA/cm^2)	[179]
3	NiCoP	0.71 (1 mA/cm^2)	0.49 (50 mA/cm^2)	[180]
4	3D Ni@NiO	0.80 (8 mA/cm^2)	0.42 (40 mA/cm^2)	[181]
5	CoP@$Ni(OH)_2$	0.69 (2 mA/cm^2)	0.49 (20 mA/cm^2)	[148]
6	MnO_2-NiO	0.11 (5 mA/cm^2)	0.06 (25 mA/cm^2)	[182]
7	$NiMoO_4$@$Co(OH)_2$	0.32 (5 mA/cm^2)	0.13 (50 mA/cm^2)	[183]
8	Co_3O_4@C@Ni_3S_2	0.49 (1 mA/cm^2)	0.24 (30 mA/cm^2)	[184]
9	NiZnCoP	0.24 (1 mA/cm^2)	0.21 (10 mA/cm^2)	[120]
10	ZNCO@$Ni(OH)_2$	1.49 (4 mA/cm^2)	1.28 (40 mA/cm^2)	This work

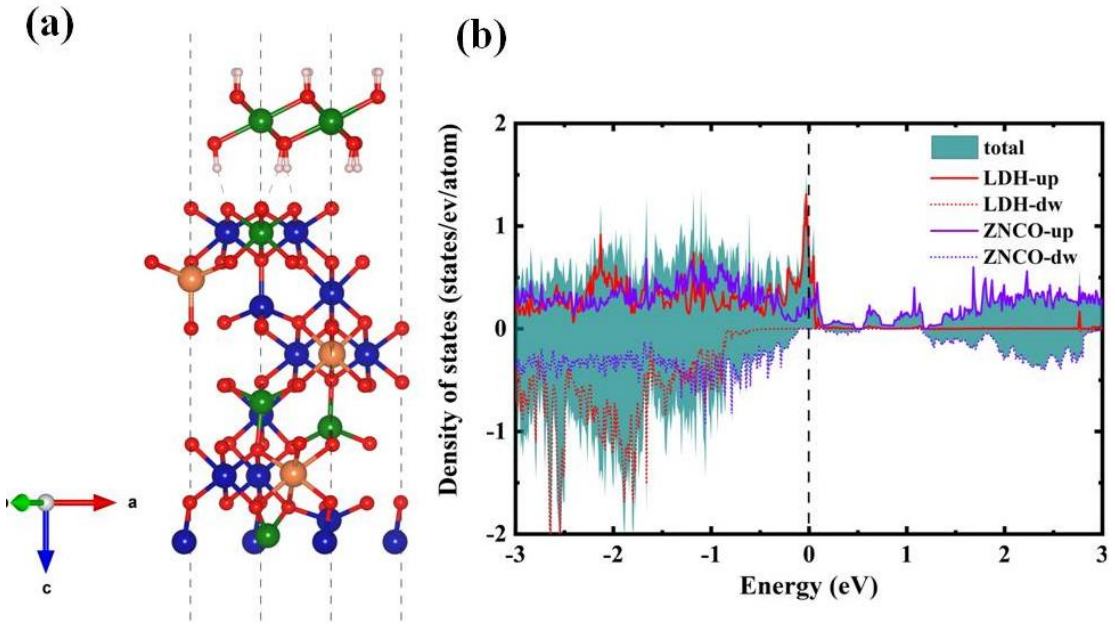

Figure 4-23 (a) Calculated interfacial structure and (b) projected density of states of $Ni(OH)_2$@ZNCO. Solid and dashed lines are corresponding to the spin up and spin down states.

To assemble NiCo-Fe battery, as shown in Figure 4-24a, both S-Fe_2O_3 NWAs/CNTF and ZNCO@$Ni(OH)_2$ NWAs/CNTF were twisted into a hybrid wire using PVA-KOH gel electrolyte. The CV curves of S-Fe_2O_3/CNTF anode and ZNCO@$Ni(OH)_2$/CNTF cathode obtained using a three-electrode system are shown in Figure 4-24b, where the operating windows S-Fe_2O_3 electrode and ZNCO@$Ni(OH)_2$ are -1.4~0V and 0~0.5V, respectively. The as-assembled full battery device with high voltage is thus expected. CV curves of fiber-shaped NiCo-Fe batteries measured at various scanning rates in the 0~1.6 V range demonstrated several strong redox peaks (Figure 4-25a). When the scanning rate increases, the shapes of CV curves maintain well with no obvious deformation except for a slight change in peak position, which indicates the good stability of the assembled device. GCD curves of fiber-shaped NiCo-Fe batteries at various current densities showed two distinct characteristic plateaus at 1.37 V and 1.02 V (Figure 4-25b). Very high capacity equal to 0.46 mAh/cm^2 at 2 mA/cm^2 was achieved. 68.9% of this value (which is equal to 0.31 mAh/cm^2) was kept under a high current density of 10 mA/cm^2.

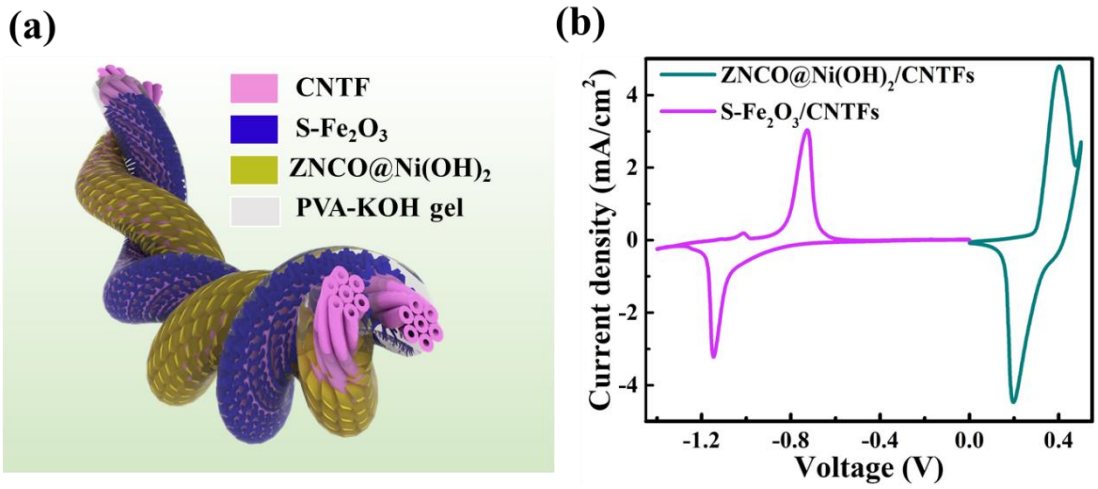

Figure 4-24 (a) Schematics of the fiber-shaped NiCo-Fe battery. (b) CV curves for the S-Fe_2O_3 NWAs/CNTF-based anode and ZNCO@$Ni(OH)_2$ NWAs/CNTF-based cathode collected using a three-electrode system.

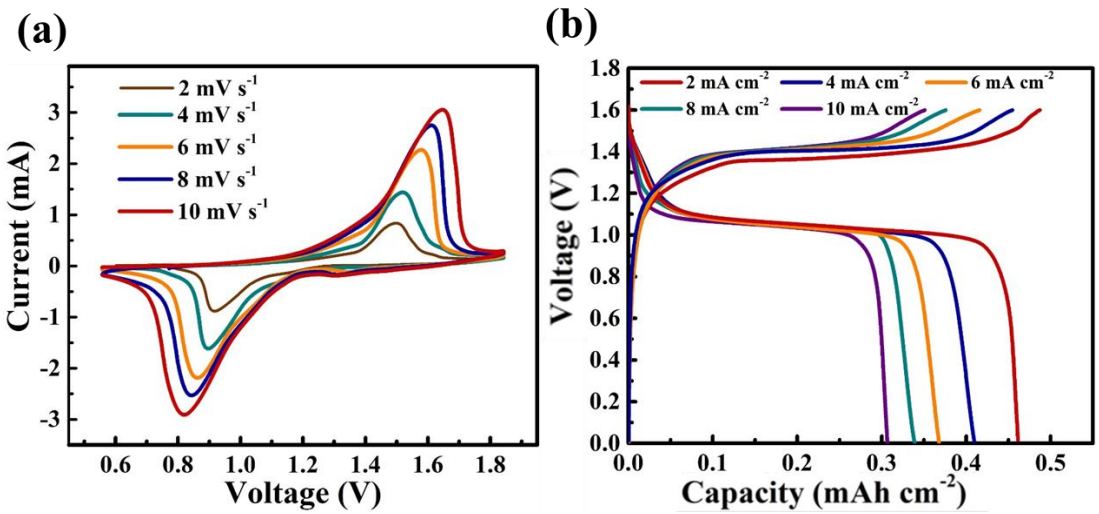

Figure 4-25 (a) CV and (b) GCD curves of the fiber-shaped NiCo-Fe battery.

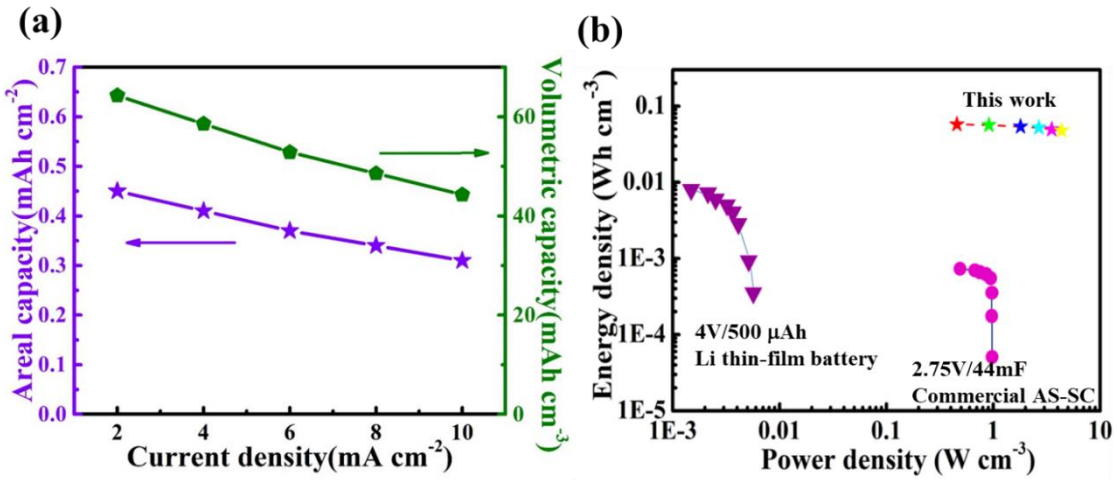

Figure 4-26 (a) The areal and volumetric capacity of fiber-shaped NiCo-Fe battery. (b) Ragone plots of the areal energies and power densities of our fiber-shaped NiCo-Fe battery and recently reported fiber-shaped aqueous rechargeable batteries.

The areal and volumetric capacity plotted as a function of the discharge current density is shown in Figure 4-26a. The Ragone plots comparing volumetric energy and power densities of our fiber-shaped NiCo-Fe batteries with the recently reported fiber-shaped aqueous rechargeable batteries are shown in Figure 4-26b. Devices fabricated in this work showed outstanding volumetric energy density (equal to 67.32 mWh/cm^3 with a power density of 591.12 mWh/cm^3), outperforming most of the previously reported fiber-shaped aqueous rechargeable batteries (Table 4-3). Additionally, the mass capacities, energy densities and power densities for our fiber-shaped NiCo-Fe battery based on the masses of active material and whole device are shown in Figures 4-27 and Figure 4-28. As demonstrated in Figures 4-27a and 4-27b the discharge capacities maintain 174.37 mAh/g at a current density of 0.76 A/g and 117.51 mAh/g at a high current density of 3.80 A/g based the active material' mass for our fiber-shaped NiCo-Fe battery. As presented in Figure 4-27c, the device can deliver an ultrahigh energy density of 177.86 Wh/Kg at a power density of 773.31 W/Kg, and still deliver 119.86 Wh/Kg even at a high power density of 3866.55 W/Kg. While in the Figure 4-28a and 4-28b, the discharge capacities maintain 43.33 mAh/g at a current density of 0.19 A/g and 29.20 mAh/g at a high current density of 0.95 A/g based the whole device' mass for our fiber-shaped NiCo-Fe battery. As presented in Figure 4-28c, the device can deliver an ultrahigh

energy density of 44.20 Wh/Kg at a power density of 192.17 W/Kg, and still deliver 29.79 Wh/Kg even at a high power density of 960.84 W/Kg.

Table 4-3 Comparison of the electrochemical performances of our assembled fiber-shaped NiCo-Fe battery with other previously reported energy storage devices.

Device configuration	Electrode materials	Electrolyte	Capacity	EV-max (mWh /cm^3)	PV-max (W/cm^3)	Reference
Twisted	NiZnCoP// α-Fe_2O_3	KOH-PVA	0.092 mAh/cm^2	30.61	3.33	[120]
Twisted	FeP//NiCoP	KOH-PVA	0.294 mAh/cm^2	39.48	NA	[177]
Parallel	NiCo LDH//Zn	KOH-PVA	5 mAh/cm^2	8	2.2	[185]
Twisted	Mn-NiO// Mn-Fe_2O_3	KOH-PVA	46.0 mAh/cm^3	61	48.4	[82]
Twisted	Ni-NiO//Zn	KOH-PVA	120 $\mu Ah/cm^3$	0.67	0.22	[186]
Coaxial	Polyaniline//Zn	$Zn(CF_3SO_3)_2$ - PVA	100 mAh/g	NA	NA	[187]
Twisted	MnO_2//Zn	$ZnSO_4$-PAM	260 mAh/g	53.8	NA	[188]
Parallel	$Na_{0.44}MnO_2$//$NaTi_2(PO_4)_3$@C	Na_2SO_4	46 mAh/g	25.7	0.7	[189]
Parallel	CC-ZnO@C-Zn //$Co(CO_3)_{0.5}(OH)_x \bullet 0.11H_2O$@$CoMoO_4$	KOH-PVA	3 mAh/cm^3	4.6	0.42	[118]
Twisted	S-Fe_2O_3 //ZNCO@$Ni(OH)_2$	KOH-PVA	0.46 mAh/cm^2	67.32	1.4	This work

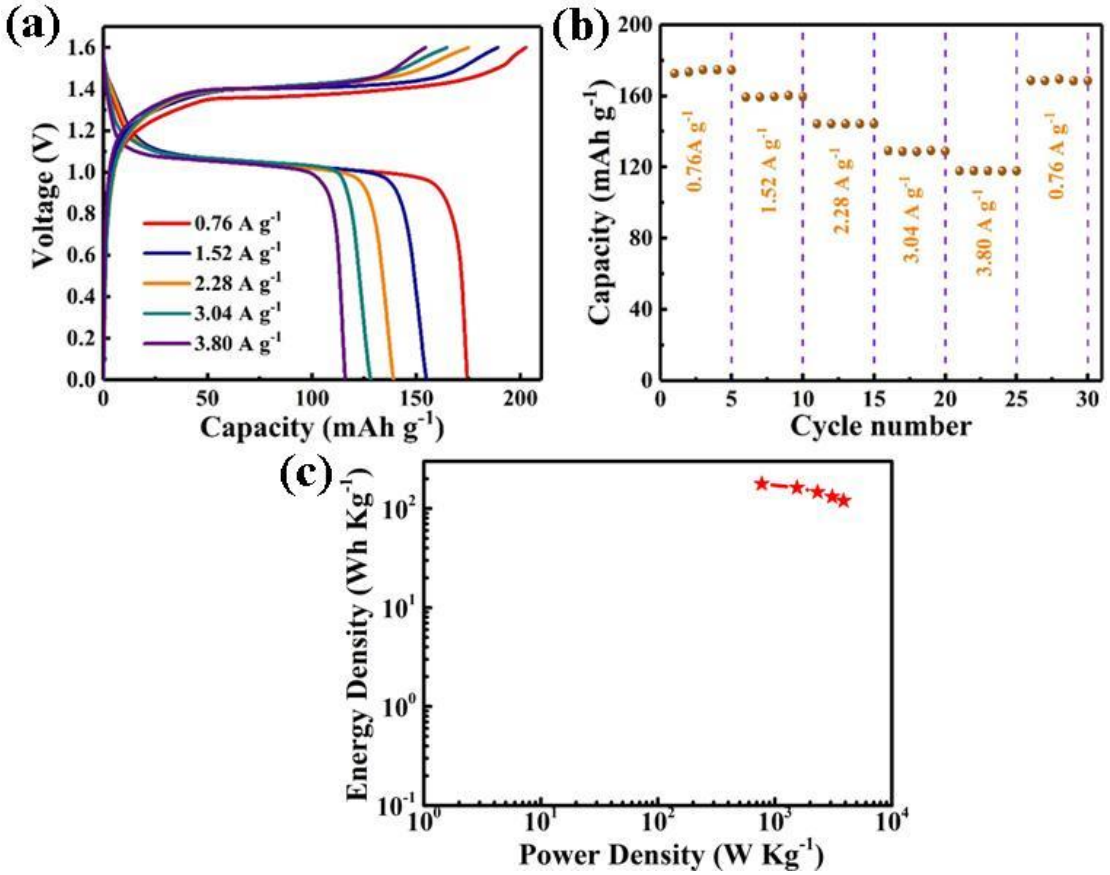

Figure 4-27 (a) GCD curves and (b) rate capability of the fiber-shaped NiCo-Fe battery based on active material' mass at different mass current density. (c) Mass energy and power densities of our fiber-shaped NiCo-Fe battery based on active material' mass.

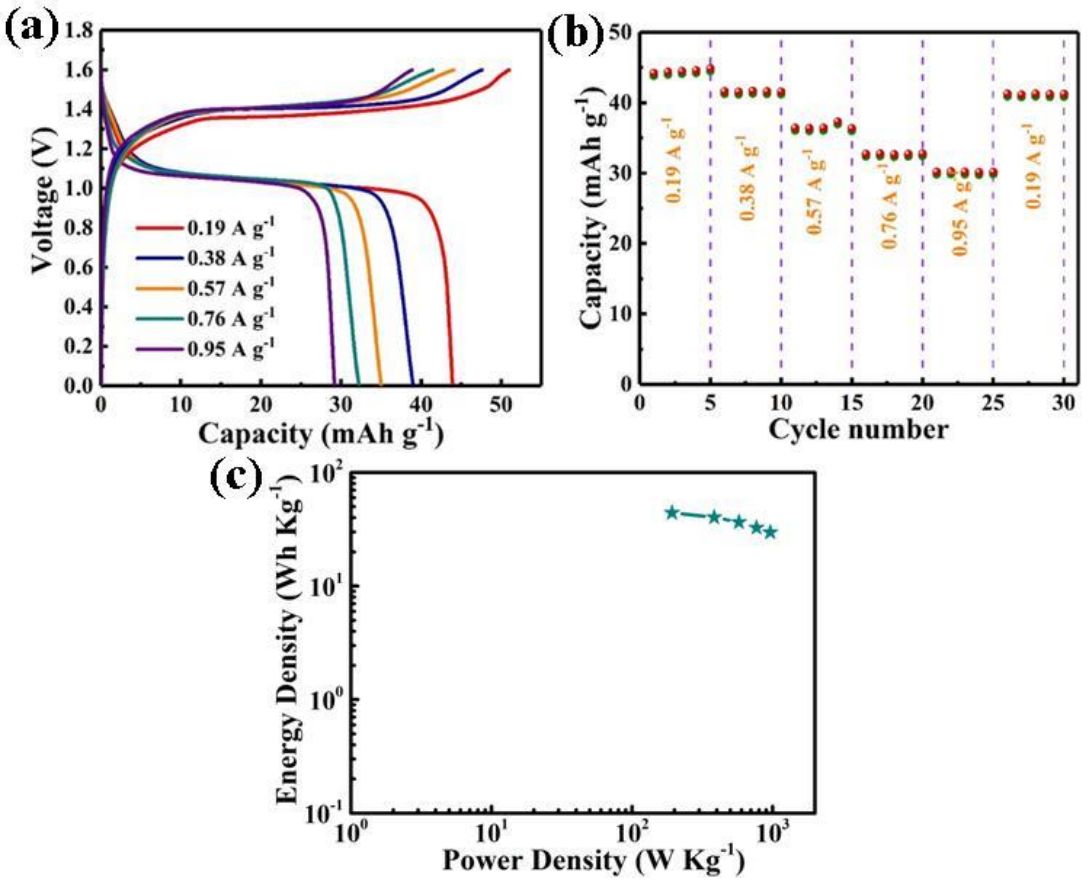

Figure 4-28 (a) GCD curves and (b) rate capability of the fiber-shaped NiCo-Fe battery based on whole device' mass at different mass current density. (c) Mass energy and power densities of our fiber-shaped NiCo-Fe battery based on whole device' mass.

In order to explore the practical applications of our devices for portable electronics, a variety of flexibility tests were conducted. The collecting GCD curves are basically stable and overlapped under various bending angles ranging at 2 mA/cm^2 (Figure 4-29a), confirming the high mechanical stability. As shown in Figure 4-29b, the device still retains 94.8% of its initial capacity after bending at 90° for 4000 cycles, showing the excellent structural stability. Meanwhile, Figure 4-30 demonstrated stable electrochemical performance of the battery under various bending states. It is easily observed in the SEM images at different bending degrees that there is not distinct difference for the inner and outer part, indicating the stable of our device.

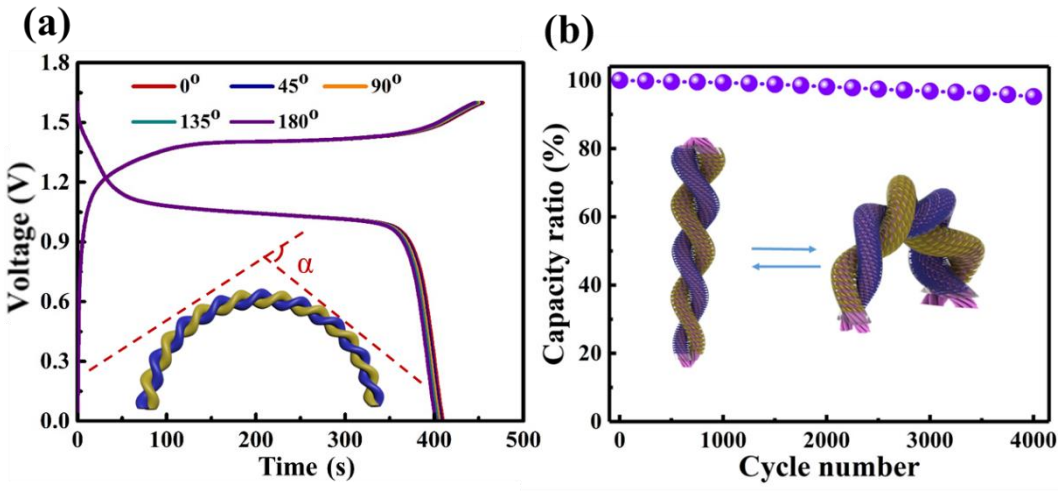

Figure 4-29 (a) GCD curves for the fiber-shaped NiCo-Fe battery bent at 0, 45, 90, 135 and 180º. (b) Normalized capacity of the as-obtained battery with a bending angle of 90° for 4000 cycles.

As depicted in Figures 4-31a and 4-31b, two devices were connected in series to obtain 3.2 V operating voltage, while the discharge time is doubled when they are connected in parallel. Meanwhile, the voltage curve remains the same initial shape, proving that the integrated device can work stably. As presented in Figure 4-32a, a red light-emitting diode (LED) was powered by two series-connected fiber-shaped NiCo-Fe batteries, further confirming their practical applications as energy supply devices. The Nyquist plot of the fiber-shaped NiCo-Fe battery is depicted in Figure 4-32b, where the equivalent resistance of the whole device was 31.2 Ω at 90° angle, which suggests the fast charge transfer and high-efficiency ion diffusion. To exemplify the wearable applications of our device, two long fiber-shaped NiCo-Fe batteries connected in series are woven into a flexible energy textile via conventional weaving technology to light up a red LED (Figure 4-33).

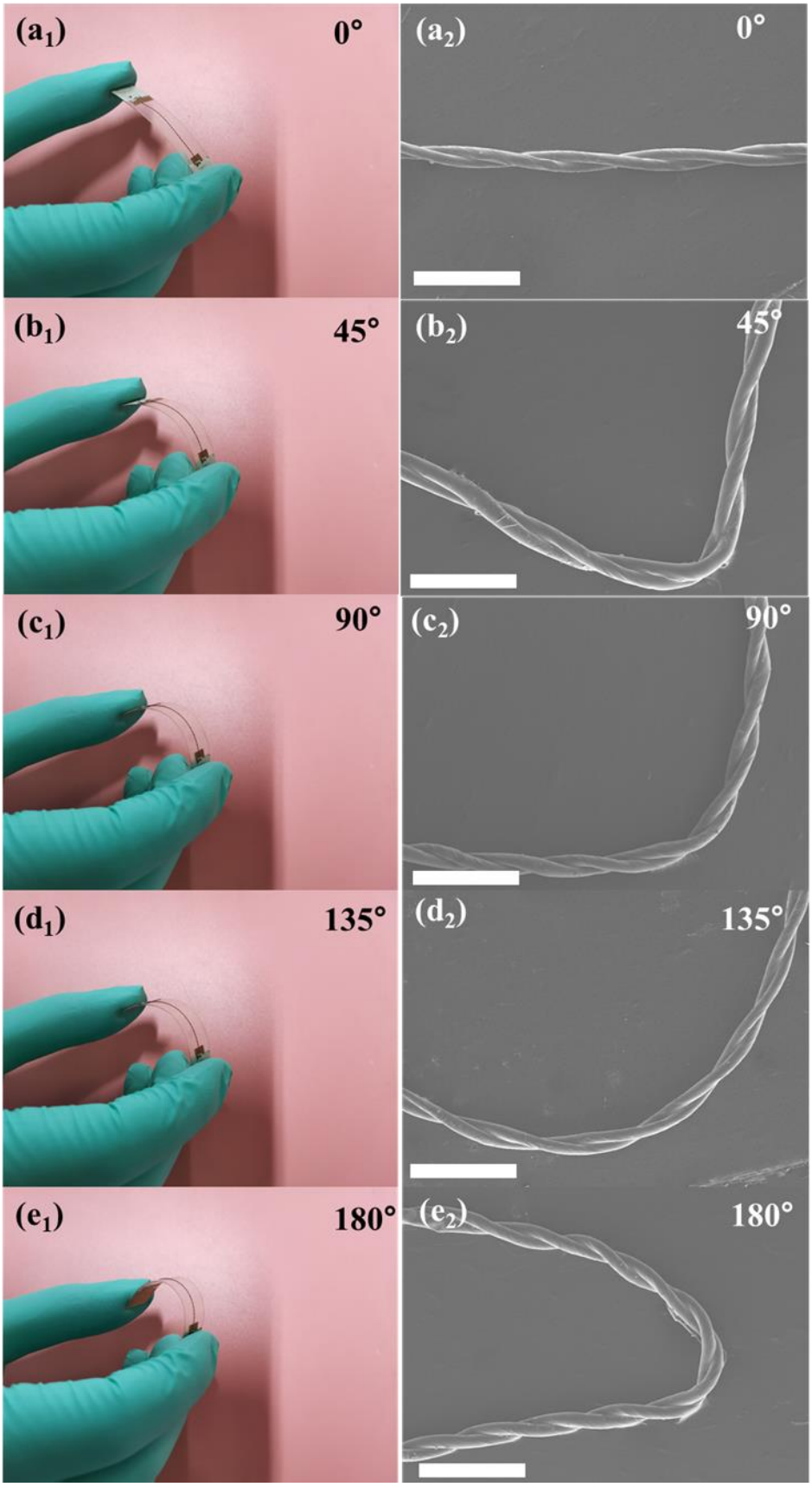
(a1)
0°
(a2)
0°
(b1)
45°
(b2)
45°
(c1)
90°
(c2)
90°
(d1)
135°
(d2)
135°
(e1)
180°
(e2)
180°

Figure 4-30 Photographs of our assembled NiCo-Fe batteries with different bending angles and their corresponding SEM images: (a1-a2) 0°, (b1-b2) 45°, (c1-c2) 90°, (d1-d2) 135° and (e1-e2) 180°. The scale bar is 1mm (a2-e2).

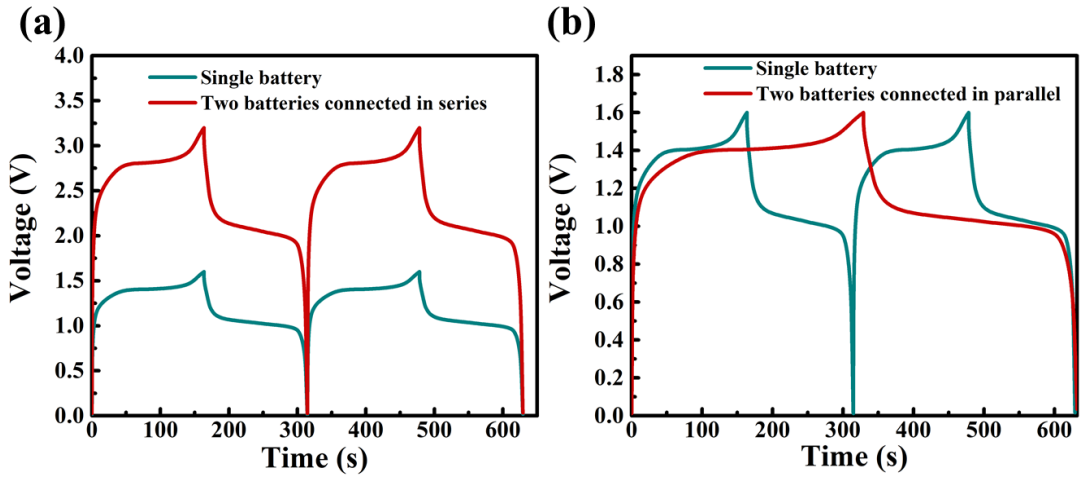

Figure 4-31 GCD curves of single fiber-shaped NiCo-Fe battery and two fiber-shaped NiCo-Fe batteries connected (a) in series and (b) in parallel.

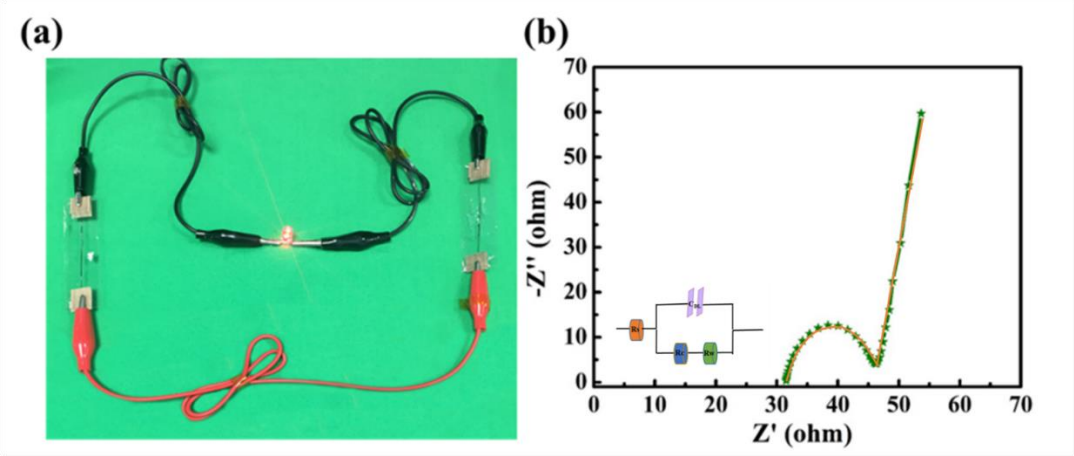

Figure 4-32 (a) Photograph showing a red LED powered by two series-connected fiber-shaped NiCo-Fe batteries. (b)Nyquist plot of assembled fiber-shaped NiCo-Fe battery.

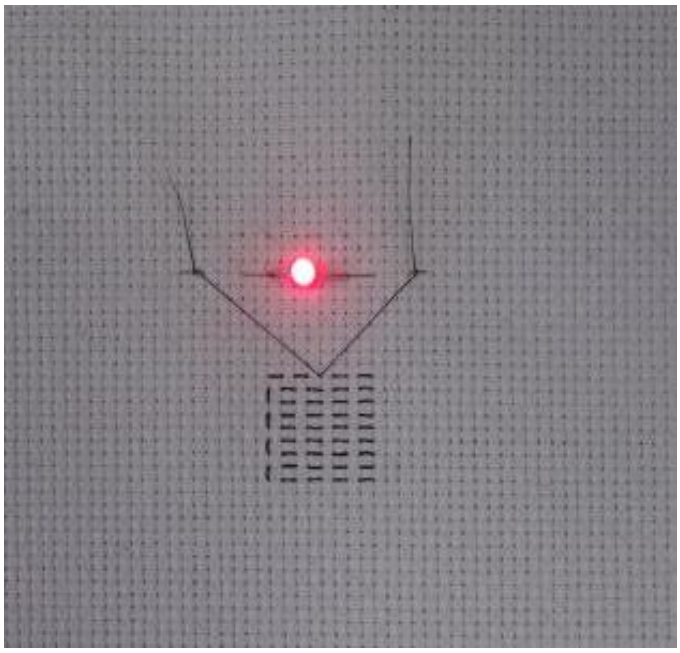

Figure 4-33 Photograph of a red LED illuminated by the charged energy textile consisting of our NiCo-Fe battery.

4.4 Conclusion

This chapter demonstrated an effective approach to dramatically increase the capacity, cycling stability and rate capability of Fe_2O_3 via S doping due to its reduced band gap and enhanced electrical conductivity, rendering it as an attractive anode for aqueous rechargeable Ni-Fe batteries. As demonstrated by the experimental results, the well-designed S-Fe_2O_3 NWAs/CNTF electrode presents a remarkable capacity of areal capacity of 0.81 mAh/cm^2 at 4 mA/cm^2, which is nearly seven times higher areal capacity of the pristine Fe_2O_3 NWAs/CNTF-based electrodes. Furthermore, a prototype fiber-shaped NiCo-Fe battery with a stable operating voltage of 1.05 V fabricated using S-Fe_2O_3 NWAs/CNTF-based anode, and ZNCO@$Ni(OH)_2$ NWAs/CNTF-based cathode demonstrated remarkable areal capacity (equal to 0.46 mAh/cm^2) and volumetric energy density (equal 67.32 mWh/cm^3), substantially outperforming most of the recently reported aqueous rechargeable batteries. Additionally, our wearable NiCo-Fe battery showed impressive flexibility, with negligible capacity loss at different bending angles. This work provides new insights on the design of novel Fe-based anodes for the next-

generation wearable Ni-Fe batteries. This technology will revolutionize and further advance applications related to flexible energy-storage technologies.

Chapter 5 All Metal Phosphide Electrodes for High-Performance Quasi-Solid-State Fiber-shaped Aqueous Rechargeable Ni-Fe Batteries

Aqueous rechargeable Ni-Fe batteries with high energy density, low cost and outstanding safety contribute significantly to the progress of high-performance portable and wearable energy storage devices. However, the common electrode materials are nickel/iron or their oxides which have suffered from poor conductivity and cycle performance. As an ideal candidate to address these issues, metal phosphides may offer outstanding theoretical specific capacity, low conversion potential, and impressive redox. In this study, a new type of high-performance flexible Ni-Fe battery with binder-free electrodes on conductive fiber substrates is successfully designed and fabricated. Hierarchical NiCoP nanosheet arrays (NSAs) and FeP NWAs grown directly on CNTFs are fabricated firstly using hydrothermal synthesis then pursuant gas phosphating process. With the assistance of PVA-KOH gel electrolyte, our fiber-shaped aqueous rechargeable battery (FARB) presents negligible capacity loss after bending 3000 times and shows excellent stability with the capacity retention rate of 89% after 4000 cycles. Meanwhile, our assembled FARB has a significant capacity of 0.294 mAh/cm^2 under 2 mA/cm^2 current density and a high volumetric energy density of 39.48 mWh cm^{-3}.

5.1 Introduction

Aqueous rechargeable batteries using water as an electrolyte solvent can fundamentally solve the safety problems caused by flammable organic electrolytes; meanwhile, it can also potentially lower the cost of strict manufacturing conditions of organic systems and expensive electrolyte, and radically improve the power characteristics of battery systems [190-199]. In addition, water-based solvents are more environmentally friendly than organic solvents [200-203]. Based on the above-mentioned advantages, constructing a high performance aqueous rechargeable battery is a very efficient stratagem to meet future requirements of efficient and safe energy storage.

Iron-nickel batteries have been widely used due to their indestructibility (overcharge, over-discharge and indiscriminate), long cycle and shelf life[43-204]. Meanwhile, the inherent high safety, low cost and good comprehensive electrochemical performance of aqueous iron-nickel batteries enable them to be hotspots in worldwide research and development[205-206]. The cathode of Ni-Fe battery is nickel oxide or nickel hydroxide, the anode is an iron or iron oxide, and the electrolyte is always an aqueous potassium hydroxide solution [207-212]. However, the self-discharge rate of the iron-based electrode is pretty high due to the dissolution in the alkaline solution, while at the same time the energy efficiency and power density are quite low, thus the further application of the Ni-Fe battery has been severely limited. Meanwhile, a passivation film is always generated on the surface of the iron electrode during charge-discharge process, which has inevitably decreased the electrochemical stability of electrodes. Therefore, improving the performance of the iron-based electrode is the key to enhance the overall performance of the Ni-Fe battery.

Among all the accessible materials, metal phosphides have become one of the ideal candidates for battery, owing to its outstanding theoretical specific capacity, low conversion potential, impressive redox reactivity, and cost effectiveness [213-217]. This is due to the fact that low electronegativity of phosphorus provides good electrical conductivity and electrochemical activity, which facilitates electron transport and redox reaction [218-222]. Thus, the adoption of iron phosphides as cathodes is a scientifically sound strategy to achieve a high-performance battery. For the anode materials, rich valence states of nickel and cobalt allow multiple redox reactions in nickel-cobalt hydroxide, while the unique layered structure of nickel/cobalt hydroxide is beneficial to enlarge the contact area with electrolyte ions and then enable full participation of active sites in the electrochemical reactions, thereby harvesting the excellent electrochemical activity in nickel/cobalt hydroxides [223-225]. Albeit the above-mentioned advantages in electrochemical applications, nickel/cobalt hydroxide suffers from poor electrical conductivity and stability. Nickel/cobalt hydroxides are prone to particle agglomeration due to the hydrogen bonding between the crystal and nano-sized effects during the synthesis process, thereby reducing the specific surface area of the material, resulting in

insufficient contact between the electrolyte and the electroactive component [226-228]. Furthermore, it also have a bad effect on mass transfer rate and electron transfer rate, resulting in a significant decrease in the specific capacity and recyclability of the material. One of the methods to solve this problem is to phosphatize nickel/cobalt hydroxide due to the lower electronegativity of phosphorous than that of oxygen, thus the phosphide materials have more flexible crystal structures and structural ductility compared to the hydroxides, which can help in alleviating structural collapse of the material in continuous testing, thereby improving the stability of electrode materials [229-230].

In this chapter, a novel flexible Ni-Fe battery using all metal phosphides as electrodes on highly conductive fibers is successfully designed and fabricated with improved electrochemical performance. Hierarchical NiCoP nanosheet arrays (NSAs) and FeP NWAs directly grown on CNTFs are fabricated using hydrothermal method and subsequent gas-solid phosphating. The adhesion of nanoscale materials to carbon nanotube not only reduces their own agglomeration but also prevents the accumulation of the carbon material, which increasing the specific surface area of the composite and improving the electrical conductivity.

5.2 Experimental

5.2.1 Preparation of NiCoP NSAs/CNTFs.

The synthesis of NiCoP NWAs was also carried out in two steps, firstly, it adopts a hydrothermal process to synthesize NiCo LDH precursor on the CNTFs then subsequent the phosphating process in the Argon gas to obtain the NiCoP/CNTFs. The hydrothermal process was shown below: 0.582 g cobalt nitrate hexahydrate ($Co(NO_3)_2 \cdot 6H_2O$), 0.58 g nickel nitrate hexahydrate ($Ni(NO_3)_2 \cdot 6H_2O$) and 1.12 g hexamethylenetetramine ($C_6H_{12}N_4$) were dissolved in 40 mL DI water with agitating at room temperature for 40 mins to obtain a homogeneous solution. The homogeneous solution obtained and five CNTFs were simultaneously transferred to a 50 mL Teflon-lined stainless autoclave. Thereafter, the vessel was kept at 100 °C for 10 hours then cooled down to room temperature. The CNTFs coated by the NiCo LDH precursor were extracted and repeatedly rinsed several times with DI water and dehydrated under

vacuum in a 60 °C oven overnight. The next step phosphating reaction was similar as discussed above: placing 1.0 g of NaH_2PO_2 in the center of the tubular furnace and five NiCo LDH/CNTFs on the lower-stream end. After calcination at 350 °C (rate of heating 5°C/min) for 2 hours in Ar atmosphere (200 sccm), NiCoP/CNTFs was obtained.

5.2.2 Assembly of NiCoP NSAs/CNTF//FeP NWAs/CNTF FARB.

Firstly 10 g of poly(vinyl alcohol) (PVA) was dissolved in 85 ml DI water with heating under 90 °C for 3 hours in the meantime 11.2 g of KOH was dissolved in 15 ml DI water. After that, the KOH homogeneous solution was slowly dropped in the well-mixed PVA liquor at 90 °C. PVA-KOH gelation was generated and employed as a gel electrolyte, which also served as a diaphragm. The FARB can be obtained by soaking a pair of fibrous electrodes in the PVA-KOH gel electrolyte and twisting two electrodes together until the gel solution was solidified.

5.3 Properties of the Ni-Fe battery

The fabrication process of our flexible FARB was systematically depicted in Figure 5-1 and more details can be found in the experimental section. Firstly, hierarchical NiCoP/CNTFs anode was directly grown on the conductive CNTFs using a simple two-step method starting with the hydrothermal method followed by a subsequent gas-solid phosphating. Thereafter, the FeP/CNTFs cathode was fabricated following the same phosphating process. Then, the PVA-KOH gel electrolyte was uniformly coated on the NiCoP/CNTFs cathode and FeP/CNTFs anode. Finally, by twisting the NiCoP/CNTFs and FeP/CNTFs electrodes together and placing them overnight for full solidification, the FARB was successfully assembled.

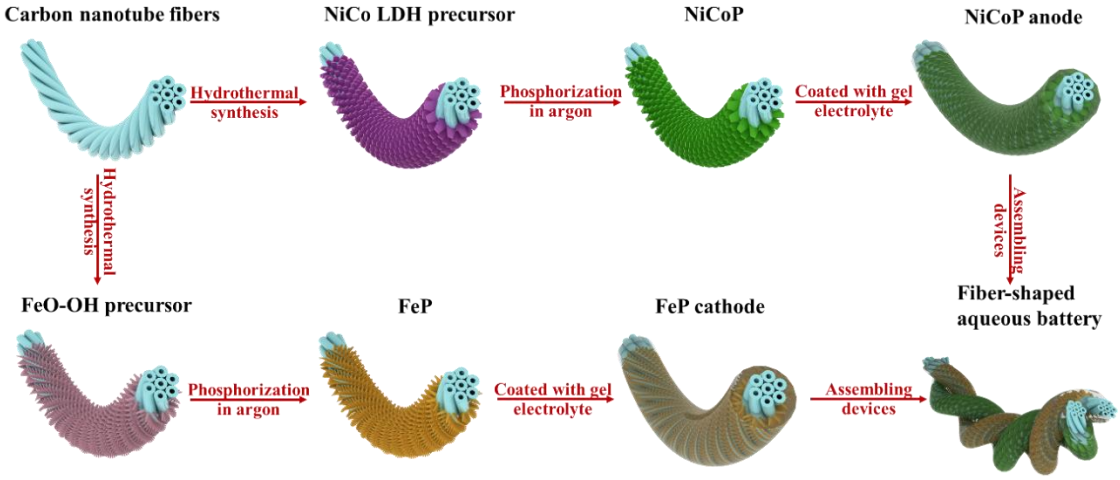

Figure 5-1 Fabrication of NiCoP NSAs/CNTFs//FeP NWAs/CNTFs FARB.

Figures 5-2a and 5-2b display SEM images of FeP NWAs grown on the CNTFs surface under different magnifications. As can be seen from Figure 2a, the FeP NWAs are well-distributed on the skeleton of the CNTFs. The magnified SEM image in Figure 2b further reveals that the vertical FeP NWAs are uniformly grown on the surface of the CNTFs, the structure was kept very well in contrast with FeO/CNTFs (Figure 5-3). The formation of the vertical structure after phosphating may be caused by the shrinkage of hydroxides during phosphating, resulting in the loss of H atoms and O atoms and the recrystallization of materials. This structure can provide more paths for ion diffusion or ion exchange, so more active sites can be exposed during the electrochemical reaction.

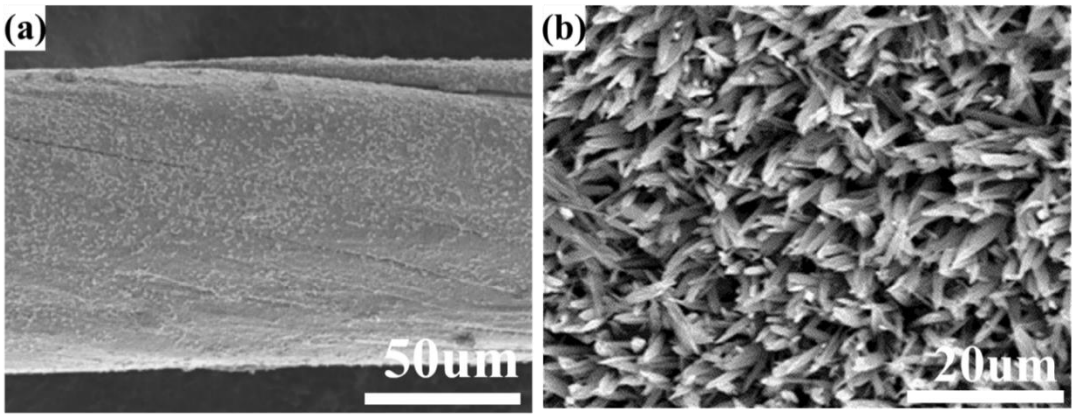

Figure 5-2 (a-b) SEM images of FeP NWAs on CNTFs under different magnifications.

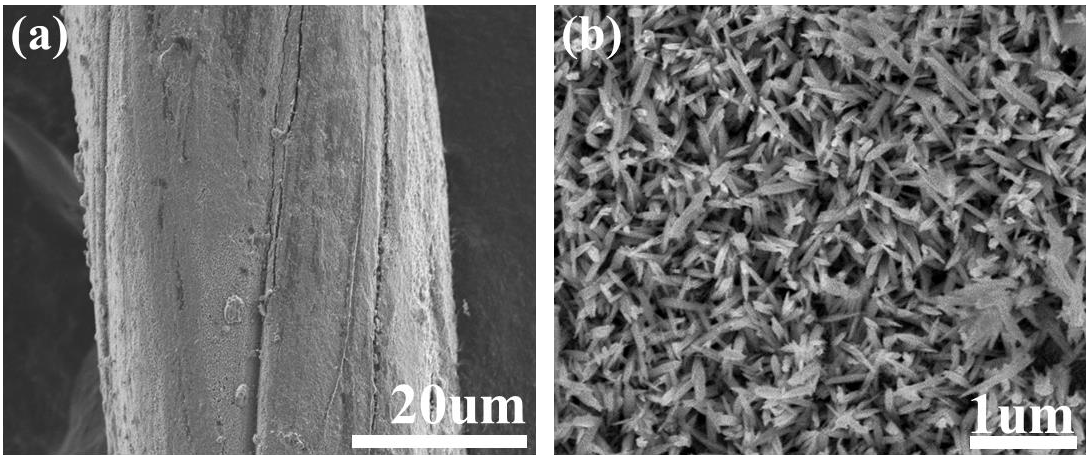

Figure 5-3 (a-b) SEM images of Fe_2O_3 NWAs/CNTF at different magnifications.

Moreover, the vertically oriented structures facilitate effective contact of the active material with the electrolyte and provide an effective channel for rapid charge transfer, thereby optimize the electrochemical performance of the electrode. Further characterization by the XRD in Figure 5-4a displays all the diffraction peaks of the red line that can be indexed to the FeP (JCPDS 65-2595) and the blue line is in accordance with the standard Fe_2O_3 (JCPDS 33-0064). Figure 5-4b shows the XPS survey spectrum of the FeP/CNTFs electrode confirming the presence of Fe, P, and O that is possibly due to the surface oxidation. Two main spin-orbit peaks are discovered in both the Fe 2p and P 2p spectrum. In the Fe 2p spectrum shown in Figure 5-4c, the two major peaks at 709.2 eV and 723.5 eV are ascribed to Fe 2p3/2 and Fe 2p1/2 and the two main peaks at 127.2

and 131.6 eV in the P 2p spectrum displayed in Figure 5-4d correspond to P 2p3/2 and P 2p1/2. The Fe 2P spectrum of FeP/CNTFs shows a slight difference with the XPS results of Fe_2O_3/CNTFs (Figure 5-5).

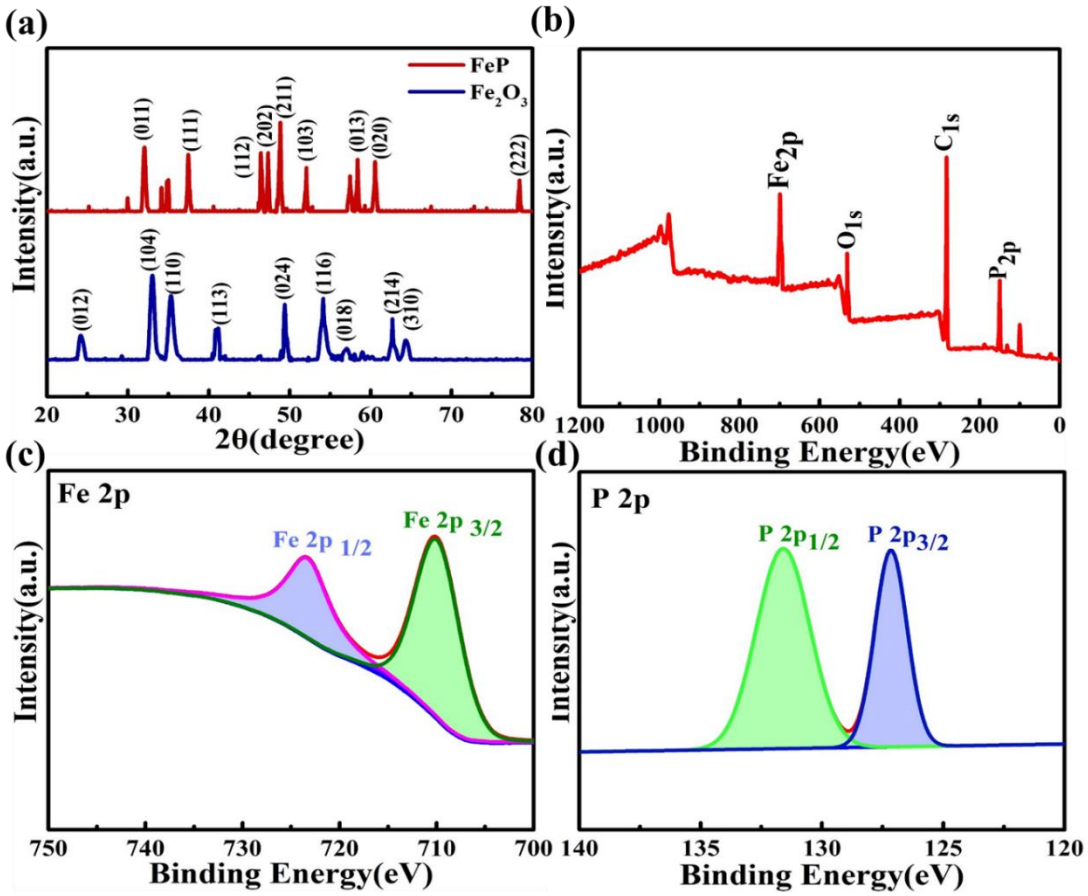

Figure 5-4 (a) XRD spectrum of FeP/CNTFs and Fe_2O_3/CNTFs. (b) XPS survey spectrum of FeP/CNTFs NWAs. High resolution XPS of (c) Fe 2p (d) P 2p spectra in FeP/CNTFs.

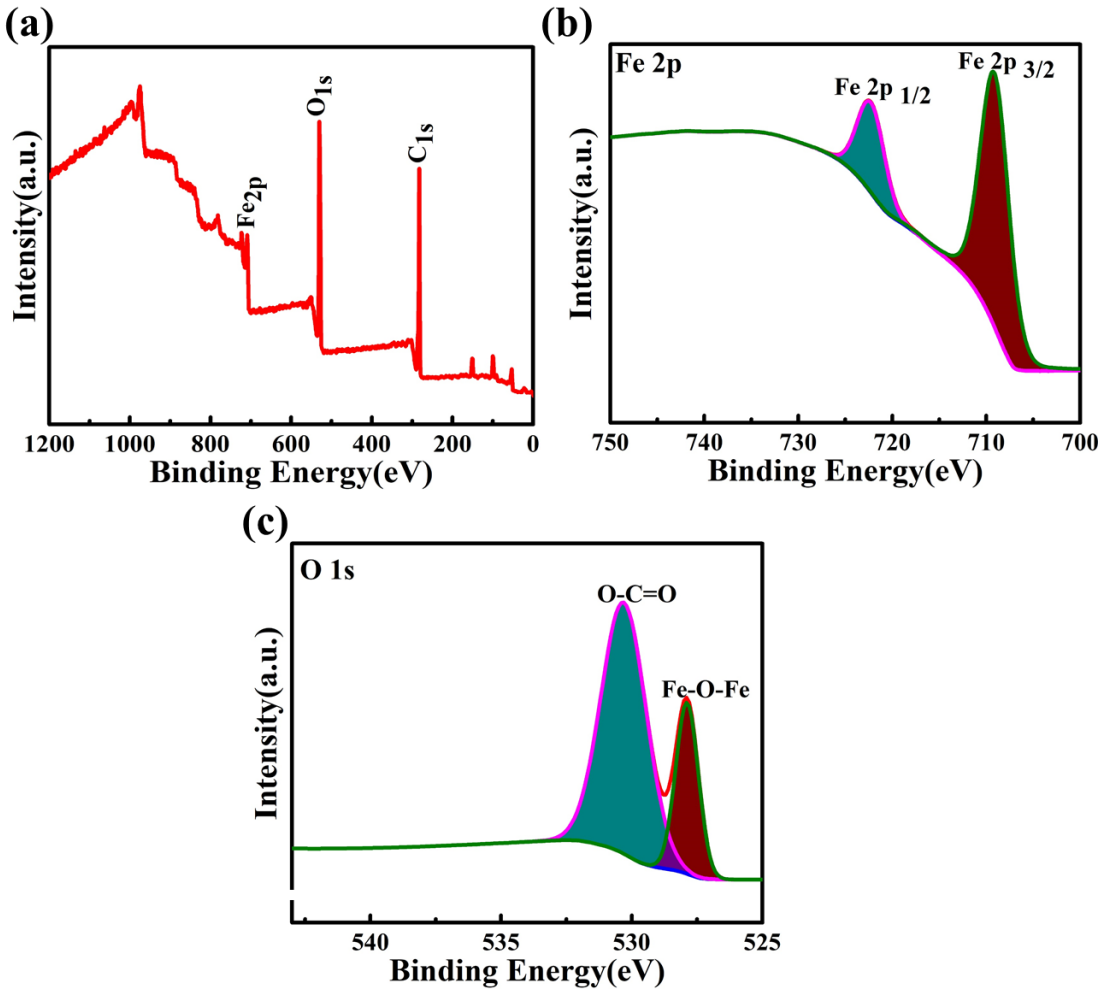

Figure 5-5 (a) XPS full survey spectrum of Fe_2O_3 NWAs/CNTF. (b) Fe 2p and (c) O 1s of Fe_2O_3.

Figure 5-6a shows the lattice fringes of the FeP/CNTFs with an inter-planar space of 0.273 nm, which can be matched to the (011) plane. The EDS spectrum in Figure 5-6b clearly indicates the existence of the Fe, P, and O. The SEM image and EDS element mappings (Figure5-7) distinctly prove the uniform distribution of the Fe, P, and O over the whole CNTFs surface, while only Fe and O are detected in Fe_2O_3/CNTFs (Figure 5-8). It is obviously that the P elements cannot be detected in the Fe_2O_3/CNTFs.

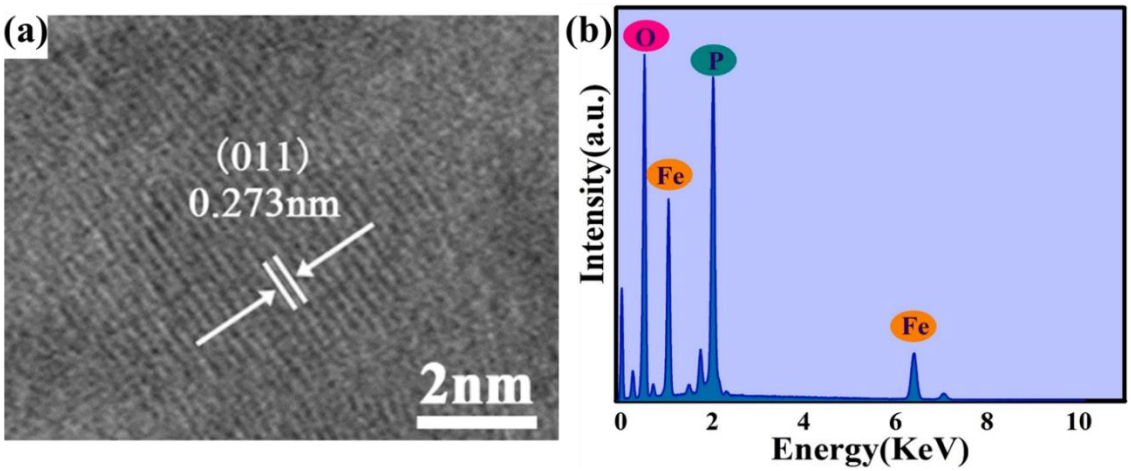

Figure 5-6 (a) HRTEM image of FeP/CNTFs. (b) EDS spectrum of FeP/CNTFs.

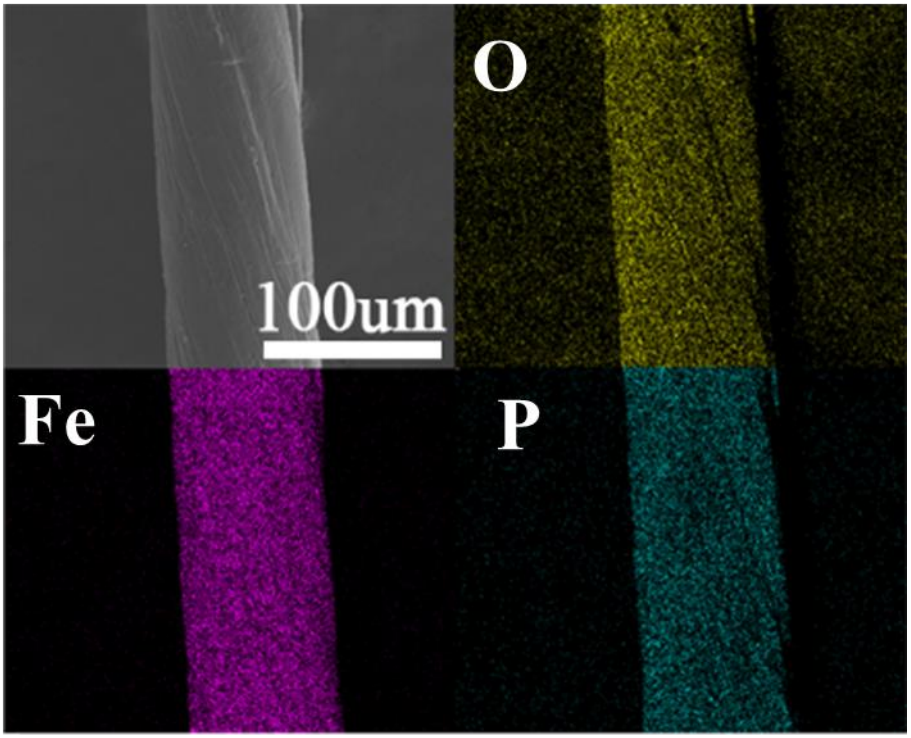

Figure 5-7 SEM graph of FeP/CNTFs and corresponding EDS mappings of O, Fe and P elements.

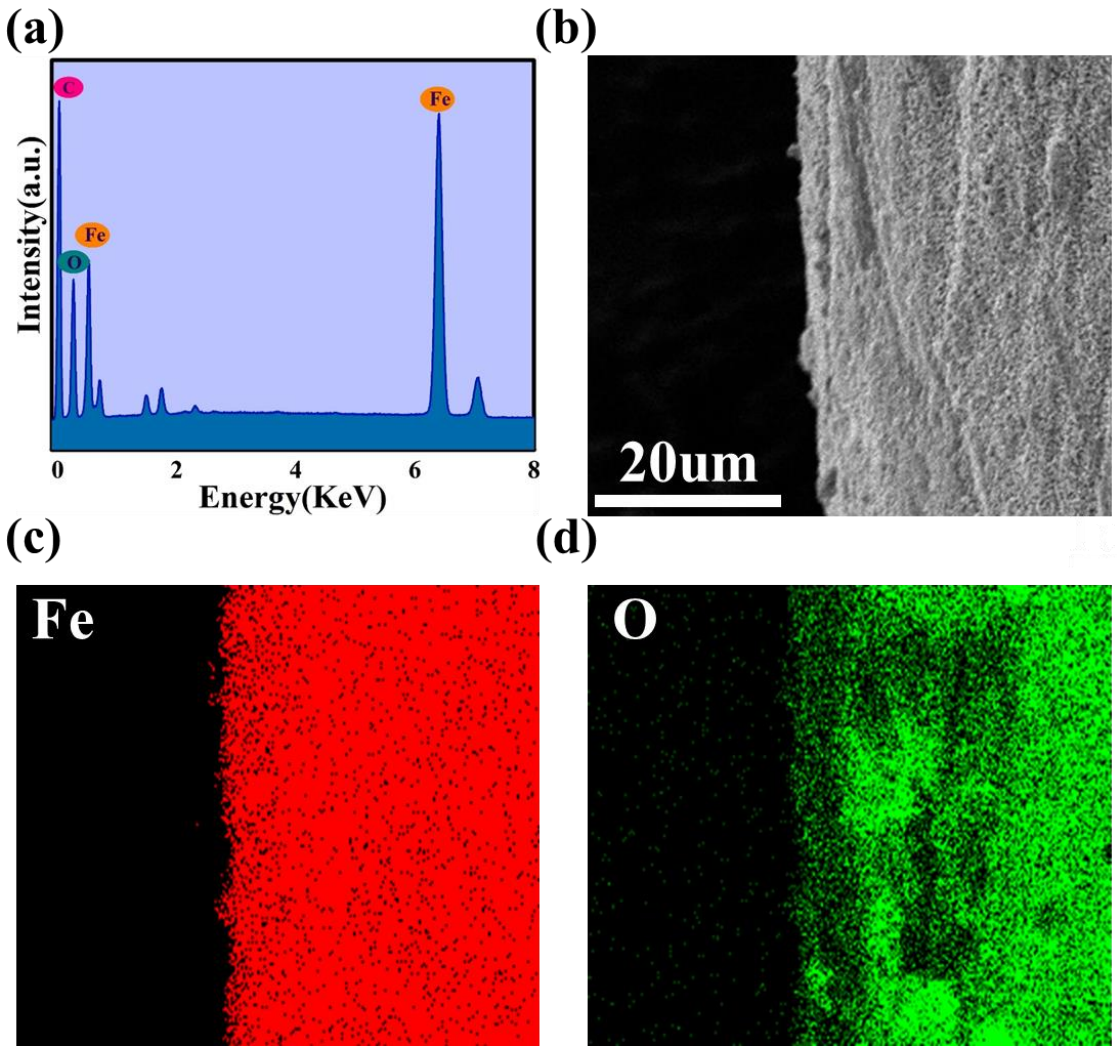

Figure 5-8 (a) EDS spectrum of Fe_2O_3 NWAs/CNTF electrode. (b) SEM image and corresponding EDS element mappings of (c) Fe and (d) O for Fe_2O_3 NWAs/CNTF.

In order to evaluate the property of the prepared samples in electrochemical energy storage, this paper studied the performance of FeP NSAs/CNTFs composite fiber electrodes. A three-electrode test was carried out in 1 M KOH aqueous solution by using FeP/CNTFs as working electrode, a Pt wire electrode as a counter electrode and an Ag/AgCl electrode as a reference electrode. Through further comparison of GCD curves (Figure 5-9a), the discharge time of FeP/CNTFs electrode is much longer than that of Fe_2O_3/CNTFs electrode because of the unique structure and composition of FeP/CNTFs electrode, which proves the enhancement in electrochemical performance. This

improvement is due to the low electronegativity of phosphorus, which provides good electrical conductivity and electrochemical activity, enabling fast electron transport and rapid redox reaction. Figure 5-9b further compares the CV curves of the original CNTFs, Fe_2O_3/CNTFs and FeP/CNTFs at the scan speed of 2 mV/s, which clearly demonstrates the negligible contribution from the original CNTFs to the fabricated fiber electrode (Figure 5-10).

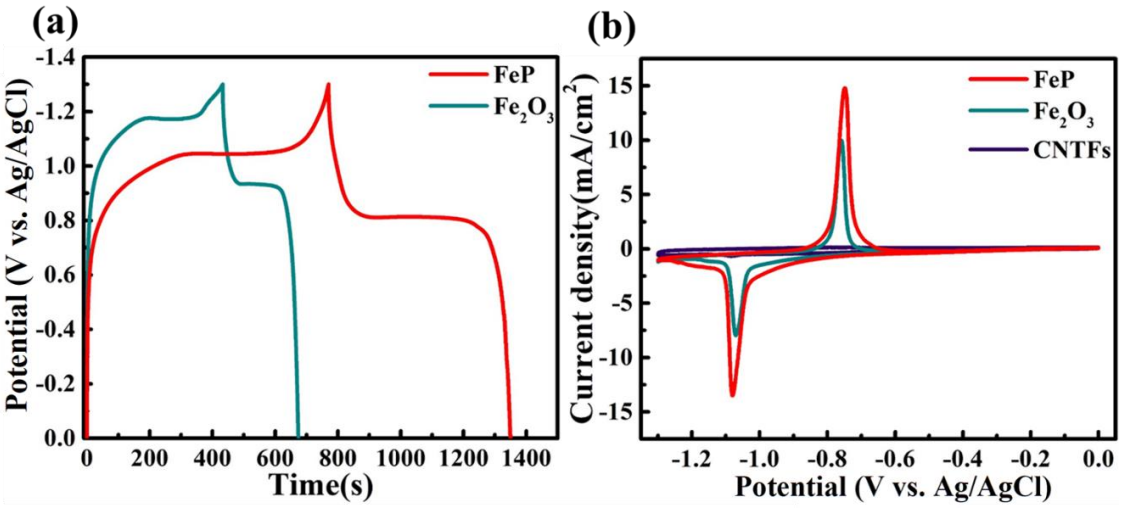

Figure 5-9 (a) GCD curves of Fe_2O_3/CNTFs and FeP/CNTFs at 4mA/cm^2. (b)CV curves of origin CNTFs, Fe_2O_3/CNTFs, and FeP/CNTFs at the scan rate of 2 mV/s.

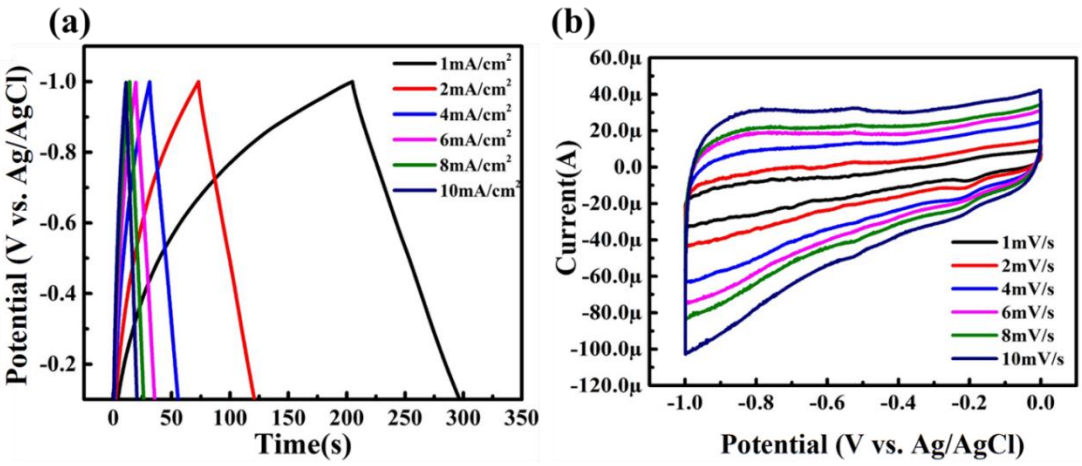

Figure 5-10 (a) GCD curves for the CNTF as the anode electrode at different current densities. (b) CV curves for the CNTF electrode at various scan rates.

Meanwhile, the obvious couple of redox peaks arise in both Fe_2O_3 and FeP, however, the FeP/CNTFs electrode has almost double integrated area and more intensive redox peaks than that of Fe_2O_3/CNTFs (Figure 5-11), implying the dramatic improvement in specific capacity and redox reactivity in the hybrid fibers via the gas-solid phosphorization. EIS comparison data has been showed in Figure 5-12, the charge transfer resistance value of FeP NWAs/CNTF electrode is lower transfer resistance of

Fe_2O_3 NWAs/CNTF electrode, demonstrating that the electronic/ionic transfer kinetics of Fe_2O_3 NWAs was significantly enhanced via the phosphorization.

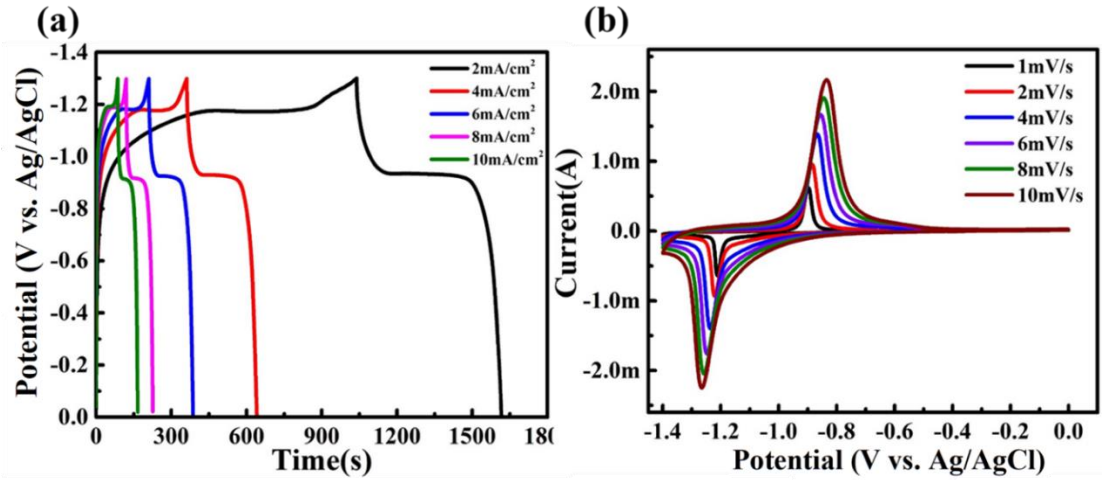

Figure 5-11 (a) GCD curves for the Fe_2O_3 NWAs/CNTF at different current densities. (b) CV curves for the Fe_2O_3 NWAs/CNTF electrode at various scan rates.

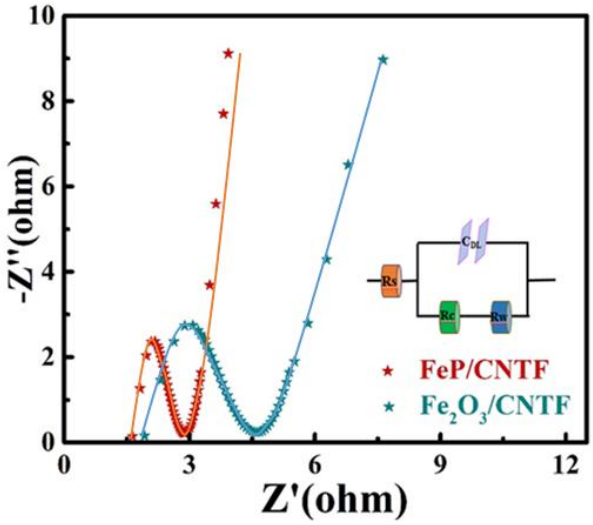

Figure 5-12 EIS analysis of the FeP NWAs/CNTF electrode and Fe_2O_3 NWAs/CNTF electrode.

Figure 5-13a shows the comparison of the CV curves of FeP/CNTFs electrodes at a series of scan rates of 1 ~ 10 mV/s. Obviously, retention of reversible redox peaks in FeP/CNTFs along with increased scan rates indicates the potential of FeP/CNTFs as a good candidate material for the battery. The discharge curves of the FeP/CNTFs

electrode at different current densities are displayed in Figure 5-13b and it can be expressively observed that a distinct discharge platform is at about -0.9 V and the capacity reached 0.634 mAh/cm^2 (volumetric capacity is 178.4 mAh/cm^3) at a current density of 2 mA/cm^2. The discharge plateau has a small shift to a low potential with the increase of the current density. Figure 5-14a displays the calculated specific capacity from the discharge curves, the specific capacity of FeP/CNTFs reaches a high value of 0.634 mAh/cm^2, approximately twice as much as Fe_2O_3. The capacity retention of 86.2% is realized in FeP/CNTFs when the current density aggrandized to 10 mA/cm^2, in contrast to the 50% capacity retention of Fe_2O_3/CNTFs, demonstrating the superior electrochemical performance of FeP/CNTFs. For the cycling stability of the FeP/CNTFs, the test is studied at the 10 mV s^{-1} scan rate and the corresponding results are shown in Figure 5-14b. After 4000 cycles, 89% of the incipient capacity is commendably maintained, illustrating the excellent cycling stability.

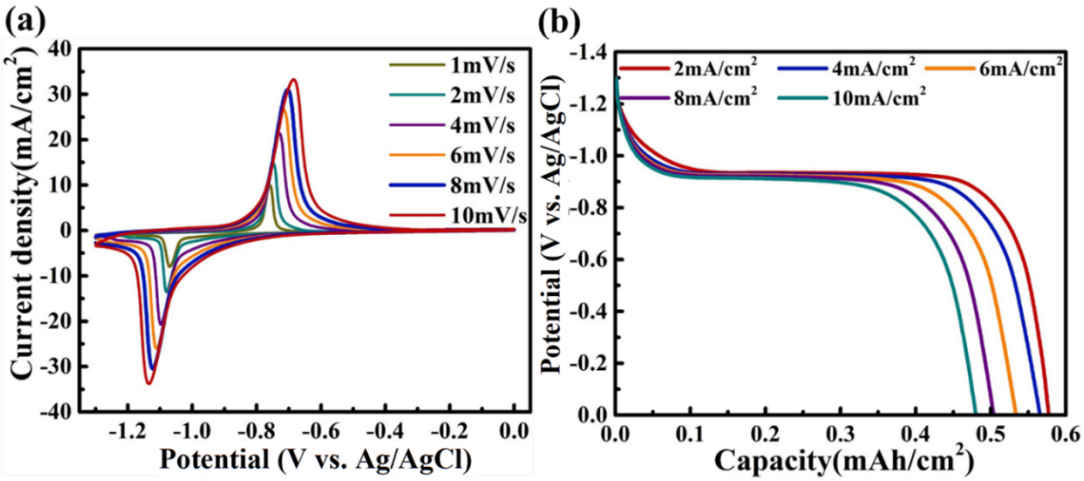

Figure 5-13 (a) CV curves of FeP/CNTFs under diverse scan rates. (b) Discharge curves of FeP/CNTFs with various current density.

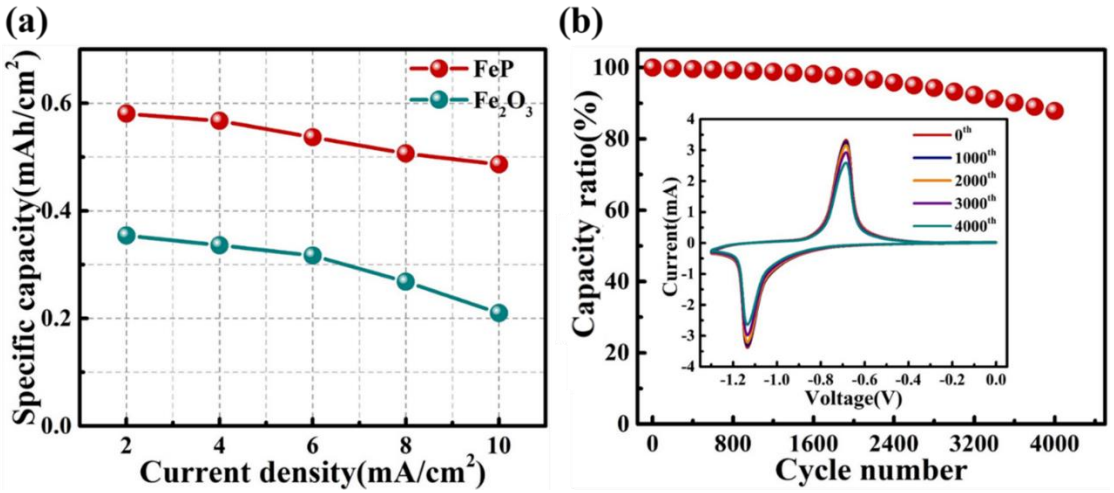

Figure 5-14 (a) The specific capacity of the Fe_2O_3/CNTFs and FeP/CNTFs with various current density. (b) Cycling performance of FeP/CNTFs electrode. The insert is the CV curves at different cycles.

Figures 5-15a and 5-15b depict the SEM images of NiCoP NSAs grown on the CNTFs surface under different magnifications. As can be concluded from Figure 5-15a, the NiCoP/CNTFs are evenly overlaid on the skeleton of the CNTFs. The magnified SEM image in Figure 5-15b further reveals that the NiCoP NSAs grown on the surface of the CNTFs are uniformly distributed. After gas-solid phosphating reaction, it is well preserved with only slight structure change from NiCo LDH NSAs (Figure 5-16). In the Figure5-16d, the 0.227 nm of internal spacing can be indexed to the (002) plane.

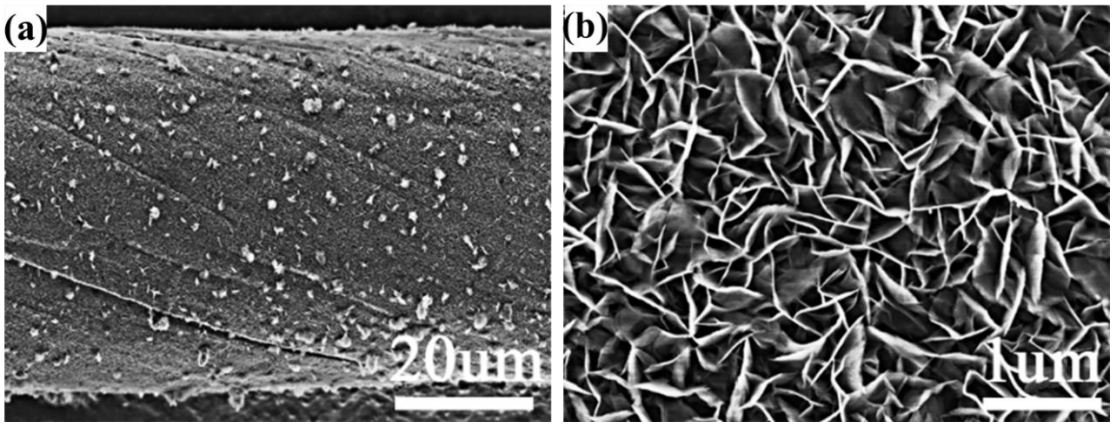

Figure 5-15 (a-b) SEM images of NiCoP NSAs on CNTFs under different magnifications.

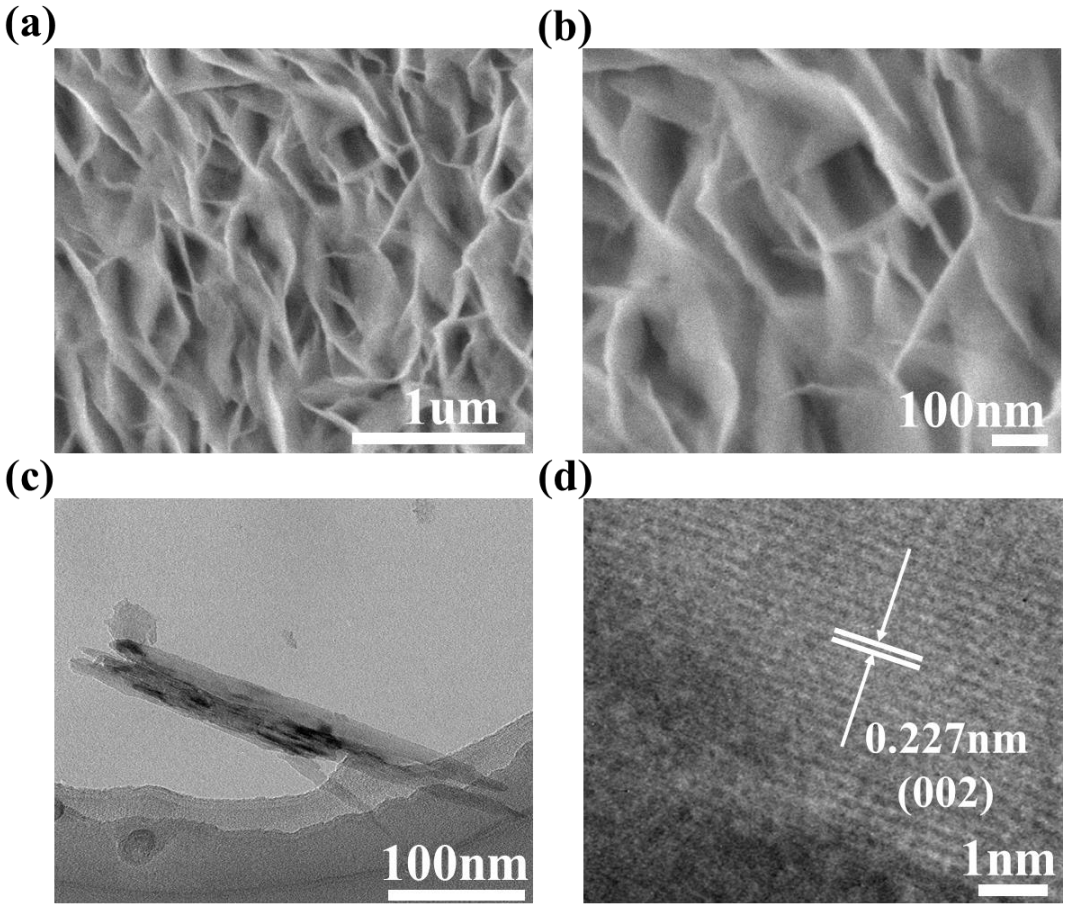

Figure 5-16 (a-b) SEM images of NiCo LDH NSAs/CNTF at different magnifications. (c) TEM image and (d) HRTEM image of the NiCo LDH nanosheet.

The unique distribution of NiCoP/CNTFs provides a large electrochemically active surface and fast ion diffusion and electron transport channels, which in turn can increase electrode specific capacity and energy density. Further characterization by the XRD in Figure 5-17a displays that all the diffraction peaks of the red line can be well matched to the NiCoP (JCPDS 71-2336) and the blue line is well matched to the NiCo LDH/CNTFs. The chemical bonding and valence states of the elements on the NiCoP/CNTFs electrode surface are assessed by XPS. Figure 5-17b shows the XPS survey spectra of the NiCoP/CNTFs electrode, which proves the existence of Ni, Co, P, and O. In the Co 2p spectrum shown in Figure 5-17c, one peak locating at 780.1 eV is corresponding to Co 2p3/2 and the other peak at 795.8 eV is assigned to Co 2p1/2. In the Ni 2p spectrum

displayed in Figure 5-17d, there are two main peaks locating at 854.3 and 871.4 eV, with the corresponding peak to Ni 2p3/2 and Ni 2p1/2, while two satellites located at 859.7 eV and 877.8 eV are also observed. Compared with NiCo LDH/CNTFs (Figure 5-18), there is a slight peak shift from NiCoP/CNTFs, the two main peaks locating at 792.3 eV and 776.9 eV in the Co 2p spectrum. In addition, there are two peaks locating in the 853.7 eV and 860.3 eV corresponding Ni 2p3/2 and Ni 2p1/2. As for the O spectrum in the Figure 5-18d, a distinct peak at 530.4 eV is easy to be observed.

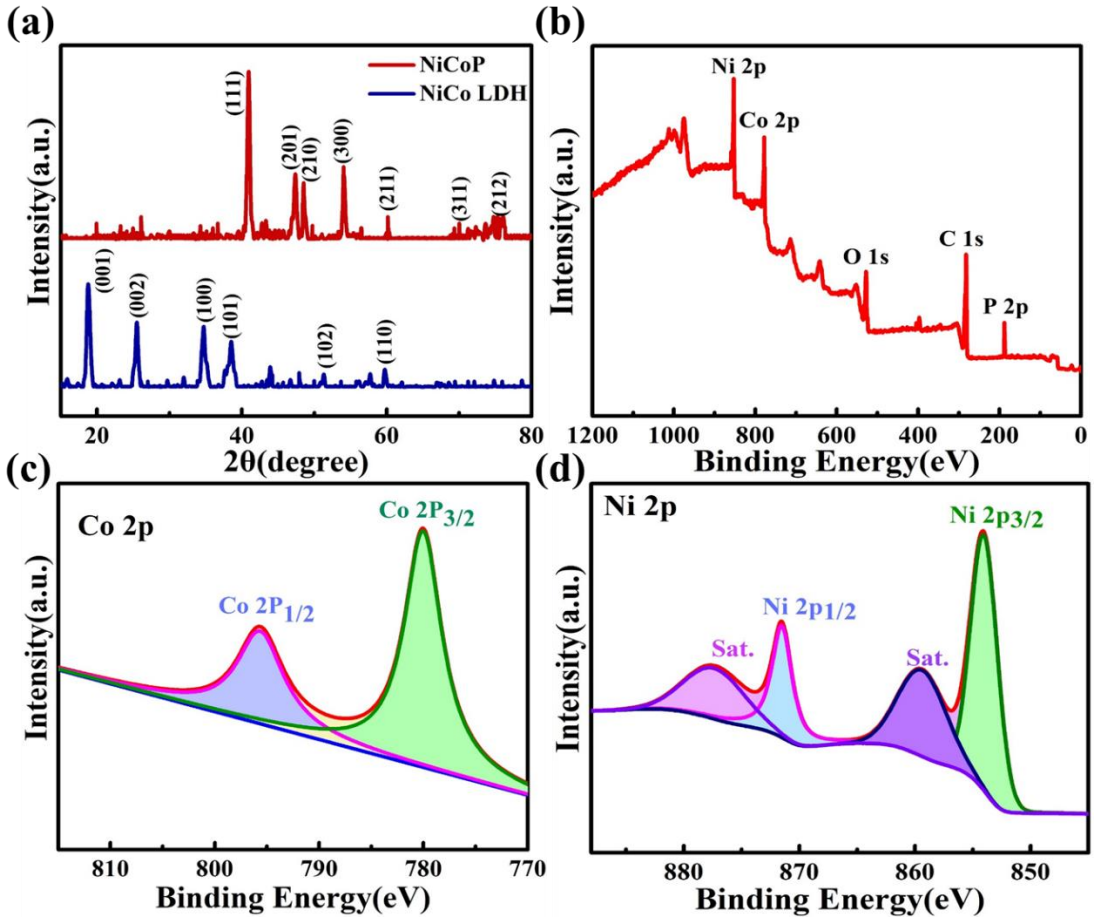

Figure 5-17 (a) XRD spectrum of NiCoP/CNTFs and NiCo LDH/CNTFs. (b) XPS survey spectrum of NiCoP/CNTFs NSAs. High resolution XPS of (c) Co 2p (d) Ni 2p spectra in NiCoP/CNTFs.

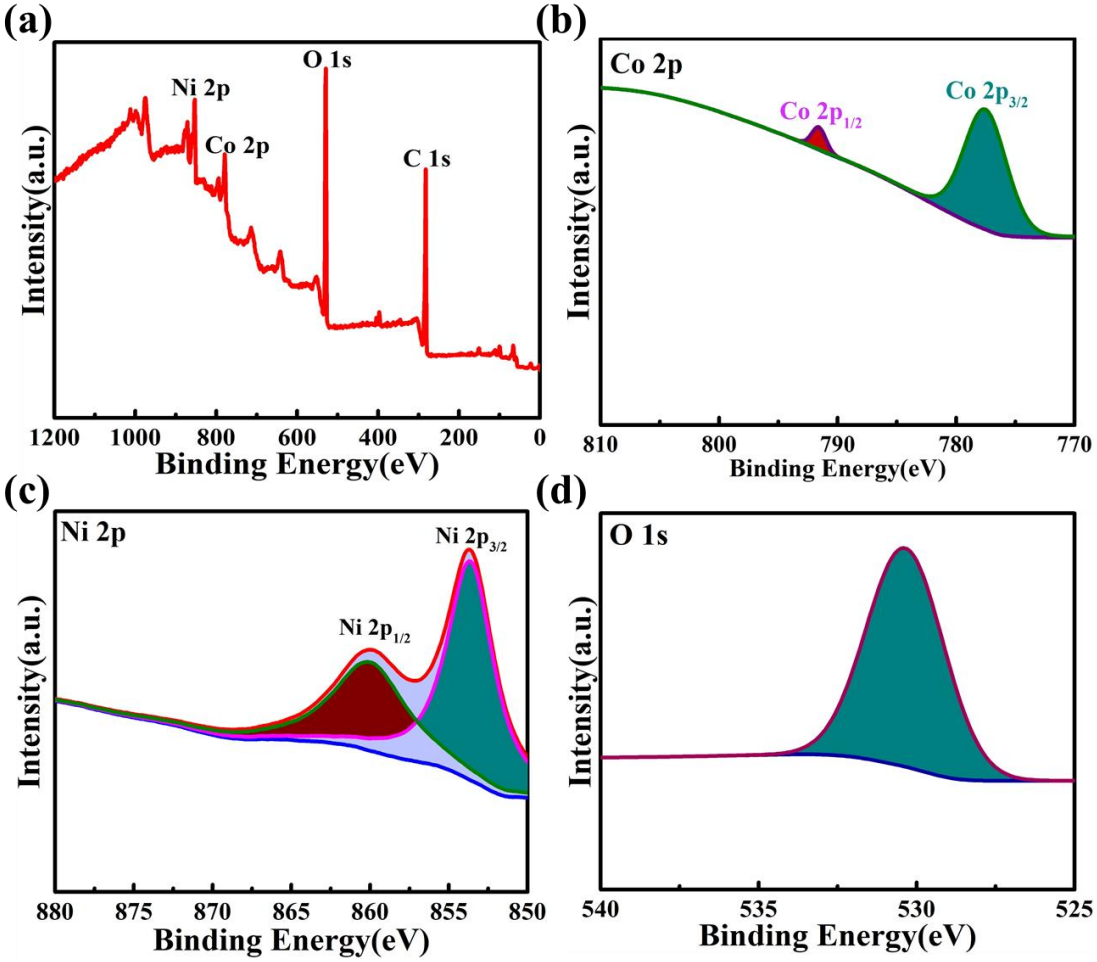

Figure 5-18 (a) XPS full survey spectrum of NiCo LDH NSAs/CNTF. XPS spectrum of (b) Co 2p, (c) Ni 2p, and (d) O 1s of NiCo LDH NSAs/CNTF.

Figure 5-19a shows the lattice fringes of the NiCoP NSAs with 0.218 nm inter-planar spacing, which can be matched to the (111) plane of NiCoP/CNTFs. The EDS spectrum in Figure 5-19b further confirms the existence of the Ni, Co, O and P. The SEM images and the corresponding EDS mapping results shown in Figure 5-20 distinctly present the uniform dispersion of the Ni, Co, and P over the whole CNTFs surface. For NiCo LDH/CNTFs, there are only Ni, Co and O distributing on the surface (Figure 5-21).

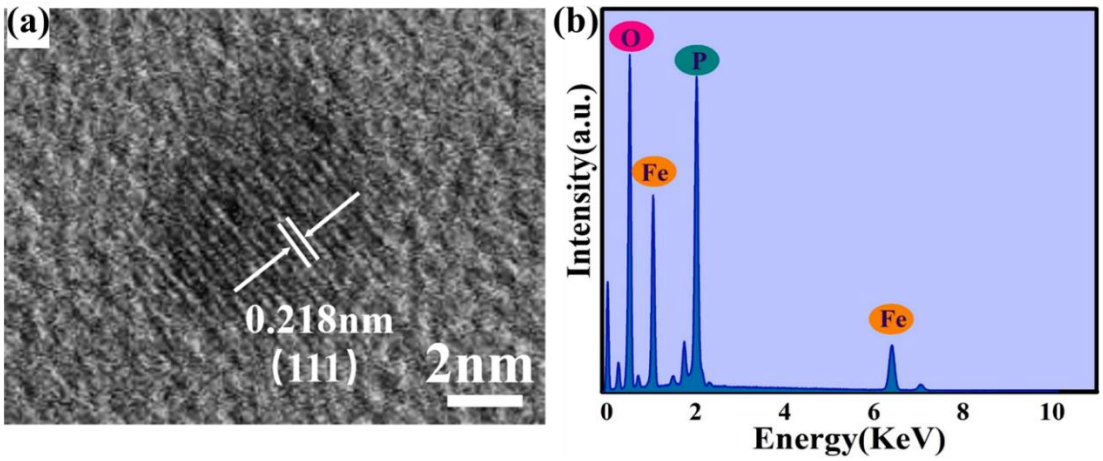

Figure 5-19 (a) The HRTEM image of NiCoP/CNTFs. (b) EDS spectrum of NiCoP/CNTFs.

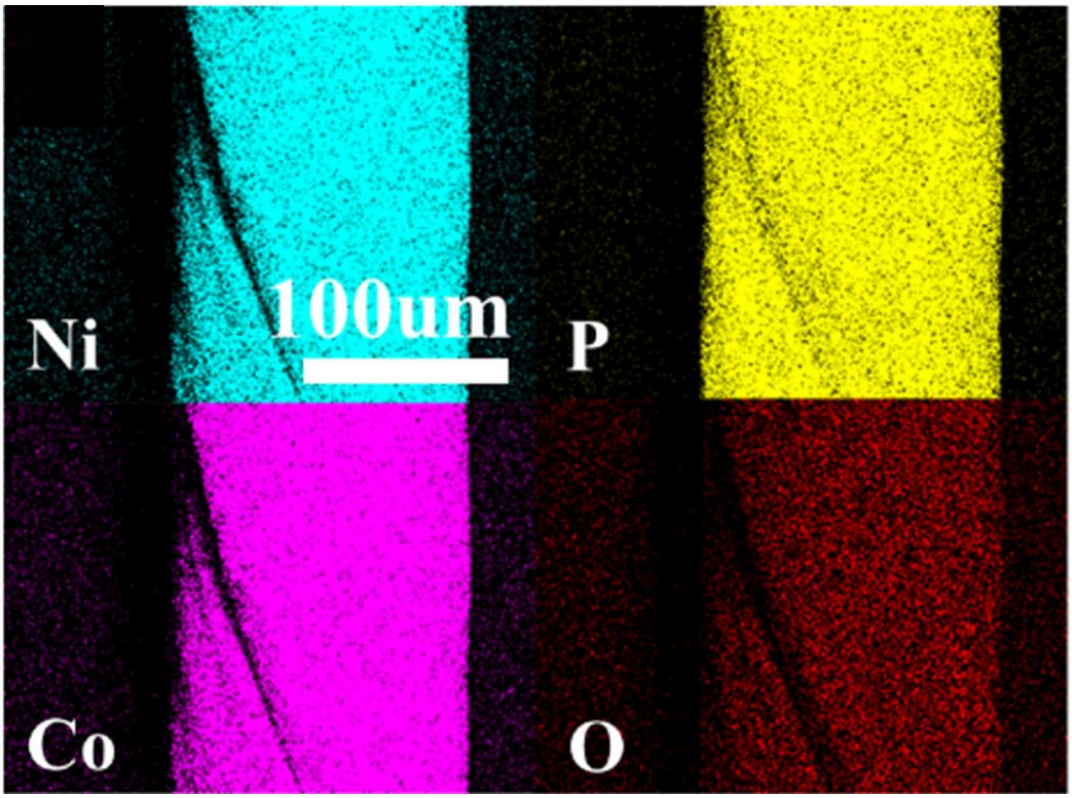

Figure 5-20 Low-resolution SEM graph of NiCoP/CNTFs and corresponding EDS mappings of Ni, P, Co and O elements.

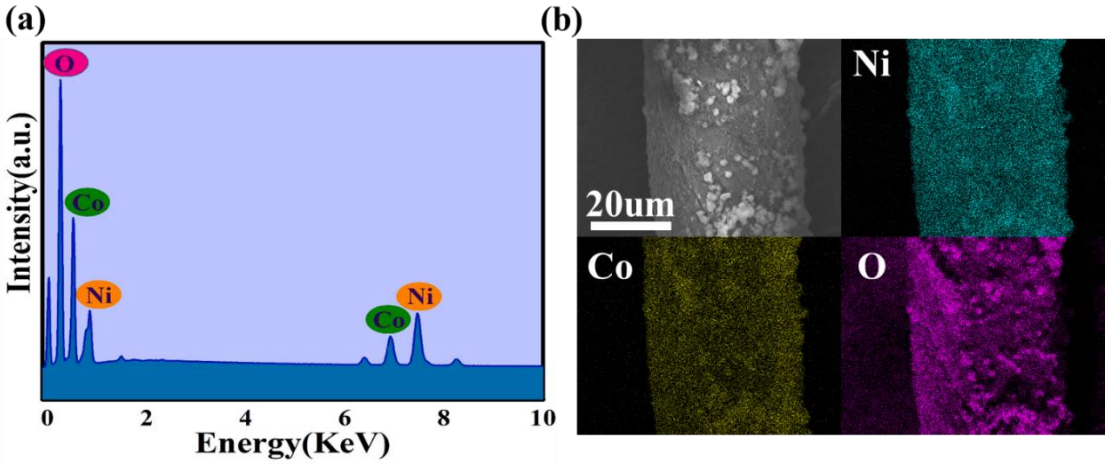

Figure 5-21 (a) EDS spectrum of NiCo LDH. (b) SEM image and corresponding EDS element mappings of Ni, Co and O for NiCo LDH NSAs/CNTF.

The CV curves of the original CNTFs, NiCo LDH/CNTFs and NiCoP/CNTFs at the scan speed of 4 mV/s are compared in Figure 5-22a. It can be easily perceived that the original CNTFs contribute little to the fabricated fiber electrode. A pair of redox peaks are observed in both NiCo LDH and NiCoP, but the NiCoP/CNTFs electrode has almost double integrated area and stronger redox peaks than that of NiCo LDH/CNTFs, implying the dramatic improvement in specific capacity and redox reactivity in the hybrid fibers via the gas-solid phosphorization. The low capacity of the NiCo LDH is due to the low reactive activity of NiCo LDH. After thermal annealing, the crystal structure of NiCo LDH is partially collapsed, which can relax ion transport with more active sites exposed. The enhancement can well be correlated to the lower electronegativity of P in metal phosphides (that facilitates redox reactions) and the increased reactive surface area. From the comparison of GCD curves displayed in Figure 5-22b at the same current density, it is noticed that the discharge time of NiCoP/CNTFs electrode is much longer than that of pristine CNTF and NiCo LDH/CNTFs electrode (Figure 5-23 and Figure 5-24), which is due to the unique structure and composition of NiCoP/CNTFs electrode, harnessing enhanced electrochemical performance. The GCD curves in the Figure 5-24a shows the excellent columbic efficiency of the NiCo LDH, meanwhile a pair of redox in the CV curves indicating the ideal battery-like performance.

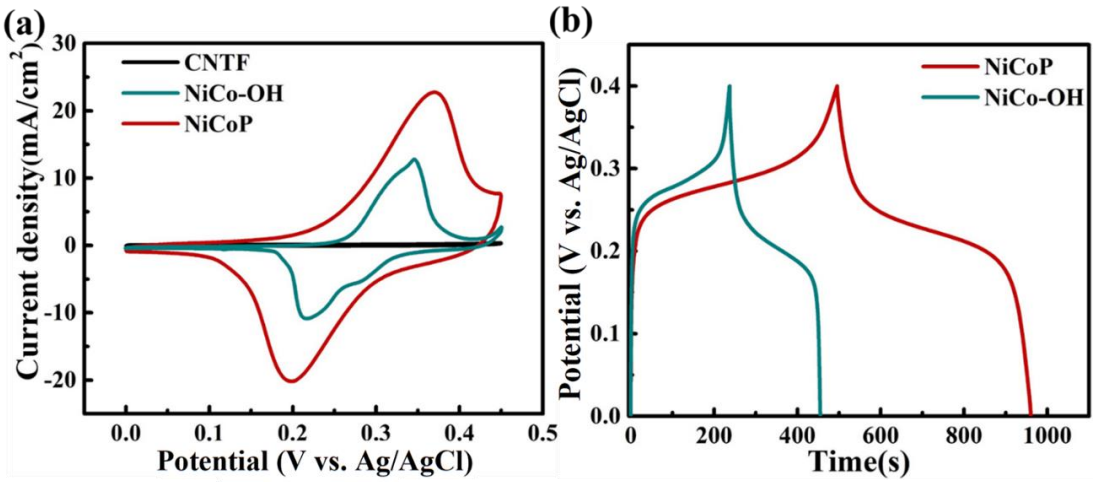

Figure 5-22 (a) CV curves of origin CNTFs, NiCo LDH/CNTFs and NiCoP/CNTFs with the scan speed of 4 mV/s. (b) Comparison GCD curves of NiCo LDH/CNTFs and NiCoP/CNTFs at a current density of 4 mA/cm^2.

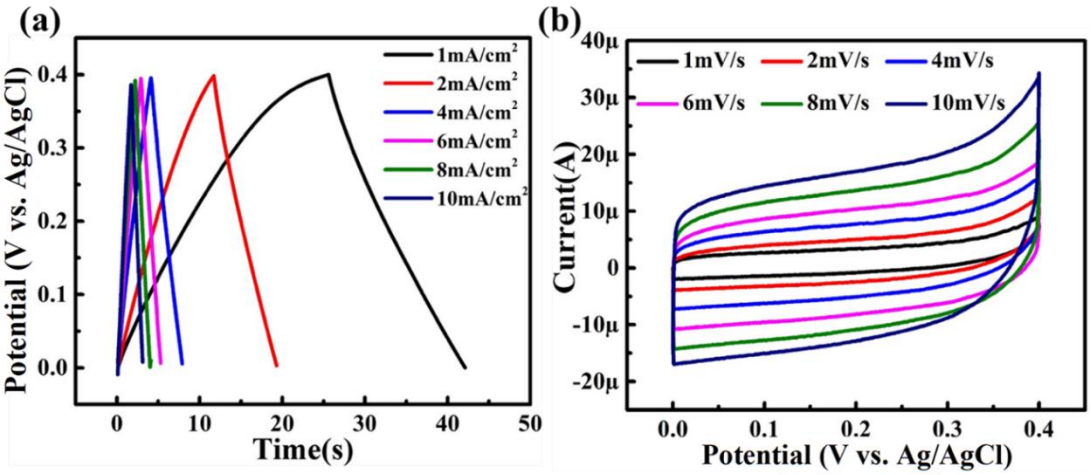

Figure 5-23 (a) GCD curves for the CNTF as cathode at different current density. (b) CV curves for the CNTF electrode at various scan rates.

Figure 5-25a shows CV curves of the NiCoP/CNTFs electrodes at various scan rates of 1 ~ 8 mV/s. A couple of redox peaks can be easily visualized, indicating the redox reaction of NiCoP/CNTFs. Figure 5-25b depicts the discharge curves of the NiCoP/CNTFs under different current densities. A well-defined discharge platform is identified at approximately 0.23 V, which is slightly decreased to a lower potential with the rise in the current density. The specific capacity quantified from the discharge curves

is shown in Figure 5-26a. The specific areal capacity reaches 0.55 mAh/cm^2 (volumetric capacity is 178.4 mAh/cm^3)at 2 mA/cm^2, approximately twice of that of the NiCo LDH/CNTFs. In addition, 82.9% of the initial specific capacity is retained when the current density reaches 10 mA/cm^2, demonstrating the outstanding rate performance. For the cycling stability of the NiCoP/CNTFs, the test was studied at the 8 mV/s scan rate and the corresponding results are shown in Figure 5-26b. 90% of the initial capacity is well retained after 4000 cycles, demonstrating excellent stability.

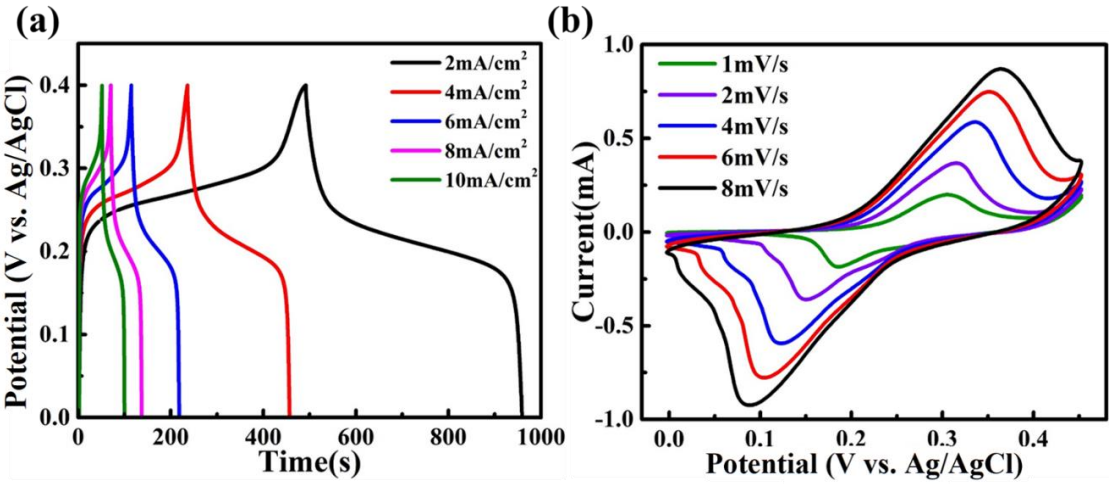

Figure 5-24 (a) GCD curves for the NiCo LDH NSAs/CNTF at different current densities. (b) CV curves for the NiCo LDH NSAs/CNTF electrode at various scan rates.

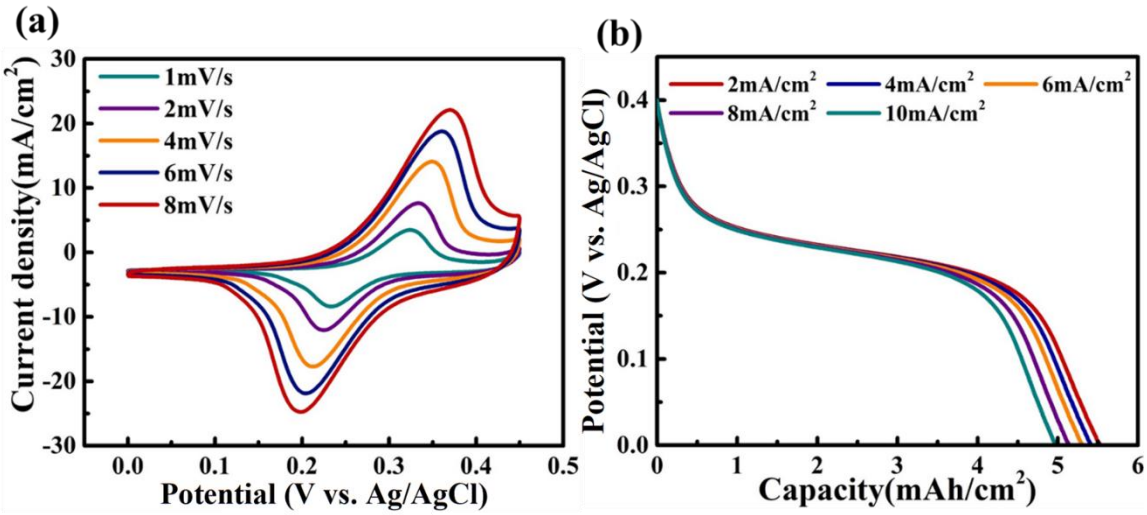

Figure 5-25 (a) CV curves of NiCoP/CNTFs at various scan rates. (b) Discharge curves of NiCoP/CNTFs at various current density.

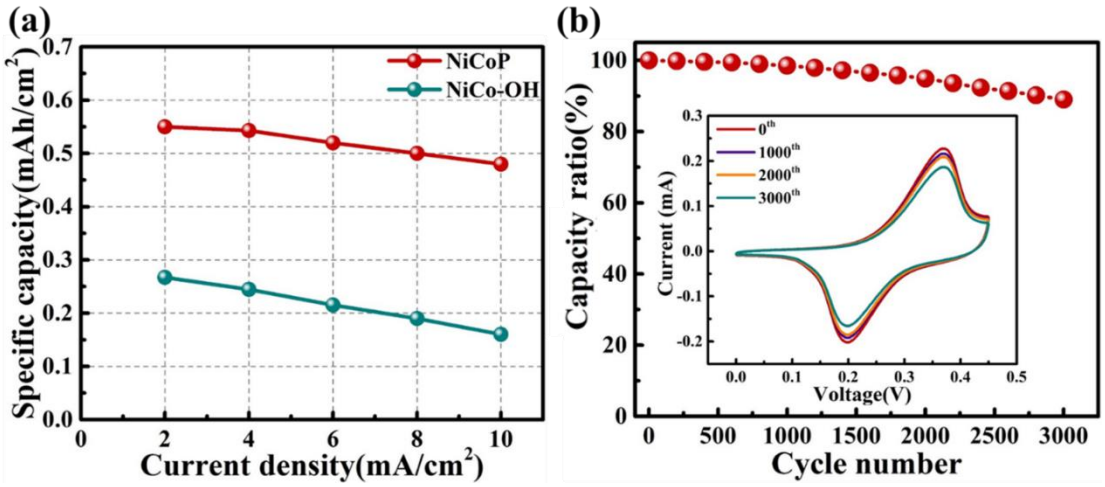

Figure 5-26 (a) The volume capacity of NiCoP/CNTFs and NiCo LDH/CNTFs at various current density. (b) Cycling performance of NiCoP/CNTFs electrode. The insert is the CV curves at different cycles.

In order to evaluate the operating voltage for the device, the CV curve is tested on the NiCoP/CNTFs anode and FeP/CNTFs cathode under a three-electrode system. The test results in Figure 5-27a shows that the operating potential windows of the NiCoP/CNTFs and FeP/CNTFs electrodes are 0~0.4 V and -1.3~0 V, respectively. It is worth noting that both electrodes have obvious redox peaks, demonstrating their good potential for developing a high-voltage aqueous battery. Figure 5-27b depicts the CV curves of the assembled FARB device under various scan rates in the operation voltage 0-1.6 V, which reveals two prominent redox peaks of the device. The low magnification SEM of the FARB was shown in Figure 5-28. It is easy to observe the smooth surface of the device wrapped with the KOH-PVA gel electrolyte.

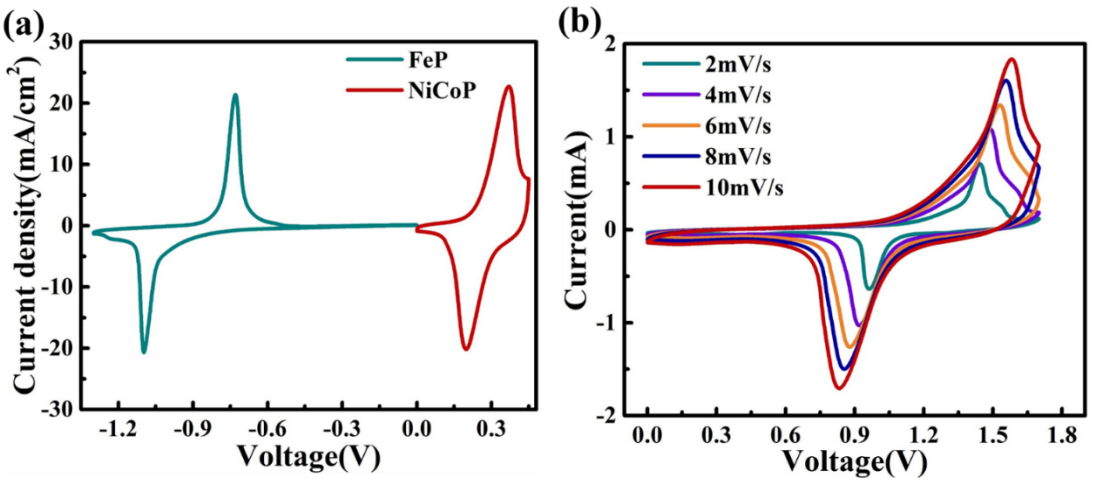

Figure 5-27 (a) CV curves of FeP/CNTFs and NiCoP/CNTFs at 4 mV/s. (b) CV curves of the FARB under various scan rates.

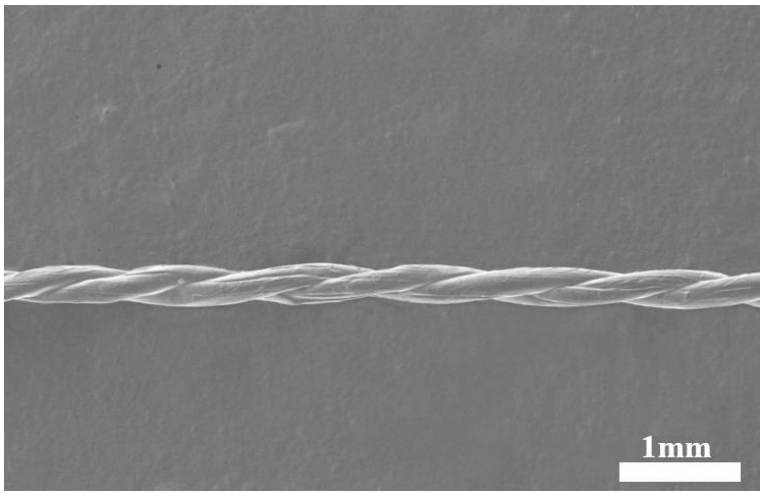

Figure 5-28 Low-magnification SEM image of the assembled fiber-shaped Ni-Fe battery device.

The GCD curve of the device is shown in Figure 5-29a, displaying characteristic charge and discharge platforms at 1.04 V and 0.94 V. More importantly, under current density of 2 mA/cm^2, our FARB achieves a high specific capacity of 0.294 mAh/cm^2 and a maximum volumetric energy density of the device is 39.484 mWh/cm^3 and the volumetric power density is 340 mW/cm^3, which greatly exceeds the previously reported fibrous energy storage devices as shown in Figure 5-29b. Moreover, our assembled Ni-

Fe battery compared with other related works have summarized in Table 5-1, which proves our device outperforms some reported batteries and devices.

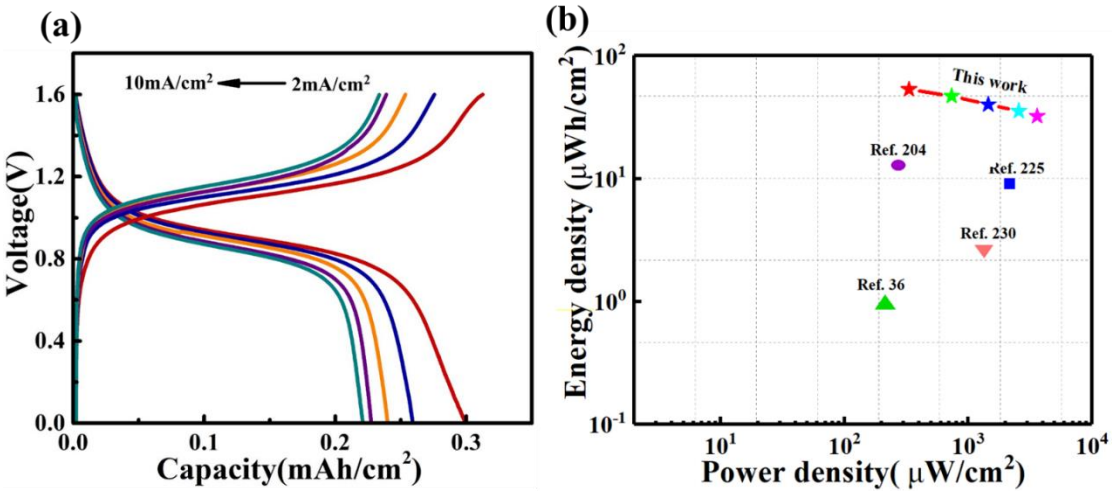

Figure 5-29 (a) GCD curves under various current densities. (b) Energy densities and power densities of the FARB comparison with previous fibrous energy storage devices.

The stability of our FARB after long cycles at 2 mA/cm^2 is further investigated and the result is shown in Figure 5-30a. The device has good stability and capacity retention is about 88% after 4000 cycles. . Bending test is carried out to demonstrate the possible usage of the assembled FARB in wearable and portable electronic devices, and the GCD curves of the FARB device are almost coincident under diverse bending angles from 0° to 180°, as shown in Figure 5-30b, illustrating the outstanding mechanical ductility of our FARB.

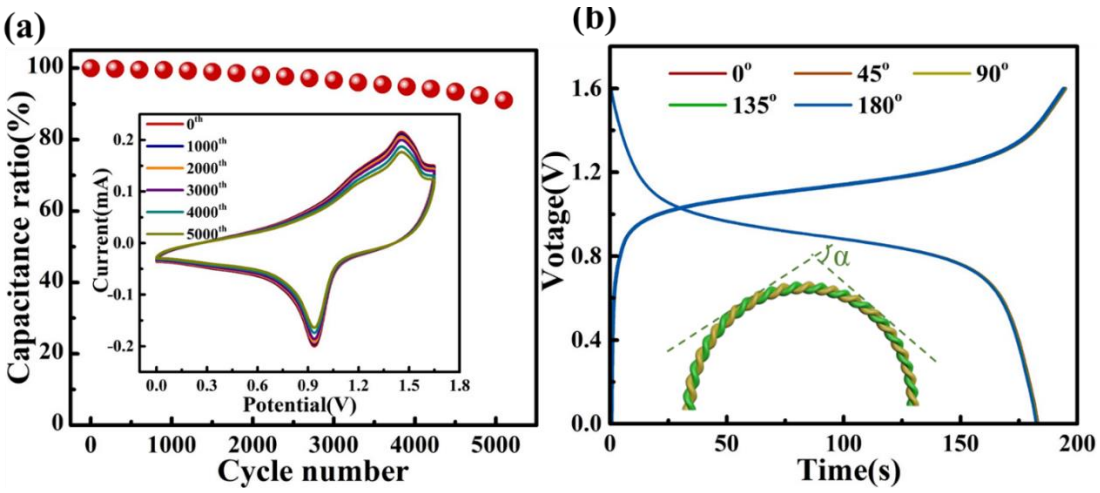

Figure 5-30 (a) Cyclic performance of the combined FARB. (The inset is the CV curves with diverse cyclic periods). (b) GCD curves of the assembled FARB being bent at different angles.

Table 5-1 Comparison of the electrochemical performances of our assembled Ni-Fe battery with other previously reported energy storage devices.

Number	Cathode	Anode	Energy density (mWh cm^{-3})	Power density (W cm^{-3})	Capacity retention (%)	Reference
1	NiO	Fe_3O_4	5.2	-	80.7	[204]
2	CoP@$Ni(OH)_2$	α-Fe_2O_3	30.5	-	85.3	[148]
3	NiZnCoP	α-Fe_2O_3	30.1	-	88.6	[120]
4	CNT	FeO-C	1.56	-	-	[104]
5	NiCo LDH	Zn	10.67	-	60	[185]

6	α-MnO_2	Fe_2O_3	0.55	-	84	[231]
7	NiO	ZnO	7.76	0.21	72.9	[108]
8	MnO_2	Fe_2O_3	0.22	0.165	-	[232]
9	TiO_2	Fe_2N	0.51	0.211	-	[233]
10	Ni@Ni	rGO	18.4	-	90.5	[234]
11	NiCoP	FeP	39.48	0.34	89	This work

The two batteries was connected in the series way to lighten the commercial red LED under normal and bend state shown in Figure 5-31. Meanwhile, the volumetric energy density, power density of assembled device and the excellent rate capability is also manifested in Figure 5-32a and Figure 5-32b respectively. The rate capability can maintain well as the current density increases higher. In addition, the linear relationship between the square root of scan rate and redox peak current under different scan rates and the relationship between log (peak current) and log (scan rate) are shown in Figure 5-33, which reveals that the redox reaction of the electrode material is a quasi-reversible and diffusion-controlled process.

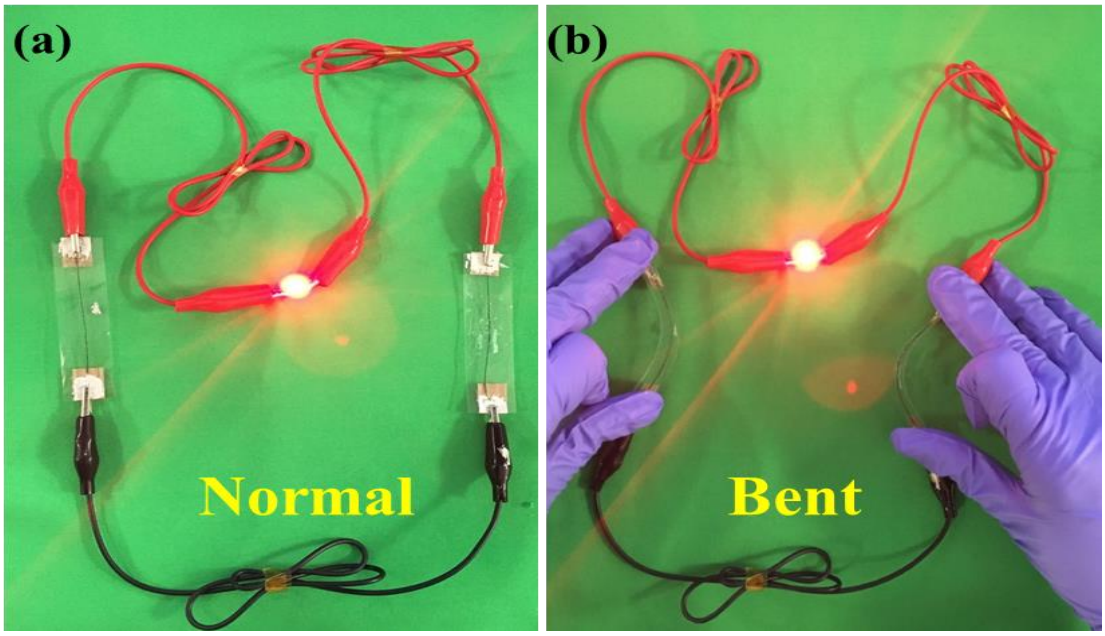

Figure 5-31 Photograph of two fiber-shaped Ni-Fe batteries connected in series to power a commercial red LED.

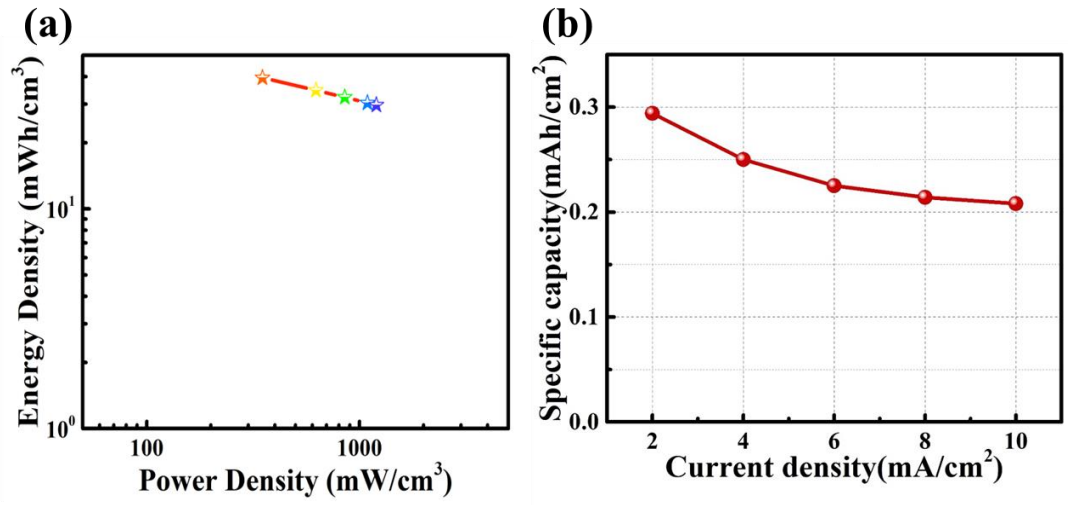

Figure 5-32 (a) The volumetric energy density and power density of the fiber-shaped Ni-Fe battery.

(b) Capacity of the fiber-shaped Ni-Fe battery as a function of current density.

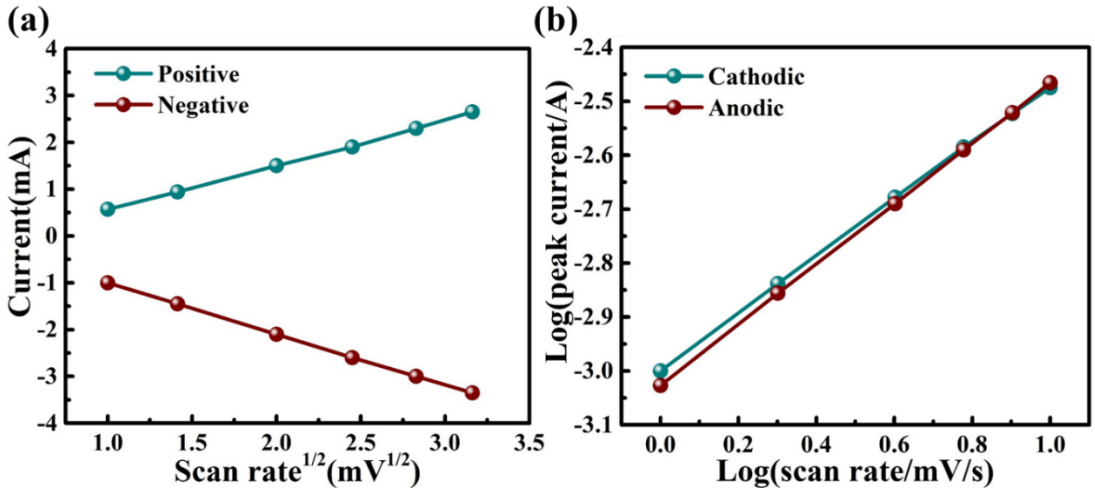

Figure 5-33 (a) Plots of the cathode and anode peak currents versus the square root of the scan rate for the fiber-shaped Ni-Fe battery. (b) Linear fitting of the peak current versus scan rate for the cathodic and anodic peaks.

5.4 Conclusion

In summary, a flexible and portable FARB is successfully fabricated using the synthesized NiCoP NSAs/CNTFs as the cathode and FeP NWAs/CNTFs as the anode with the PVA-KOH as the gel electrode. Nanostructured metal phosphides directly grown on the CNTFs have a larger electrochemically active surface and fast ion diffusion and electron transport channels, which in turn can increase electrode specific capacity and energy density. Our FARB has shown impressive electrochemical performance with the significant capacity of 0.294 mAh /cm^2 at 2 mA/cm^2 current density and an admirable energy density of 39.48 mW/cm^3. Moreover, after 4000 cycles our device can maintain 89% of initial capacity, which demonstrates excellent cycle stability. Apart from the excellent electrochemical stability, good mechanical flexibility is also realized in our FARB device with almost no capacity loss after bending for 3000 times. This work may expand the pathway to generate high-performance rechargeable aqueous batteries.

Chapter 6 Summary and Future Work

6.1 Summary

In this thesis, we integrate recent aqueous secondary Ni-Zn and Ni-Fe batteries, they take the advantages of the abundant constituent elements, low cost, and ultra-flat discharge plateau have attracted widespread attention. Moreover, with the ever-growing consumer usage of portable and wearable electronics, small, flexible and lightweight fiber-shaped batteries are regarded as promising energy supply devices. Therefore, the exploration of high-performance fibrous electrodes is still highly valuable and significant for the use in high-energy-density wearable batteries.

The first contribution is to develop the flexible high-performance Ni-Zn batteries. A facile and cost-effective method strategy is reported to fabricate three-dimensionally well-aligned ZNCO@$Ni(OH)_2$ NWAs on a carbon nanotube fiber CNTF as a promising heterostructure anode for fiber-shaped Ni-Zn batteries. Taking advantage of the accessible surface area, rich reaction sites and short electron/ion diffusion path of ZNCO@$Ni(OH)_2$ NWAs, a high capacity of 2.07 mAh/cm^2 (516.7 mAh/g) and an impressive energy density of 3.71 mWh/cm^2 (916.6 Wh/kg) were achieved for our as-assembled fiber-shaped Ni-Zn batteries, outperforming most previously reported aqueous Zn-based batteries.

The second contribution is to demonstrate the sulfur-doped Fe_2O_3 nanowire arrays grown on carbon nanotube fibers as an innovative anode material. Through the first-principle calculations to calculate that S-doping in Fe_2O_3 can dramatically reduce the bandgap from 2.34 eV to 1.18 eV and thus enhance electronic conductivity. The novel developed S- Fe_2O_3 NWAs/CNTF electrode is further demonstrated to deliver very high capacity of 0.81 mAh/cm^2 at 4 mA/cm^2. This value is almost 6-fold higher than of the pristine Fe_2O_3 NWAs/CNTF electrode. When a cathode containing ZNCO@$Ni(OH)_2$ NWAs heterostructures is used, 0.46 mAh/cm^2 capacity and 67.32 mWh/cm^3 energy density are

obtained for quasi-solid-state fiber-shaped NiCo-Fe batteries, which outperform most state-of-the-art fiber-shaped aqueous rechargeable batteries.

The third contribution is to construct a new type of high-performance flexible Ni-Fe battery with binder-free electrodes on conductive fiber substrates is successfully designed and fabricated. Hierarchical NiCoP nanosheet arrays and FeP nanowire arrays grown directly on carbon nanotube fibers are fabricated firstly using hydrothermal synthesis then pursuant gas phosphating process. With the assistance of PVA-KOH gel electrolyte, the fiber-shaped aqueous rechargeable battery presents negligible capacity loss after bending 3000 times and shows excellent stability with the capacity retention rate of 89% after 4000 cycles. Meanwhile, the assembled rechargeable battery has a significant capacity of 0.294 mAh/cm^2 under 2 mA/ cm^2 current density and a high volumetric energy density of 39.48 mWh/cm^3.

6.2 Perspectives

Despite the intensive efforts made for better development and the significant progress made so far, the electrochemical performances of iron-based anodes are still far below the satisfaction for industrial application. It is noteworthy that cation and anion co-doping in iron-based compounds is a promising approach to increase capacity and stabilize structure for next-generation iron-based anode materials.

Therefore, it is desirable to further understand the relationship between the type/amount of doping ions and crystal structures/electrochemical performance. Encouragingly, some early efforts have demonstrated that MOF-derived iron-based electrodes possesses large surface area and rich reaction sites, whose electrochemical performance can be further enhanced after phosphorization, sulfuration or selenidation processes. Particularly, amorphous frameworks can not only provide more exposed ion channels, accelerate rapid charge transfer across the electrode/electrolyte interface, and further facilitate fast ion intercalation, but also offer low internal energy and outstanding chemical stability.

Thus, it is critically important to explore innovative synthesis of amorphous iron-based anodes for next-generation alkaline aqueous batteries.

To date, the underlying energy storage mechanism of electrodes in aqueous Ni−Fe/Zn batteries are still uncertain. Advanced characterization methods, especially in situ characterization techniques (operando Raman, X-ray diffraction and high-resolution TEM imaging) can be helpful in understanding the transition of electrodes in electrochemical reaction processes. Simultaneously, theoretical calculations can be of very importance to understand the electrochemical reaction mechanism and can provide deeper insight. In addition, synthesis methods and procedures should be simplified in the premise of maximally maintaining the electrochemical performance, in a bid to open up possibilities for scalable preparation.

Publications

J. Yang, Q. Zhang, Z. Wang, Z. Wang, L. Kang, M. Qi, M. Chen, W. Liu, W. Gong, W. Lu, P. Shum, and L. Wei, Rational construction of self-standing sulphur-doped Fe_2O_3 anodes with promoted energy storage capability for wearable aqueous rechargeable NiCo-Fe batteries**,** ***Advanced Energy Materials***, (2020).

J. Yang, Z. Wang, Z. Wang, J. Zhang, Q. Zhang, P. Shum, and L. Wei, All metal phosphide electrodes for high-performance quasi-solid-state fiber-shaped aqueous rechargeable Ni-Fe batteries, ***ACS Applied Materials & Interfaces*** 12, 12801-12808 (2020).

J. Yang, J. Chen, Z. Wang, Z. Wang, Q. Zhang, B. He, T. Zhang, W. Gong, M. Chen, M. Qi, P. Coquet, P. Shum, and L. Wei, High-capacity Fe-based anodes for aqueous secondary nickel-iron batteries: recent progress and prospects, ChemElectroChem, 8, 274-290 (2021)

P. Man, Q. Zhang, Z. Zhou, M. Chen, **J. Yang**, Z. Wang, Z. Wang, B. He, Q. Li, W. Gong, W. Lu, Y. Yao, and L. Wei, Engineering MoS_2 nanosheets on spindle-like α-Fe_2O_3 as high-performance core-shell pseudocapacitive anodes for fiber-shaped aqueous lithium-ion capacitors, ***Advanced Functional Materials***, (2020).

Q. Zhang, P. Man, B. He, C. Li, Q. Li, Z. Pan, Z. Wang, **J. Yang**, Z. Wang, Z. Zhou, X. Lu, Z. Niu, Y. Yao, and L. Wei, Binder-free $NaTi_2(PO_4)_3$ anodes for high-performance coaxial-fiber aqueous rechargeable sodium-ion batteries, ***Nano Energy*** 67, 104212 (2020).

Z. Wang, T. Wu, Z. Wang, T. Zhang, M. Chen, J. Zhang, L. Liu, M. Qi, Q. Zhang, **J. Yang**, W. Liu, H. Chen, Y. Luo, and L. Wei, Designer patterned functional fibers via direct imprinting in thermal drawing, ***Nature Communications,*** (2020).

Q. Zhang, C. Li, Q. Li, Z. Pan, J. Sun, Z. Zhou, B. He, P. Man, L. Xie, L. Kang, X. Wang, **J. Yang,** T. Zhang, P. Shum, Q. Li, Y. Yao, and L. Wei, Flexible and high-voltage coaxial-fiber aqueous rechargeable zinc-ion battery, ***Nano Letters*** 19, 4035-4042 (2019).

References

1. Statistical Review of World Energy. (https://www.bp.com/en/global/corporate/energy-economics/statistical-review-of-world-energy.html, 2020)
2. K. Nagy, K. Körmendi, Use of renewable energy sources in light of the "New Energy Strategy for Europe 2011–2020". Applied Energy **96**, 393-399 (2012).
3. R. M. Dutra, A. S. Szklo, Incentive policies for promoting wind power production in Brazil: Scenarios for the Alternative Energy Sources Incentive Program (PROINFA) under the New Brazilian electric power sector regulation. Renewable Energy **33**, 65-76 (2008).
4. H. Bevrani, A. Ghosh, G. Ledwich, Renewable energy sources and frequency regulation: survey and new perspectives. IET Renewable Power Generation **4**, 438-457 (2010).
5. H. Chen, T. N. Cong, W. Yang, C. Tan, Y. Li, Y. Ding, Progress in electrical energy storage system: A critical review. Progress in natural science **19**, 291-312 (2009).
6. J. Liu, Addressing the grand challenges in energy storage. Advanced Functional Materials **23**, 924-928 (2013).
7. X. Luo, J. Wang, M. Dooner, J. Clarke, Overview of current development in electrical energy storage technologies and the application potential in power system operation. Applied energy **137**, 511-536 (2015).
8. B. Dunn, H. Kamath, J.-M. Tarascon, Electrical energy storage for the grid: a battery of choices. Science **334**, 928-935 (2011).
9. Y. Gogotsi, P. Simon, True performance metrics in electrochemical energy storage. Science **334**, 917-918 (2011).
10. M. Armand, J. Tarascon, Building better batteries. Nature, 451. (2008).
11. G. Wang, L. Zhang, J. Zhang, A review of electrode materials for electrochemical supercapacitors. Chemical Society Reviews **41**, 797-828 (2012).
12. A. Z. Weber, M. M. Mench, J. P. Meyers, P. N. Ross, J. T. Gostick, Q. Liu, Redox flow batteries: a review. Journal of applied electrochemistry **41**, 1137 (2011).
13. A. S. Arico, P. Bruce, B. Scrosati, J.-M. Tarascon, W. Van Schalkwijk, in Materials for sustainable energy: a collection of peer-reviewed research and review articles from Nature Publishing Group. (World Scientific, 2011), pp. 148-159.

14. P. Simon, Y. Gogotsi, in Nanoscience and technology: a collection of reviews from Nature journals. (World Scientific, 2010), pp. 320-329.
15. P. Azaïs, L. Duclaux, P. Florian, D. Massiot, M.-A. Lillo-Rodenas, A. Linares-Solano, J.-P. Peres, C. Jehoulet, F. Béguin, Causes of supercapacitors ageing in organic electrolyte. Journal of power sources **171**, 1046-1053 (2007).
16. J. Gamby, P. Taberna, P. Simon, J. Fauvarque, M. Chesneau, Studies and characterisations of various activated carbons used for carbon/carbon supercapacitors. Journal of power sources **101**, 109-116 (2001).
17. A. G. Pandolfo, A. F. Hollenkamp, Carbon properties and their role in supercapacitors. Journal of power sources **157**, 11-27 (2006).
18. R. Kötz, M. Carlen, Principles and applications of electrochemical capacitors. Electrochimica acta **45**, 2483-2498 (2000).
19. F. Wang, X. Wu, X. Yuan, Z. Liu, Y. Zhang, L. Fu, Y. Zhu, Q. Zhou, Y. Wu, W. Huang, Latest advances in supercapacitors: from new electrode materials to novel device designs. Chemical Society Reviews **46**, 6816-6854 (2017).
20. M. Skyllas-Kazacos, M. Rychcik, R. G. Robins, A. Fane, M. Green, New all-vanadium redox flow cell. JElS **133**, 1057 (1986).
21. L. Li, S. Kim, W. Wang, M. Vijayakumar, Z. Nie, B. Chen, J. Zhang, G. Xia, J. Hu, G. Graff, A stable vanadium redox-flow battery with high energy density for large-scale energy storage. Advanced Energy Materials **1**, 394-400 (2011).
22. W. Wang, Q. Luo, B. Li, X. Wei, L. Li, Z. Yang, Recent progress in redox flow battery research and development. Advanced Functional Materials **23**, 970-986 (2013).
23. M. Skyllas-Kazacos, C. Menictas, M. Kazacos, Thermal stability of concentrated V (V) electrolytes in the vanadium redox cell. Journal of the Electrochemical Society **143**, L86 (1996).
24. S. Eckroad, Vanadium redox flow batteries: an in-depth analysis. Electric Power Research Institute, Palo Alto, CA **1014836**, (2007).
25. F. Rahman, M. Skyllas-Kazacos, Vanadium redox battery: Positive half-cell electrolyte studies. Journal of Power Sources **189**, 1212-1219 (2009).
26. M. Vijayakumar, L. Li, G. Graff, J. Liu, H. Zhang, Z. Yang, J. Z. Hu, Towards understanding the poor thermal stability of V5+ electrolyte solution in vanadium redox flow batteries. Journal of Power Sources **196**, 3669-3672 (2011).
27. S. Kim, J. Yan, B. Schwenzer, J. Zhang, L. Li, J. Liu, Z. G. Yang, M. A. Hickner, Cycling performance and efficiency of sulfonated poly (sulfone) membranes in

vanadium redox flow batteries. Electrochemistry Communications **12**, 1650-1653 (2010).

28. M. Duduta, B. Ho, V. C. Wood, P. Limthongkul, V. E. Brunini, W. C. Carter, Y. M. Chiang, Semi-Solid lithium rechargeable flow battery. Advanced Energy Materials **1**, 511-516 (2011).
29. M. Skyllas-Kazacos, M. Chakrabarti, S. Hajimolana, F. Mjalli, M. Saleem, Progress in flow battery research and development. Journal of the electrochemical society **158**, R55 (2011).
30. M. R. Palacin, Recent advances in rechargeable battery materials: a chemist's perspective. Chemical Society Reviews **38**, 2565-2575 (2009).
31. J. B. Goodenough, K.-S. Park, The Li-ion rechargeable battery: a perspective. Journal of the American Chemical Society **135**, 1167-1176 (2013).
32. H. Cha, J. Kim, Y. Lee, J. Cho, M. Park, Issues and Challenges Facing Flexible Lithium-Ion Batteries for Practical Application. Small **14**, 1702989 (2018).
33. G. Qian, X. Liao, Y. Zhu, F. Pan, X. Chen, Y. Yang, Designing flexible lithium-ion batteries by structural engineering. ACS Energy Letters **4**, 690-701 (2019).
34. Z. Liu, H. Li, M. Zhu, Y. Huang, Z. Tang, Z. Pei, Z. Wang, Z. Shi, J. Liu, Y. Huang, Towards wearable electronic devices: A quasi-solid-state aqueous lithium-ion battery with outstanding stability, flexibility, safety and breathability. Nano Energy **44**, 164-173 (2018).
35. G. Fang, J. Zhou, A. Pan, S. Liang, Recent advances in aqueous zinc-ion batteries. ACS Energy Letters **3**, 2480-2501 (2018).
36. Q. Zhang, C. Li, Q. Li, Z. Pan, J. Sun, Z. Zhou, B. He, P. Man, L. Xie, L. Kang, Flexible and high-voltage coaxial-fiber aqueous rechargeable zinc-ion battery. Nano letters **19**, 4035-4042 (2019).
37. Q. Zhang, P. Man, B. He, C. Li, Q. Li, Z. Pan, Z. Wang, J. Yang, Z. Wang, Z. Zhou, Binder-free NaTi2 (PO4) 3 anodes for high-performance coaxial-fiber aqueous rechargeable sodium-ion batteries. Nano Energy **67**, 104212 (2020).
38. K. T. Nam, D.-W. Kim, P. J. Yoo, C.-Y. Chiang, N. Meethong, P. T. Hammond, Y.-M. Chiang, A. M. Belcher, Virus-enabled synthesis and assembly of nanowires for lithium ion battery electrodes. science **312**, 885-888 (2006).
39. D. U. Sauer, H. Wenzl, Comparison of different approaches for lifetime prediction of electrochemical systems—Using lead-acid batteries as example. Journal of Power sources **176**, 534-546 (2008).

40. M. Manickam, P. Singh, T. B. Issa, S. Thurgate, R. De Marco, Lithium insertion into manganese dioxide electrode in MnO2/Zn aqueous battery: Part I. A preliminary study. Journal of Power Sources **130**, 254-259 (2004).
41. H. Manjunatha, G. Suresh, T. Venkatesha, Electrode materials for aqueous rechargeable lithium batteries. Journal of Solid State Electrochemistry **15**, 431-445 (2011).
42. R. Ma, J. Liang, K. Takada, T. Sasaki, Topochemical synthesis of Co− Fe layered double hydroxides at varied Fe/Co ratios: unique intercalation of triiodide and its profound effect. Journal of the American chemical society **133**, 613-620 (2011).
43. J. Liu, M. Chen, L. Zhang, J. Jiang, J. Yan, Y. Huang, J. Lin, H. J. Fan, Z. X. Shen, A flexible alkaline rechargeable Ni/Fe battery based on graphene foam/carbon nanotubes hybrid film. Nano letters **14**, 7180-7187 (2014).
44. C. Vincent, B. Scrosati, *Modern batteries*. (Elsevier, 1997).
45. H. Bode, Lead-acid batteries. (1977).
46. C. Caldas, M. Lopes, I. Carlos, The role of FeS and (NH4) 2CO3 additives on the pressed type Fe electrode. Journal of power sources **74**, 108-112 (1998).
47. H. Wang, Y. Liang, M. Gong, Y. Li, W. Chang, T. Mefford, J. Zhou, J. Wang, T. Regier, F. Wei, An ultrafast nickel–iron battery from strongly coupled inorganic nanoparticle/nanocarbon hybrid materials. Nature communications **3**, 1-8 (2012).
48. D. Fan, R. E. White, A Mathematical Model of a Sealed Nickel-Cadmium Battery. Journal of the Electrochemical Society **138**, 17 (1991).
49. S. Ovshinsky, M. Fetcenko, J. Ross, A nickel metal hydride battery for electric vehicles. Science **260**, 176-181 (1993).
50. F. S. Cai, G. Y. Zhang, J. Chen, X. L. Gou, H. K. Liu, S. X. Dou, Ni (OH) 2 tubes with mesoscale dimensions as positive-electrode materials of alkaline rechargeable batteries. Angewandte Chemie **116**, 4308-4312 (2004).
51. G. Fu, K. Chang, E. Shangguan, H. Tang, B. Li, Z. Chang, X.-Z. Yuan, H. Wang, Synthesis of CoO/reduced graphene oxide composite as an alternative additive for the nickel electrode in alkaline secondary batteries. Electrochimica Acta **180**, 373-381 (2015).
52. Wikipedia, *Electric battery*. (The Free Encyclopedia, 2020)
53. J. McBreen, Nickel/zinc batteries. Journal of power sources **51**, 37-44 (1994).
54. J. McBreen, Rechargeable zinc batteries. Journal of Electroanalytical Chemistry and Interfacial Electrochemistry **168**, 415-432 (1984).
55. C. Spanos, D. E. Turney, V. Fthenakis, Life-cycle analysis of flow-assisted nickel zinc-, manganese dioxide-, and valve-regulated lead-acid batteries designed for

demand-charge reduction. Renewable and Sustainable Energy Reviews **43**, 478-494 (2015).

56. A. P. Pavlov, L. K. Grigorieva, S. P. Chizhik, V. K. Stankov, Nickel-zinc batteries with long cycle life. Journal of power sources **62**, 113-116 (1996).
57. A. L. Zhu, D. P. Wilkinson, X. Zhang, Y. Xing, A. G. Rozhin, S. A. Kulinich, Zinc regeneration in rechargeable zinc-air fuel cells—A review. Journal of Energy Storage **8**, 35-50 (2016).
58. J. Shin, J. Lee, Y. Park, J. W. Choi, Aqueous zinc ion batteries: focus on zinc metal anodes. Chemical Science **11**, 2028-2044 (2020).
59. K. Wang, P. Pei, Z. Ma, H. Chen, H. Xu, D. Chen, X. Wang, Dendrite growth in the recharging process of zinc–air batteries. Journal of Materials Chemistry A **3**, 22648-22655 (2015).
60. J. Fu, Z. P. Cano, M. G. Park, A. Yu, M. Fowler, Z. Chen, Electrically rechargeable zinc–air batteries: progress, challenges, and perspectives. Advanced materials **29**, 1604685 (2017).
61. A. R. Mainar, E. Iruin, L. C. Colmenares, A. Kvasha, I. De Meatza, M. Bengoechea, O. Leonet, I. Boyano, Z. Zhang, J. A. Blazquez, An overview of progress in electrolytes for secondary zinc-air batteries and other storage systems based on zinc. Journal of Energy Storage **15**, 304-328 (2018).
62. Z. Kang, C. Wu, L. Dong, W. Liu, J. Mou, J. Zhang, Z. Chang, B. Jiang, G. Wang, F. Kang, 3D porous copper skeleton supported zinc anode toward high capacity and long cycle life zinc ion batteries. ACS Sustainable Chemistry & Engineering **7**, 3364-3371 (2019).
63. J. F. Parker, C. N. Chervin, I. R. Pala, M. Machler, M. F. Burz, J. W. Long, D. R. Rolison, Rechargeable nickel–3D zinc batteries: An energy-dense, safer alternative to lithium-ion. Science **356**, 415-418 (2017).
64. L. Kang, M. Cui, F. Jiang, Y. Gao, H. Luo, J. Liu, W. Liang, C. Zhi, Nanoporous CaCO3 coatings enabled uniform Zn stripping/plating for long-life zinc rechargeable aqueous batteries. Advanced Energy Materials **8**, 1801090 (2018).
65. K. Zhao, C. Wang, Y. Yu, M. Yan, Q. Wei, P. He, Y. Dong, Z. Zhang, X. Wang, L. Mai, Ultrathin surface coating enables stabilized zinc metal anode. Advanced Materials Interfaces **5**, 1800848 (2018).
66. Z. Zhao, J. Zhao, Z. Hu, J. Li, J. Li, Y. Zhang, C. Wang, G. Cui, Long-life and deeply rechargeable aqueous Zn anodes enabled by a multifunctional brightener-inspired interphase. Energy & Environmental Science **12**, 1938-1949 (2019).

67. M. Xiao, Y. Tian, Y. Yan, K. Feng, Y. Miao, Electrodeposition of Ni (OH) 2/NiOOH in the presence of urea for the improved oxygen evolution. Electrochimica Acta **164**, 196-202 (2015).
68. E. Shangguan, J. Li, D. Guo, L. Guo, M. Nie, Z. Chang, X.-Z. Yuan, H. Wang, A comparative study of structural and electrochemical properties of high-density aluminum substituted α-nickel hydroxide containing different interlayer anions. Journal of Power Sources **282**, 158-168 (2015).
69. Z. Zhang, Y. Zhu, J. Bao, X. Lin, H. Zheng, Electrochemical performance of multi-element doped α-nickel hydroxide prepared by supersonic co-precipitation method. Journal of Alloys and Compounds **509**, 7034-7037 (2011).
70. A. Van der Ven, D. Morgan, Y. Meng, G. Ceder, Phase stability of nickel hydroxides and oxyhydroxides. Journal of The Electrochemical Society **153**, A210 (2005).
71. T. Maca, J. Vondrák, M. Sedlaříková, Incorporation of multielement doping into LDH structure of alpha nickel hydroxide. ECS Transactions **40**, 119 (2012).
72. X. Kong, J. Zhao, W. Shi, Y. Zhao, M. Shao, M. Wei, L. Wang, X. Duan, Fabrication of aluminum-doped α-Ni (OH) 2 with hierarchical architecture and its largely enhanced electrocatalytic performance. Electrochimica acta **80**, 257-263 (2012).
73. J. W. Lee, J. M. Ko, J.-D. Kim, Hierarchical microspheres based on α-Ni (OH) 2 nanosheets intercalated with different anions: synthesis, anion exchange, and effect of intercalated anions on electrochemical capacitance. The Journal of Physical Chemistry C **115**, 19445-19454 (2011).
74. H. Li, J. Ma, D. G. Evans, T. Zhou, F. Li, X. Duan, Molecular dynamics modeling of the structures and binding energies of α-nickel hydroxides and nickel− aluminum layered double hydroxides containing various interlayer guest anions. Chemistry of Materials **18**, 4405-4414 (2006).
75. V. Gupta, S. Gupta, N. Miura, Potentiostatically deposited nanostructured CoxNi1− x layered double hydroxides as electrode materials for redox-supercapacitors. Journal of Power Sources **175**, 680-685 (2008).
76. Y. Wang, D. Zhang, W. Peng, L. Liu, M. Li, Electrocatalytic oxidation of methanol at Ni–Al layered double hydroxide film modified electrode in alkaline medium. Electrochimica Acta **56**, 5754-5758 (2011).
77. J. Tronto, A. C. Bordonal, Z. Naal, J. B. Valim, Conducting polymers/layered double hydroxides intercalated nanocomposites. Materials Science-Advanced Topics, 3-30 (2013).

78. J. Hu, G. Lei, Z. Lu, K. Liu, S. Sang, H. Liu, Alternating assembly of Ni–Al layered double hydroxide and graphene for high-rate alkaline battery cathode. Chemical Communications **51**, 9983-9986 (2015).
79. Y. Zhao, X. Jia, G. Chen, L. Shang, G. I. Waterhouse, L.-Z. Wu, C.-H. Tung, D. O'Hare, T. Zhang, Ultrafine NiO nanosheets stabilized by TiO2 from monolayer NiTi-LDH precursors: an active water oxidation electrocatalyst. Journal of the American Chemical Society **138**, 6517-6524 (2016).
80. J.-T. Ren, G.-G. Yuan, C.-C. Weng, L. Chen, Z.-Y. Yuan, Uniquely integrated Fe-doped Ni (OH) 2 nanosheets for highly efficient oxygen and hydrogen evolution reactions. Nanoscale **10**, 10620-10628 (2018).
81. T. B. Reddy, *Linden's handbook of batteries*. (Mcgraw-hill New York, 2011), vol. 4.
82. Z. Jin, P. Li, Y. Jin, D. Xiao, Superficial-defect engineered nickel/iron oxide nanocrystals enable high-efficient flexible fiber battery. Energy Storage Materials **13**, 160-167 (2018).
83. W. Qiu, H. Xiao, W. He, Y. Li, Y. Tong, A flexible rechargeable quasi-solid-state Ni–Fe battery based on surface engineering exhibits high energy and long durability. Inorganic Chemistry Frontiers **5**, 1805-1815 (2018).
84. Y. Wang, Z. Chen, T. Lei, Y. Ai, Z. Peng, X. Yan, H. Li, J. Zhang, Z. M. Wang, Y. L. Chueh, Hollow NiCo2S4 Nanospheres Hybridized with 3D Hierarchical Porous rGO/Fe2O3 Composites toward High-Performance Energy Storage Device. Advanced Energy Materials **8**, 1703453 (2018).
85. D. Li, X. Li, X. Hou, X. Sun, B. Liu, D. He, Building a Ni 3 S 2 nanotube array and investigating its application as an electrode for lithium ion batteries. Chemical Communications **50**, 9361-9364 (2014).
86. X. Miao, R. Yin, X. Ge, Z. Li, L. Yin, Ni2P@ carbon core–shell nanoparticle-arched 3D interconnected graphene aerogel architectures as anodes for high-performance sodium-ion batteries. Small **13**, 1702138 (2017).
87. L. Yan, H. Jiang, Y. Xing, Y. Wang, D. Liu, X. Gu, P. Dai, L. Li, X. Zhao, Nickel metal–organic framework implanted on graphene and incubated to be ultrasmall nickel phosphide nanocrystals acts as a highly efficient water splitting electrocatalyst. Journal of Materials Chemistry A **6**, 1682-1691 (2018).
88. U. Köhler, C. Antonius, P. Bäuerlein, Advances in alkaline batteries. Journal of Power Sources **127**, 45-52 (2004).
89. X.-P. Gao, H.-X. Yang, Multi-electron reaction materials for high energy density batteries. Energy & Environmental Science **3**, 174-189 (2010).

90. X. Wu, H. B. Wu, W. Xiong, Z. Le, F. Sun, F. Liu, J. Chen, Z. Zhu, Y. Lu, Robust iron nanoparticles with graphitic shells for high-performance Ni-Fe battery. Nano Energy **30**, 217-224 (2016).
91. C. Chan, E. Lo, S. Weixiang, The available capacity computation model based on artificial neural network for lead–acid batteries in electric vehicles. Journal of power sources **87**, 201-204 (2000).
92. F. Mulder, B. Weninger, J. Middelkoop, F. Ooms, H. Schreuders, Efficient electricity storage with a battolyser, an integrated Ni–Fe battery and electrolyser. Energy & Environmental Science **10**, 756-764 (2017).
93. S. Narayanan, G. S. Prakash, A. Manohar, B. Yang, S. Malkhandi, A. Kindler, Materials challenges and technical approaches for realizing inexpensive and robust iron–air batteries for large-scale energy storage. Solid State Ionics **216**, 105-109 (2012).
94. W. Jiang, F. Liang, J. Wang, L. Su, Y. Wu, L. Wang, Enhanced electrochemical performances of FeO x–graphene nanocomposites as anode materials for alkaline nickel–iron batteries. RSC Advances **4**, 15394-15399 (2014).
95. J. Lin, A. R. O. Raji, K. Nan, Z. Peng, Z. Yan, E. L. Samuel, D. Natelson, J. M. Tour, Iron oxide nanoparticle and graphene nanoribbon composite as an anode material for high-performance Li-ion batteries. Advanced Functional Materials **24**, 2044-2048 (2014).
96. H. Quan, B. Cheng, Y. Xiao, S. Lei, One-pot synthesis of α-Fe2O3 nanoplates-reduced graphene oxide composites for supercapacitor application. Chemical Engineering Journal **286**, 165-173 (2016).
97. M. Aadil, W. Shaheen, M. F. Warsi, M. Shahid, M. A. Khan, Z. Ali, S. Haider, I. Shakir, Superior electrochemical activity of α-Fe2O3/rGO nanocomposite for advance energy storage devices. Journal of Alloys and Compounds **689**, 648-654 (2016).
98. Y. Gao, D. Wu, T. Wang, D. Jia, W. Xia, Y. Lv, Y. Cao, Y. Tan, P. Liu, One-step solvothermal synthesis of quasi-hexagonal Fe2O3 nanoplates/graphene composite as high performance electrode material for supercapacitor. Electrochimica Acta **191**, 275-283 (2016).
99. G. Zhang, J. Li, J. Sha, C. He, E. Liu, N. Zhao, C. Shi, Preparation of Fe3O4/rebar graphene composite via solvothermal route as binder free anode for lithium ion batteries. Journal of Alloys and Compounds **661**, 448-454 (2016).
100. B. Qiu, Q. Li, B. Shen, M. Xing, J. Zhang, Stöber-like method to synthesize ultradispersed Fe3O4 nanoparticles on graphene with excellent Photo-Fenton

reaction and high-performance lithium storage. Applied Catalysis B: Environmental **183**, 216-223 (2016).

101. P. Zhao, W. Li, G. Wang, B. Yu, X. Li, J. Bai, Z. Ren, Facile hydrothermal fabrication of nitrogen-doped graphene/Fe2O3 composites as high performance electrode materials for supercapacitor. Journal of alloys and compounds **604**, 87-93 (2014).
102. A. K. Manohar, S. Malkhandi, B. Yang, C. Yang, G. S. Prakash, S. Narayanan, A high-performance rechargeable iron electrode for large-scale battery-based energy storage. Journal of The Electrochemical Society **159**, A1209 (2012).
103. C.-Y. Kao, Y.-R. Tsai, K.-S. Chou, Synthesis and characterization of the iron/copper composite as an electrode material for the rechargeable alkaline battery. Journal of Power Sources **196**, 5746-5750 (2011).
104. R. Li, Y. Wang, C. Zhou, C. Wang, X. Ba, Y. Li, X. Huang, J. Liu, Carbon-stabilized high-capacity ferroferric oxide nanorod array for flexible solid-state alkaline battery–supercapacitor hybrid device with high environmental suitability. Advanced Functional Materials **25**, 5384-5394 (2015).
105. W. Chen, G. Li, A. Pei, Y. Li, L. Liao, H. Wang, J. Wan, Z. Liang, G. Chen, H. Zhang, A manganese–hydrogen battery with potential for grid-scale energy storage. Nature Energy **3**, 428-435 (2018).
106. Y. Huang, J. Liu, J. Wang, M. Hu, F. Mo, G. Liang, C. Zhi, An Intrinsically Self-Healing NiCo‖ Zn Rechargeable Battery with a Self-Healable Ferric-Ion-Crosslinking Sodium Polyacrylate Hydrogel Electrolyte. Angewandte Chemie International Edition **57**, 9810-9813 (2018).
107. C. Liu, X. Wang, W. Deng, C. Li, J. Chen, M. Xue, R. Li, F. Pan, Engineering Fast Ion Conduction and Selective Cation Channels for a High-Rate and High-Voltage Hybrid Aqueous Battery. Angewandte Chemie **130**, 7164-7168 (2018).
108. J. Liu, C. Guan, C. Zhou, Z. Fan, Q. Ke, G. Zhang, C. Liu, J. Wang, A flexible quasi-solid-state nickel–zinc battery with high energy and power densities based on 3D electrode design. Advanced materials **28**, 8732-8739 (2016).
109. C. Liu, Z. Neale, J. Zheng, X. Jia, J. Huang, M. Yan, M. Tian, M. Wang, J. Yang, G. Cao, Expanded hydrated vanadate for high-performance aqueous zinc-ion batteries. Energy & Environmental Science **12**, 2273-2285 (2019).
110. M. Gu, W.-J. Song, J. Hong, S. Y. Kim, T. J. Shin, N. A. Kotov, S. Park, B.-S. Kim, Stretchable batteries with gradient multilayer conductors. Science advances **5**, eaaw1879 (2019).

111. Y. Zeng, Y. Meng, Z. Lai, X. Zhang, M. Yu, P. Fang, M. Wu, Y. Tong, X. Lu, An ultrastable and high-performance flexible fiber-shaped Ni–Zn battery based on a Ni–NiO heterostructured nanosheet cathode. Advanced Materials **29**, 1702698 (2017).
112. P. Hu, T. Wang, J. Zhao, C. Zhang, J. Ma, H. Du, X. Wang, G. Cui, Ultrafast alkaline Ni/Zn battery based on Ni-foam-supported Ni3S2 nanosheets. ACS applied materials & interfaces **7**, 26396-26399 (2015).
113. Q. Chen, J. Li, C. Liao, G. Hu, Y. Fu, O. K. Asare, S. Shi, Z. Liu, L. Zhou, L. Mai, Ni foam supported NiO nanosheets as high-performance free-standing electrodes for hybrid supercapacitors and Ni–Zn batteries. Journal of Materials Chemistry A **6**, 19488-19494 (2018).
114. H. Chen, Z. Shen, Z. Pan, Z. Kou, X. Liu, H. Zhang, Q. Gu, C. Guan, J. Wang, Hierarchical Micro-Nano Sheet Arrays of Nickel–Cobalt Double Hydroxides for High-Rate Ni–Zn Batteries. Advanced Science **6**, 1802002 (2019).
115. S.-B. Lai, M.-I. Jamesh, X.-C. Wu, Y.-L. Dong, J.-H. Wang, M. Gao, J.-F. Liu, X.-M. Sun, A promising energy storage system: rechargeable Ni–Zn battery. Rare Metals **36**, 381-396 (2017).
116. P. Man, B. He, Q. Zhang, Z. Zhou, C. Li, Q. Li, L. Wei, Y. Yao, A one-dimensional channel self-standing MOF cathode for ultrahigh-energy-density flexible Ni–Zn batteries. Journal of Materials Chemistry A **7**, 27217-27224 (2019).
117. P. Li, Z. Jin, D. Xiao, Three-dimensional nanotube-array anode enables a flexible Ni/Zn fibrous battery to ultrafast charge and discharge in seconds. Energy Storage Materials **12**, 232-240 (2018).
118. M. Li, J. Meng, Q. Li, M. Huang, X. Liu, K. A. Owusu, Z. Liu, L. Mai, Finely Crafted 3D Electrodes for Dendrite-Free and High-Performance Flexible Fiber-Shaped Zn–Co Batteries. Advanced Functional Materials **28**, 1802016 (2018).
119. K. Wang, X. Zhang, J. Han, X. Zhang, X. Sun, C. Li, W. Liu, Q. Li, Y. Ma, High-performance cable-type flexible rechargeable Zn battery based on MnO2@ CNT fiber microelectrode. ACS applied materials & interfaces **10**, 24573-24582 (2018).
120. Q. Zhang, Z. Zhou, Z. Pan, J. Sun, B. He, Q. Li, T. Zhang, J. Zhao, L. Tang, Z. Zhang, All-Metal-Organic Framework-Derived Battery Materials on Carbon Nanotube Fibers for Wearable Energy-Storage Device. Advanced Science **5**, 1801462 (2018).

121. M. Gong, Y. Li, H. Zhang, B. Zhang, W. Zhou, J. Feng, H. Wang, Y. Liang, Z. Fan, J. Liu, Ultrafast high-capacity NiZn battery with NiAlCo-layered double hydroxide. Energy & Environmental Science **7**, 2025-2032 (2014).
122. H. Zhang, R. Wang, D. Lin, Y. Zeng, X. Lu, Ni-based Nanostructures as High-performance Cathodes for Rechargeable Ni− Zn Battery. ChemNanoMat **4**, 525-536 (2018).
123. Y. Zhu, J. Cui, S. An, Z. Li, Y. Zhang, W. He, Facile preparation of sulfur/nitrogen co-doped graphene coupled with Ni (OH) 2 for battery-type electrode with superior electrochemical performance. Journal of Alloys and Compounds **810**, 151932 (2019).
124. J. Pu, Y. Tong, S. Wang, E. Sheng, Z. Wang, Nickel–cobalt hydroxide nanosheets arrays on Ni foam for pseudocapacitor applications. Journal of Power Sources **250**, 250-256 (2014).
125. H. Zhang, X. Zhang, H. Li, Y. Zhang, Y. Zeng, Y. Tong, P. Zhang, X. Lu, Flexible rechargeable Ni//Zn battery based on self-supported NiCo2O4 nanosheets with high power density and good cycling stability. Green Energy & Environment **3**, 56-62 (2018).
126. L. Zhou, X. Zhang, D. Zheng, W. Xu, J. Liu, X. Lu, Ni 3 S 2@ PANI core–shell nanosheets as a durable and high-energy binder-free cathode for aqueous rechargeable nickel–zinc batteries. Journal of Materials Chemistry A **7**, 10629-10635 (2019).
127. Y. Zeng, Z. Lai, Y. Han, H. Zhang, S. Xie, X. Lu, Oxygen-Vacancy and Surface Modulation of Ultrathin Nickel Cobaltite Nanosheets as a High-Energy Cathode for Advanced Zn-Ion Batteries. Advanced Materials **30**, 1802396 (2018).
128. C. Zhang, Y. Huang, S. Tang, M. Deng, Y. Du, High-energy all-solid-state symmetric supercapacitor based on Ni3S2 mesoporous nanosheet-decorated three-dimensional reduced graphene oxide. ACS Energy Letters **2**, 759-768 (2017).
129. P. Wang, C. Li, S. Dong, X. Ge, P. Zhang, X. Miao, R. Wang, Z. Zhang, L. Yin, Hierarchical NiCo2S4@ NiO Core–Shell Heterostructures as Catalytic Cathode for Long-Life Li-O2 Batteries. Advanced Energy Materials **9**, 1900788 (2019).
130. Z. Ma, F. Jing, Y. Fan, L. Hou, L. Su, L. Fan, G. Shao, High-Stability MnOx Nanowires@ C@ MnOx Nanosheet Core–Shell Heterostructure Pseudocapacitance Electrode Based on Reversible Phase Transition Mechanism. Small **15**, 1900862 (2019).

131. M. Wang, Y. Song, Z. Sun, Y. Shao, C. Wei, Z. Xia, Z. Tian, Z. Liu, J. Sun, Conductive and Catalytic VTe2@ MgO Heterostructure as Effective Polysulfide Promotor for Lithium–Sulfur Batteries. ACS nano **13**, 13235-13243 (2019).
132. Q. Li, Q. Zhang, J. Sun, C. Liu, J. Guo, B. He, Z. Zhou, P. Man, C. Li, L. Xie, All Hierarchical Core–Shell Heterostructures as Novel Binder-Free Electrode Materials for Ultrahigh-Energy-Density Wearable Asymmetric Supercapacitors. Advanced Science **6**, 1801379 (2019).
133. Q. Zong, H. Yang, Q. Wang, Q. Zhang, Y. Zhu, H. Wang, Q. Shen, Three-dimensional coral-like NiCoP@ C@ Ni (OH) 2 core-shell nanoarrays as battery-type electrodes to enhance cycle stability and energy density for hybrid supercapacitors. Chemical Engineering Journal **361**, 1-11 (2019).
134. F. Li, G. Luo, J. Yu, W. Huang, D. Xu, W. Chen, X. Huang, S. Yang, Y. Fang, X. Yu, Terminal hollowed Fe2O3@ SnO2 heterojunction nanorods anode materials with enhanced performance for lithium-ion battery. Journal of Alloys and Compounds **773**, 778-787 (2019).
135. Q. Liu, X. Hong, X. You, X. Zhang, X. Zhao, X. Chen, M. Ye, X. Liu, Designing heterostructured metal sulfide core-shell nanoneedle films as battery-type electrodes for hybrid supercapacitors. Energy Storage Materials **24**, 541-549 (2020).
136. X. Min, B. Sun, S. Chen, M. Fang, X. Wu, Y. g. Liu, A. Abdelkader, Z. Huang, T. Liu, K. Xi, A textile-based SnO2 ultra-flexible electrode for lithium-ion batteries. Energy Storage Materials **16**, 597-606 (2019).
137. H. Lei, Z. Wang, F. Yang, X. Huang, J. Liu, Y. Liang, J. Xie, M. S. Javed, X. Lu, S. Tan, NiFe nanoparticles embedded N-doped carbon nanotubes as high-efficient electrocatalysts for wearable solid-state Zn-air batteries. Nano Energy **68**, 104293 (2020).
138. Y. Huang, H. Yang, T. Xiong, D. Adekoya, W. Qiu, Z. Wang, S. Zhang, M.-S. Balogun, Adsorption energy engineering of nickel oxide hybrid nanosheets for high areal capacity flexible lithium-ion batteries. Energy Storage Materials **25**, 41-51 (2020).
139. Y. Zhao, J. Cao, Y. Zhang, H. Peng, Gradually Crosslinking Carbon Nanotube Array in Mimicking the Beak of Giant Squid for Compression-Sensing Supercapacitor. Advanced Functional Materials, 1902971 (2019).
140. Q. Zhang, B. He, L. Tang, Z. Zhou, L. Kang, J. Sun, T. Zhang, Q. Li, C. Li, J. Zhao, Fully Solar-Powered Uninterrupted Overall Water-Splitting Systems. Advanced Functional Materials **29**, 1808889 (2019).

141. Q. Zhang, L. Li, H. Li, L. Tang, B. He, C. Li, Z. Pan, Z. Zhou, Q. Li, J. Sun, Ultra-endurance coaxial-fiber stretchable sensing systems fully powered by sunlight. Nano Energy **60**, 267-274 (2019).
142. S. Guo, S. Liang, B. Zhang, G. Fang, D. Ma, J. Zhou, Cathode interfacial layer formation via in situ electrochemically charging in aqueous zinc-ion battery. ACS nano **13**, 13456-13464 (2019).
143. Q. Li, Q. Zhang, C. Liu, Z. Zhou, C. Li, B. He, P. Man, X. Wang, Y. Yao, Anchoring V 2 O 5 nanosheets on hierarchical titanium nitride nanowire arrays to form core–shell heterostructures as a superior cathode for high-performance wearable aqueous rechargeable zinc-ion batteries. Journal of Materials Chemistry A **7**, 12997-13006 (2019).
144. X. Li, Y. Tang, H. Lv, W. Wang, F. Mo, G. Liang, C. Zhi, H. Li, Recent advances in flexible aqueous zinc-based rechargeable batteries. Nanoscale **11**, 17992-18008 (2019).
145. Z. Pan, J. Yang, Y. Zhang, X. Gao, J. Wang, Quasi-solid-state fiber-shaped aqueous energy storage devices: recent advances and prospects. Journal of Materials Chemistry A **8**, 6406-6433 (2020).
146. D. Wang, C. Han, F. Mo, Q. Yang, Y. Zhao, Q. Li, G. Liang, B. Dong, C. Zhi, Energy density issues of flexible energy storage devices. Energy Storage Materials, (2020).
147. L. Shan, J. Zhou, M. Han, G. Fang, X. Cao, X. Wu, S. Liang, Reversible Zn-driven reduction displacement reaction in aqueous zinc-ion battery. Journal of Materials Chemistry A **7**, 7355-7359 (2019).
148. Q. Li, Q. Zhang, C. Liu, J. Sun, J. Guo, J. Zhang, Z. Zhou, B. He, Z. Pan, Y. Yao, Flexible all-solid-state fiber-shaped Ni–Fe batteries with high electrochemical performance. Journal of Materials Chemistry A **7**, 520-530 (2019).
149. X. Wang, R. Ding, X. Ren, L. Shi, Q. Li, Y. Yang, H. Wang, M. Wang, L. Wang, B. Lv, Micron iron oxide particles with thickness-controllable carbon coating for Ni-Fe battery. Electrochimica Acta **299**, 800-808 (2019).
150. X. Wu, H. Zhang, K.-J. Huang, Z. Chen, Stabilizing Metallic Iron Nanoparticles by Conformal Graphitic Carbon Coating for High-Rate Anode in Ni–Fe Batteries. Nano Letters **20**, 1700-1706 (2020).
151. L. Ye, L. Feng, L. Zhao, X. Yang, Y. Zhao, Z. Guo, X. Liu, D. He, Constructing efficient quasi-solid-state alkaline Ni–Fe battery based on Ni–Mn hydroxides/Ni 3 S 2 and FeOOH@ RGO electrodes. Journal of Materials Science: Materials in Electronics **30**, 13076-13089 (2019).

152. C. Liu, Q. Li, J. Cao, Q. Zhang, P. Man, Z. Zhou, C. Li, Y. Yao, Superstructured α-Fe2O3 nanorods as novel binder-free anodes for high-performing fiber-shaped Ni/Fe battery. Science Bulletin, (2020).
153. J. Yang, Z. Wang, Z. Wang, J. Zhang, Q. Zhang, P. P. Shum, L. Wei, All-Metal Phosphide Electrodes for High-Performance Quasi-Solid-State Fiber-Shaped Aqueous Rechargeable Ni–Fe Batteries. ACS Applied Materials & Interfaces **12**, 12801-12808 (2020).
154. Q. Li, Q. Zhang, C. Liu, W. Gong, Z. Zhou, P. Man, J. Guo, B. He, K. Zhang, W. Lu, Interface engineered and surface modulated electrode materials for ultrahigh-energy-density wearable NiCo//Fe batteries. Energy Storage Materials **27**, 316-326 (2020).
155. J. Yao, Y. Liu, H. Zhang, L. Ma, T. Meng, N. Li, J. Jiang, J. Zhu, C. M. Li, Configuring Optimal FeS2@ Carbon Nanoreactor Anodes: Toward Insights into Pyrite Phase Change/Failure Mechanism in Rechargeable Ni–Fe Cells. ACS applied materials & interfaces **11**, 42032-42041 (2019).
156. L. Ma, Y. Xu, Y. Liu, H. Zhang, J. Yao, N. Li, C. M. Li, W. Zhou, J. Jiang, Smart Colloid-Assisted Technique Prompts the Evolution of Bamboo Wastes into Nanometal-Inlaid Carbon Microfibers for Sustainable Ni–Fe Batteries. ACS Sustainable Chemistry & Engineering **7**, 17919-17928 (2019).
157. B. M. Weninger, F. M. Mulder, Renewable Hydrogen and Electricity Dispatch with Multiple Ni–Fe Electrode Storage. ACS energy letters **4**, 567-571 (2019).
158. X. Li, H. Dong, Y. Song, L. Zhang, S. Wang, Copper sulfate as additive for Fe3O4 electrodes of rechargeable Ni–Fe batteries. Asia-Pacific Journal of Chemical Engineering, e2475 (2020).
159. K. C. B. Naidu, N. S. Kumar, H. Manjunatha, P. Benerjee, D. B. Basha, S. N. Kumar, R. Pothu, R. Boddula, Recent Advances in Ni-Fe Batteries as Electrical Energy Storage Devices. Rechargeable Batteries: History, Progress, and Applications, 115 (2020).
160. Y. Wang, H. Wei, H. Lv, Z. Chen, J. Zhang, X. Yan, L. Lee, Z. M. Wang, Y.-L. Chueh, Highly Stable Three-Dimensional Nickel–Cobalt Hydroxide Hierarchical Heterostructures Hybridized with Carbon Nanotubes for High-Performance Energy Storage Devices. ACS nano **13**, 11235-11248 (2019).
161. D. Lei, D.-C. Lee, E. Zhao, A. Magasinski, H.-R. Jung, G. Berdichevsky, D. Steingart, G. Yushin, Iron oxide nanoconfined in carbon nanopores as high capacity anode for rechargeable alkaline batteries. Nano Energy **48**, 170-179 (2018).

162. C. X. Guo, C. M. Li, Molecule-confined FeOx nanocrystals mounted on carbon as stable anode material for high energy density nickel-iron batteries. Nano Energy **42**, 166-172 (2017).
163. M. Yu, X. Cheng, Y. Zeng, Z. Wang, Y. Tong, X. Lu, S. Yang, Dual-doped molybdenum trioxide nanowires: a bifunctional anode for fiber-shaped asymmetric supercapacitors and microbial fuel cells. Angewandte Chemie **128**, 6874-6878 (2016).
164. L. An, J. Feng, Y. Zhang, R. Wang, H. Liu, G. C. Wang, F. Cheng, P. Xi, Epitaxial heterogeneous interfaces on N-NiMoO4/NiS2 nanowires/nanosheets to boost hydrogen and oxygen production for overall water splitting. Advanced Functional Materials **29**, 1805298 (2019).
165. Z. Wang, H. Liu, R. Ge, X. Ren, J. Ren, D. Yang, L. Zhang, X. Sun, Phosphorus-doped Co3O4 nanowire array: a highly efficient bifunctional electrocatalyst for overall water splitting. ACS Catalysis **8**, 2236-2241 (2018).
166. M. Yu, Z. Wang, C. Hou, Z. Wang, C. Liang, C. Zhao, Y. Tong, X. Lu, S. Yang, Nitrogen-Doped Co3O4 Mesoporous Nanowire Arrays as an Additive-Free Air-Cathode for Flexible Solid-State Zinc–Air Batteries. Advanced materials **29**, 1602868 (2017).
167. J. Liu, D. Zhu, T. Ling, A. Vasileff, S.-Z. Qiao, S-NiFe2O4 ultra-small nanoparticle built nanosheets for efficient water splitting in alkaline and neutral pH. Nano Energy **40**, 264-273 (2017).
168. X. Lu, Y. Zeng, M. Yu, T. Zhai, C. Liang, S. Xie, M. S. Balogun, Y. Tong, Oxygen-deficient hematite nanorods as high-performance and novel negative electrodes for flexible asymmetric supercapacitors. Advanced materials **26**, 3148-3155 (2014).
169. Y. Zeng, Y. Han, Y. Zhao, Y. Zeng, M. Yu, Y. Liu, H. Tang, Y. Tong, X. Lu, Advanced Ti-doped Fe2O3@ PEDOT core/shell anode for high-energy asymmetric Supercapacitors. Advanced energy materials **5**, 1402176 (2015).
170. Z. Zhou, Q. Zhang, J. Sun, B. He, J. Guo, Q. Li, C. Li, L. Xie, Y. Yao, Metal–organic framework derived spindle-like carbon incorporated α-Fe2O3 grown on carbon nanotube fiber as anodes for high-performance wearable asymmetric supercapacitors. ACS nano **12**, 9333-9341 (2018).
171. Q. Zhang, J. Sun, Z. Pan, J. Zhang, J. Zhao, X. Wang, C. Zhang, Y. Yao, W. Lu, Q. Li, Stretchable fiber-shaped asymmetric supercapacitors with ultrahigh energy density. Nano Energy **39**, 219-228 (2017).

172. J. Ren, L. Li, C. Chen, X. Chen, Z. Cai, L. Qiu, Y. Wang, X. Zhu, H. Peng, Twisting carbon nanotube fibers for both wire-shaped micro-supercapacitor and micro-battery. Advanced Materials **25**, 1155-1159 (2013).
173. C. Zhao, X. Shao, Y. Zhang, X. Qian, Fe2O3/reduced graphene oxide/Fe3O4 composite in situ grown on Fe foil for high-performance supercapacitors. ACS applied materials & interfaces **8**, 30133-30142 (2016).
174. K. Chi, Z. Zhang, Q. Lv, C. Xie, J. Xiao, F. Xiao, S. Wang, Well-ordered oxygen-deficient CoMoO4 and Fe2O3 nanoplate arrays on 3D graphene foam: toward flexible asymmetric supercapacitors with enhanced capacitive properties. ACS applied materials & interfaces **9**, 6044-6053 (2017).
175. T. Li, H. Yu, L. Zhi, W. Zhang, L. Dang, Z. Liu, Z. Lei, Facile electrochemical fabrication of porous Fe2O3 nanosheets for flexible asymmetric supercapacitors. The Journal of Physical Chemistry C **121**, 18982-18991 (2017).
176. K. A. Owusu, L. Qu, J. Li, Z. Wang, K. Zhao, C. Yang, K. M. Hercule, C. Lin, C. Shi, Q. Wei, Low-crystalline iron oxide hydroxide nanoparticle anode for high-performance supercapacitors. Nature communications **8**, 1-11 (2017).
177. J. Yang, Z. Wang, Z. Wang, J. Zhang, Q. Zhang, P. P. Shum, L. Wei, All Metal Phosphide Electrodes for High-Performance Quasi-Solid-State Fiber-shaped Aqueous Rechargeable Ni-Fe Batteries. ACS Applied Materials & Interfaces, (2020).
178. G. Q. Zhang, H. B. Wu, H. E. Hoster, M. B. Chan-Park, X. W. D. Lou, Single-crystalline NiCo 2 O 4 nanoneedle arrays grown on conductive substrates as binder-free electrodes for high-performance supercapacitors. Energy & Environmental Science **5**, 9453-9456 (2012).
179. G. Zhang, X. W. Lou, General solution growth of mesoporous NiCo2O4 nanosheets on various conductive substrates as high-performance electrodes for supercapacitors. Advanced materials **25**, 976-979 (2013).
180. L. Xie, Q. Zong, Q. Zhang, J. Sun, Z. Zhou, B. He, Z. Zhu, E. Songfeng, Y. Yao, Hierarchical NiCoP nanosheet arrays with enhanced electrochemical properties for high-performance wearable hybrid capacitors. Journal of Alloys and Compounds **781**, 783-789 (2019).
181. R. Wang, Y. Han, Z. Wang, J. Jiang, Y. Tong, X. Lu, Nickel@ Nickel Oxide Core–Shell Electrode with Significantly Boosted Reactivity for Ultrahigh-Energy and Stable Aqueous Ni–Zn Battery. Advanced Functional Materials **28**, 1802157 (2018).

182. J. Liu, J. Jiang, M. Bosman, H. J. Fan, Three-dimensional tubular arrays of MnO 2–NiO nanoflakes with high areal pseudocapacitance. Journal of Materials Chemistry **22**, 2419-2426 (2012).
183. W. Ren, D. Guo, M. Zhuo, B. Guan, D. Zhang, Q. Li, NiMoO 4@ Co (OH) 2 core/shell structure nanowire arrays supported on Ni foam for high-performance supercapacitors. RSC Advances **5**, 21881-21887 (2015).
184. D. Kong, C. Cheng, Y. Wang, J. I. Wong, Y. Yang, H. Y. Yang, Three-dimensional Co 3 O 4@ C@ Ni 3 S 2 sandwich-structured nanoneedle arrays: towards high-performance flexible all-solid-state asymmetric supercapacitors. Journal of Materials Chemistry A **3**, 16150-16161 (2015).
185. Y. Huang, W. S. Ip, Y. Y. Lau, J. Sun, J. Zeng, N. S. S. Yeung, W. S. Ng, H. Li, Z. Pei, Q. Xue, Weavable, conductive yarn-based NiCo//Zn textile battery with high energy density and rate capability. ACS nano **11**, 8953-8961 (2017).
186. Y. Zeng, X. Zhang, Y. Meng, M. Yu, J. Yi, Y. Wu, X. Lu, Y. Tong, Achieving Ultrahigh Energy Density and Long Durability in a Flexible Rechargeable Quasi-Solid-State Zn–MnO2 Battery. Advanced Materials **29**, 1700274 (2017).
187. F. Wan, L. Zhang, X. Wang, S. Bi, Z. Niu, J. Chen, An Aqueous Rechargeable Zinc-Organic Battery with Hybrid Mechanism. Advanced Functional Materials **28**, 1804975 (2018).
188. H. Li, Z. Liu, G. Liang, Y. Huang, Y. Huang, M. Zhu, Z. Pei, Q. Xue, Z. Tang, Y. Wang, Waterproof and tailorable elastic rechargeable yarn zinc ion batteries by a cross-linked polyacrylamide electrolyte. ACS nano **12**, 3140-3148 (2018).
189. Z. Guo, Y. Zhao, Y. Ding, X. Dong, L. Chen, J. Cao, C. Wang, Y. Xia, H. Peng, Y. Wang, Multi-functional flexible aqueous sodium-ion batteries with high safety. Chem **3**, 348-362 (2017).
190. L. Ji, Z. Lin, M. Alcoutlabi, X. Zhang, Recent developments in nanostructured anode materials for rechargeable lithium-ion batteries. Energy & Environmental Science **4**, 2682-2699 (2011).
191. Y. Zhao, Y. Zhang, H. Sun, X. Dong, J. Cao, L. Wang, Y. Xu, J. Ren, Y. Hwang, I. H. Son, A self-healing aqueous lithium-ion battery. Angewandte Chemie International Edition **55**, 14384-14388 (2016).
192. Y. Tang, Y. Zhang, W. Li, B. Ma, X. Chen, Rational material design for ultrafast rechargeable lithium-ion batteries. Chemical Society Reviews **44**, 5926-5940 (2015).
193. Y. Zhang, W. Bai, X. Cheng, J. Ren, W. Weng, P. Chen, X. Fang, Z. Zhang, H. Peng, Flexible and stretchable lithium-ion batteries and supercapacitors based on

electrically conducting carbon nanotube fiber springs. Angewandte Chemie International Edition **53**, 14564-14568 (2014).

194. D. Kong, W. Ren, C. Cheng, Y. Wang, Z. Huang, H. Y. Yang, Three-dimensional NiCo2O4@ polypyrrole coaxial nanowire arrays on carbon textiles for high-performance flexible asymmetric solid-state supercapacitor. ACS applied materials & interfaces **7**, 21334-21346 (2015).
195. Y. Zhang, Y. Wang, L. Wang, C.-M. Lo, Y. Zhao, Y. Jiao, G. Zheng, H. Peng, A fiber-shaped aqueous lithium ion battery with high power density. Journal of Materials Chemistry A **4**, 9002-9008 (2016).
196. S. Huang, F. Wan, S. Bi, J. Zhu, Z. Niu, J. Chen, A self-healing integrated all-in-one zinc-ion battery. Angewandte Chemie **131**, 4357-4361 (2019).
197. C. Li, Q. Zhang, J. Sun, T. Li, S. E, Z. Zhu, B. He, Z. Zhou, Q. Li, Y. Yao, High-performance quasi-solid-state flexible aqueous rechargeable Ag–Zn battery based on metal–organic framework-derived Ag nanowires. ACS Energy Letters **3**, 2761-2768 (2018).
198. H. Li, L. Ma, C. Han, Z. Wang, Z. Liu, Z. Tang, C. Zhi, Advanced rechargeable zinc-based batteries: Recent progress and future perspectives. Nano Energy **62**, 550-587 (2019).
199. F. Wan, Y. Zhang, L. Zhang, D. Liu, C. Wang, L. Song, Z. Niu, J. Chen, Reversible Oxygen Redox Chemistry in Aqueous Zinc-Ion Batteries. Angewandte Chemie International Edition **58**, 7062-7067 (2019).
200. P. He, M. Yan, G. Zhang, R. Sun, L. Chen, Q. An, L. Mai, Layered VS2 nanosheet-based aqueous Zn ion battery cathode. Advanced Energy Materials **7**, 1601920 (2017).
201. F. Wan, Z. Niu, Design Strategies for Vanadium-based Aqueous Zinc-Ion Batteries. Angewandte Chemie International Edition **58**, 16358-16367 (2019).
202. H. Zhang, J. Wang, Q. Liu, W. He, Z. Lai, X. Zhang, M. Yu, Y. Tong, X. Lu, Extracting oxygen anions from ZnMn2O4: robust cathode for flexible all-solid-state Zn-ion batteries. Energy Storage Materials **21**, 154-161 (2019).
203. Y. Xu, Y. Zhang, Z. Guo, J. Ren, Y. Wang, H. Peng, Flexible, stretchable, and rechargeable fiber-shaped zinc–air battery based on cross-stacked carbon nanotube sheets. Angewandte Chemie **127**, 15610-15614 (2015).
204. C. Guan, W. Zhao, Y. Hu, Q. Ke, X. Li, H. Zhang, J. Wang, High-performance flexible solid-state Ni/Fe battery consisting of metal oxides coated carbon cloth/carbon nanofiber electrodes. Advanced Energy Materials **6**, 1601034 (2016).

205. Y. Xu, Y. Zheng, C. Wang, Q. Chen, An All-Organic Aqueous Battery Powered by Adsorbed Quinone. ACS applied materials & interfaces **11**, 23222-23228 (2019).
206. M. Gong, Y. Li, H. Wang, Y. Liang, J. Z. Wu, J. Zhou, J. Wang, T. Regier, F. Wei, H. Dai, An advanced Ni–Fe layered double hydroxide electrocatalyst for water oxidation. Journal of the American Chemical Society **135**, 8452-8455 (2013).
207. C. Guan, Y. Wang, Y. Hu, J. Liu, K. H. Ho, W. Zhao, Z. Fan, Z. Shen, H. Zhang, J. Wang, Conformally deposited NiO on a hierarchical carbon support for high-power and durable asymmetric supercapacitors. Journal of Materials Chemistry A **3**, 23283-23288 (2015).
208. K.-N. Kang, I.-H. Kim, A. Ramadoss, S.-I. Kim, J.-C. Yoon, J.-H. Jang, Ultrathin nickel hydroxide on carbon coated 3D-porous copper structures for high performance supercapacitors. Physical Chemistry Chemical Physics **20**, 719-727 (2018).
209. X. Xiong, D. Ding, D. Chen, G. Waller, Y. Bu, Z. Wang, M. Liu, Three-dimensional ultrathin Ni (OH) 2 nanosheets grown on nickel foam for high-performance supercapacitors. Nano Energy **11**, 154-161 (2015).
210. J. Sun, Y. Huang, C. Fu, Y. Huang, M. Zhu, X. Tao, C. Zhi, H. Hu, A high performance fiber-shaped PEDOT@ MnO 2//C@ Fe 3 O 4 asymmetric supercapacitor for wearable electronics. Journal of materials chemistry A **4**, 14877-14883 (2016).
211. X. Wang, W. Tian, D. Liu, C. Zhi, Y. Bando, D. Golberg, Unusual formation of α-Fe2O3 hexagonal nanoplatelets in N-doped sandwiched graphene chamber for high-performance lithium-ions batteries. Nano Energy **2**, 257-267 (2013).
212. Y. Zeng, M. Yu, Y. Meng, P. Fang, X. Lu, Y. Tong, Iron-based supercapacitor electrodes: advances and challenges. Advanced Energy Materials **6**, 1601053 (2016).
213. M. Sun, H. Liu, J. Qu, J. Li, Earth-rich transition metal phosphide for energy conversion and storage. Advanced Energy Materials **6**, 1600087 (2016).
214. Z. Zhang, S. Liu, J. Xiao, S. Wang, Fiber-based multifunctional nickel phosphide electrodes for flexible energy conversion and storage. Journal of Materials Chemistry A **4**, 9691-9699 (2016).
215. X.-L. Qi, D.-D. Zhou, J. Zhang, S. Hu, M. Haranczyk, D.-Y. Wang, Simultaneous improvement of mechanical and fire-safety properties of polymer composites

with phosphonate-loaded MOF additives. ACS applied materials & interfaces **11**, 20325-20332 (2019).

216. H. Liang, C. Xia, Q. Jiang, A. N. Gandi, U. Schwingenschlögl, H. N. Alshareef, Low temperature synthesis of ternary metal phosphides using plasma for asymmetric supercapacitors. Nano Energy **35**, 331-340 (2017).
217. Y. Lan, H. Zhao, Y. Zong, X. Li, Y. Sun, J. Feng, Y. Wang, X. Zheng, Y. Du, Phosphorization boosts the capacitance of mixed metal nanosheet arrays for high performance supercapacitor electrodes. Nanoscale **10**, 11775-11781 (2018).
218. X. Li, A. M. Elshahawy, C. Guan, J. Wang, Metal phosphides and phosphates-based electrodes for electrochemical supercapacitors. Small **13**, 1701530 (2017).
219. S. Liu, K. V. Sankar, A. Kundu, M. Ma, J.-Y. Kwon, S. C. Jun, Honeycomb-like interconnected network of nickel phosphide heteronanoparticles with superior electrochemical performance for supercapacitors. ACS Applied Materials & Interfaces **9**, 21829-21838 (2017).
220. P. E. Blanchard, A. P. Grosvenor, R. G. Cavell, A. Mar, X-ray Photoelectron and Absorption Spectroscopy of Metal-Rich Phosphides M 2P and M 3P (M= Cr–Ni). Chemistry of Materials **20**, 7081-7088 (2008).
221. S. T. Oyama, Novel catalysts for advanced hydroprocessing: transition metal phosphides. Journal of catalysis **216**, 343-352 (2003).
222. X. Chen, M. Cheng, D. Chen, R. Wang, Shape-controlled synthesis of Co2P nanostructures and their application in supercapacitors. ACS applied materials & interfaces **8**, 3892-3900 (2016).
223. J. Sun, Q. Zhang, X. Wang, J. Zhao, J. Guo, Z. Zhou, J. Zhang, P. Man, J. Sun, Q. Li, Correction: Constructing hierarchical dandelion-like molybdenum–nickel–cobalt ternary oxide nanowire arrays on carbon nanotube fiber for high-performance wearable fiber-shaped asymmetric supercapacitors. Journal of Materials Chemistry A **6**, 8120-8120 (2018).
224. C. Guan, X. Liu, W. Ren, X. Li, C. Cheng, J. Wang, Rational design of metal-organic framework derived hollow NiCo2O4 arrays for flexible supercapacitor and electrocatalysis. Advanced Energy Materials **7**, 1602391 (2017).
225. Q. Zhang, W. Xu, J. Sun, Z. Pan, J. Zhao, X. Wang, J. Zhang, P. Man, J. Guo, Z. Zhou, Constructing ultrahigh-capacity zinc–nickel–cobalt oxide@ Ni (OH) 2 core–shell nanowire arrays for high-performance coaxial fiber-shaped asymmetric supercapacitors. Nano letters **17**, 7552-7560 (2017).

226. Y. Li, J. Xu, T. Feng, Q. Yao, J. Xie, H. Xia, Fe2O3 nanoneedles on ultrafine nickel nanotube arrays as efficient anode for high-performance asymmetric supercapacitors. Advanced Functional Materials **27**, 1606728 (2017).
227. L. Gao, J. U. Surjadi, K. Cao, H. Zhang, P. Li, S. Xu, C. Jiang, J. Song, D. Sun, Y. Lu, Flexible fiber-shaped supercapacitor based on nickel–cobalt double hydroxide and pen ink electrodes on metallized carbon fiber. ACS applied materials & interfaces **9**, 5409-5418 (2017).
228. Z.-A. Hu, Y.-L. Xie, Y.-X. Wang, H.-Y. Wu, Y.-Y. Yang, Z.-Y. Zhang, Synthesis and electrochemical characterization of mesoporous CoxNi1− x layered double hydroxides as electrode materials for supercapacitors. Electrochimica Acta **54**, 2737-2741 (2009).
229. Z. Cai, A. Wu, H. Yan, Y. Xiao, C. Chen, C. Tian, L. Wang, R. Wang, H. Fu, Hierarchical whisker-on-sheet NiCoP with adjustable surface structure for efficient hydrogen evolution reaction. Nanoscale **10**, 7619-7629 (2018).
230. X. Li, H. Wu, A. M. Elshahawy, L. Wang, S. J. Pennycook, C. Guan, J. Wang, Cactus-like NiCoP/NiCo-OH 3D architecture with tunable composition for high-performance electrochemical capacitors. Advanced Functional Materials **28**, 1800036 (2018).
231. P. Yang, Y. Ding, Z. Lin, Z. Chen, Y. Li, P. Qiang, M. Ebrahimi, W. Mai, C. P. Wong, Z. L. Wang, Low-cost high-performance solid-state asymmetric supercapacitors based on MnO2 nanowires and Fe2O3 nanotubes. Nano letters **14**, 731-736 (2014).
232. L. Wang, H. Yang, X. Liu, R. Zeng, M. Li, Y. Huang, X. Hu, Constructing hierarchical tectorum-like α-Fe2O3/PPy nanoarrays on carbon cloth for solid-state asymmetric supercapacitors. Angewandte Chemie International Edition **56**, 1105-1110 (2017).
233. C. Zhu, P. Yang, D. Chao, X. Wang, X. Zhang, S. Chen, B. K. Tay, H. Huang, H. Zhang, W. Mai, All metal nitrides solid-state asymmetric supercapacitors. Advanced Materials **27**, 4566-4571 (2015).
234. S. Xu, C. Su, T. Wang, Y. Ma, J. Hu, J. Hu, N. Hu, Y. Su, Y. Zhang, Z. Yang, One-step electrodeposition of nickel cobalt sulfide nanosheets on Ni nanowire film for hybrid supercapacitor. Electrochimica Acta **259**, 617-625 (2018).